UNIVERSITÀ DEGLI STUDI DI SIENA
Dipartimento di Biotecnologie, Chimica e Farmacia
Dottorato in Chemical and Pharmaceutical Sciences
XXXVIII Ciclo

Coordinatore: Prof. Maurizio Taddei

Food traceability and valorization of bioactive molecules for advanced delivery system

Settore scientifico disciplinare: CHIM 02

Candidata

Sara Costantini

Firma digitale della candidata

Firmato digitalmente da COSTANTINI SARA
C = IT

Supervisore

Prof.ssa Claudia Bonechi

Anno accademico di conseguimento del titolo di Dottore di ricerca

2024/2025

Università degli Studi di Siena

Dottorato in Chemical and Pharmaceutical Sciences

XXXVIII° Ciclo

Data dell'esame finale

14/04/2026

Commissione giudicatrice

Lorenzo Cecchi - Ricercatore, Università di Firenze

Giuseppe Capobianco - Professore Associato, Sapienza Università di Roma

Alessandro Donati - Professore Associato, Università di Siena

Supplenti

Lorenzo Cotrozzi – Professore Associato, Università di Pisa

Summary

Abstract

Proper nutrition is essential for ensuring overall well-being and preventing numerous chronic diseases.

Selecting high-quality foods, rich in nutrients and bioactive compounds, is fundamental for maintaining physiological balance and promoting a healthy lifestyle. In this context, the geographical traceability of food products plays a crucial role: accurately knowing the origin and characteristics of a product allows not only to guarantee food safety but also to ensure authenticity, quality, and transparency throughout the entire production chain.

Moreover, traceability enhances territorial specificities, protects local agricultural traditions, and encourages sustainable practices that respect the environment and preserve biodiversity.

At the same time, food waste (often caused by overproduction and inefficiencies along the supply chain) represents a significant environmental and social challenge. The innovative recycling of food by-products offers a promising solution: transforming waste into valuable ingredients for industrial applications not only reduces environmental impact but also contributes to the conservation of natural resources. The food industry generates large amounts of by-products (such as peels, seeds, stems, and fruit and vegetable pulp) that are often discarded despite being rich in bioactive compounds including antioxidants, fibres, proteins, and essential fatty acids. Recovering and valorising these materials enables the development of innovative products in the food, pharmaceutical, and agricultural sectors.

Among the most relevant bioactive compounds found in foods are polyphenols, a widespread class of natural antioxidants. From a biological perspective, polyphenols are substances capable of preventing or slowing cellular oxidative damage caused by reactive species such as free radicals and nitrogen and oxygen oxides. Due to these properties, they have become the focus of extensive research as therapeutic agents integrated into innovative drug delivery systems, which improve their stability, bioavailability, and controlled release at target tissues, thereby enhancing their efficacy while reducing side effects.

The challenge of synthesizing formulations for drug delivery has also involved purely synthetic molecules, particularly corticosteroids used in the treatment of inflammatory ocular diseases.

Chapter 1

Drug Delivery Systems

A drug delivery system is responsible for the controlled release of the active pharmaceutical ingredient in order to achieve the desired therapeutic effect[1]. Conventional dosage forms (such as tablets, capsules, syrups, and ointments) are often associated with poor bioavailability and significant fluctuations in plasma drug concentrations, making them unable to ensure sustained and consistent release. Without an efficient delivery mechanism, the entire therapeutic process may be compromised[2].

Many pharmacological properties of conventional ("free") drugs can be significantly improved through the use of drug delivery systems (DDS), which typically employ particulate carriers composed primarily of lipids and/or polymers to transport and protect their associated therapeutic agents.

By enhancing drug stability, modulating pharmacokinetics, and enabling controlled or targeted release, DDS offer a strategic approach to overcoming the intrinsic limitations of traditional formulations and improving overall therapeutic outcomes. In particular, lipid-based drug delivery systems (LBDDS) are those most commonly used when the pharmaceutical ingredient has poor solubility and low permeability to biological membranes. LBDDS have attracted growing interest due to their size-dependent properties and their high biocompatibility and versatility. These advantages have made them one of the most promising solutions in the field of drug delivery. LBDDS are also commercially viable and suitable for the formulation of pharmaceutical products intended for various routes of administration, including topical, oral, pulmonary, and parenteral.

Another strength of these formulations is their structural flexibility, which allows for specific modifications based on the disease to be treated, the desired route of administration, and economic or technical factors such as product stability, toxicity, and therapeutic efficacy. Thanks to their safety and efficiency, lipid carriers are ideal candidates not only for drug formulation, but also for vaccines, diagnostic agents, and nutraceuticals[3].

Lipids, fundamental elements of biological membranes, have an extraordinary affinity for both hydrophilic and hydrophobic molecules, giving them exceptional biocompatibility and bioavailability. This intrinsic versatility has led to their widespread use in various modes of drug delivery, ranging from simple encapsulation in liposomes to sophisticated lipid-based nanoparticles.

The double lipid layer structure protects the active ingredient from the action of enzymes and premature elimination, while allowing controlled and targeted release at the site of action. The typical "double layer system" is formed due to the intrinsic ability of lipids to self-assemble into orderly and stable structures (**Figure 1**). When combined with the active ingredient and subjected to specific processes, these lipids create effective vehicles capable of transporting the drug and releasing it in a controlled manner at the site of action.[4]

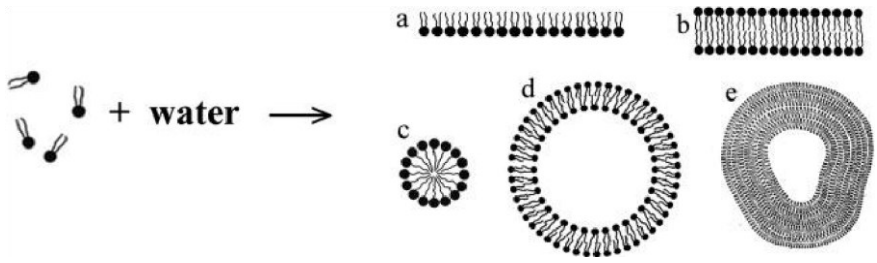

Figure 1. Schematic illustration of the self-assembly process of lipids in water, forming aggregates such as (a) a monolayer on the air-water interface, (b) a lipid bilayer, (c) a micelle, (d) a unilamellar liposome (vesicle), and (e) a multilamellar liposome.

The forces that allow amphiphiles to self-assemble into these structures derive from their molecular conformation. Hydrocarbon chains tend to attract each other, mainly due to hydrophobic interactions or interfacial tension forces at the boundary between hydrocarbons and water. In contrast, the head groups undergo hydrophilic, ionic, or steric interactions, which allow them to meet water. These two types of interactions manifest themselves as a competition between two opposing forces: one pushes to reduce the interface area, while the other tends to increase it[5]. The balance between these forces determines an optimal area per molecule exposed to the aqueous phase, called α_0 or "effective head group area," which minimizes the total interaction energy per molecule. The shape and properties of lipid structures also depend on the volume (v) and the maximum effective length (l), known as the critical chain length, which corresponds approximately to the length of the fully extended chain. Knowing these geometric limitations—optimal area α_0, volume v, and critical length l—it is possible to predict the structures that molecules can form (**Figure 2**). A key parameter for this analysis is the critical packing parameter, a dimensionless factor that describes the shape of molecules and their modes of self-assembly.

$$\text{CPP} = \frac{v}{\alpha_0 l_c} \qquad (1)$$

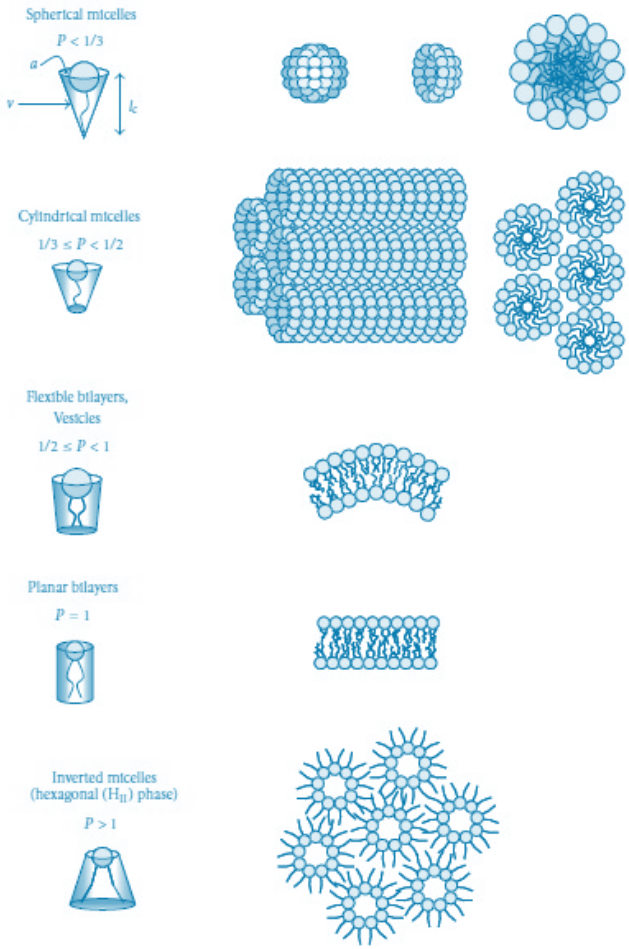

Figure 2. shows the relationship between the critical packing parameter and the shape of the molecules.

The family of lipid-based drug delivery systems includes classical structures such as emulsions and liposomes, as well as more advanced systems like vesosomes, phytosomes, solid lipid nanoparticles (SLNs), nanostructured lipid carriers (NLCs), and archaeosomes. These next-generation platforms offer unique structural and functional features, enabling innovative applications in drug delivery.[5]

Liposomes come from the Greek words “lipos” and “soma” and was first described in 1964 by Dr. Alec D Bangham at the Babraham Institute in Cambridge. Liposomes are spherical vesicles made up of the same components as cell membranes and are formed thanks to the ability of phospholipids to spontaneously self-assemble in aqueous environments. Their classification is based on three main criteria: size, number of lipid bilayers present in the particle, and structural arrangement of the membranes[6-7]. They are classified as multilamellar large vesicles, typically larger than 0.5 µm in size. Multilamellar liposomes are characterized by the presence of multiple concentric lipid bilayers. A

subtype, known as oligolamellar vesicles, contains between 2 and 5 lipid bilayers and is structurally similar to multilamellar vesicles; however, when the number of bilayers exceeds five, the vesicles are generally classified as truly multilamellar. In contrast, unilamellar vesicles (ULVs) consist of a single lipid bilayer and are further subdivided based on size into small unilamellar vesicles (SUVs) and large unilamellar vesicles (LUVs). While their internal structure is similar, they differ significantly in diameter. For drug delivery applications, the lamellar structure of liposomes is less important than the homogeneity and size of these systems; liposomes in the range of 50-200 nm are preferred[9].

Other possible classifications of liposomes concern the formulation, the type of lipids used, or the method of preparation: among the main classes of natural lipids, the most commonly used are phospholipids, sphingolipids, and sterols. In addition, natural lipids can be negative, positive, or zwitterionic based on the charge present on the polar heads of the molecule[10]. Liposome synthesis is a heavily investigated area of research with many recent and modified techniques, but the most common method is the 'Thini Film Idratation': it consists of solubilizing the lipids of interest in an organic solvent, which is then evaporated, resulting in the formation of a lipid film. The film is rehydrated using an aqueous solution, leading to the formation of liposomes. If the active ingredient is hydrophilic, it can be incorporated directly into the aqueous solution; if it is lipophilic, it is initially inserted into the lipid film. This method leads to the synthesis of liposomes with high polydispersity index, therefore requiring postformation treatments such as extrusion, high-pressure homogenization, or sonication to ensure the formation of homogeneous unilamellar vesicles[11-12].

Liposomes are notorious for their physical instability. Over time, liposomal particles can aggregate due to electrostatic or van der Waals interactions, forming larger particles. This phenomenon can compromise the size distribution, bioavailability, and efficacy of the delivery system. In addition, liposomes can fuse together (coalescence of two or more vesicles into a single structure), causing uncontrolled release of the active ingredient and loss of the original properties of the system. The water present in the aqueous core of liposomes can promote undesirable chemical reactions, causing the drug to degrade before it reaches the site of action. This compromises both the chemical stability of the active ingredient and the overall therapeutic efficacy of the formulation. Another significant limitation of liposomes is their tendency to release the drug prematurely, through leakage (loss through the lipid bilayer) or leaching (release due to interactions with the external environment). These processes can be aggravated by changes in temperature, pH, or ionic strength, making it difficult to ensure controlled and targeted release. As a result, a significant portion of the active ingredient may be lost during storage or before reaching the desired therapeutic site.

Solid lipid nanoparticles (SLNs) were developed to overcome the limitations associated with traditional colloidal systems: they are formulated using a variety of lipids that share key characteristics, such as a low melting point and solidity at both room temperature and body temperature, together with a combination of surfactants and/or co-surfactants. The appropriate selection of lipids and surfactants plays a crucial role in determining their physicochemical properties, including particle size, polydispersity index, surface charge, stability (both short- and long-term), drug loading capacity, and drug release behavior[13]. One of the main drivers behind the rapid development of solid lipid nanoparticles (SLNs) has been their remarkable ability to effectively deliver both lipophilic and hydrophilic drugs across a variety of diseased tissues. Beyond conventional small molecules, SLNs have demonstrated the capability to transport a wide range of therapeutic agents; this versatility significantly broadens their potential applications in targeted therapy and nanomedicine. A further advantage of SLNs lies in their ability to reduce the inherent toxicity of the therapeutic agents they carry by encapsulating these molecules, SLNs provide a protective environment that not only minimizes direct cytotoxic effects but also shields the cargo from premature degradation and rapid clearance by the reticuloendothelial system (RES). This extended circulation time can greatly enhance bioavailability and therapeutic efficacy.
Moreover, SLNs exhibit excellent long-term physical and chemical stability, making them suitable for prolonged storage and use[14]. However, despite their many advantages, SLNs are not without limitations. Some of the challenges associated with these nanocarriers include drug expulsion during storage, the tendency to undergo gelation, and low encapsulation efficiency (EE). The latter is particularly significant and is attributed to the highly ordered crystalline structure of the lipid core. During crystallization, the formation of dense, defect-free lattices leaves little room for accommodating drug molecules, especially those that do not integrate well into the lipid matrix, resulting in suboptimal drug loading[15]. The next generation of lipid nanoparticles (NLC) consists of a mixture of solid and liquid phases (oil) that forms a shapeless matrix, in order to meet the challenge of improving stability and loading capacity.[16] These colloidal drug carrier systems offer targeted delivery of drugs and increase the bioavailability of hydrophobic drugs, and protect sensitive active compounds.

Another possibility is lipid nanoparticles (LNPs), spherical vesicles consisting of ionizable lipids, which are positive at low pH, widely used in complexation with RNA, and neutral at physiological pH, thus reducing potential toxic effects compared to lipids that are always positive, such as those found in liposomes.[17] Due to their size and chemical-physical properties, LNPs are absorbed by cells

via endocytosis, and the ability of lipids to ionize at low pH probably allows endosomal escape, enabling the release of the contents into the cytoplasm. In addition to ionizable lipids, LNPs usually contain a helper lipid that promotes adhesion to cell membranes, cholesterol that fills the spaces between lipids and provides structural stability, and polyethylene glycol (PEG) that reduces opsonization by serum proteins and clearance by the reticuloendothelial system. The relative composition of the different lipid components significantly affects the efficacy of LNPs and must be carefully optimized according to the therapeutic application and route of administration.
In addition, the type of lipid, size, and surface charge of the nanoparticles determine their behavior in vivo, affecting their bioavailability, distribution, and efficiency in releasing the active ingredient.

Synthesis

About the synthesis of these nanocarrier, there is one more possibility compared to manual techniques, Microfluidic. Microfluidic technologies are revolutionizing the synthesis of nanoscale lipid particles and enabling new opportunities for the production of lipid-based nanomedicines.[18]
In this process, nanoparticle formation occurs as a result of strong solubility gradients, which emerge from the rapid mixing of solutions. This mixing is precisely controlled by convective flows within microchannels, which generally range in size from a few tens to several hundred micrometers. There are a number of factors to consider, such as the choice of solvent for the aqueous and organic phases, the solubility and concentration of the lipids selected for the formulation; these all are part of the 'input parameters' that can affect the outcome of the synthesis. There are also instrumental parameters that must be carefully chosen, such as chip design, total flow rate (the flow rate of solvents through the chip), flow rate ratio (the ratio between the aqueous and organic phases), and the transition temperature of the lipids used.[19]
The main advantages of using microfluidics therefore concern high reproducibility, system automation, greater control over experimental conditions, the possibility of customizing the characteristics of nanoparticles (shape, size), and obtaining monodisperse systems.

Dynamic Light Scattering

When developing drug delivery systems (DDS) based on nanoparticles, it is essential to consider a range of physicochemical parameters that directly influence the behavior of the particles in a biological environment.

Among these, particle size and surface charge are two of the most critical factors, as they affect several biological responses, including cellular uptake, toxicity, and the dissolution rate of the active pharmaceutical ingredient. These two properties appear to play a key role not only in pharmacokinetics but also in the drug release profile; furthermore, the ability to selectively release the drug at specific target sites largely depends on the size and charge of the nanoparticles.

An additional layer of complexity arises from the interaction of nanoparticles with biological matrices, such as bodily fluids or intestinal mucus, which can significantly alter their surface properties. Therefore, accurate characterization of particle size and zeta potential is crucial during the design and optimization stages of DDS formulations to ensure both efficacy and safety[20]

The Dynamic Light Scattering (DLS) technique is based on the analysis of fluctuations in the intensity of light scattered by particles suspended in a liquid, and it is widely used to determine the hydrodynamic diameter of nanoparticles. The fundamental principle of this technique lies in the relationship between the Brownian motion of the particles and the temporal variation in the light they scatter.

When a sample containing nanoparticles is illuminated by a laser beam, the particles in suspension scatter light in various directions. However, due to their random (Brownian) motion, the intensity of the scattered light does not remain constant over time but rather fluctuates depending on the speed at which the particles move. Under controlled temperature and viscosity conditions, smaller particles exhibit faster Brownian motion, resulting in rapid fluctuations in scattered light intensity.

In contrast, larger particles move more slowly, producing slower variations in intensity.

These fluctuations are detected by a photodetector and analyzed using a correlator, which calculates the autocorrelation function of the signal. This function describes how the scattered light intensity at a given time correlates with that at a later time. The rate at which this correlation decays allows the calculation of the translational diffusion coefficient of the particles.

Finally, by applying the Stokes-Einstein equation, the diffusion coefficient can be converted into a hydrodynamic diameter, a measure of the effective size of the particle in solution, which accounts not only for the solid core but also for the surrounding solvation layer. This information is essential for the characterization of nanoparticle-based drug delivery systems, as particle size influences critical parameters such as bioavailability, tissue distribution, and drug release profile[21].

Among the various parameters, particle size stands out as a key attribute, as it influences several critical aspects of nanocarrier performance, including colloidal stability, encapsulation efficiency, drug release kinetics, biodistribution, mucoadhesiveness, and cellular interaction[22].

Vesicle size is one of the main parameters that determines clearance by the reticuloendothelial system (RES): the rate of uptake by the immune system cells increases by the increase in the size of the lipidic carriers.

Another key parameter used to characterize the size distribution of lipid-based nanocarrier systems is the polydispersity index (PDI). The term "polydispersity" refers to the degree of non-uniformity in particle size distribution within a given sample[23]; the PDI quantifies how broad or narrow the range of particle sizes is.

Numerically, PDI values range from 0.0, indicating a perfectly monodisperse system to 1.0, which represents a highly polydisperse system with significant variation and the presence of multiple size populations. For polymeric nanoparticles, a PDI of 0.2 or lower is generally considered acceptable, indicating a sufficiently uniform size distribution[24].

In the context of lipid-based drug delivery systems a PDI value of 0.3 or below is typically regarded as acceptable. Such a value suggests a homogeneous population of vesicles, which is crucial for ensuring reproducibility, stability, and consistent biological performance of the formulation.

Nuclear Magnetic Resonance

Nuclear magnetic resonance (NMR) spectroscopy is a powerful tool to probe the structure and dynamics of virtually all types of molecules at atomic resolution.

In the context of lipid drug delivery systems, quality control is essential to ensure batch-to-batch reproducibility and the overall reliability of experimental outcomes. Furthermore, the optimization of liposomal formulations requires a deep understanding of the molecular interactions between the liposome and its cargo, as these interactions directly influence encapsulation efficiency and release kinetics.

In this context, we highlight the versatility of liquid-state NMR spectroscopy, to investigate the structural features of both lipid components and bioactive compound, as well as their mutual interactions.

Unlike many other analytical methods, NMR allows for simultaneous, in situ, and real-time monitoring of all NMR-visible species within a sample. Moreover, it does not require chemical modifications that could potentially alter the physicochemical properties of the system under investigation.

Despite limitations - such as lower sensitivity compared to more conventional techniques - the richness of structural and dynamic information offered by NMR makes it an invaluable tool for the design and optimization of liposomes and other lipid based drug delivery systems.[25]

Infrared Spectroscopy

The structural characterization of lipid bilayers plays a fundamental role not only in elucidating key biological mechanisms—such as membrane fluidity, permeability, and protein-lipid interactions—but also in the rational design of lipid-based drug delivery systems (LDDS). Among the available analytical techniques, Attenuated Total Reflection Fourier Transform Infrared (ATR-FTIR) spectroscopy has emerged as a valuable tool for investigating the physicochemical properties of lipid membranes at the molecular level.

ATR-FTIR allows for the identification of specific functional groups and provides insight into conformational order, phase transitions, and hydrogen bonding within the bilayer. This makes it particularly suitable for studying how variations in lipid composition or the incorporation of therapeutic agents influence membrane structure and stability.

However, conventional FTIR approaches often struggle to provide detailed information regarding molecular orientation, chain packing, and intermolecular interactions, especially in complex or dynamic systems such as those involving liposomes or nanostructured lipid carriers. These limitations arise from factors such as signal overlap, low sensitivity to directional alignment, and the inability to distinguish between overlapping vibrational modes in heterogeneous environments. When carefully interpreted, ATR-FTIR data can offer crucial insights into how lipid membranes behave under physiological conditions and how they interact with encapsulated drugs, thus informing the development of more effective and targeted LDDS formulations[26].

Thermal analysis

Among the various analytical techniques used for the characterization of liposomal systems, Differential Scanning Calorimetry (DSC) stands out as a key method for investigating their thermotropic behavior and thermal stability. This technique offers valuable insights that can be used to optimize the quality, performance, and therapeutic efficiency of liposomal formulations.

In recent years, numerous studies have employed DSC to elucidate the behavior of lipid-based drug carriers, underscoring its growing relevance in pharmaceutical research.

Differential Scanning Calorimetry enables the monitoring of thermal transitions by measuring differences in heat flow between a sample and a reference, providing rapid and accurate data regarding the physical state and energetic properties of the materials analyzed[27].

Encapsulation Efficiency

A crucial factor in the success of drug delivery systems is the encapsulation efficiency, which directly impacts drug loading capacity and therapeutic outcome.

Despite the availability of various strategies to improve drug loading, achieving high encapsulation efficiency remains particularly challenging for small unilamellar liposomes (typically 50–150 nm in diameter), primarily due to their limited internal volume. This constraint can reduce the amount of drug that can be stably entrapped, making the optimization of formulation an essential parameters.[10]

Among the most widely used techniques for the quantification of EE are HighPerformance Liquid Chromatography (HPLC) and Ultraviolet-Visible (UV-Vis) spectroscopy, which provide accurate and reproducible measurements of the drug content, both free and encapsulated.

The typical procedure involves separating the non-encapsulated (free) drug from the lipid nanoparticles, followed by quantification of the drug in the formulation[28].

UV-Vis spectroscopy is often employed when the drug molecule exhibits strong absorbance at a specific wavelength, offering a simple and rapid quantification method; however, its applicability may be limited by spectral interferences or low sensitivity in formulations with low drug loading. In contrast, HPLC provides higher specificity and sensitivity, allowing for precise quantification even in complex matrices and this makes it especially suitable for formulations containing multiple components or drugs with weak UV absorbance. Additionally, HPLC enables the use of internal standards and method validation parameters (e.g., linearity, precision, accuracy), ensuring robust and reproducible analysis.

Encapsulation efficiency is typically expressed as the percentage of drug encapsulated within the nanoparticles relative to the total amount used in the formulation. Achieving high EE is particularly challenging in small-sized lipid carriers; nevertheless, optimizing formulation variables - such as lipid composition, drug-to-lipid ratio, preparation method, and surface modifications - can significantly enhance the encapsulation and stability of the active pharmaceutical ingredient.

Ocular Inflammatory Diseas

The structural and physiological complexity of the eye makes ocular drug delivery one of the most challenging areas in pharmaceutical research. Ocular inflammation is among the most prevalent eye disorders, and topical administration of anti-inflammatory agents is frequently employed as an adjunct therapy in tissue repair and regeneration; however, the presence of both physical and chemical barriers in the eye significantly limits drug bioavailability[29]. The unique features infact, make the eye a highly specialized organ with multiple barriers that must be overcome to effectively deliver drugs to specific ocular tissues. The human eye, a globular organ, is divided into two main segments: the anterior and posterior (**Figure 3**).

Both regions are protected by numerous biological barriers, which can be broadly categorized as anatomical and physiological. Anatomical barriers are further classified into static and dynamic components: static barriers include the corneal epithelium and the blood-aqueous barrier (BAB), while dynamic barriers encompass tear turnover, conjunctival blood flow, and lymphatic drainage. Physiological barriers, on the other hand, consist of metabolic mechanisms and the intraocular environment, including both the BAB and the blood-retina barrier (BRB)[30]. The BRB plays a vital role in maintaining homeostasis in the posterior segment of the eye. It is composed of two main layers: the outer retinal pigment epithelium (RPE) and the inner retinal capillary endothelium and together, the BAB and BRB present significant challenges for effective drug delivery to intraocular tissues through various administration routes.

Lipid nanoparticles represent a promising alternative for ocular drug delivery: their unique characteristics (including excellent biocompatibility, safety, and mucoadhesive properties) enhance drug bioavailability, improve patient compliance and enable sustained drug release.

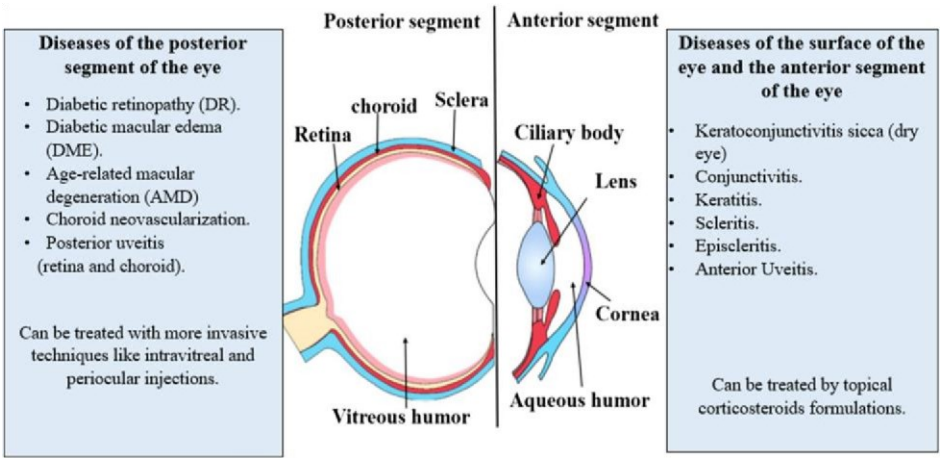

Figure 3. The image shows a sagittal section of the human eye, illustrating its division into anterior and posterior segments.

1 Triamcinolone Acetonide

Corticosteroids continue to be a key-component in the treatment of numerous ocular diseases involving the ocular surface as well as the anterior and posterior segments of the eye, due to their potent anti-inflammatory, anti-oedematous, and anti-angiogenic effects. Their therapeutic efficacy in the eye varies depending on their pharmacological activity and formulation characteristics[31]. Although all corticosteroids share a common sterane backbone — composed of 21 carbon atoms arranged in four rings — structural modifications lead to derivatives with distinct physicochemical properties and biological potencies (**Figure 4**). Most anti-inflammatory corticosteroids typically include functional groups such as a hydroxyl group at the C17 position (in α-configuration), a double bond between C4 and C5, a ketone at C3, and an oxygen-containing group at C11[32]. Additional structural changes, such as introducing a double bond between C1 and C2 (as seen in prednisolone), can slow metabolic degradation; moreover, the incorporation of a fluorine atom at the C9 position, as in triamcinolone, significantly enhances anti-inflammatory potency.

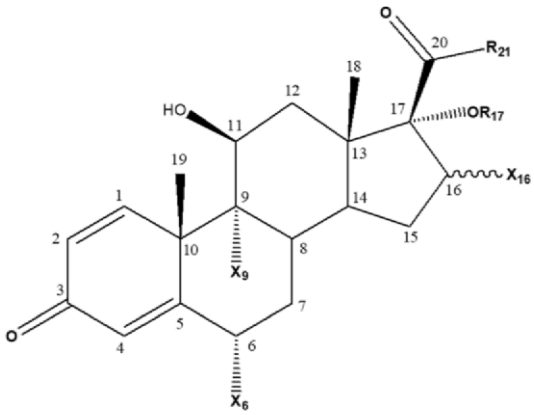

	X_6	X_9	X_{16}	R_{17}	R_{21}
Dexamethasone	H	F	CH_3	H	—OH
Dexamethasone sodium phosphate	H	F	CH_3	H	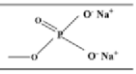
Prednisolone	H	H	H	H	—OH
Prednisolone acetate	H	H	H	H	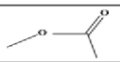
Prednisolone sodium phosphate	H	H	H	H	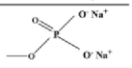
Triamcinolone acetonide	H	F	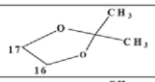		—OH
Fluocinolone acetonide	F	F	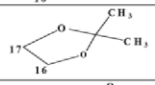		—OH
Loteprednol etabonate	H	H	H	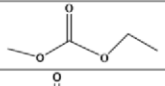	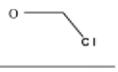
Difluprednate	F	F	H	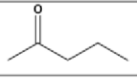	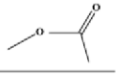
Fluorometholone	CH_3	F	H	CH_3	H

Figure 4. Structures of the most used corticosteroids for ocular application.

Corticosteroids can be delivered through various ocular administration routes. Topical application remains the preferred approach for treating conditions of the ocular surface and anterior segment. However, for diseases affecting the posterior segment, periocular, intravitreal, or suprachoroidal injections offer more targeted and effective drug delivery[31].

For all these reasons and for the poor solubility of the molecule, the encapsulation of triamcinolone acetonide in liposomal systems has been studied.

Specifically, cationic liposomes were synthesized: a solution of the cationic lipid 1,2-dioleoyl 3-trimethylammonio-propane (DOTAP) was combined with a neutral helper lipid, 1,2-dioleoyl-sn-glycero-3-phosphoethanolamine (DOPE). This phospholipid is essential for stabilizing most types of cationic lipids within a lipid bilayer and may contribute to the cell-penetrating properties of cationic liposomes[33]. SoyPC was also added to the formulation, serving as a stabilizing agent[34].

Cation lipids offer several significant advantages: they can enhance the encapsulation efficiency of negatively charged drugs and active compounds, thereby increasing the amount of active substance that can be delivered within the liposome. Furthermore, they facilitate penetration through biological membranes in vitro, an essential aspect in processes such as transfection, where the goal is to introduce genetic material into cells.

Triamcinolone-based cationic liposomes were used for the preparation of a hyaluronic acid-based ocular gel. This delivery system is designed to enhance the therapeutic efficacy of the corticosteroid by improving ocular penetration, extending the drug release duration, and increasing formulation tolerability. It offers a promising strategy for the management of chronic inflammatory ocular disorders.

1.1 Hyaluronic Acid

Hyaluronic acid (HA) is a polysaccharide to the glycosaminoglycan (GAG) family, and it’s widely used in ophthalmology for a variety of applications, including the treatment of dry eye syndrome, as a vitreous substitute, and in ophthalmic viscoelastic surgical devices (OVDs). In addition, HA serves as an effective drug delivery carrier for ocular diseases due to its excellent bioadhesive properties, viscoelasticity, and ability to interact with specific cellular receptors.

The formation of an electrostatic complex between the cationic liposomes and hyaluronic acid can be classified as a polymer–vesicle system, a well-documented approach in the literature, which has also been shown to effectively retain the active ingredient encapsulated within the nanosystem[35]. These hydrogels represent highly versatile platforms, ranging from static systems to smart,

stimuliresponsive systems. This means they maintain a stable shape and function once formed, while also being designed to respond to specific environmental changes (such as variations in temperature, pH, light, or the presence of certain chemical substances).

1.2 Materials and Methods

SoyPC (Soy Phoshatidylcholine), DOPE (1,2-dioleoyl-sn-glycero-3-phosphoethanolamine), DOTAP (1,2-dioleoyl-3-trimethylammonium propane) (Avanti Polar Lipids Inc).
The following reagents were used: ethanol (EtOH, purity ≥ 99%, Merck Italia), ultra-pure water (18.2 MΩ·cm, Rephile Direct-Pure purifier).

1.2.1 Preparation of Triamcinolone Acetonide liposomes

The synthesis of triamcinolone acetonide-based liposomes was carried out via microfluidics using an Automated Nanoparticle (ANP) System (Particle Works, Alfatest). All lipids were added to the organic phase (ethanol) in the ratios of 0.5 SoyPC 0.25 Dope 0.25 Dotap, and the active molecule was also added to the organic phase. After adjusting the aqueous and organic phase ratio and the Total Flow Rate, the solutions flow into the chip: the organic phase in the central channel, while the aqueous phase (ultra-pure water) flows in the two lateral channels. The flow of the organic phase diffuses into the aqueous phase until the ethanol concentration decreases to the point that the lipids are no longer soluble.
This diffusion process leads to the self-assembly of the liposomes.

1.2.2 Preparation of Ocular gel

The synthesized liposomes were dialyzed using a Midi Pur-A-Lyzer device. Prior to dialysis, the membrane was equilibrated with ultrapure water. Then, the liposomal suspension was loaded into the Pur-A-Lyzer, which was subsequently immersed in a beaker containing the exchange solvent. The purpose of dialysis was to remove ethanol and establish a fully aqueous environment in preparation for the subsequent synthesis of the ocular gel: water plays a crucial role in hydrogel systems, as it supports their structural integrity, solubility, and the diffusion of incorporated substances. High molecular weight hyaluronic acid (HA) was gradually added to the liposomes to reach the final

concentration of 10 mg/ml, maintaining the suspension under continuous stirring until the polymer was completely solubilized.

The same gel was made using both loaded and empty liposomes, synthesized in the same way but without including triamcinolone in the organic phase.

1.2.3 Dynamic Light Scattering

Particle size and zeta potential were verified using dynamic light scattering (DLS) with a Zetasizer Nano ZS90 (Malvern Instrument Ltd., UK). Samples were diluted in ultra-pure water and the measurement was performed at room temperature (25°C). Measurements were conducted in triplicate.

1.2.4 Encapsulation Efficiency

Encapsulation efficiency (EE) represents the measure of the amount of drug actually encapsulated within the liposome during the formulation process; it is an essential parameter for determining the ability of liposomes to transport the active ingredient and ensure effective administration. Encapsulation efficiency was calculated using an HPLC instrument (Thermo Fisher Scientific UltiMate 3000) using a UV-Vis diode array detector (DAD).

A 2.6 µm Kinetex reversed-phase C18 column with a length of 150 × 2.1 mm was used.

H2O (A) and acetonitrile (B), both acidified to 0.1% formic acid, were used as the mobile phase. The sample was diluted in methanol (MeOH) in a ratio of 1:10 and subsequently subjected to solid phase extraction (SPE) before being introduced into the column. Chromatograms were recorded at 241 nm. For the quantitative determination of the encapsulated active molecule, a calibration curve was constructed in the concentration range of 1–50 ppm. The encapsulation efficiency was calculated using the following equation (2):

$$\%EE = \frac{[TA]_{lip}}{[TA]_{tot}} \times 100 \quad (2)$$

Where [TA]lip represents the amount of active molecule encapsulated in the liposomes, determined by the calibration curve, and [TA]tot is the total amount of triamcinolone used in the synthesis.

1.2.5 NMR Analysis

A Bruker DRX-600 Avance III spectrometer operating at 600.13 MHz was used to acquire ^{1}H NMR spectra. Data processing was performed using Mestre Nova software.
To acquire spectra, the sample were dried under N_2 and resuspended in D_2O, the ^{1}H NMR spectra were recorded using the pulse sequence zgesgp.

1.2.6 Frequency-Sweep test

To evaluate mechanical properties such as elasticity (elastic modulus G') and viscosity (viscous modulus G"), the hyaluronic acid-based gel and the hyaluronic acid-based gel combined with liposomes (both with triamcinolone acetonide and empty) were subjected to a frequency-sweep test. The test was performed by applying a constant strain (γ) equal to 0.1%, to maintain the material in the linear viscoelastic regime, thus avoiding breakage or permanent deformation of the sample. The oscillation frequency was varied within a range from 0.01 Hz to 10 Hz, to explore the material's behaviour across a broad frequency spectrum (from the low-frequency regime—in which the material behaves predominantly as a viscous fluid—to the high-frequency regime—in which elastic behaviour is predominant). The test was conducted at a constant temperature of 25°C, to minimize the influence of thermal variations on the sample's mechanical properties. In addition to recording the elastic (G') and viscous (G") moduli, the crossover frequency (the point at which G' and G" become equal) was analysed. This parameter provides critical information on the balance between the solid and elastic behaviour of the material: the crossover frequency represents the transition point from a regime of predominantly viscous behaviour (G" > G') to a regime in which elastic behaviour becomes dominant (G' > G").

1.2.7 Flow-Sweep test

To determine the viscosity of the three samples as a function of the applied shear rate, a flow-sweep test was performed. The test was conducted by applying an increasing shear rate ($\dot{\gamma}$), with values ranging from 0.01 s^{-1} to 10,000 s^{-1}, to cover a wide range of flow conditions. The temperature was kept constant at 25°C throughout the experiment.

1.2.8 Differential Scanning Calorimetry (DSC)

The instrument used is a DSC Q1000 (TA Instruments Leatherhead, United Kingdom). The instrument management software is Thermal Advantage Release 5.5.22; the data management software is TA Instruments Universal Analysis 2000 (v4.5.4). The experimental protocol involves an initial controlled cooling, applying a ramp rate of 0.20°C/min, until a temperature of - 40.00°C is reached; the samples was subsequently held at an isothermal temperature of - 40.00°C for 5.00 minutes, to uniform the sample temperature. At the end of the isothermal cooling, heating was performed with a ramp rate of 0.20°C/min until a final temperature of 70.00°C was reached.

1.3 Results and Discussions

1.3.1 Dynamic light Scattering

The z-average, polydispersity index (PDI) and zeta potential (ζ) of both loaded and empty liposomal samples were measured. The polydispersity index (PDI) is a key parameter for assessing the uniformity of particle size distribution. A low PDI indicates a monodisperse system, characterized by particles of homogeneous size; a PDI above 0.4 reflects a heterogeneous system, with higher variability in particle size.

The ζ potential plays a crucial role in determining the stability of nanoparticles in dispersion[36]. When a material comes into contact with a liquid, the functional groups present on its surface interact with the molecules in the solution, and this interaction generates a surface charge that attracts oppositely charged ions from the liquid. These ions naturally arrange themselves, forming a double electrochemical layer around the surface of the material, composed of a layer of strongly bound ions (Stern layer) and an external "diffuse layer" of loosely bound ions.

When the particle moves due to Brownian motion, a difference is created between the ions in the diffuse layer, which move with the particle, and those that remain in the solvent. This separation gives rise to the so-called slip plane[37]. The ζ potential represents the electric potential measured at this plane during the movement of the nanoparticle in an electric field. Nanoparticle dispersions can be classified based on the value of the ζ potential: dispersions with ζ values between ± 0 –10 mV are considered highly unstable, while values between ± 10–20 mV, ± 20–30 mV and above ± 30 mV correspond to relatively stable, moderately stable and highly stable systems, respectively[24]. Furthermore, the ζ potential can be used to classify nanoparticles as neutral (−10 to +10 mV), cationic (> +30 mV) or anionic (< −30 mV)[38].

	Z-average (nm) ±sd	PDI ± sd	z-pot ± sd
TA sample (SoyPC, Dope, Dotap, TA)	227 ± 0,7	0,130 ± 0,004	37,52 ± 1,17
Empty sample (SoyPC, Dope, Dotap)	171,8 ± 3,9	0,177 ± 0,026	35,65 ± 0,70

Table 1. Liposomes' medium size, PDI and ζ -pot.

The average particle size of 227 nm observed for the triamcinolone-loaded liposomal system indicates a narrow and uniform size distribution, reflecting a high level of control and reproducibility in the synthesis process. Such consistency in particle size is crucial for ensuring predictable pharmacokinetic and pharmacodynamic behavior upon administration. The polydispersity index (PDI) of 0.130 further supports this observation, as it suggests the presence of predominantly homogeneous particles with minimal size variation. A low PDI is particularly important in nanoparticle formulations, as it correlates with improved physical stability, reduced aggregation, and enhanced reproducibility of biological responses.

The measured zeta potential (ζ) value of 37.52 ± 1.17 mV signifies strong electrostatic repulsion among the liposomal particles, which is a key factor contributing to colloidal stability by preventing aggregation and sedimentation over time. Such a high positive zeta potential is indicative of a robust, stable colloidal system that can maintain its structural integrity in physiological environments, thereby enhancing the potential for effective drug delivery in clinical settings.

In contrast, the formulation prepared without the active molecule (blank liposomes) exhibited an average size of 171.8 ± 3.9 nm, which is significantly smaller and consistent with the absence of drug loading. This size difference aligns with the expected behavior whereby the encapsulation of the triamcinolone molecule leads to an increase in liposomal diameter, confirming that drug incorporation directly influences vesicle size. The PDI for the blank liposomes was slightly higher than that of the loaded system, indicating a marginally broader size distribution. While this suggests somewhat greater heterogeneity in particle sizes, the value remains within acceptable limits for liposomal formulations, indicating an overall stable and functional system.

Finally, the zeta potential of the empty liposomes closely mirrors that of the triamcinolone-loaded liposomes, reaffirming the intrinsic stability of the liposomal carrier regardless of drug encapsulation. Taken together, these physicochemical parameters demonstrate that the developed liposomal system

possesses desirable attributes, which are essential prerequisites for potential clinical application as an effective ocular drug delivery platform.

1.3.2 Encapsulation Efficiency

The quantitative determination of triamcinolone was carried out using the method previously described and interpolating the area of the peak obtained with the calibration line shown in **Figure 5**, where the absorbance (measured in mAU*min) is reported on the ordinate axis (Y) and the concentration of the compound (ppm) on the abscissa axis (X).

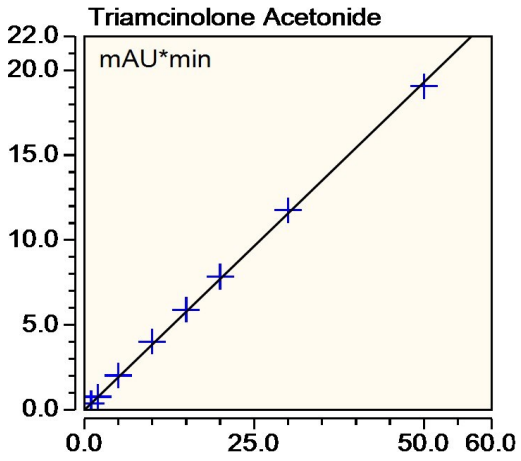

Figure 5. Calibration line for triamcinolone acetonide.

HPLC analysis showed that the amount of triamcinolone effectively encapsulated in the liposomes was 86%. This data highlights the system's good ability to retain triamcinolone. Such a high efficiency also indicates that the liposomal formulation has the potential to ensure controlled release of the drug, improving the bioavailability of the active ingredient. Furthermore, the obtained value suggests good stability of the liposomal structure, indicative of a system capable of containing the active ingredient without significant losses or rapid degradation[39].

1.3.3 NMR Analysis

Nuclear magnetic resonance was used to verify the presence of triamcinolone inside the liposomes, comparing the ^{1}H NMR spectra of the two liposomal solutions (**Figure 6**).

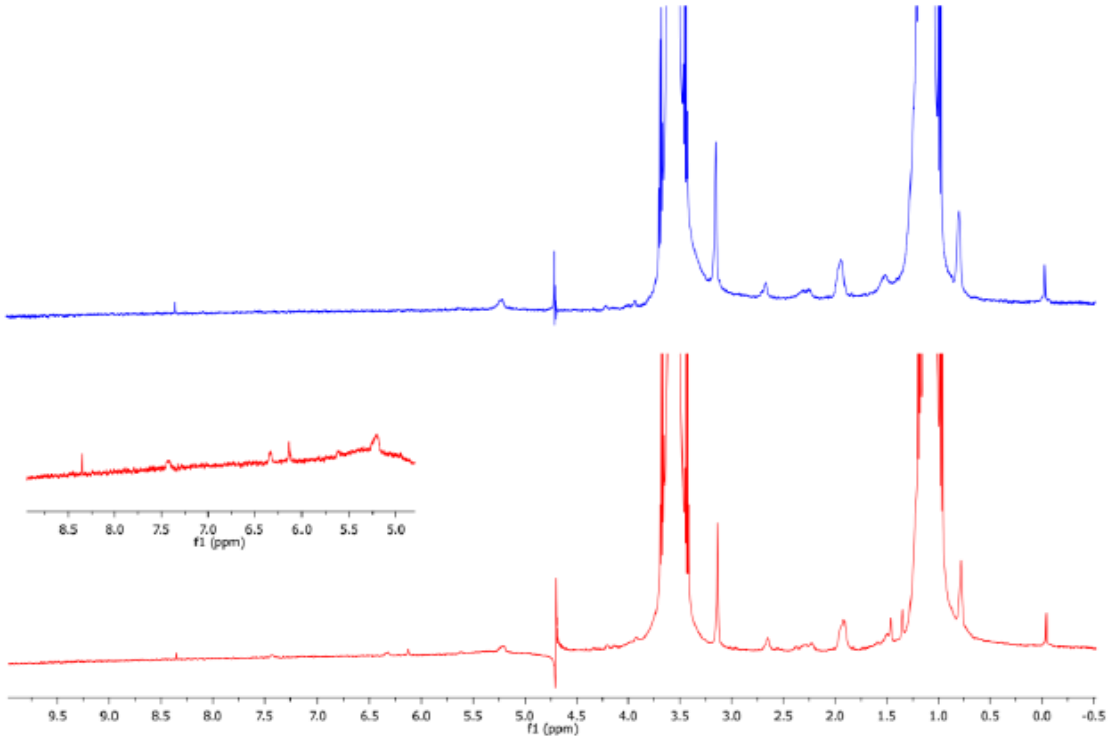

Figure 6. ^{1}H NMR spectrum of triamcinolone, SoyPC, Dope, Dotap liposomes (red) and SoyPC, Dope, Dotap liposomes (blue). These spectra are recorded at 600 MHz and 298 K.

Microfluidic synthesis involves the use of ethanol (organic phase), which appears in the spectrum, masking the weaker peaks of the lipid components. Interference caused by ethanol and the excessively low concentration of the systems therefore made it difficult to accurately identify the specific signals of the active ingredient and its interactions with the liposomes. For this reason, **figures 6** show ^{1}H NMR spectra with increased intensity.

In this case, both spectra highlight peaks associated with the lipid components of the liposomal system (SoyPC, Dope, Dotap), particularly in the region between 1 and 5 ppm. These peaks correspond to the methyl, methylene, and aliphatic protons of the lipids, common to both formulations. In the sample containing triamcinolone, a significant variation emerges in the range between 6 ppm and 7.5 ppm, which is absent in the empty liposome formulation: these signals can be attributed to the aromatic or unsaturated protons of triamcinolone, suggesting good encapsulation of the active molecule within the liposomal structure.

This evidence is further supported by the literature, which shows the ^{1}H NMR spectrum (600 MHz, CD_3OD, 25 °C) of triamcinolone, highlighting peaks at 6.09 ppm (1H, H4, t, 1.8 Hz), 6.29 ppm (1H, H2, dd, J2–1 = 10.1 Hz, J2–4 = 1.8 Hz), and 7.38 ppm (1H, H1, d, J1–2 = 10.1 Hz)[40]. The presence of these peaks reflects the interaction of the drug with the lipid matrix and confirms its effective inclusion in the formulation.

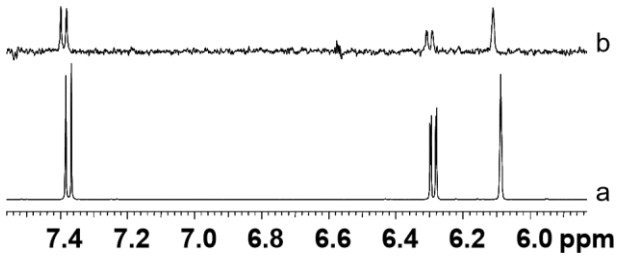

Figure 7. ^{1}H NMR (600 MHz, 25 °C) spectral regions of olefinic protons of TrA in CD_3OD (a) and in D_2O (vertical scale x 1000) (b). Comparison demonstrated that the patterns of the spectral parameters in the two solvents were quite similar[40].

1.3.4 Rheological property analysis

Viscoelastic behaviour describes a sample's response to controlled external stimuli: this behaviour can be measured using the elastic modulus (G') and the viscous modulus (G''). The G' modulus represents the elastic portion of the material and indicates the mechanically conservative portion of the sample, while the G'' modulus represents the mechanically dissipative portion of the sample. Both moduli were measured as a function of frequency by subjecting them to a Frequency-Sweep test: a constant shear strain is applied to the sample in oscillatory mode, within a given frequency range. This distinction between the two moduli allows us to understand the sample's response to the dynamic forces to which it is subjected, providing information on its ability to store and dissipate energy[41].

$$G' = \frac{\tau 0}{\gamma 0} cos\ \delta$$

$$G'' = \frac{\tau 0}{\gamma 0} sin\ \delta$$

$$tan\ \delta = \frac{G''}{G'}$$

Table 2. Mathematical relations for viscoelastic characterization.

Table 2 illustrates the mathematical relationships for the viscoelastic characterization, where τ0 and γ0 represent the maximum stress and strain amplitudes, respectively. The phase angle δ is a key parameter that indicates the delay between the applied stress and the resulting strain during the oscillatory test, and therefore between the applied stress and the material response. For predominantly elastic materials, the value of tan δ is less than 1, implying that G′ is greater than G″. This behaviour suggests that the material acts primarily as an elastic solid, with a significant capacity to store energy. Conversely, for predominantly viscous materials, tan δ is greater than 1, indicating that G″ is greater than G′: this indicates that the material dissipates a greater amount of energy in the form of heat than it stores[42].

Figure 8 depicts the viscoelastic behaviour of the three systems.

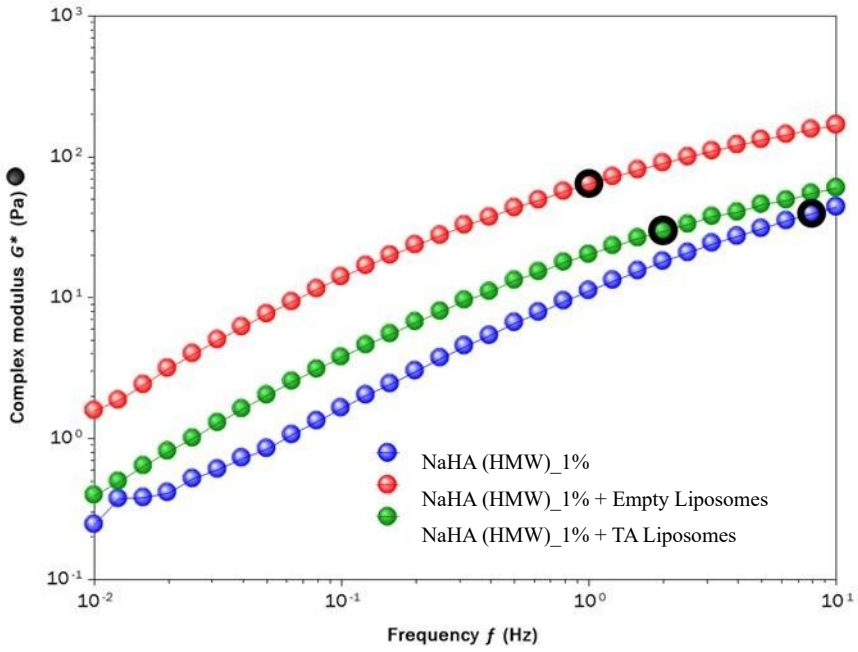

Figure 8. Viscoelastic behavior of the three solutions.

The graph shows frequency on the X-axis and the complex modulus G* on the Y-axis, which is a measure of a material's resistance to mechanical deformation. The complex modulus is defined as G*= |G'|+i|G''|[43].

The graph shows the three systems, where the blue curve represents 1% NaHA (HMW), i.e., 1% w/v high molecular weight hyaluronic acid, the red curve represents 1% w/v NaHA (HMW) with the addition of empty liposomes, and the green curve represents 1% w/v NaHA (HMW) with loaded liposomes. From an analysis of the curves, it is noted that the 1% w/v NaHA (HMW) solution (blue curve) has the lowest complex modulus compared to the other solutions, which is consistent with the fact that it is the base solution, without colloidal reinforcement. The addition of liposomes (red curve) causes an increase in the complex modulus G*, indicating an increase in overall mechanical properties compared to the base solution. This phenomenon can be attributed to the interaction between the liposomes and the hyaluronic acid matrix. The addition of loaded liposomes (green curve) results in a lower G* compared to the formulation with empty liposomes. This suggests that liposome loading may interfere with the structuring of the matrix, reducing the interactions between the polymer and empty liposomes.

In addition to the measurement of the complex modulus, the tan δ (**Figure 9**) was analyzed to evaluate the viscoelastic behavior of the materials at different frequencies and to compare their respective cross-over frequencies. This parameter, defined as the point where tan δ = 1, represents the condition in which the elastic and viscous contributions of the material are equivalent.

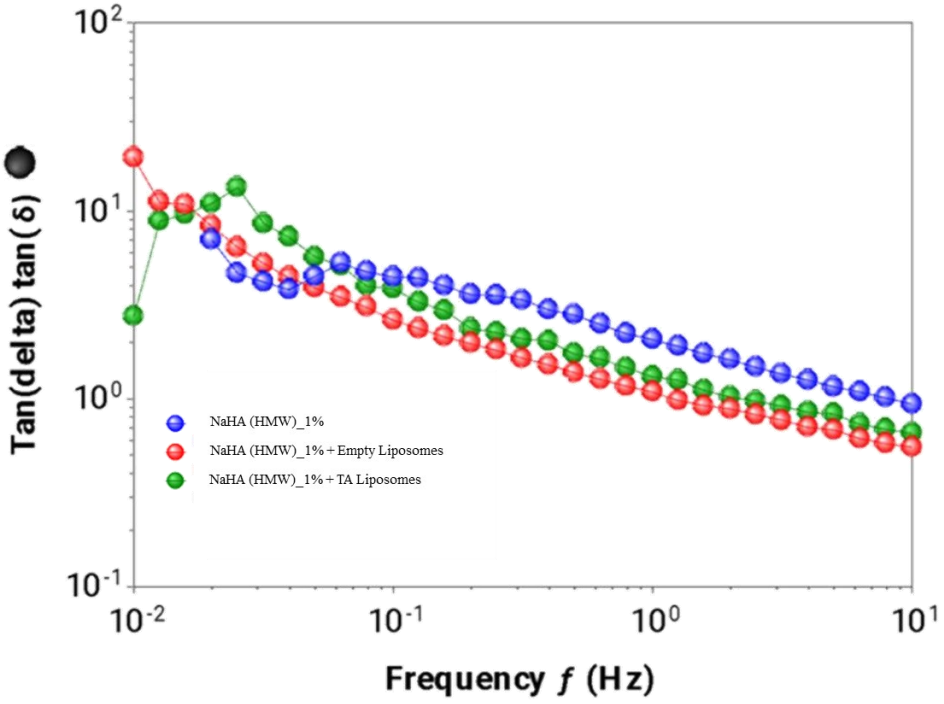

Figure 9. Trend of tan δ as a function of frequency for the three samples.

The cross-over frequency therefore marks the transition from a regime dominated by viscous behavior (G" > G') to one where the elastic response becomes predominant (G' > G"). **Figure 9** shows the trend of tan δ as a function of frequency for the three analyzed samples: NaHA HMW 1%, NaHA HMW 1% with empty liposomes, and NaHA HMW 1% with TA-loaded liposomes. In all cases, tan δ decreases with increasing frequency, indicating a progressive enhancement of the elastic character of the materials.

At higher frequencies, the material gradually exhibits a more elastic response, storing energy rather than dissipating it. This behavior corresponds to an increase in rigidity and highlights the transition from a predominantly viscous to a more elastic regime.

The hyaluronic acid-based gel shows higher tan δ values compared to the other samples, with a curve that remains above the others across the entire frequency range. This behavior indicates greater energy dissipation and a more pronounced viscous component.

Conversely, the sample containing empty liposomes exhibits lower tan δ values, suggesting a more elastic behavior and reduced energy dissipation.

The TA-loaded liposome sample occupies an intermediate position: at low frequencies, it displays higher tan δ values than the empty liposomes, reflecting increased energy dissipation and a more viscous character; however, at higher frequencies, the difference between the two samples diminishes, suggesting that the influence of the active ingredient becomes less significant as frequency increases.

The crossover points (indicated in black) are shown in the **Figure 8** but also the table below shows the frequencies at which the crossover points fall.

Table 3. Cross-over frequency of the tree samples.

Sample	***Frequency di Cross-over (Hz)***
NaHA (HMW) 1%	7,9
NaHA (HMW) 1% p/v + Empty liposomes	1,0
NaHA (HMW) 1% p/v + liposomes TA	2,0

The table shows that the cross-over frequency is highest for *NaHA HMW 1%*, with a value of 7.9 Hz, indicating that the base gel exhibits a more pronounced viscous component compared to the other formulations. In this case, a higher cross-over frequency suggests that the base gel retains its viscous nature up to higher frequencies.

The TA liposomes display a more pronounced viscous behavior than the empty liposomes; this implies that, even beyond the cross-over frequency of the empty liposomes, the TA liposome formulation continues to dissipate energy effectively before transitioning to a predominantly elastic behavior.

The differences in cross-over frequency among the three samples highlight how their physicochemical characteristics significantly influence the mechanical properties and rheological behavior of the systems.

To evaluate the viscosity of the three systems, a flow-sweep test was performed: the measurement is taken as a function of the rotation speed, in a range of values from 0.01 s-1 to 10000 s^{-1}. The test results are shown in **Figure 10**.

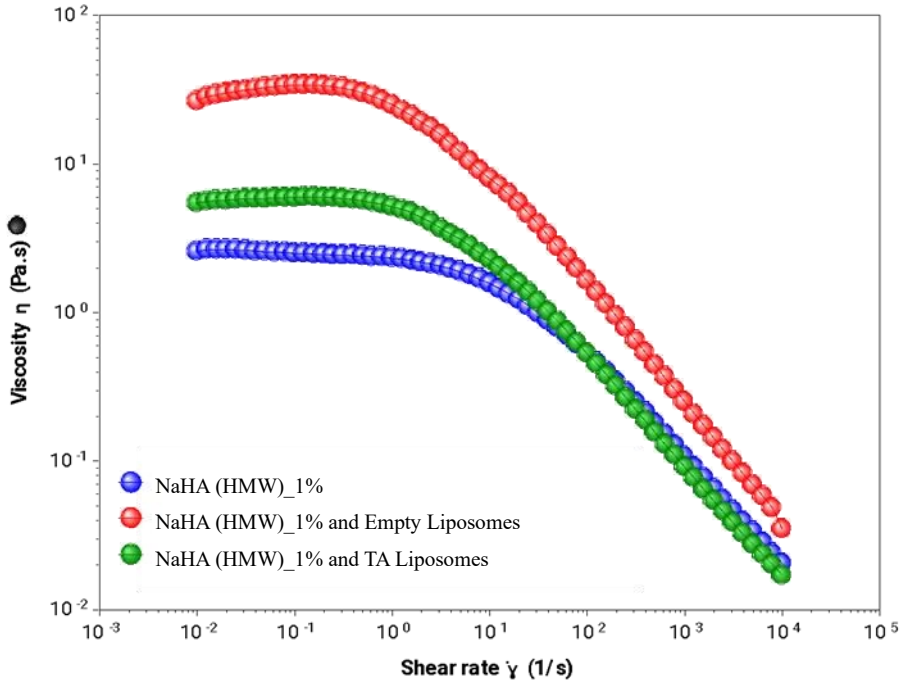

Figure 10. Viscosity trend of the three solutions.

From the analysis of the graph, it is possible to state that a shear thinning or pseudoplastic behaviour clearly emerges for all systems: this type of behaviour implies that the viscosity decreases as the shear rate increases, a behaviour typical of polymer solutions[34]. When empty liposomes are present in the system (red curve), the viscosity at low shear rate is higher than that of the NaHA-only solution. This confirms what was observed in the oscillation tests, namely how liposomes increase the internal interaction within the system, conferring greater resistance to flow. However, the difference in viscosity between the system with the empty liposome and that with the polymer alone decreases as the shear rate increases. Instead, the solution containing concentrated loaded liposomes (green curve)

exhibits a behaviour like that of the polymer alone, with an increase in viscosity at low shear rates compared to the pure NaHA solution, but starting from 10s-[1] the two viscosity values become comparable.

Table 4 shows the results obtained from the rheological analysis of the three samples subjected to the flow-sweep test.

Rheological analyses	Model: Carreau-Yasuda		Flow Sweep test (0.01 s^{-1} ÷ 10 000 s^{-1})	
Samples	η_0	R^2	η (1 s^{-1})	η (10 000 s^{-1})
NaHA	2.60 Pa.s	1.000	2.32 Pa.s	20.35 mPa.s
NaHA + Empty Liposomes	32.5 Pa.s	0.999	25.00 Pa.s	34.94 mPa.s
NaHA + TA Liposomes	6.02 Pa.s	1.000	5.14 Pa.s	17.06 mPa.s
Threshold value of ocular discomfort : 30 mPa.s; Retention limit: 10 mPa.s				

Table 4. Rheological flow analysis of the three samples: Carreau-Yasuda model and Flow Sweep test.

The Carreau-Yasuda model is one of the equations used to describe the rheological behaviour of non-Newtonian fluids, such as polymer solutions or colloidal suspensions. This model describes the apparent viscosity of a fluid as a function of rotational speed and is particularly useful for representing materials that exhibit pseudoplastic behaviour (materials whose viscosity decreases as the shear rate increases). The Carreau-Yasuda model equation is given by (3):

$$\eta(\dot{\gamma}) = \eta_\infty + (\eta_0 - \eta_\infty)\,[1 + (\lambda\dot{\gamma})^a]^{\frac{n-1}{a}} \quad (3)$$

$\eta(\dot{\gamma})$ is the apparent viscosity at a certain $\dot{\gamma}$; η_0 is the zero-shear rate viscosity; η_∞ is the infinite viscosity or shear thinning limit; λ is a characteristic time parameter indicating the shear rate at which the transition between the two viscosity regimes occurs; a is a parameter that governs the width of the transition between the low and high-shear rate viscosities; n is the shear thinning exponent or power index that describes the degree of viscosity decrease with shear rate[35]. **Table 4** reports the values of η_0, showing that empty liposomes (in red) have a higher viscosity than the other two solutions, in agreement with what was shown previously. The Flow-Sweep test values demonstrate that by applying an increasing shear rate, with values between 0.01 s^{-1} and 10,000 s^{-1}, to cover a wide range of flow conditions, shear thinning behaviour is observed for all three solutions, with a slightly

different tendency between them. The coefficient of determination R2 (or squared correlation coefficient) is also shown in the table.

The R2 values reported in the table suggest that the Carreau-Yasuda model fits the experimental data very well for all analysed samples. As shown in the table, the threshold values for ocular discomfort and the retention limit are critical in the evaluation of ophthalmic materials. Recent studies have identified a threshold value of 30 mPa s for ocular discomfort at a shear rate of 10,000 s^{-1}, suggesting that viscosities above this limit can cause sensations of heaviness or irritation due to the material's resistance to movement in the eye[36]. In parallel, a retention limit of 10 mPa s has been established. This value is crucial to ensure that the materials remain in contact with the ocular surface long enough to perform their function. If the viscosity drops below this limit, the materials may not adhere sufficiently to the eye, being expelled prematurely and reducing the effectiveness of the treatment[37]. The triamcinolone-loaded liposome gel (NaHA + loaded liposomes) falls perfectly within the established threshold values, with a viscosity of 17 mPa s. This value effectively balances good retention without exceeding the limit that could cause ocular discomfort.

DSC calorimetry measures the difference in heat flow between a sample and a reference, both subjected to the same thermal program. This technique allows monitoring all transitions involving heat flow, such as melting or crystallization, providing crucial information on the thermal stability and structural organization of the analysed materials[38]. In this study, the melting temperatures and enthalpies of water in the three samples were analysed, allowing us to identify differences and providing evidence of possible interactions between the liposomal systems and the polymer, as already detected by rheological analyses. In **Figure 11**, the energetic changes of the three solutions as a function of temperature were examined, allowing us to observe the thermal transitions and the related enthalpy changes, highlighting differences between the analysed samples.

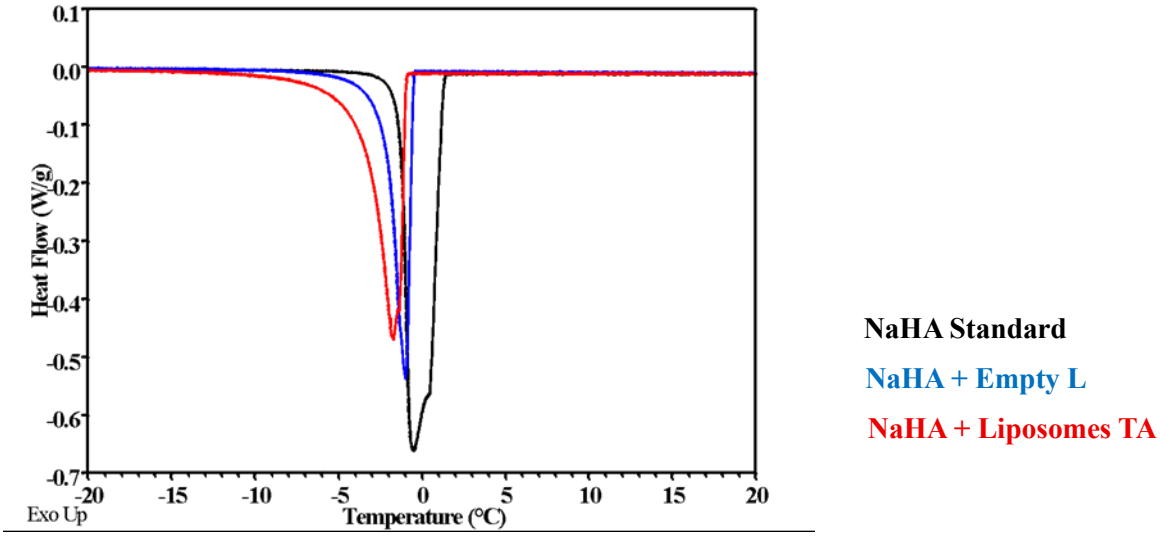

Figure 11. Thermal profile by DSC of the three solutions: variation of heat flux as a function of temperature.

The graph shows the temperature (°C) on the X-axis and the normalized heat flux (W/g) on the Yaxis. The analysis shows that the blank sample (NaHA_blank) exhibits a well-defined endothermic peak, with a melting temperature of approximately -0.5°C and a melting enthalpy of 322.2 J/g (**Table 5**). These results confirm the presence of a crystalline or semi-crystalline structure in the sample, suggesting good molecular organization. This organization implies that a significant amount of heat is required to cause the thermal transition, highlighting the thermal stability of the material. This behaviour is consistent with the typical characteristics of well-organized and thermally stable polymers[44].The sample consisting of empty liposomes (empty NaHA+L), however, shows a lower intensity endothermic peak than the blank sample, with a melting point of approximately -1.0°C and a melting enthalpy of 175.5 J/g, implying that the structure melts more easily than the blank sample. Finally, the sample containing liposomes loaded with active ingredient (filled NaHA+L+PA) shows an endothermic peak at a melting point of approximately -1.8°C and a melting enthalpy of 283.1 J/g. These results highlight that the melting point of water within the system is the lowest among the analysed samples, which can be attributed to the influence of the active ingredient, which modifies the molecular interactions in the system. The presence of the active ingredient, therefore, contributes to a decrease in the melting point, indicating a greater ease of phase transition compared to the other samples. Despite the lower melting temperature, the enthalpy of fusion remains at an intermediate level, suggesting that the system maintains good molecular organization.

In conclusion, the analysis of the three solutions highlighted how the temperatures and enthalpies of melting of the water in the samples reflect the influence of the different systems on the thermal properties. In particular, the bilayer structure of the liposomes and the insertion of the active ingredient facilitate a series of molecular interactions with the surrounding environment, significantly modifying the thermal behaviour of the system. These interactions not only confirm the importance of the liposome structure but also suggest a substantial influence of the active ingredient in determining the heat transfer properties and stability of the system[45].

Table 5. Maximum temperatures and enthalpies of fusion of the three samples.

Sample	**T_f (°C)**	**Enthalpies of fusion (J/g)**
Standard	-0,5	322,2
Empty Liposomes	-1,0	175,5
Liposomes TA	-1,8	283,1

1.4 Conclusions

Experimental data obtained by DLS revealed small differences between the two liposomal formulations, particularly in size, suggesting that drug loading influenced particle size, making them larger than empty liposomes. The synthesized liposomes exhibited good encapsulation efficiency, demonstrating that the system is capable of containing the active ingredient without significant losses or rapid degradation. Nuclear magnetic resonance imaging, despite the presence of ethanol and the low concentration of the systems, still revealed characteristic peaks of triamcinolone acetonide and lipid components, confirming the interaction of the drug with the lipid matrix.

The rheological properties of liposomes, such as viscoelasticity and viscosity, were analyzed to understand how liposomes behave under the influence of external forces; specifically, the viscoelastic behaviour of the three solutions (HA gel, HA gel with empty liposomes, HA gel with TA liposomes) was compared using the Frequency-Sweep test. The results demonstrate that the viscoelastic behaviour of liposomes containing the active ingredient is intermediate compared to the other two solutions tested. Specifically, the base solution exhibited a more elastic behaviour, as evidenced by the higher crossover frequency, while empty liposomes had a slightly lower crossover frequency than loaded liposomes; this indicates that loaded liposomes contribute greater network stabilization than

empty liposomes. The differences observed in crossover frequencies confirm that the chemical and physical properties of the three solutions significantly influence the mechanical characteristics and rheological behaviour of the system, suggesting that encapsulation of the active ingredient has a positive impact on the structural stability and rheological performance of the liposomal system.

Analysis of the viscosity of the three solutions, conducted using the Flow-Sweep test, revealed significant differences between them. In particular, the gel based on liposomes loaded with triamcinolone showed a viscosity trend that fell perfectly within the established threshold values. This result is of great importance, as it ensures an effective balance between good retention of the active ingredient and the maintenance of viscosity levels sufficient to avoid ocular discomfort. Therefore, the loaded liposome formulation proves suitable for ophthalmic application, ensuring both stability and tolerability.

Finally, the thermal properties of the liposomes were examined using differential scanning calorimetry (DSC), revealing that the temperatures and enthalpies of water fusion in the samples clearly reflect the influence of the different systems on the thermal characteristics. In particular, the bilayer structure of the liposomes and the incorporation of the active ingredient facilitated a series of molecular interactions with the surrounding environment, significantly altering the thermal behaviour of the system. These interactions not only confirm the crucial role of the liposomal structure in determining thermal properties but also suggest that the incorporation of the active ingredient has a substantial impact on the heat transfer dynamics and the overall stability of the system.

2 Triamcinolone Acetonide Experimental Design

The production of nanoparticles is a complex process, in that even minute variations in synthesis conditions can significantly affect their properties; these modifications can relate to physicochemical characteristics (such as size, polydispersity and morphology), biological parameters (such as absorption, permeability and stability in biological fluids) and pharmacological activity. One of the critical aspects is reproducibility, which is essential to ensure consistent results, especially on a production scale. Each type of nanoparticle has specific factors that influence its final formulation, making careful control of the entire process necessary. The Quality by Design (QbD) approach has emerged to establish strict guidelines for the approval of pharmaceutical products: product quality can only be guaranteed if the critical factors involved in product variability are understood and appropriately eliminated or controlled within a predetermined design space[46].

The QbD approach involves using experimental design (DoE) for the systematic optimization of nanocarriers. In univariate analysis, in fact, all factors are set at a basic level, and a single factor is modified at different levels, analysing the result of this modification on the final product. This classic single-factor plan ultimately identifies the most important factors (or main effects) but does not consider possible synergies/antagonisms between factors (interactions between factors). Furthermore, it is not guaranteed that the best factor setting leading to an optimal product is correctly clarified. A more efficient approach to unravel these critical interactions, of extreme interest in the QbD framework, is the so-called statistical design of experiments (DoE). The DoE is a multivariate statistical tool that allows identifying the relationships between the factors that influence a process and the observed results, thus helping to identify the optimal synthesis conditions and the design space: it consists of a series of randomized experiments (the number of experiments is defined by the type of project) with different combinations of input factors, followed by a statistical analysis of changes in the monitored responses. The measured response (y) is, consequently, the overall sum of the effects due to individual factors, interactions between factors and experimental noise. The equation of the resulting regression model that considers, for example, two quantitative factors (A and B) can be expressed according to the general formula (4):

$$y = \beta 0 + \beta 1 x1 + \beta 2 x2 + \beta 12 x1 x2 + \epsilon \qquad (4)$$

where x1 and x2 represent the two independent factors, the beta parameters are the coefficients determined by the experimental design and ε is the experimental error[47]. The existence of the term

β12x1x2 indicates that factors A and B contribute synergistically (if the sign is positive) or antagonistically (if the sign is negative) to modify the response. The response equations can be represented graphically by creating 3 D graphs and their respective 2 D contour plot graphs (**Figure 12**). The simplest first-degree linear polynomial is represented in **Figure 12a**. In this way, it is easy to determine how a change in factor A or factor B produces a change on the response surface. The progressive inclusion of higher-order terms in the polynomial leads to the curvature of the model (**Figure 12b,c**). For optimization purposes, it may usually be necessary to include quadratic (**Figure 12c**) or, rarely, cubic terms to find a suitable fit of the model to the observed response. If more than two factors are studied, the graphical representation can only be obtained by fixing a constant value for the other factors studied.

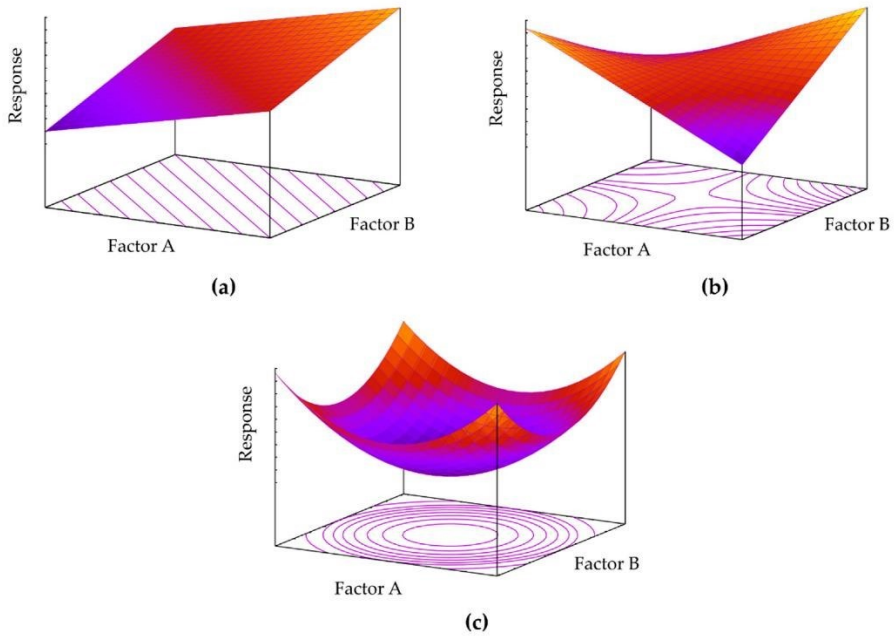

Figure 12. Three-dimensional response surfaces and respective two-dimensional contour graphs following (a) a linear or first-order function and (b) a second-order equation. The inclusion of quadratic terms in the function allows detecting the maximum or minimum values of the response (c).

It is convenient to start with experimental screening designs, which help to identify the variables truly capable of influencing the response. Among these, the most used is the two-level factorial design, which allows only two values to be studied for each factor: considering k = the number of factors studied, 2 k possible combinations between factors and levels are explored. Comprehensive factorial experimental designs are a particularly advantageous solution when working with a limited number

of factors. In these drawings, all possible combinations between the factors and their respective levels are analyzed, allowing maximum information to be obtained from each experiment conducted.

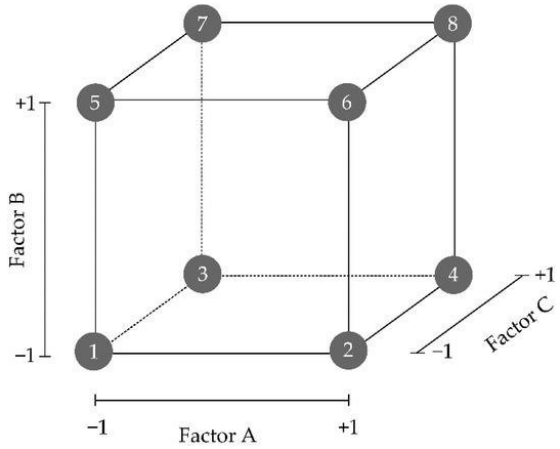

Figure 13. Geometric representation of the eight series (dark spheres at vertices 1 to 8) of a complete three-factor, twolevel factorial design (2 3). Each factor (A, B and C) is established at two levels, coded as -1 (low level) and +1 (high level). Note that each experimental series (vertices of the cube, numbered 1 to 8) is a unique combination of the different levels for the factors.

A two-level factorial design that included three factors was used to optimize the synthesis of triamcinolone-based liposomes achieved through microfluidics.

- Flow Rate Ratio (FRR), the aqueous phase/organic phase (H2O/EtOH) ratios, where the 1:1 ratio has been assigned the level (-1) and the 1:3 ratio (+1)
- Total Flow Rate (TFR), flow 3000 µL/min (-1) and 5000 µL/min (+1)
- Amount of active substance, 0.2 mg/mL (-1) and 0.4 mg/mL (+1)

The project was carried out using Design Expert13 (StatEase, Minneapolis, MN), which suggested a total of 16 experiments (8 runs and their duplicates). Responses monitored during DoE are size, PDI (polydispersion index), and encapsulation efficiency.

A PVA-based eye gel and an inulin-based one were synthesized using the optimized formulation.

2.2 PVA

Polyvinyl alcohol (PVA) represents a valid alternative to other polymers, thanks to its good compatibility with ocular tissue, the ability to increase the viscosity of the formulation and prolonged retention on the ocular surface. Unlike some high molecular weight polymers, PVA can be used at concentrations that ensure filtration sterilizability and stability during thermal sterilization, without generating potentially pro-inflammatory fragments[48].

It is commonly used to treat Dry Eye Disease (DED), a multifactorial condition that affects more than 20% of the world's population, with a significant economic and health impact.
To treat DED, artificial tears are commonly used, which must lubricate effectively, remain on the ocular surface for as long as possible, and prevent the formation of dry areas. This is achieved via viscoelastic formulations, based on water-soluble polymers or lipid nanocarriers[49].

2.3 Inulin

Inulin is a natural polysaccharide, consisting mainly of fructose chains, known for its biocompatible, biodegradable and non-toxic properties. The great potential of polysaccharides (particularly inulin), due to their favourable characteristics such as mucoadhesion, cytocompatibility and innate ability to interact with human cells and tissues has meant it founds promising applications in the pharmaceutical field, including systems for ocular administration[50].
Additionally, the opportunity to enhance the polymer backbone was the driving force behind the creation of a new inulin derivative (liposome based).

2.4 Materials and Methods

Soy Phoshatidylcholine, DOPE (1,2-dioleoyl-sn-glycero-3phosphoethanolamine), DOTAP (1,2-dioleoyl-3-trimethylammonium propane) (Avanti Polar Lipids Inc).
The following reagents were used: ethanol (EtOH, purity ≥ 99%, Merck Italia), methanol (MeOH, Merck Italia), soda (NaOH, Merck Italia), ultra-pure water (18.2 MΩ·cm, Rephile Direct-Pure purifier), polyvinyl alcohol (PVA 31), inulin (C6nH10n+2O5n+1), sodium trimetaphosphate (STMP).

2.4.1 Preparation of Triamcinolone acetonide liposomes

An Automated Nanoparticle (ANP) System (Particle Works, Alfatest) was used for the synthesis of liposomes via microfluidics. The lipids were mixed according to a molar ratio of SoyPC 0.5 Dope 0.25 DOTAP 0.25 in ethanol (organic phase) with the active molecule too. A total of eight samples were synthesized, each with the corresponding duplicate, using a 190 μm (channel size/section) junction chip. So, the lipids composition is the same for every formulation, we change only the amount of TA and some instrumental parameters.

The synthesis was conducted by varying the three factors considered for experimental design **(table 6**).

Table 6. Parameters for liposome synthesis: FRR, TFR, amount of TA.

Samples	***Flow Rate Ratio (FRR)***	***Total Flow Rate (TFR), (µL/min)***	***Triamcinolone (mg/mL)***
1	1:1	3000	0,2
2	1:3	3000	0,2
3	1:1	5000	0,2
4	1:3	5000	0,2
5	1:1	3000	0,4
6	1:3	3000	0,4
7	1:1	5000	0,4
8	1:3	5000	0,4

The synthesized liposomes were dialyzed by Midi Pur-A-Lyzer. Prior to dialysis the membrane was equilibrated with ultra-pure water. Dialysis was carried out with the aim of eliminating ethanol and maintaining a totally aqueous environment in view of the subsequent synthesis of the ocular gel.

2.4.2 Preparation of Ocular gel

A solution of 31 kDa PVA (5% v/v) was used: the optimal behaviour of polysaccharides as viscosifiers is due to their anionic nature. PVA has been modified by adding, along its chains, phosphate groups which can both stabilize the pH without altering osmolality and give the polymer an adequate thinning behaviour thanks to its anionic structure. Moreover, since the phosphate groups are chemically bound to the polymer chains, the risks typically associated with the use of phosphate-buffered systems are significantly reduced: phosphate buffers infact, are commonly employed to regulate osmolality; however, recent studies have shown that high concentrations of phosphate buffer can lead to irreversible corneal calcification, potentially resulting in vision loss.

The PVA phosphorylation reaction was performed following the procedure reported in the article "Modified low molecular weight poly-vinyl alcohol as viscosity enhancer," Leone et al[49].

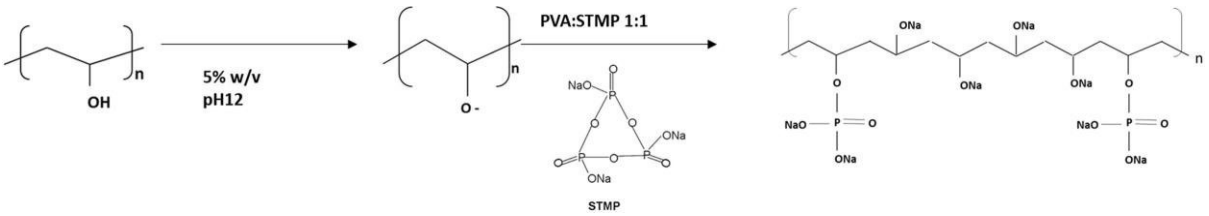

Figure 14. Schematic representation of polymer phosphorylation.

The inulin was reacted with Trisodium trimetaphosphate (STMP) using the same process.
At the end of the reaction, both products were purified by dialysis with ultrapure water in order to remove unreacted STMP and phosphates. The purified product was then frozen and subsequently lyophilized.
Liposomes were added to the PVA and inulin solutions separately to obtain a final solution respectively 10 mg/mL and 2 mg/mL: the suspension was maintained under magnetic stirring until the two polymers were completely solubilized.

2.4.3 Dynamic Light Scattering

Particle size and zeta potential were verified using dynamic light scattering (DLS) with a Zetasizer Nano ZS90 (Malvern Instrument Ltd., UK). Samples were diluted in ultra-pure water and the measurement was performed at room temperature (25°C). Measurements were conducted in triplicate.

2.4.4 Encapsulation Efficiency

The encapsulation efficiency (EE) represents the amount of active molecule actually encapsulated in the liposome compared to the initial amount employed for loading; such a parameter is critical for assessing the potential use of vesicles as drug delivery systems. The encapsulation efficiency was determined by HPLC (Thermo Fisher Scientific UltiMate 3000) using a UV-Vis diode array detector (DAD).
For analysis at HPLC, a 2.6 μm C18 reversed phase Kinetex column with a length of 150 × 2.1 mm was employed. For the mobile phase, H_2O (A) and Acetonitrile (B) were used, both acidified to 0.1% with formic acid. The samples were diluted in methanol, vortexed and subsequently subjected to solid

phase extraction (SPE), with the aim of retaining the phospholipids and releasing only the active ingredient. The samples were then injected in column and the chromatograms recorded at a wavelength of 254 nm. For the quantitative determination of the encapsulated active ingredient, a calibration line was constructed in the concentration range 1-50 ppm of triamcinolone.
The calculation of the encapsulation efficiency percentage (%EE) was carried out by the following equation (5):

$$\%EE = \frac{[TA]lip}{[TA]tot} * 100 \quad (5)$$

Where [TA] lip, calculated by means of the calibration line, indicates the amount of Triamcinolone encapsulated within the liposomes, while [TA] tot represents the total amount of active ingredient used at the time of liposome synthesis.

2.4.5 Infrared Spectroscopy

To verify the occurrence of PVA and inulin phosphorylation, a FTIR-ATR (Fourier Transform Infrared Spectroscopy, Attenuated Total Reflectance) analysis was performed both before and after synthesis. IR analyses were performed with a ThermoNicolet IS20 spectrometer equipped with a multiple ATR diffusion cell and a 45° germanium crystal as an internal reflection element. Spectra were acquired between 4000 and 450 cm-1 at the spectral resolution of 4 cm-^{1}.

2.4.6 Flow-Sweep test

To determine the viscosity of the three samples as a function of the applied shear rate, a flow-sweep test was performed. The test was conducted by applying an increasing shear rate ($\dot{\gamma}$), with values ranging from 0.01 s^{-1} to 10,000 s^{-1}, to cover a wide range of flow conditions. The temperature was kept constant at 25°C throughout the experiment.

2.4.7 Creep test

The creep test is a mechanical test used to study the behavior of a material subjected to a constant load over time: a constant stress is applied to the material, and the resulting deformation is measured

throughout the duration of the test. In this case, the measurements were conducted at a temperature of 25 °C, applying a constant stress of 1 Pa for a total duration of 180 seconds.

2. 5 Results and Discussions

2.5.1 Experimental Design

For each of the 16 conducted syntheses the mean size, PDI, zeta potential was measured via Dynamic Light Scattering, and the system encapsulation efficiency was verified via High Performance Liquid Chromatography (HPLC). The results are shown in **Table 7** (refer to table 6 for coding the samples). For ocular drug delivery systems, the average size of the nanoparticles and the polydispersion index (PDI) are the factors that are mainly optimized in experimental projects. In general, particles of size ≤ 200 nm are believed to offer adequate permeability and mobility across eye barriers, while small particles (approximately 20 nm) are rapidly eliminated; populations with a narrow particle size distribution (PDI < 0.2) are also desirable. The zeta potential determines the degree and sign of electrostatic forces between nanoparticles, which influence their stability and aggregation behaviour. Regarding colloidal stability, high absolute values (about ±20 mV) are of interest, since lower values could be exceeded by attractive forces between particles, leading to instability of the formulation[47]. Furthermore, following a topical route of administration, the presence of a cationic surface charge is believed to improve residence time due to interaction with the negatively charged corneal epithelium and mucins (high molecular weight glycoproteins) of the lacrimal fluid and conjunctiva. The amount of drug loadable and the encapsulation efficiency are also variables to be optimized through DoE. The first represents the maximum percentage of drug that can be encapsulated in nanoparticles, while the second quantifies the efficiency of this loading process during formulation production.

Table 7. Z-average, PDI, ζ potential and encapsulation efficiency measured for each sample.

Campione	Z-average ± sd (nm)	PDI± sd	Z-pot± sd (mV)	EE (%)
1	243,6 ± 3,5	0,165 ± 0,027	19,9±0,7	84%
2	128,6 ± 20,9	0,340 ± 0,109	11,2±0,3	74%
3	125,0 ± 0,5	0,238 ± 0,002	18,1±0,3	83%
4	134,4 ± 25,5	0,434 ± 0,090	31,1±1,3	77%
5	166,6 ± 4,4	0,283 ± 0,024	17,2±1,0	76%
6	285,4 ± 2,2	0,449 ± 0,052	20,4±2,1	69%
7	101,0 ± 7,6	0,363 ± 0,055	47,4±2,2	82%
8	266,9 ± 106,4	0,306 ± 0,065	44,6±2,0	69%

For each answer, a statistical analysis was conducted, through which a mathematical model and a polynomial equation were developed that take into account individual effects and interactions between factors. The validity of the model was evaluated considering the value of p, the value of F, the difference between adjusted and predicted R^2. These criteria ensure sufficient model power to discriminate effectively between real variations and statistical noise.

Z-average model

The full factorial 2^3 experimental design allowed us to analyse the effect of three factors (Flow Rate Ratio, Total Flow Rate and the amount of active compound used in the formulation) on the Zaverage response.

The experimental model includes the main effects, two- and three-factor interactions. The model has a p-value of less than 0.05 and an F-value of 10.76 which indicates correlation between the response variable and the three factors taken into consideration.

The term Adequate Precision is an indicator of the quality of the model that measures the signal/noise ratio: the value 8.772 indicates an adequate signal and that this model can be used to navigate the design space. Predicted R^2 is reasonably in line with Adjusted R^2 since the difference is less than 0.2.

Of the three factors chosen, only the A Flow Rate Ratio factor has a statistically significant value ($p < 0.05$) and the combination of the A and C factors. **Table 8** shows the values of F and p for each of the first and second order factors taken into consideration obtained through ANOVA.

	F-value	**p-value**
A Flow Rate Ratio	7,61	0,0008
B Total Flow Rate	2,52	0,1406
C Triamcinolone	3,10	0,1060
AC	29,82	0,0002

Table 8. F-value and p-value for the first and second order coefficients.

The generated coded equation for the Z-average response is:

$$185{,}919 + 25{,}5312 * A \ -14{,}6937 * B + 16{,}2937 * C + 50{,}5313 * AC$$

The sign of the coefficients provides an indication of the trend of the variable to be determined as a function of that factor: a positive value indicates a direct proportionality between factor and response, while a negative value indicates an inverse relationship. In this case, the combined factors A Total Flow Rate and C quantity of active ingredient are those that have the greatest impact on size, with a direct proportionality trend.

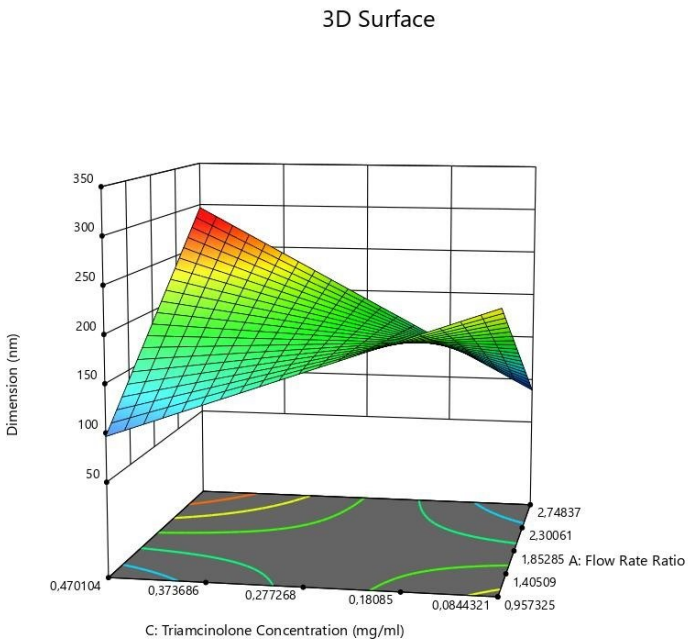

Figure 15. 3D response surface graph for the factor A e C.

The 3D model graph helps us to better visualize the combination of the two significant variables A and C, while the third factor B is kept constant at an intermediate value. The graph highlights an increase in size with the use of the combination A +1 and C +1, while the remaining combinations show conditions in agreement with the literature: using greater ratios of aqueous phase, compared to the organic phase favors the formation of nanoparticles lower. This phenomenon is explained by the fact that the self-assembly of liposomes, under conditions of increasing polarity of the solution, occurs from intermediate structures of bilayer phospholipids. When the aqueous phase prevails over the organic phase, the ethanol concentration can easily reach a critical value that prevents the magnification of these intermediate structures, thus limiting their final dimensions.

PDI model

For the polydispersity index (PDI) the selected factor model is significant, with a p-value of 0.0018 and an F-value of 9.43. The term Adequate Precision, an indicator of the quality of the model and which measures the signal/noise ratio, is equal to 7.002 which indicates an adequate signal and that this model can be used to navigate the design space. Predicted R^2 is reasonably in line with Adjusted R^2 since the difference is less than 0.2. Again, only the A Flow Rate Ratio factor is significant, along with the combination of A and C factors.

Table 9. F-value and p-value of the first and second order coefficients obtained through ANOVA.

	F-value	**p-value**
A Flow Rate Ratio	16,19	0,0017
B Triamcinolone	3,24	0,0970
AC	8,88	0,0115

The coded equation generated for the PDI model is:

$$0{,}31345 + 0{,}07345 * A + 0{,}0328625 * C - 0{,}0543875 * AC$$

It should be noted that a positive value indicates a direct relationship between factor and response, while a negative value indicates an inverse relationship. The significance of the PDI factor coefficients is related to the significance of the size coefficients.

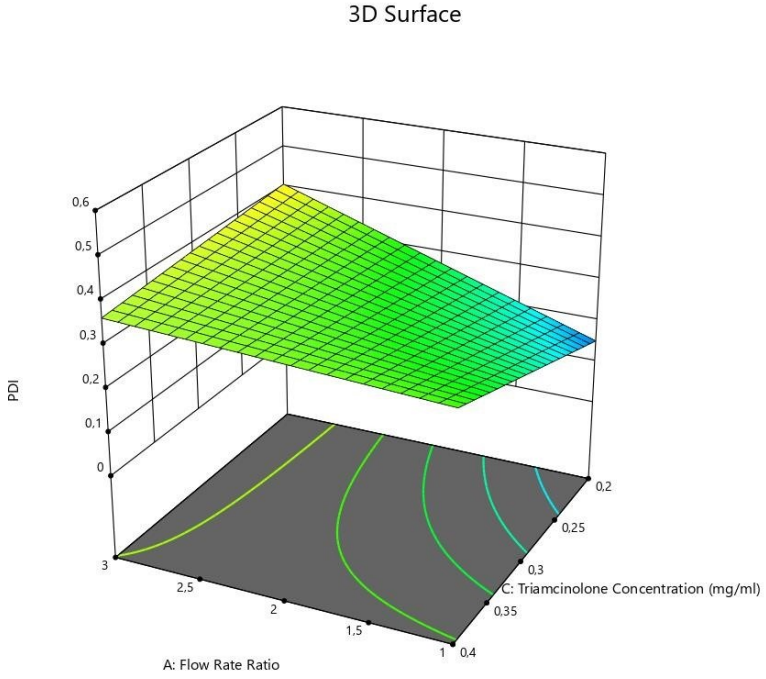

Figure 16. 3D response surface graph for the factors A e C.

Again, we report the 3D response surface graph for significant factors A and C, keeping factor B constant at an intermediate value. As the coefficients of the equation suggested, the negative combination of both variables leads to obtaining lower values of PDI.

Encapsulation Efficiency (EE) model

The model obtained for the encapsulation efficiency is not statistically significant: the p-value is greater than 0.05 while F-value is equal to 1.70. Consequently, all factors studied are also not statistically significant. These results suggest that the independent factors considered in this study do not significantly influence the value of the encapsulation efficiency; thus, a statistical model describing the response variation as a function of the selected variables cannot be obtained.

TA Liposomes Optimized Formulation

Experimental Design was used with the idea of improving the SoyPC/Dope/Dotap liposomal formulation loaded with triamcinolone by reducing its size and PDI and maximizing encapsulation efficiency. For this last point, the model was not significant and was therefore not included in the optimisation. The utmost importance was given to the PDI (+++++), while for the dimensions it is important to remain in the range from 100 to 200 nm. Through the Software Design Expert, the solution that meets the set criteria and has the highest desirability index (0.869) has been identified and includes: A Flow Rate Ratio -1, B Total Flow Rate +1 and C Triamcinolone -1.

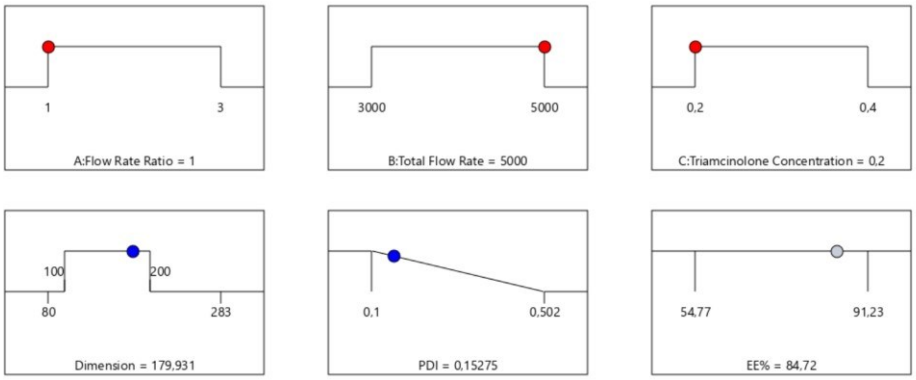

Desirability = 0,869
Solution 1 out of 73

Figure 17. The figure gives the three factors chosen to conduct Experimental Design, the conditions in which to use them for optimized synthesis and the predicted values for each factor.

The liposomes thus obtained showed an average size of 128.9 ± 1.055 nm and a PDI of 0.1992 ± 0.0245. Both values were compared with the model prediction (Z-average 179.9 and PDI 0.153) and were similar, confirming the validity of the model. The zeta potential of the liposomes was also measured, for a value of +41.26 ± 7.58. The encapsulation efficiency was still measured and found to be 76%. The optimized formulation was used for subsequent ocular gel synthesis.

2.5.2 Infrared Spectroscopy

Infrared analysis was performed to verify the introduction of phosphate moieties along the chains. **Figures 18** and **19** show the comparison between the polymers before and after phosphorylation, while the main observed wavenumbers are summarized in **Table 10** along with their corresponding assignments.

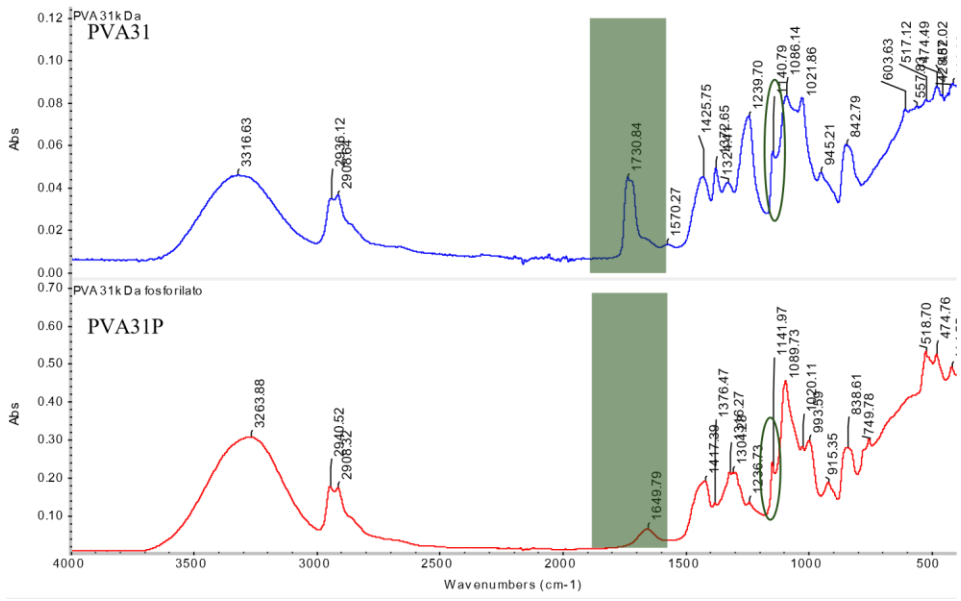

Figure 18. PVA31 and PVA31 Phosphorilate infrared spectra.

The most notable difference between the PVA31 and PVA31 P spectra is the appearance, in the latter, of intense absorption bands attributed to phosphate groups, observed at 1304 cm^{-1} and 1020 cm^{-1},

corresponding to the O=P–O stretching and P–O bending vibrations, respectively. In both spectra, a broad band is observed in the 3000–3500 cm^{-1} region, attributable to the stretching vibrations of hydroxyl (OH) groups involved in hydrogen bonding, which are characteristic of the PVA structure. Additionally, a band appears between 2908 and 2940 cm^{-1}, corresponding to the symmetric and asymmetric stretching of CH_2 groups along the polymer backbone.

For PVA31, a distinct band is visible at approximately 1730 cm^{-1}, associated with the stretching vibration of the carbonyl group (C=O) from residual acetyl groups. The presence of these groups is indicative of a low degree of hydrolysis of the commercial polymer. In contrast, in the PVA31P spectrum, this band shows a significant decrease in intensity and is shifted to around 1649 cm^{-1}. This shift is attributed to the strongly basic environment (pH ≈ 12) used during the phosphorylation reaction, which promotes the deprotonation of hydroxyl groups. The reduced intensity of the 1147 cm^{-1} band, along with the shift of the OH stretching band toward higher wavenumbers in the PVA31P spectrum, confirms a partial disruption of the hydrogen bonding network. This effect can be attributed to the involvement of some hydroxyl groups in the phosphorylation process, as deprotonated hydroxyls serve as the nucleophilic sites for phosphate group attachment[49].

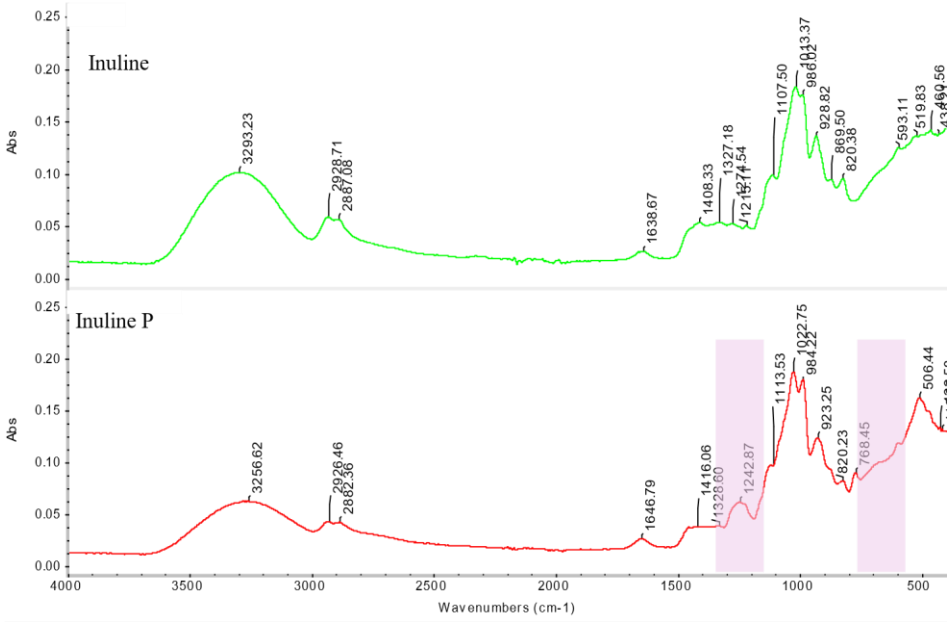

Figure 19. Inulin and Inulin Phosporilated spectra.

Regarding inulin, both spectra show the presence of the broad OH stretching band in the 3000–3500 cm^{-1} region, as well as the characteristic band corresponding to CH_2 stretching vibrations[51]. Evidence

of successful phosphorylation of inulin is provided by the appearance, in the spectrum of phosphorylated inulin (Inulin P), of two bands that are absent in the spectrum of the unmodified polymer. Specifically, a band at 1242 cm^{-1}, attributed to the stretching vibration of the O–P=O group, and a band at 768 cm^{-1}, which—despite being slightly shifted from the expected value—can be associated with the P–O bending vibration. The presence of these two bands clearly indicates the successful functionalization of inulin with phosphate groups.

Table 10. Main observed wavenumbers in FTIR spectra of phosphorylated PVA 31, PVA 3, inulin and phosphorylated inulin together with their assignments.

PVA31	PVA31P
Wave number (cm^{-1}) and Functional Groups	
3316 Stretching ν OH	3263 Stretching ν OH
2936-2908 Stretching ν CH_2	2940-2908 Stretching ν CH_2
1730 Stretching ν COOR	1649 Stretching ν COOR
1425 Bending CH_2	1417 Bending CH_2
1086 Bending OH	1304 Stretching -O-P=O
	1089 Bending OH
	1020 Bending P-O

INULIN	INULIN P
Wave number (cm^{-1}) and Functional Groups	
3293 Stretching ν OH	2926-2882 Stretching ν CH[1]
2928-2887 Stretching ν CH_2	1646 Stretching ν C=O
1638 Stretching ν C=O	1242 Stretching O-P=O
1107 Stretching ν C-O	1113 Bending OH
1013 Bending OH	923 Bending CH_2
928 Bending CH_2	768 Bending P-O
3293 Stretching ν OH	2926-2882 Stretching ν CH_2

2.5.3 Rheological property analysis

Rheological properties describe how a material responds when subjected to mechanical stress, providing detailed information about its ability to flow and deform. In particular, viscosity and time-dependent viscoelastic behavior were analyzed in order to understand how the formulations respond under stress and how they can be optimized for various applications. These properties directly influence the formulation's stability, ease of handling, and ability to achieve controlled drug release. These analyses were performed on the two PVA and inulin-based gels, respectively enriched with triamcinolone-loaded liposomes; each of the two samples was compared with the gel formulation with no liposomes added and the liposome loaded with dialyzed triamcinolone alone.

The viscosity of the two systems was evaluated through a flow sweep test. **Figure 20** shows the viscosity versus shear rate curves for the phosphorylated inulin-based gel with, drug-loaded liposomes and inulin P.

[1]

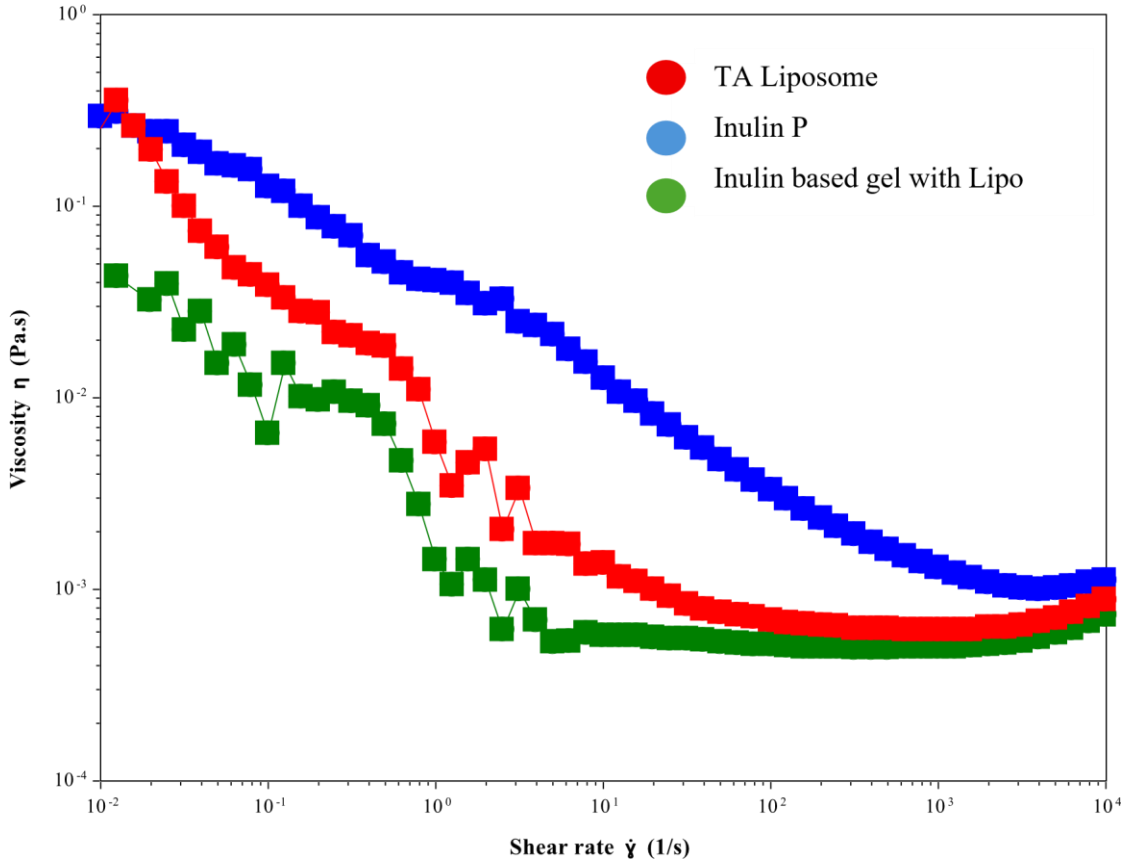

Figure 20. Viscosity versus shear rate curves for the phosphorylated inulin-based gel with liposomes (green curve), drug-loaded liposomes (red curve) and inulin P (blue curve).

It is observed that all curves show a decrease in viscosity as the shear rate increases, typical shear thinning (pseudoplastic) behavior, characterized by low viscosity at high shear rates and high viscosity at rest[52]. The Inulin P system has higher viscosity values than the other two solutions, indicating a more robust structure, capable of resisting the flow more. This effect could be attributed to polymer-water interaction by hydrogen bonds.

The solution containing only liposomes is characterized by viscosity values lower than phosphorylated inulin but higher than the Inulin P system with liposomes up to about 102 s-1; above this shear rate, the viscosity values become comparable instead. This suggests that the inclusion of liposomes within the phosphorylated inulin matrix likely interferes with polymer interactions, reducing their resistance to flow.

Figure 21 shows the results of the flow sweep test for the PVA-based gel with the addition of liposomes; as in the previous case, PVA31 and Triamcinolone-based liposomes were used for comparison.

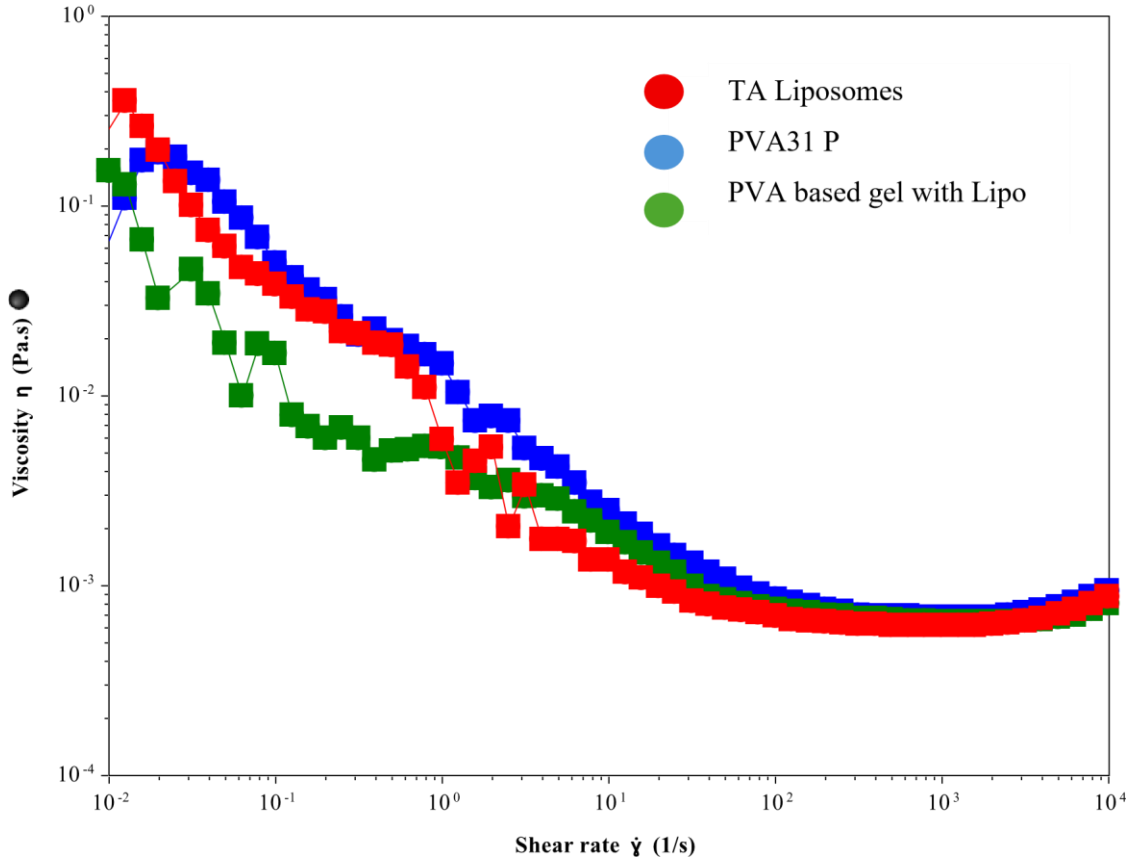

Figure 21. Viscosity vs. shear rate curves for: phosphorylated PVA-based gel with liposomes (green curve), drug-loaded liposomes (red curve) and phosphorylated PVA (blue curve).

The three samples analyzed clearly exhibit shear-thinning behavior, as their viscosity progressively decreases with increasing shear rate. At shear rates around 10^2 s^{-1}, the viscosity values tend to converge; at lower shear rates, however (albeit to a lesser extent than what was observed for inulin) some differences emerge, indicating distinct resistance of the internal structures in the three systems to flow.

The PVA31 P sample presents slightly higher viscosity values compared to the TA liposomes solution. Conversely, the TA liposomes sample shows higher viscosity than the PVA-based gel with liposomes system, which displays the lowest viscosity values at low shear rates. This trend suggests that, similarly to what was observed for inulin, the system composed only of polymer resists flow more, albeit to a limited degree. This effect can be attributed to polymer–polymer interactions fostered by the phosphate groups. The addition of liposomes into the polymer matrix, on the other hand, appears to disrupt these interactions, reducing the compactness of the network and resulting in lower viscosity. Both gels therefore demonstrate shear-thinning behavior, a beneficial trait for ocular drug delivery applications. In particular, a low viscosity at high shear rates minimizes stress on the ocular surface during blinking, while a high viscosity at rest enhances retention during the inter-blink interval. In

this way, the gel remains in contact with the eye long enough to allow effective release of the active compound. Additionally, it is important that the viscosity values are maintained within defined threshold ranges: recent studies recommend a lower threshold of about 10 mPa·s to ensure adequate retention, and an upper limit around 30 mPa·s, beyond which issues such as blurred vision or irritation may arise[49]. The measured viscosities for the phosphorylated inulin and PVA-based gels containing triamcinolone-loaded liposomes are approximately 1.0 mPa·s at high shear rate (10,000 s^{-1}) in both cases, thus falling below the retention threshold. This suggests that the synthesized systems can be applied, provided they are delivered and used at lower shear rates where the retention parameter is satisfied.

The viscosity data obtained from the flow sweep test were complemented by a creep test, aimed at evaluating the time-dependent behavior of the gels under a constant applied stress[53].

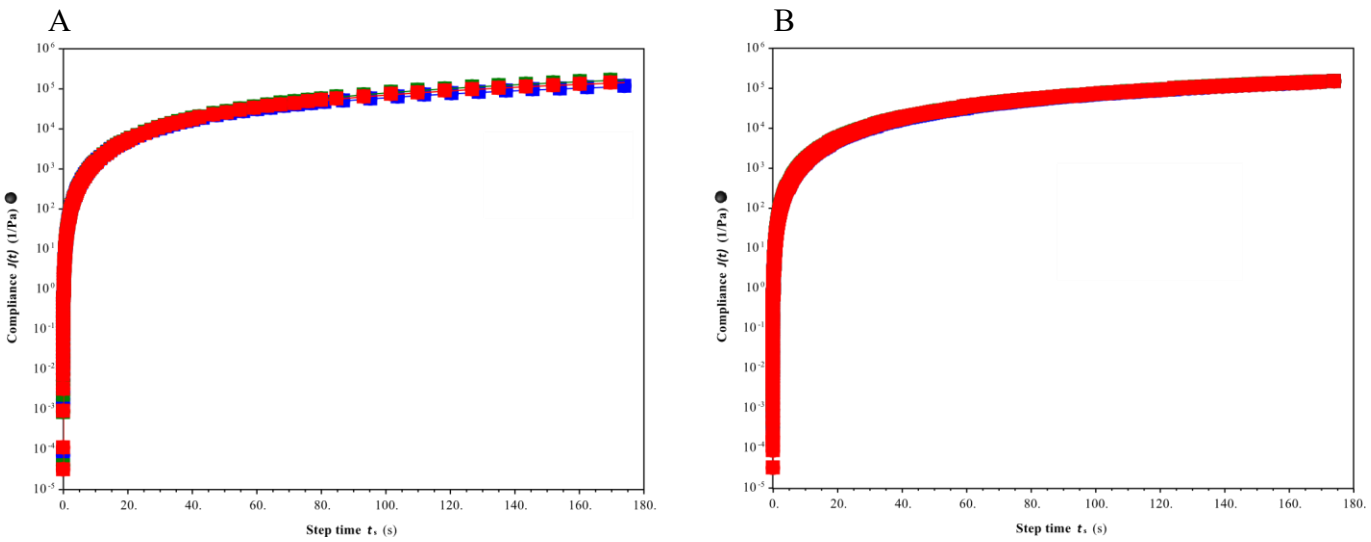

Figure 22. The figure A show the Compliance/Step time curves for: 1. gel based on inulin phosphorylated with liposomes (green curve), 2. loaded liposomes in water (red curve) and 3. inulin phosphorylated in water (blu curve). Figure B instead shows the compliance/step time curves for: PVA-based gel phosphorylated with liposomes (green curve), charged liposomes (red curve) and PVA31 P (blue curve).

The analysis of the creep compliance curves reveals a typical viscoelastic behavior for all samples, with the curves reaching a steady state after approximately 120 seconds, where the compliance tends to stabilize.

For the phosphorylated inulin-based systems, only minimal differences are observed between the sample TA liposomes and the pure polymer matrix, suggesting that the incorporation of liposomes does not significantly alter the viscoelastic properties of the gel. This indicates that the structural

rigidity of the inulin-based matrix is maintained even in the presence of loaded liposomes, which is a crucial requirement for drug delivery applications.

Similarly, the addition of liposomes to the phosphorylated PVA matrix does not appear to modify its time-dependent mechanical response, as the creep behavior remains comparable to both the pure polymer and the liposomes in solution. Interestingly, this finding contrasts with the results obtained from the flow sweep test, where the phosphorylated PVA gel exhibited greater structural compactness. Nevertheless, the creep test confirms that the phosphorylated PVA remains a robust and stable system, capable of encapsulating liposomes without compromising its mechanical integrity, thus making it a promising candidate for controlled drug delivery applications.

2.6 Conclusion

Cationic liposomes (composed of SoyPC, DOPE, and DOTAP) loaded with triamcinolone were synthesized for use in the preparation of two potential ocular gels based on PVA and inulin. The liposomes were manufactured via microfluidics, combined with an Experimental Design (DoE) study. This approach enabled optimization of the nanosystems' formulation by identifying the operational conditions most suitable for obtaining liposomes with acceptable mean size and polydispersity index (PDI), as well as high encapsulation efficiency (EE). The DoE methodology allowed definition of the relationships between input variables (flow rate ratio (FRR), total flow rate (TFR), and amount of active ingredient) and liposome output properties (PDI, mean size, and EE%). From this study, it emerged that factor A (Flow Rate Ratio) and the interaction between factors A and C (amount of triamcinolone) significantly influence both PDI and particle size, thereby establishing a correlation between these factors and the responses (i.e. Z-average and PDI). In contrast, no independent factor was found to significantly affect encapsulation efficiency; consequently, no predictive statistical model could be developed for that parameter.

The optimized liposome formulation was then used in the synthesis of the two gels: both base materials (PVA and inulin) underwent a phosphorylation reaction, the success of which was verified via FTIR-ATR spectroscopy.

Rheological analyses enabled investigation of the mechanical properties of the synthesized gels. In particular, the viscosity profiles showed that both systems exhibit a shear-thinning behavior, which is appropriate for ophthalmic application as it facilitates administration and reduces the mechanical stress on the ocular surface during blinking. However, the measured viscosity values do not exceed

the minimum threshold considered necessary for adequate ocular retention. If the retention time is insufficient, the therapeutic efficacy of the formulation may be compromised.

3 Dexamethasone

Although triamcinolone acetonide has been more widely used due to its availability, pharmacokinetic profile, and ease of administration, dexamethasone is pharmacologically a much stronger ocular corticosteroid; in fact, dexamethasone is five times more potent than triamcinolone acetonide and, being more hydrophilic, it can achieve higher concentrations in the vitreous humor[51].

Dexamethasone is used in ocular therapy, especially to treat conditions that affect the inside of the eye. It is given topically for conditions such as uveitis (inflammation of the uvea) or macular edema, where it acts as a powerful anti-inflammatory, effectively reducing tissue damage caused by inflammatory processes[54].

The long duration of action is a crucial aspect: the half-life of dexamethasone is significantly longer than other short- or medium-acting glucocorticoids. Due to its clinical effect lasting between 36 and 72 hours, it allows for less frequent administration than molecules like cortisone, which have an action limited to approximately 5-12 hours. An exploratory study was conducted to evaluate the potential of encapsulating dexamethasone in drug delivery systems intended for ophthalmic use. The selected formulations were liposomes and solid lipid nanoparticles (SLNs). Liposomes are particularly well-suited for ocular applications due to their excellent biocompatibility and structural similarity to biological membranes. This resemblance promotes fusion with corneal epithelial cells, thereby enhancing the absorption of dexamethasone into ocular tissues. Moreover, liposomes can be engineered to deliver the drug to both the anterior and posterior segments of the eye and are capable of crossing challenging physiological barriers such as the blood-retinal barrier, especially when appropriately modified. However, problems related to the stability of liposomes, along with their limited drug retention capacity (which results in the need for more frequent administrations) has led to the exploration of alternative formulations. Solid lipid nanoparticles represent an interesting alternative for topical ocular application, particularly when a prolonged release of dexamethasone is desired. Due to their solid structure and modifiable surface, SLNs can adhere to the ocular mucosa and release the active compound in a slower and more controlled manner. This enables a reduction in dosing frequency, thereby improving patient adherence to the treatment regimen. The main limitations of SLNs lie in their reduced ability to penetrate deeper ocular tissues, which may limit their effectiveness in targeting the posterior segment of the eye[55].

3.1 Materials and Methods

DOPC(1,2-dioleoyl-sn-glycero-3-phosphocholine),DSPC(1,2-Distearoyl-sn-glycero-3-phosphocholine) (Avanti Polar Lipids Inc.), Precirol ATO 5 was kindly supplied by Gattefossè (France).

The following reagents were used: ethanol (EtOH, purity ± 99%, Merck Italia), methanol (MeOH, purity ± 99%), ultra-pure water (18.2 MΩ·cm, Rephile Direct-Pure purifier).

3.1.2 Liposomes preparation

An Automated Nanoparticle (ANP) system (Particle Works, Alfatest) was used for the synthesis of liposomes using microfluidics.

Two different samples were synthesized using DOPC (1,2-dioleoyl-sn-glycero-3-phosphocholine) and DSPC (1,2-distearoyl-sn-glycero-3-phosphocholine): the main difference lies in the fatty acid chains, in fact DOPC has two chains of unsaturated fatty acids (called oleoyls) which contain a cis double bond in their structure while the DSPC is made up of two chains of saturated fatty acids without double bonds. This structural difference greatly affects the physical properties of the two lipids. DOPC has a very low phase transition temperature and membranes formed by DOPC are more flexible and dynamic; in contrast, DSPC has a much higher transition temperature, around 55 °C. DSPC-based membranes are therefore more stable and less permeable. Both were treated with cholesterol. The addition of cholesterol to lipid membranes formed by DOPC or DSPC has a stabilizing effect and significantly modulates membrane properties. In the case of DOPC, which is naturally fluid at room temperature due to its unsaturated chains, cholesterol works by reducing fluidity and increasing membrane stiffness. This happens because cholesterol inserts itself between the fatty acid chains, limiting their movement and making the membrane less permeable and more resistant to physical and chemical stress.

In the case of DSPC, which is already quite rigid and stable at room temperature due to its saturated chains, cholesterol acts instead to prevent excessive stiffness and crystallization. By inserting itself between saturated chains, cholesterol prevents the orderly organization of lipid molecules, keeping the membrane more elastic and less fragile, improving its relative fluidity without compromising overall stability.

The organic phase (ethanol) had lipid components and active ingredient added, while the aqueous phase only contains deionized water. the corresponding lipid system without active compound was also synthesized for both formulations.

3.1.2 Solid Lipid Nanoparticles preparation

For the synthesis of Solid Lipid Nanoparticles using microfluidics, an aqueous solution based on Poloxamer was used, while Precirol ATO 5 and Dexamethasone in ethanol were mixed in the organic phase. Precirol ATO forms the solid lipid matrix of the nanoparticle, where the drug is trapped, while Poloxamer acts as a surface stabilizer, preventing aggregation and improving the dispersion of nanoparticles in the aqueous phase; ocular tolerability largely depends on the nature of the surfactant (non-ionic, ionic, cationic, or anionic) as well as the concentration used. Non-ionic surfactants, such as Poloxamer 188, are generally better tolerated[56]. Both empty SLNs and Dexamethasone-loaded SLNs were synthesized.

3.1.3 Dynamic Light Scattering

Particle size and zeta potential were verified using dynamic light scattering (DLS) with a Zetasizer Nano ZS90 (Malvern Instrument Ltd., UK). Samples were diluted in ultra-pure water (10% v/v) and the measurement was performed at room temperature (25°C). Measurements were conducted in triplicate.

3.1.4 Encapsulation Efficiency

Quantification of dexamethasone for the determination of encapsulation efficiency was achieved using an HPLC-DAD instrument (Thermo Fisher Scientific UltiMate 3000). A Kinetex 2.6 µm Polar C18 column (150 x 2.1 mm 100 Å) was used at a temperature of 40 ±1°C.
Dexamethasone elution was achieved by exploiting a 60:40 mobile phase (%v/v) isocratic method of water and acetonitrile both 1% acidified with formic acid. All chromatograms were recorded at 241 nm. For the quantitative determination of the encapsulated active molecule, a calibration line was constructed in the concentration range 1-50 ppm of dexamethasone. . The encapsulation efficiency was calculated using the following equation (6):

$$EE(\%) = \frac{[DXT]lip}{[DXT]tot} \times 100 \qquad (6)$$

Where [DXT]lip represents the amount of active molecule encapsulated in the liposomes, determined by the calibration curve, and [DXT]tot is the total amount of dexamethasone used in the synthesis.

3.1.5 Infrared Spectroscopy

An FTIR-ATR analysis of the synthesized samples was performed for the qualitative characterization of liposomes and solid lipid nanoparticles loaded with dexamethasone.
Before being analyzed the sample was lyophilized (0.3 mbar, -41 °C, 24 h, 5-Pascal). The spectra were acquired by means of a Nicolet iS50 FTIR-ATR (ThermoFisher scientific) spectrometer operating in the 4000-800 cm-1 spectrum and equipped with an ATR (attenuated total reflectance) multiple reflection cell with germanium crystal.

3.2 Results and Discussions

3.2.1 Dynamic Light Scattering

Particle size is typically expressed as the average diameter, which represents an intensity-weighted measure of the scattered light. The Polydispersity Index (PDI) is essential for understanding the size distribution within the sample: values close to 0.2 indicate a monodisperse sample, a preferred condition in pharmaceutical applications as it ensures uniformity. The zeta potential reflects the surface charge of a particle in suspension and provides information regarding the colloidal stability of the system.

Sample	**Z-average ± sd (nm)**	**PDI ± sd**	**Z-pot ± sd (mV)**
Empty Liposome DOPC	191,7 ± 4,6	0,23 ± 0,003	-20,73 ± 0,9
Dexamethasone Lipo	116,9 ± 2,2	0,27 ± 0,001	-28,17 ± 1,5

Table 11. Z-average, PDI and zeta potential of synthesized liposomes.

Empty liposomes have an average diameter of 191.7 ± 4.6, while full liposomes show a smaller average diameter (116.9 ± 2.2) this difference could suggest that the addition of dexamethasone resulted in a reduction in the overall volume of the liposome. Both liposomes (with a PDI around 0.2) are monodisperse. Furthermore, the zeta potential of full liposomes has slightly higher values than that of empty liposomes, which means greater colloidal stability and, therefore, greater electrostatic repulsion, which reduces the risk of aggregation.

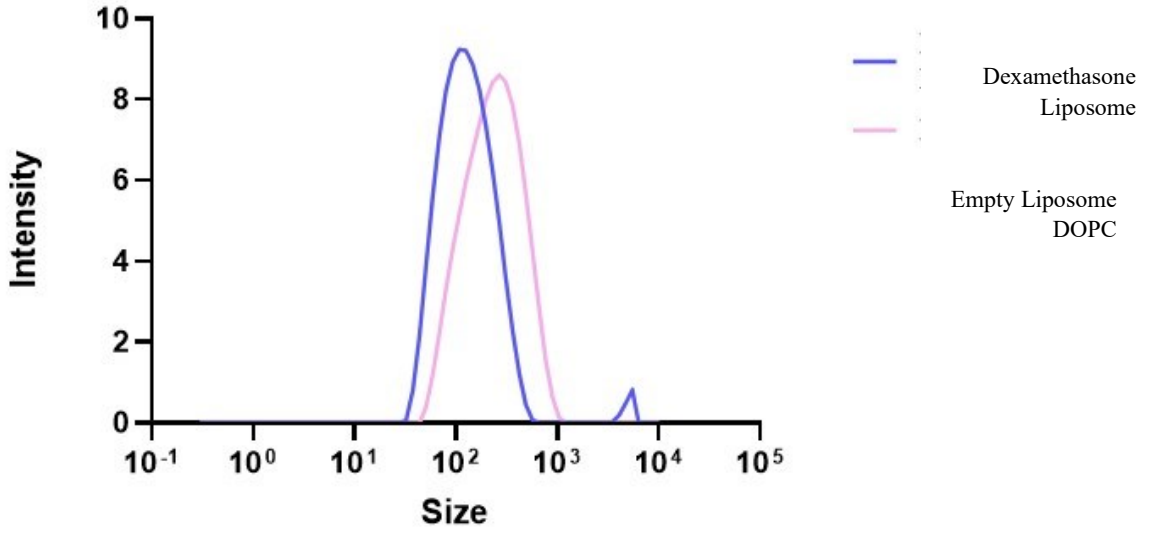

Figure 23. Intensity distribution as a function of particle size obtained by Dynamic Light Scattering (DLS) analysis of DOPC Liposomes.

Table 12 show the DLS results for DSPC liposomes:

Sample	**Z-Average ± sd (nm)**	**PDI ± sd**	**Z-pot ± sd (mV)**
Empty Liposome DSPC	210,2 ± 7,2	0,27 ± 0,04	-24,63 ± 1,0
Dexamethasone Lipo	230,3 ± 2,4	0,12 ± 0,003	-7, 97 ± 1,1

The dexamethasone-containing liposome has a slightly larger average diameter than the empty liposome, with an increase of approximately 20 nm. This increase in size may suggest that incorporation of the drug resulted in an expansion of the liposome lipid structure, possibly due to the interaction between dexamethasone molecules and membrane lipid components. Such interactions can in effect change lipid organization and packaging.

Both systems are monodispersed, as indicated by size distribution analysis, which suggests good uniformity in the particle population and a controlled and reproducible preparation. However, the zeta potential detected for the dexamethasone-containing liposome is lower than for the empty liposome, indicating less colloidal stability. This reduction in stability could be attributable to the presence of the drug which affects the ability of the particles to electrostatically repel each other, by altering the surface charge or organization of the lipid membrane.

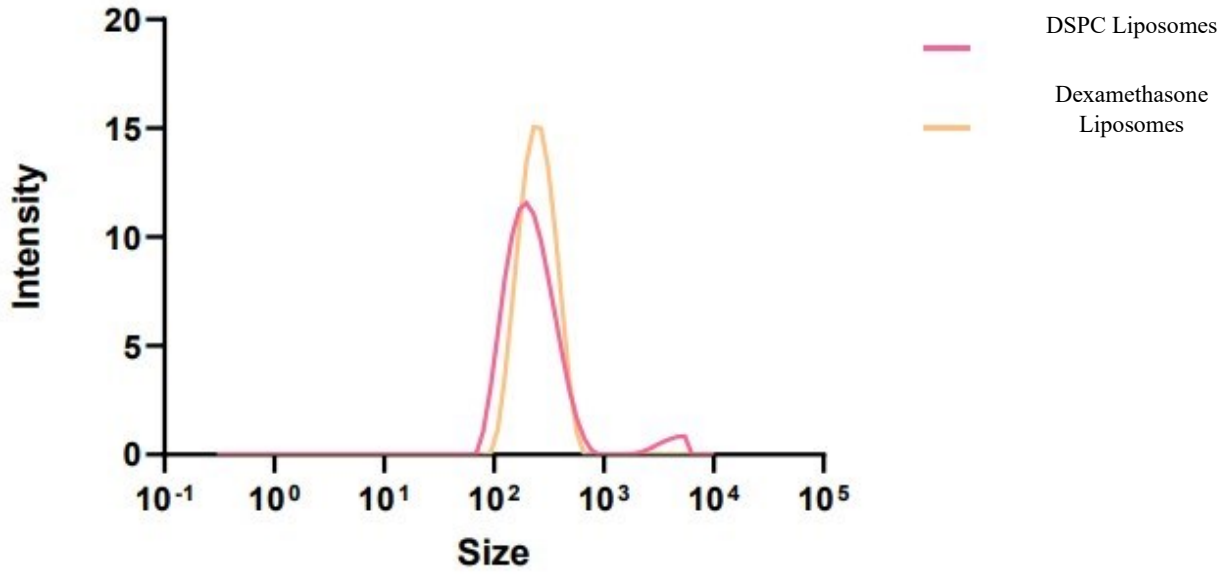

Figure 24. Intensity distribution as a function of particle size obtained by Dynamic Light Scattering (DLS) analysis of DSPC Liposomes.

Table 13 show the DLS results for Solid Lipid Nanoparticles:

Sample	Z-average ± sd (nm)	PDI ± sd	Z-pot ± sd (mV)
SLN	61,3 ± 2,5	0,31 ± 0,04	-20,58 ± 0,54
SLN Dexamethasone	104,6 ± 1,8	0,29 ± 0,01	-26,17 ± 1,1

Solid lipid nanoparticles formulated with Poloxamer and Precirol ATO as the main lipid exhibit distinctive physicochemical characteristics in relation to the presence or absence of the active molecule dexamethasone. Dexamethasone-laden SLNs exhibit a significantly greater average size of about 43 nm than empty SLNs. This increase in size can be attributed to the incorporation of the drug within the solid lipid matrix of Precirol, which induces structural dilation or changes the internal arrangement of lipids. In addition, the presence of dexamethasone could also affect the organization of the Poloxamer corona on the surface, thus contributing to the overall increase in particle size.

The index polydispersity (PDI) of both formulations, both empty and loaded, remains around 0.3, indicating that both particle populations are relatively monodispersed and homogeneous regarding size distribution. This finding confirms the effectiveness of the formulation process in maintaining a stable and well-defined population of nanoparticles, an essential characteristic for the reproducibility and performance of the system.

The zeta potential of SLN containing dexamethasone is greater than that of empty SLN in terms of colloidal stability. The synergy between Poloxamer, a recognized steric stabilizer, and the drug's increase in surface charge is likely to enhance SLNs' resistance to coalescence and sedimentation.

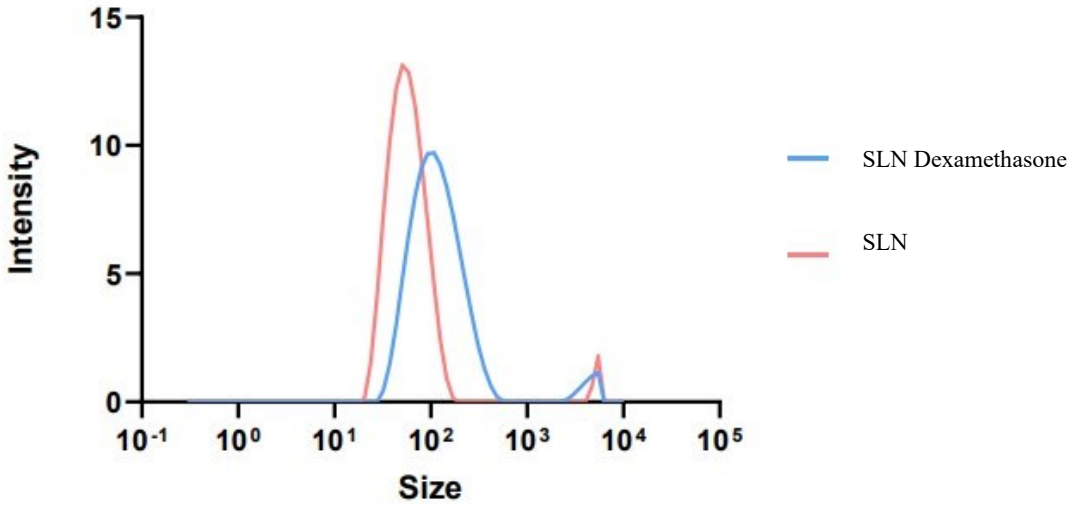

Figure 25. Intensity distribution as a function of particle size obtained by Dynamic Light Scattering (DLS) analysis of Solid Lipid Nanoparticles.

3.2.2 Encapsulation Efficiency

Using high-performance liquid chromatography (HPLC) and a calibration line, the amount of dexamethasone encapsulated in liposomes and SLNs was determined.

Table 14. Encapsulation Efficiency of Liposomes and SLN.

Sample	EE%
DOPC/ cholesterol/ Dexamethasone	50%
DSPC/cholesterol/ Dexamethasone	37%
SLN Dexamethasone	75%

In the table (**table 14**) the values of the encapsulation efficiency obtained for each sample (EE%) are given. SLNs show the highest percentage, as we expected from precirol ATO for a lipophilic molecule such as dexamethasone. The presence of cholesterol in liposomal formulations significantly affects membrane characteristics and the encapsulation efficiency of dexamethasone. While in the DOPC/cholesterol system cholesterol improves stability without excessively compromising

encapsulation, in the DSPC/cholesterol formulation the stabilizing effect is more marked, with a consequent decrease in the retention capacity of the drug.

3.2.3 Infrared Spectroscopy

Attenuated reflectance Fourier transform infrared spectroscopy (FTIR-ATR) is a spectroscopy method useful for studying liposomes and SLN: it allows measuring the vibration and rotation of molecules influenced by infrared radiation at a specific wavelength, obtaining information on molecular interactions.

This section shows the FTIR-ATR spectra of the DOPC/Cholesterol and DOPC/Cholesterol/Dexamethasone liposome (**Figure 26**), the DSPC/Cholesterol and DSPC/Cholesterol/Dexamethasone liposome (**Figure 27**) and empty SLN and SLN with dexamethasone (**Figure 28**).

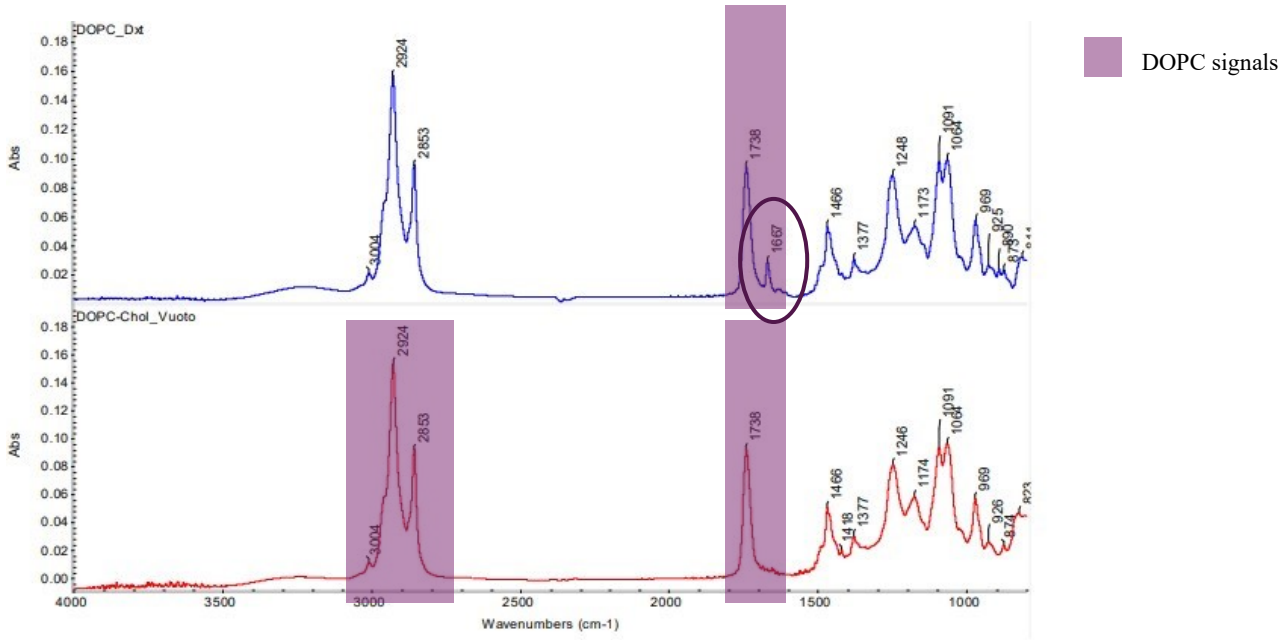

Figure 26. Dopc/Cholesterol and Dopc/Cholesterol/Dexamethasone liposomes spectra.

About DOPC, the 3000–2800 cm^{-1} region in infrared spectra usually corresponds to the ν(C–H) vibrations of methylene and methyl groups in aliphatic molecules. Two bands with the highest absorbance in that area are close to 2924 and 2854 cm−1 and are assigned to the antisymmetric and

symmetric stretching vibrations of methylene, respectively. The band observed at 3004 cm^{-1} corresponds to the stretching vibration of the cis-olefin groups =C–H while the shoulder near 2959 $cm^{-}1$ is attributed to the antisymmetric stretching of methyl groups. A strong band close to 1737 cm^{-1} is assigned to the stretching of the carbonyl band.[53]

The influence of cholesterol can be seen from changes in the phosphate region (1200–1000 cm^{-1}) for changes in polar head orientation and hydration and in changes in CH_2 bands, indicative of variations in chain order or fluidity. The peak at 1667 cm^{-1} could be an intense peak for the C=O (carbonyl) of the ketone group, characteristic of corticosteroids. In dexamethasone, the ketone group is well present and is one of the most distinctive signals

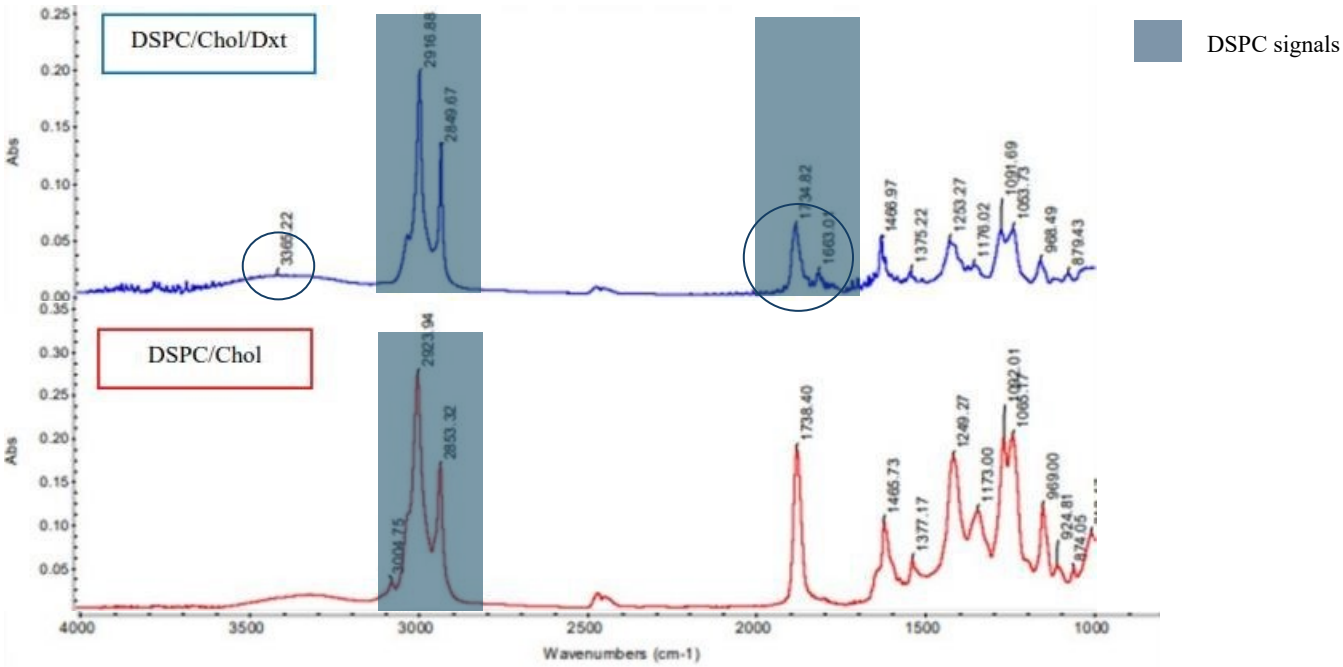

Figure 27. Dspc/Cholesterol and Dspc/Cholesterol/Dexamethasone liposomes FT-IR spectra.

Regarding DSPC, the most obvious bands are those due to the stretching of methylene (CH2) groups in alkyl chains, which are around 2850 cm^{-1} for symmetric stretch and 2920 cm^{-1} for asymmetric stretch. These bands are indicators of the ordering and conformation of lipid chains.

A well-defined band around 1735 cm^{-1} is also noted, attributable to the stretching of the carbonyl group (C=O) present in the esters of the DSPC molecule. In addition, bands associated with the phosphate group (PO_2^-) appear between 1220 and 1250 cm^{-1} for asymmetric stretching and around 1085 cm^{-1} for symmetric stretching. These regions are important because they can be affected by

interactions with cholesterol The peak at 1667 cm^{-1} could be an intense peak for the C=O (carbonyl) of the ketone group, characteristic of corticosteroids, furthermore, the band at approximately 3365 cm^{-1} could correspond to the stretching of the hydroxyl group (OH) present in its structure.

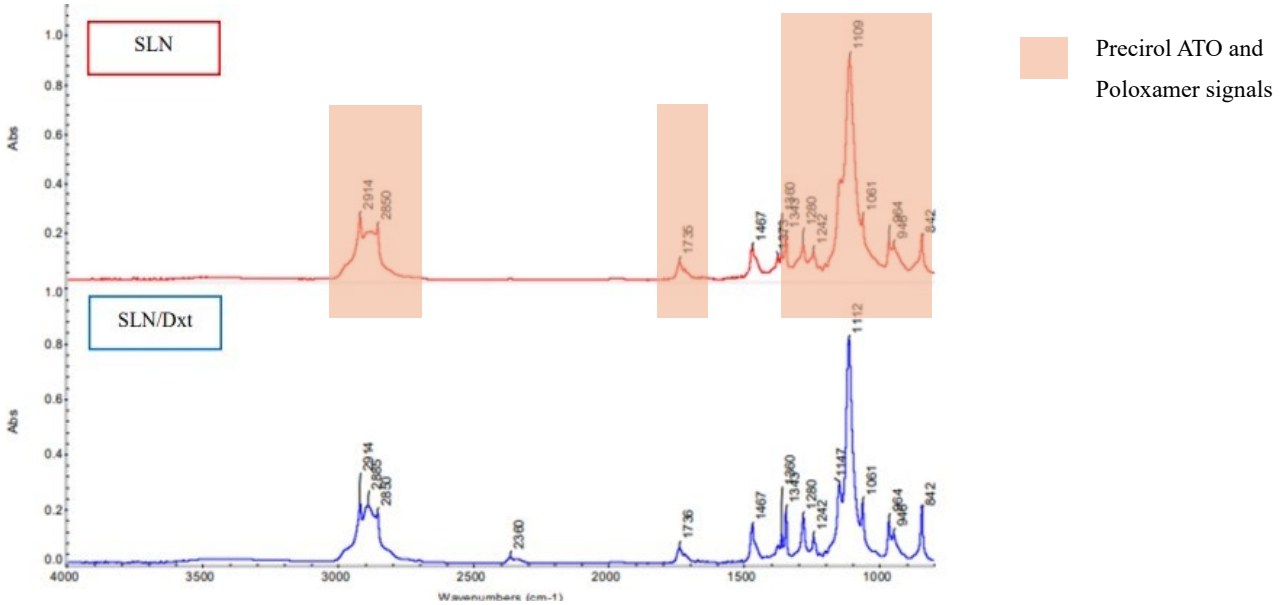

Figure 28. Solid Lipid Nanoparticles and Solid Lipid Nanoparticles /Dexamethasone FT-IR spectra.

Precirol ATO, being a glycerol ester with saturated fatty acids, shows intense bands attributable to alkyl chains, in particular the stretching bands of methylene CH2 groups at about 2850 cm^{-1} and 2920 cm^{-1}. Furthermore, there is a band around 1735 cm^{-1}, associated with stretching of the ester carbonyl group, and CH2 bending bands near 1465 cm^{-1}.

Interactions between the carbonyl group of Precirol esters and the hydroxyl or ether groups of Poloxamer may cause slight shifts or changes in the shape of the C=O and OH bands (1050 - 1150 cm^{-1}). Dexamethasone, a lipophilic molecule incorporated into the lipid matrix, in this case does not show evident peaks.

3.2.3 Stability in time

The formulations loaded with dexamethasone, both liposomes and SLN, were stored at a temperature of 4° C to verify their stability: Dynamic Light Scattering measurements were carried out one month after synthesis with the aim of evaluating any structural changes. The table shows the experimental results.

Sample	Z-average ± sd (nm)	PDI ± sd
DOPC Liposome	809 ± 2,7	0,47 ± 0,07
DSPC Liposome	109,1 ± 3	0,35 ± 0,10
SLN Dexamethasone	150,6 ± 3,31	0,20 ± 0,04

Table 15. Average size and polydispersity index of liposomes and solid lipid nanoparticles one month after synthesis.

In the case of liposomes, after a month at 4°C we notice a diametrically opposite behavior: the DOPC-based system had a notable increase in size (going from 116.9 to over 800 nm), while the DSPC-based formulation went from 230 nm to approximately 100 nm. In the case of the DSPC based formulation the PDI of 0.3 allows us to consider it still monodisperse, while the same cannot be said for the DSPC-based formulation. In the case of SLNs, however, it is possible to notice an increase in the average size of the formulation, but a PDI that is still rather low, indicates a system that is still perfectly monodisperse. The Dynamic Light Scattering measurements were repeated by gradually increasing the temperature of the sample, starting from 25°C of the first measurement up to 70°C, in order to verify the stability and chemical-physical behavior of the formulations (in the case of liposomes, only the DSPC-based formulation was used).

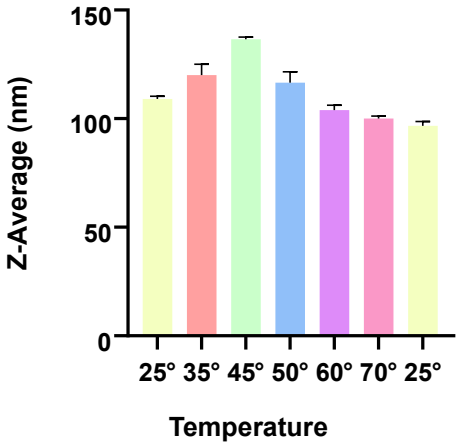

Figure 29. DLS measurements of DSPC liposome size as a function of temperature.

A progressive increase in size from 25°C is noted until reaching a peak around 45°C, where the liposomes reach a maximum size of around 140 nm. This behaviour indicates a change in lipid

membrane structure or fluidity, possibly due to the combined effect of DSPC phospholipid and cholesterol, along with the loaded drug. Above this temperature, the size of the liposomes gradually decreases until it stabilizes around 100 nm at 70°C. This trend suggests that, beyond a certain thermal threshold, the membrane becomes more fluid and reorganizes, but cholesterol helps maintain stability by avoiding significant aggregations or breakages.

A very important point is that at body temperature (about 37°C), the size of the liposomes is stable and quite small, which is crucial to ensure the stability of the formulation during administration and controlled release of the drug. Furthermore, the reversibility of the size, which returns to the initial values once the liposomes are brought back to 25°C, indicates that these lipid systems are robust and resist heating and cooling cycles well without suffering permanent damage.

From an application point of view, this thermal behaviour is interesting because it suggests that the release of dexamethasone could be modulated by temperature: at higher temperatures, such as those of inflamed tissues or in the presence of heat treatments, the lipid membrane becomes more fluid and permeable, facilitating faster release of the drug. On the contrary, at physiological temperature the membrane remains more rigid, ensuring a slower and more controlled release.

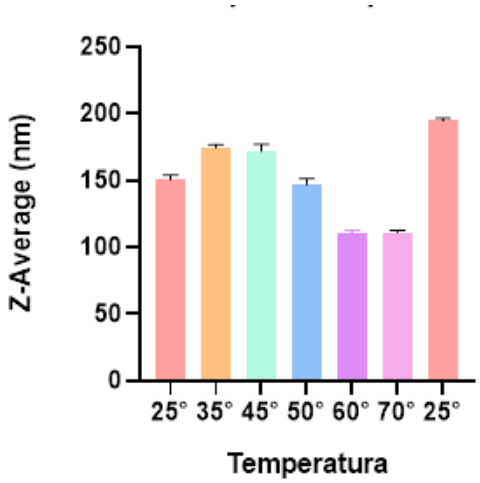

Figure 30. DLS measurements of Solid Lipid Nanoparticles size as a function of temperature.

The graph shows how the average size of solid lipid nanoparticles varies as a function of temperature. It is observed that the average size (Z-Average) progressively increases from 25°C until reaching a maximum peak around 45°C, with values close to 200 nm. Thereafter, the size decreases with increasing temperature until it stabilizes around 100-110 nm at 60-70°C. This trend suggests that, at moderate temperatures, nanoparticles tend to swell or aggregate slightly, increasing their size.

However, at higher temperatures, structural reorganization or partial melting likely occurs leading to a reduction in the observed average size.

Interestingly, by bringing the temperature back to 25°C, the size returns to values similar to the initial ones, indicating good reversibility of the system and stability of the nanoparticles with respect to the heating and cooling cycles. This characteristic is relevant because it indicates that solid lipid nanoparticles can maintain their integrity in variable temperature conditions, but at the same time they can adapt structurally in response to thermal stimuli and this could suggest a release of the drug in a thermoreresponsive way.

3.3 Conclusion

This was intended as an exploratory study focused on two drug delivery systems (liposomes and solid lipid nanoparticles) for potential ophthalmic application.

Experimental data obtained through DLS allowed obtaining information on size distribution, polydispersity index (PDI) and surface charge of systems. HPLC allowed assessing the encapsulation efficiency of liposomes, they show markedly higher values of encapsulated drug in the case of solid lipid nanoparticles; infrared spectroscopy (FTIR-ATR) was used both to verify the correct encapsulation of dexamethasone in individual formulations, both to obtain experimental information on functional groups.

Finally, the temporal stability of the liposomes and SLNs loaded with dexamethasone via DLS was verified one month later: the results showed an increase in the average size for SLNs compared to the initial measurements, while maintaining a good polydispersity index. A notable increase in size was recorded in the DOPC/Cholesterol/Dexamethasone liposome sample, while the DSPC/Cholesterol/Dexamethasone liposomes showed a decrease, going from 230 nm to approximately 100 nm. Both liposomes displayed high PDI values, SLNs were the most suitable sample.

Sperm Cryopreservation[1]

Sperm cryopreservation is an important technique in the field of male fertility; however, the quality of thawed sperm is poor, and this is due to several mechanisms during the freezing-thawing process, including temperature variations, ice crystal formation, osmotic stress and oxidative stress (OS). OS is the result of an overproduction of reactive oxygen species (ROS) that damages cellular structures and compromises sperm function, including the membrane, which is particularly rich in polyunsaturated fatty acids (PUFA), and molecules such as DNA and proteins.[55]

OS modulation is an important issue in freezing human sperm. To minimize cryoinjection lesions of spermatozoa, several strategies have been adopted, including supplementing culture media with antioxidants. Thanks to the regenerative capabilities capable of repairing spermatozoa damaged during the freezing-thawing process, liposomes have been used as a complement to freezing media essentially in the field of animal reproduction, in which sperm cryopreservation is even more widespread than that human[56].

Chlorogenic acid (CGA) is a significant and biologically active polyphenol widely distributed in the plant kingdom and commonly found in a variety of foods and beverages, including coffee, fruits such as apples and pears, and different types of tea; this compound has garnered considerable scientific interest due to its broad spectrum of pharmacological activities, which contribute to various health benefits. Among its most notable effects, CGA exhibits potent antioxidant properties that help neutralize harmful free radicals, thereby protecting cells from oxidative stress and damage; additionally, it possesses anti-inflammatory capabilities, which can reduce inflammation and potentially alleviate symptoms associated with chronic inflammatory diseases[57].

From a chemical perspective, chlorogenic acid is classified as a phenolic acid, structurally derived from the combination of caffeic acid and quinic acid: it contains five hydroxyl (-OH) groups and one carboxyl (-COOH) group, which are essential for its chemical reactivity. The phenolic hydroxyl groups are especially important because they can readily donate hydrogen atoms to free radicals, effectively neutralizing them and thereby exhibiting strong antioxidant activity.

This ability to scavenge reactive oxygen species contributes significantly to the health-promoting effects attributed to CGA. Moreover, these chemical groups facilitate interactions with various

[1] This chapter partially reports results already published in: Moretti, E., **Bonechi, C.**, Signorini, C., Corsaro, R., Micheli, L., Liguori, L., ... & Collodel, G. (2024). In Vitro Effects of Charged and Zwitterionic Liposomes on Human Spermatozoa and Supplementation with Liposomes and Chlorogenic Acid during Sperm Freezing. *Cells*, *13*(6), 542.

biomolecules, which might explain the diverse pharmacological effects observed in biological system[58].

In this study, chlorogenic acid-loaded zwitterionic liposomes were synthesized for use as soil supplements in a freeze–thaw procedure to study a possible effect on the cryostability of human sperm.

1.2 Materials and Methods

DOPE (1,2-dioleoyl-sn-glycero-3-phosphoethanolamine) and DOPC (1,2-dioleoyl-sn-glycero-3-phosphocholine) (Avanti Polar Lipids Inc). The following reagents were used: ethanol (EtOH, purity ± 99%, Merck Italia), ultra-pure water (18.2 MΩ·cm, Rephile Direct-Pure purifier) and PBS (phosphate salt buffer, pH 7.4, Sigma-Aldrich, Milan).

1.2.1 Preparation of CHA liposomes

At first, Dopc/Dope liposomes were synthesized using the lipid film technique: lipids dissolved in chloroform were dried under nitrogen flow and kept in an oven at 40° for about 12 hours. The lipid film was rehydrated with one millilitre of ultra-pure water; nine steps of freeze-thaw were performed to improve monodispersity and unilamellar vesicle formation[59]. Then, the solution was extruded through a LiposoFast apparatus extruder equipped with a fixed pore membrane (100 nm).

Figure 31. The Thin Film Hydration method.

The synthesized liposomes showed good characteristics at DLS, were monodisperse, and had dimensions smaller than 150 nm. The Z potential was also within the expected values, but problems related to the purification of the system led us to perform the synthesis using microfluidics. In fact, microfluidics, by precisely removing the head and tail fractions, produces liposomes that do not require further purification. In the transition from manual synthesis to microfluidics-based

production, a series of tests had to be carried out: unlike manual methods, the microfluidic process involves several parameters (such as reagent concentrations, the ratio between the aqueous and organic phases, and flow rates) that can significantly influence the result. The most promising values for total flow rate (TFR) and flow rate ratio (FRR) were therefore identified and based on the physicochemical characterization, stability studies were conducted on some formulations over time.

1.2.2 Preparation of CHA liposomes by Microfluidics

A first screening approach focused on Flow Rate Ratio values and, based on the tests carried out, only two ratios were considered possible, namely 2:1 (aqueous and organic solution) and 1:2 (aqueous and organic solution).

Also based on a screening approach, dilution was used (the addition of 80 microliters of aqueous phase via a second chip to the liposomal solution already passed through the first pass) and two volumes were selected for the total flow rate, 5000 and 8000 µL/minute, respectively. **Table 16** shows the combinations obtained.

Table 16. Synthesis conditions of CHA Liposomes.

Sample	Flow Rate Ratio	Total Flow Rate
Sample 1 CHA	2:1	8000
Sample 2 CHA	1:2	8000
Sample 3 CHA	2:1	5000
Sample 4 CHA	1:2	5000

It was decided not to use an experimental design because the results shown by DLS were immediately satisfactory and it was not possible to identify any discriminating factors for our "response variables."

1.2.3 Dynamic Light Scattering

Particle size and zeta potential were verified using dynamic light scattering (DLS) with a Zetasizer Nano ZS90 (Malvern Instrument Ltd., UK). Samples were diluted in ultra-pure water (10% v/v) and

the measurement was performed at room temperature (25°C). Measurements were conducted in triplicate.

1.2.4 Encapsulation Efficiency

Encapsulation efficiency (EE) is a measure of the amount of active compound encapsulated within the liposome at the time of formation. The quantity of chlorogenic acid encapsulated in the samples was determined using a UV-Vis spectrophotometer (Specord 210, Analytik Jena). For the analysis, samples were diluted in ethanol and subsequently subjected to agitation to disrupt the nanosystems and release the chlorogenic acid. The absorbance of the liposomal solutions was measured spectrophotometrically at the wavelength corresponding to the maximum absorption of chlorogenic acid (320 nm). For the quantitative determination of the encapsulated active compound, a calibration curve was constructed within the concentration range of 1-16 mg/mL
The encapsulation efficiency percentage was calculated using the following equation (7):

$$\%EE = \frac{[\mathrm{AC}]\mathrm{lip}}{[\mathrm{AC}]\mathrm{tot}} * 100 \qquad (7)$$

Where [AC]lip is the amount of Chlorogenic acid incapsulated in the system determinate by quantification curve and [AC]tot is the total amount of Chlorogenic acid used in the synthesis.

1.2.5 Infrared Spectroscopy

An FTIR-ATR analysis of the synthesized samples was performed for the qualitative characterization of liposomes and solid lipid nanoparticles loaded with chlorogenic acid. Before being analyzed the sample was lyophilized (0.3 mbar, -41 °C, 24 h, 5-Pascal). The spectra were acquired by means of a Nicolet iS50 FTIR-ATR (ThermoFisher scientific) spectrometer operating in the 4000-800 cm^{-1} spectrum and equipped with an ATR (attenuated total reflectance) multiple reflection cell with germanium crystal.

1.3 Results and discussion

1.3.1 Dynamic Light Scattering

Particle size is generally reported as the mean hydrodynamic diameter; accurate determination of particle size is crucial in pharmaceutical formulations, as it directly affects bioavailability, tissue penetration, and the release profile of the active compound.

The Polydispersity Index (PDI) is a dimensionless parameter that provides insight into the homogeneity of the particle size distribution within the sample. A PDI value below 0.1 indicates a highly monodisperse system, while values between 0.1 and 0.3 are generally considered acceptable for most pharmaceutical applications. In contrast, values above 0.3 suggest a broad size distribution, which may compromise the stability, reproducibility, and performance of the formulation. Therefore, achieving a low PDI is often a key formulation goal, as it ensures uniform behavior of the particles in biological environments.

The zeta potential is another critical physicochemical parameter, reflecting the electrostatic potential at the slipping plane of particles in suspension. It serves as an indirect measure of surface charge and plays a central role in determining the colloidal stability of nanosystems. Particles with high absolute zeta potential values (typically > ±30 mV) are considered electrostatically stable due to strong repulsive forces that prevent aggregation. Conversely, systems with low zeta potential values may be prone to flocculation or sedimentation, reducing their stability.

In addition to stability, zeta potential also influences cellular uptake, mucosal interaction, and biodistribution, making it a valuable parameter in the design of effective drug delivery systems. In the case of zwitterionic liposomes, the zeta potential is typically expected to be close to neutral, often ranging between −10 mV and +10 mV.

Table 17 reports DLS results for the CHA liposomes samples.

Sample	Z-average ± sd (nm)	PDI ± sd	Z-pot ± sd (mV)
Sample 1 CHA	140,7 ± 2,2	0,086 ± 0,006	-22,0 ± 0,8
Sample 2 CHA	162,0 ± 5,3	0,220 ± 0,005	-25,5 ± 0,8
Sample 3 CHA	148,2 ± 1,9	0,110 ± 0,009	-23,8 ± 1,6
Sample 4 CHA	424,3 ± 7,6	0,460 ± 0,013	-26,8 ± 0,7

All the liposomal formulations exhibited comparable z-average, except for sample 4, which showed a significantly larger mean diameter (424.3 ± 7.6 nm). This marked increase in size suggests a

deviation from the expected nanoscale distribution; however, it is not possible to attribute this difference to any specific formulation parameter with certainty.

Notably, the Total Flow Rate (TFR) used for sample 4 (5000 µL/min) was identical to that employed in formulation 3, which did not display any anomalies in either Z-average or Polydispersity Index (PDI). Both parameters remained well within the range typically reported in the literature for liposomes of similar composition and preparation methods.

Furthermore, the Flow Rate Ratio (FRR) used in the preparation of sample 4 (1:2) was also applied in formulation 2, which again yielded size and PDI values consistent with expected outcomes. These comparisons suggest that the abnormal size observed in sample 4 is unlikely to be due to either the TFR or the FRR and may instead result from uncontrolled variables.

The Polydispersity Index (PDI) was found to be below 0.2 for all samples, indicating a narrow and homogeneous size distribution, except for sample 3, which exhibited a slightly higher value (0.220 ± 0.005). Despite exceeding the commonly accepted threshold of 0.2, this value still falls within a range generally considered acceptable for classifying a system as monodisperse, particularly in the context of pharmaceutical formulations. In contrast, sample 4 showed a considerably higher PDI (0.460 ± 0.013), clearly indicating a polydisperse system. This high value suggests heterogeneity in vesicle formation, potential aggregation or instability during the formulation process. Such a high degree of polydispersity could negatively impact the colloidal stability, reproducibility and performance of the liposomal system. The zeta potential (ζ) values measured for all samples are consistent with the zwitterionic nature of the phospholipids employed.

1.3.2 Encapsulation Efficiency

The quantitative determination of chlorogenic acid encapsulated in liposomes was performed using spectrophotometric measurements and by constructing a calibration curve shown in **Figure 32.**

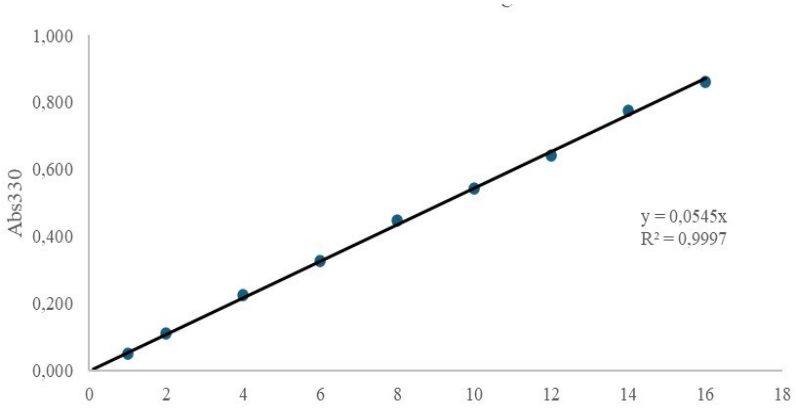

Figure 32. Calibration curve for chlorogenic acid mg/mL.

The results obtained by UV-vis spectrophotometric analysis of liposomes loaded with chlorogenic acid and synthesized using microfluidics are shown in **Table 18.**

Sample	Encapsulation Efficiency %
Sample 1 CHA	88%
Sample 2 CHA	61%
Sample 3 CHA	75%
Sample 4 CHA	66%

The results obtained for the encapsulation efficiency of chlorogenic acid in liposomes show high values in the range of 61%–88%, confirming the correct encapsulation of the active compound. In particular, sample 1 with EE% of 88% has the highest encapsulation efficiency.

1.3.3 Infrared Spectroscopy

This section presents the FTIR-ATR spectra of the empty Dopc/Dope liposome, pure chlorogenic acid, and the liposome loaded with chlorogenic acid.

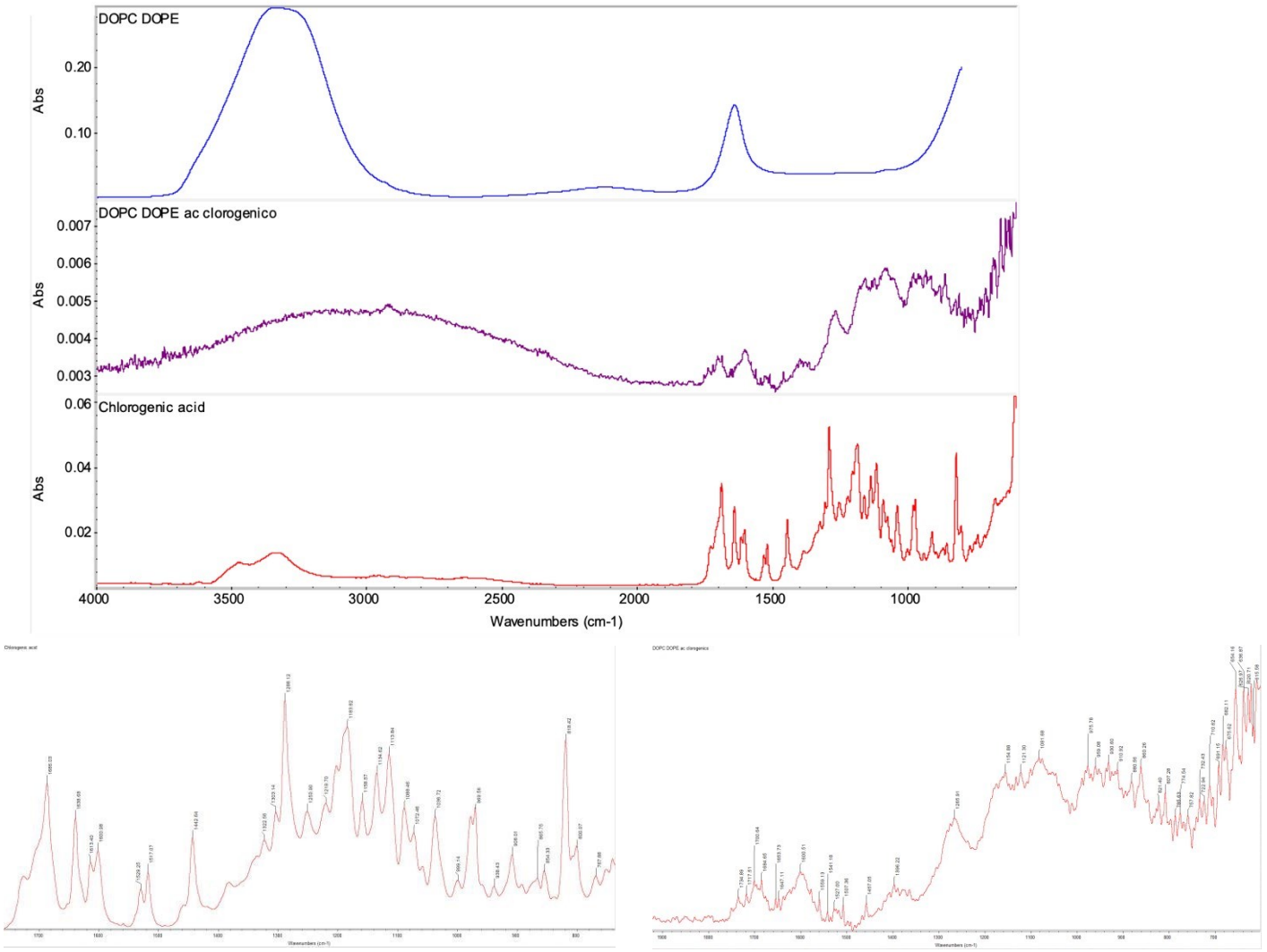

Figure 33. A FTIR-ATR spectra of Dopc/Dope liposome (1), Dopc/Dope CA liposome (2) and Chlorogenic Acid (3); **B** FTIR-ATR spectrum of pure chlorogenic acid in the range 1700-800 cm-^{1}; **C** FTIR-ATR spectrum of chlorogenic acid loaded liposome in range 1900-700 cm-^{1}..

By comparing the FTIR-ATR spectra of pure chlorogenic acid and the liposome loaded with the active molecule (**Figure 33 A,B** and **C**) it is possible to confirm the effective encapsulation of chlorogenic acid. In fact, the FTIR-ATR spectrum of the loaded liposome shows the shift of some characteristic bands of pure chlorogenic acid. In particular, in the FTIR-ATR spectrum of the loaded liposome (**Figure 33**) the characteristic band of the ν (C=O) stretching moved from 1686.03 cm^{-1} to 1700.64 cm^{-1}. The ν (aromatic C=C) stretching at 1613.40-1600.98 cm-1 shifted to 1653.73-1647.11 cm-1. The two bands related to the ν stretching (C-O ester) from 1288.12-1183.82 cm^{-1} are at 1265.91-1154.88 cm^{-1}. Finally, the bending band (C-H) from 818.42 cm^{-1} has shifted to 860.26 cm^{-1}. The shifts of the characteristic absorption bands of pure chlorogenic acid in the FTIR-ATR spectrum of the

liposome loaded with the active molecule, together with the high encapsulation efficiency present in the previous section, confirm the presence and correct encapsulation of chlorogenic acid within the liposomal system.

Table 19. Characteristic absorption bands of chlorogenic acid and their functional groups.

Wave number (cm^{-1})	Functional Groups
1686.03	Stretching ν (C=O ester, carboxyl)
1613.40-1600.98	Stretching ν (C=C aromatic)
1529.25-1517.07	Stretching ν (C=C aromatic)
1442.67	Bending (O-H carboxyl)
1288.12-1183.82	Stretching ν (C-O ester)
818.42	Bending (C-H)

1.3.4 Sperm Cryopreservation

Recalling the objective of the study, which was to evaluate whether the use of zwitterionic liposomes could reduce damage to human spermatozoa during the freezing-thawing processes, human spermatozoa were cryopreserved at -196 °C using a cryopreservation medium (Test Yolk Buffer with gentamicin sulfate; FujiFilm, Irvine Scientific, Santa Ana, CA) supplemented with chlorogenic acid (CGA)-loaded liposomes diluted 1:10000, as well as a control group without supplementation. After two weeks, the samples were thawed at 37 °C, smeared onto glass slides, and treated with TRITC-conjugated *Pisum sativum* agglutinin (PSA, Vector Laboratories Inc., Burlingame, CA, USA), a lectin that binds to the carbohydrate portion of glycoproteins. The slides were processed as described in Vaccaro et al. (2023)[33]. The sperm nuclei were stained with a 4',6diamidino-2-phenylindole (DAPI) solution diluted 1:20,000 in PBS for 10 minutes (in the dark and at room temperature), followed by rinsing with PBS. Finally, the slides were mounted with 1,4diazabicyclo[2.2.2]octane (DABCO) and examined using a Leica DMI 6000 fluorescence microscope (Leica Microsystems, Germany). Image acquisition was performed using the Leica AF6500 integrated imaging and analysis system (Leica

Microsystems, Germany). Spermatozoa with an intact acrosome exhibited a homogeneously stained red cap (normal acrosome), while those with altered acrosomes included spermatozoa displaying shrunken, reduced, or deformed acrosomal structures (altered acrosome). This procedure is reported in Moretti, Elena, et al. "In Vitro Effects of Charged and Zwitterionic Liposomes on Human Spermatozoa and Supplementation with Liposomes and Chlorogenic Acid during Sperm Freezing." *Cells* 13.6 (2024): 542.

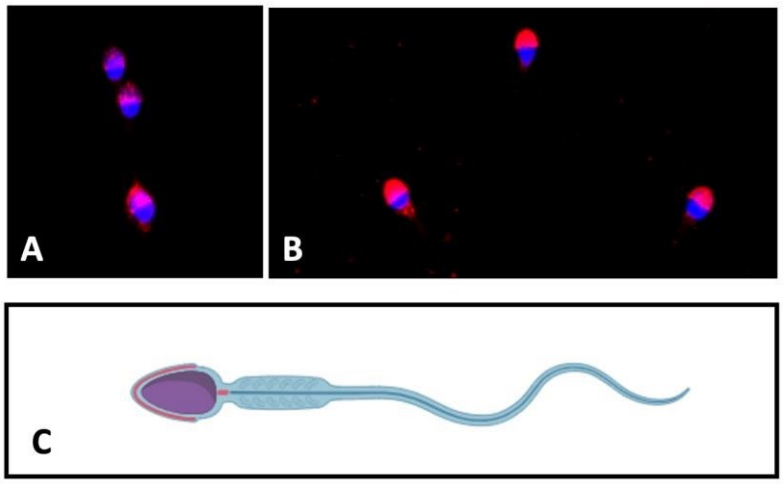

Figure 34. UV micrographs of frozen and thawed spermatozoa treated with Pisum sativum agglutinin (PSA). (A) In unsupplemented samples, spermatozoa showed alterations in the acrosome. (B) In samples treated with CGA-loaded liposomes, spermatozoa showed evident labelling in the well-formed acrosome. (C) Schematic of a human spermatozoon. The arrow indicates the acrosomal cap.

Samples supplemented with CGA-loaded liposomes showed improved acrosome preservation (**Figure 34**). A dual effect of CGA-loaded liposomes was hypothesized: the antioxidant scavenges ROS, minimizing OS damage, and the liposomes facilitate membrane repair, thus improving sperm cryostability.

1.4 Conclusion

Zwitterionic liposomes composed of DOPC/DOPE were synthesized for the encapsulation of chlorogenic acid (CGA). Due to challenges encountered during the purification of the nanosystems, a microfluidic approach was adopted for their formulation. Initial exploratory tests were conducted to identify the optimal experimental parameters, and the most suitable combination of flow conditions and lipid concentrations was selected for further development.

The successful assembly of the nanosystems and the efficient encapsulation of CGA were confirmed through Dynamic Light Scattering (DLS) and UV-Vis spectrophotometry.

Among the four formulations developed, sample 1 exhibited the highest encapsulation efficiency and also demonstrated favourable DLS parameters, including a narrow size distribution and a low polydispersity index, indicative of a monodisperse system.

Stability studies conducted over a one-month period at 4 °C further supported the robustness of this formulation. A slight increase in particle size was observed over time; however, the values remained within acceptable limits, and the system retained its monodisperse nature, suggesting good colloidal stability.

These zwitterionic liposomes were subsequently tested as cryoprotective additives for freezing media used in the cryopreservation of human spermatozoa. Similar zwitterionic liposomal systems have previously been reported to be non-toxic and well-tolerated in porcine Sertoli cells[64] and fibroblasts[65], providing a solid basis for their use in biomedical applications. In the present study as well, no signs of cytotoxicity were observed, and the results were promising.

In particular, sperm samples cryopreserved with CGA-loaded liposomes exhibited a higher postthaw acrosome integrity, suggesting a protective effect on cellular membranes. We hypothesize that these results arise from a dual mechanism: on one hand, chlorogenic acid, known for its potent antioxidant activity, reduces reactive oxygen species (ROS) and mitigates oxidative stress-induced damage during the freeze–thaw cycle; on the other hand, the liposomal structure may facilitate membrane repair or stabilization, thereby enhancing sperm cryotolerance.

Agonist Antibody mRNA as a therapeutic tool for myocardial infarction

This project focuses on the development and optimization of modified mRNA (modRNA) delivery systems based on lipid nanoparticles (LNPs), with the aim of producing and delivering the therapeutic antibody RDO24. The study integrates molecular biology, nanotechnology, and physico-chemical characterization to design an efficient and safe mRNA-based therapeutic platform.

The first objective is the generation of RDO24 modRNA using an in vitro transcription (IVT) strategy based on the approach developed by Karikó et al. (2008). The cDNA encoding the full antibody will be inserted into an appropriate vector, and transcription will be performed using modified nucleotides (pseudouridine instead of UTP) to enhance stability and reduce immunogenicity.
In parallel, a codon-optimized eGFP modRNA will be produced as a reporter to validate functional delivery in vitro and in vivo. Protein expression and production levels will be evaluated in HEK293T cells following transfection.

The second objective concerns the design and formulation of lipid nanoparticles LNPs and liposomes for efficient mRNA delivery. Lipid nanoparticles (LNPs) have proven to be versatile nanocarriers for delivering nucleic acids in a range of medical applications: a typical LNP formulation comprises a cationic ionizable lipid, a helper lipid, cholesterol, and a PEGylated lipid, each contributing uniquely to the stability, structure, encapsulation efficiency, and in vitro and in vivo interactions. In particular, LNPs will be generated using lipid mixture, composed of SM-102, cholesterol, DSPC, and DMG-PEG2000 using a microfluidic device. Cationic liposomes (DOTMA and DOTAP, in combination with DOPE or other helper lipids) will be investigated as delivery vehicles. Particular attention will be paid to the lipid molar ratios, which strongly influence nanoparticle stability, encapsulation efficiency, and interaction with biological tissues, especially cardiac or ischemic tissues.
Both empty and mRNA-loaded liposomes will be synthesized, and the most effective preparation method will be optimized. For all drug-delivery systems, a thorough physico-chemical characterization will be performed, encompassing particle size, surface charge, encapsulation efficiency, and release behavior. A range of techniques, including infrared (IR) spectroscopy, UV–visible spectroscopy, nuclear magnetic resonance (NMR), and dynamic light scattering (DLS), will be employed to provide detailed insights into the properties of the formulations.

Overall, the project aims to develop a safe, efficient, and well-characterized modRNA-LNP delivery system for therapeutic antibody expression, with potential applications in cardiovascular and ischemic pathologies.

Chapter 2

Delivery system for sustainable agriculture

The EU pesticide database lists over 1378 active ingredients, of which 466 have been approved for use within the EU, while 858 have not received approval[1]. Each class of pesticides presents distinct advantages as well as notable limitations. For instance, carbamate insecticides are widely employed due to their broad-spectrum efficacy against numerous pest species, coupled with a low tendency for bioaccumulation and relatively low toxicity to mammals[2]. These properties make carbamates preferable in many applications compared to other pesticide classes with higher associated risks. On the other hand, organochlorine pesticides were extensively used from the 1950s through the 1970s, prized for their high effectiveness and environmental persistence[3]. However, these compounds were later identified as persistent organic pollutants (POPs), recognized for their strong resistance to environmental degradation, bioaccumulation in living organisms, and potential for long-term adverse effects on human health and ecosystems. Consequently, the Stockholm Convention[4] has mandated their restriction or complete ban in most countries.

Modern pesticide formulations, commonly referred to as Current Use Pesticides (CUP), have been developed with the objective of overcoming the limitations and adverse impacts associated with earlier generations of pesticides, particularly those exhibiting PBT characteristic (persistence, bioaccumulation, and toxicity). These properties result in a high resistance to environmental degradation, a propensity to accumulate in the tissues of living organisms along the food chain, and a potential for chronic toxic effects that can adversely affect both ecosystems and human health.

To mitigate these risks, Current Use Pesticides are formulated to ensure enhanced biodegradability and a significant reduction in bioaccumulation. This is achieved through the molecular design of chemical compounds that degrade more rapidly within environmental compartments (such as soil, water, and air) thereby limiting their persistence over time.

Controlled release (CR) of bioactive chemicals could play an important role in this context[5].

In particular, physical hydrogels consisting of natural polymers cross-linked by metal cations are considered among the best options: these systems are widely used for Controlled Release applications in pharmaceuticals, cosmetics, and agronomy due to their biodegradability, ease of preparation, scalability, and absorbent properties and, in the case of agriculture, their ability to absorb and release large amounts of water is quite valuable[6].

Hydrogels are three-dimensional polymer networks that can retain a large amount of water in their swollen state.[7] They can be classified into three main categories based on the nature of their constituent polymers: natural, synthetic, or hybrid. Hydrogel cross-linking can occur through covalent bonds, known as chemical cross-linking, or through non-covalent interactions, known as physical cross-linking, or through a combination of both mechanisms[8]. The forces responsible for water absorption in hydrogels include capillary phenomena, osmoticity, and hydration, which are counteracted by the elastic forces generated by the cross-linked polymer chains, which resist the expansion of the material[9]. The state of equilibrium swelling is determined by the balance between these opposing effects and significantly influences fundamental properties of hydrogels, such as transport and internal diffusion characteristics, as well as mechanical strength. These properties are regulated not only by the degree of swelling, but also by the chemical nature of the polymer network and its morphology.

This type of solution only partially addresses the environmental and social concerns outlined in the United Nations 2030 Agenda for Sustainable Development, which emphasizes the need for more sustainable and responsible agricultural practices.

In this context, it is essential to promote sustainable alternatives that can support large-scale agriculture while contributing to the achievement of a zero-waste circular economy model. A particularly promising approach involves the use of agricultural waste as raw materials for valueadded applications, including new materials for the controlled release of pesticides. This not only promotes waste reduction but also enhances resources that would otherwise be wasted. Food loss and waste constitute a complex and multifaceted challenge that encompasses numerous factors throughout the entire food supply chain. In the context of the ongoing global climate crisis, it is imperative to achieve substantial reductions in waste while maintaining high levels of agricultural productivity[10]. Accordingly, the recovery and utilization of valuable chemical compounds present in agricultural by-products should be prioritized as a key strategy towards sustainability.

Indeed, several plant secondary metabolites, which could be extracted from agricultural wastes, are bioactive molecules with antibacterial and antifungal properties produced by plants themselves as a defence against pathogens;[11] this is the case with Brassicaceae, plants with a high content of glucosinolates, a class of secondary metabolites that can be hydrolysed into isothiocyanates (ITCs) by the enzyme myrosinase.[12]

Once initiated, myrosinase-catalyzed hydrolysis of glucosinolates initially involves the cleavage of the thioglycosidic bond, resulting in the formation of D-glucose and O-sulfonated thiohydroxamate.

The latter is unstable and therefore spontaneously reorganizes, leading to a wide range of products, such as thiocyanates, nitriles, and, as mentioned, ITCs. The resulting chemicals are involved in defense mechanisms against phytopathogens, fungi, and insects present in the soil, and their formation is influenced by reaction conditions, such as pH: ITCs are produced at neutral pH, while nitriles are produced at acidic pH[13].

The defensive strategy of Brassicaceae is exploited with bio fumigation for the treatment of agricultural soils, given the biocidal effect of induced nitrogen compounds (ITC).

Fumigation in agriculture is a pest control technique that involves the use of chemicals, known as fumigants, with the aim of eliminating harmful organisms present in the soil or in agricultural products. It is a widely used practice for controlling pests such as insects, nematodes, fungi and bacteria. Fumigation can be carried out on the soil, after harvesting, or in closed environments such as greenhouses or warehouses. Pesticides such as metam sodium (commercially known as Vapam), metam potassium (known as Tamifum) -which are the sodium or potassium salts of dithiocarbamates- and dazomet, chemically identified as 3,5-dimethyl-1,3,5-thiadiazinane-2-thione, have been extensively utilized as soil fumigants. These compounds were introduced as comparatively milder and potentially more environmentally sustainable alternatives to methyl bromide (bromomethane), a highly effective fumigant that was globally banned under the Montreal Protocol in 1987 due to its high toxicity and significant contribution to the depletion of the stratospheric ozone layer. In recent years, research efforts have increasingly focused on the development of fully organic alternatives to conventional chemical fumigants[14]. Borrowing the basic ideas and concepts behind biofumigation and aiming at a zerowaste circular economy concept, byproducts from agrifood supply chains can represent a source of extremely interesting bioactive compounds. In this framework, numerous novel (nano)carrier systems have been proposed for controlled release (CR) applications, wherein either the carrier matrix, the bioactive compound, or both, are sourced from agrifood production residues. These bio-based delivery systems not only enhance the stability and targeted efficacy of the active agents but also contribute to waste reduction and sustainability within agricultural practices. Such advancements represent a promising direction towards environmentally responsible soil fumigation methods that reconcile agricultural productivity with ecological preservation.

1 Hydrogel Beads[2]

Hydrogel is a commonly used material for encapsulation due to its capability to absorb large amount of water or biological fluids and Alginate is one of the most widely used materials for encapsulation. Alginate is a naturally occurring polysaccharide commonly obtained from brown seaweeds and its basic structure consists of linear unbranched polymers containing β-(1 → 4)-linked d-mannuronic acid (M) and α-(1 → 4)-linked glucuronic acid (G) residues. The structure of alginate depends mainly on the composition of the monomers, the M/G ratio, the polymer sequence, and the molecular weight of the linear chain, which offers greater possibilities for the rational design and production of alginate-based delivery systems with different release rates of the encapsulated bioactive ingredients[15].

For example, alginate with a higher concentration of G blocks tends to generate stiffer hydrogels with larger pores, which facilitates the diffusion of bioactive components immobilized within the polymer networks. Conversely, a higher content of M blocks makes alginate more suitable for the formulation of softer edible coatings and capsules with lower diffusion permeability[16]. It can form stable and biocompatible hydrogel in the presence of calcium cation which bind to the carboxylates in the G-blocks to form the 'egg-box' structures.

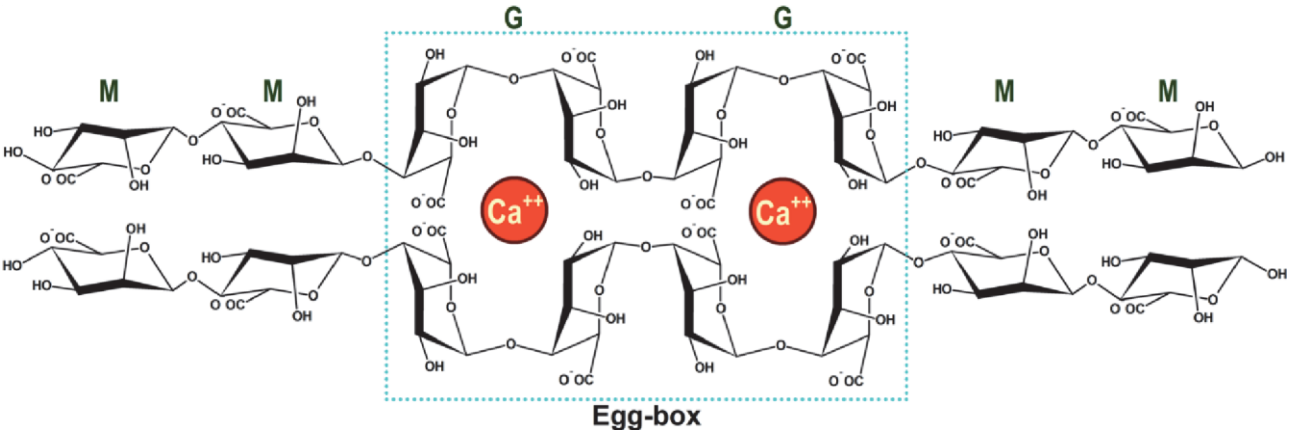

Figure 35. Egg box structure of Alginate beads

[2]This chapter partially reports results already published in: Baglioni, M.; Clemente, I.; Nardin, R.; Bisozzi, F.; **Costantini, S.**; Fattori, G.; Tamasi, G.; Rossi, C. Hydrogel Beads Loaded with Glucosinolate-Rich Brassicaceae Extract as a Controlled-Release Alternative to Biofumigation. *Molecules*, *30*(18), 3660.

The process of ion-induced polysaccharide crosslinking, divalent metal ions take place in the polyelectrolyte complex formation due to an electrostatic interaction between the negatively charged carboxyl groups of polysaccharide molecules and the positively charged metal cations. Such kind of interaction can lead to strong chemical bonding of cations with certain groups of biopolymers, being fundamentally different in the case of alkaline earth and transition metal cations[15].

Among many materials, calcium-alginate hydrogel is the most widely used due to several advantageous features such as non-toxicity, biocompatible, easily produced; thermally and chemically stable[14]. Alginate gel beads are considerably desirable for delivering food nutraceuticals to targeted locations because of the straightforward preparation and handling methods.

In this study, alginate-based hydrogels were synthesized and loaded with a commercial extract of *Brassica oleracea* var. *Italica* (broccoli) for the advanced biofumigation of agricultural soils. The extract is rich in glucoraphanin (GRF), as demonstrated by the HPLC-MS analyses reported herein. Glucoraphanin is a glucosinolate precursor to sulforaphane, a well-known isothiocyanate (ITC) possessing antimicrobial and pesticidal properties, making it an ideal candidate for soil treatment applications. The decision to load the hydrogels with a Brassicaceae extract rich in glucosinolates—particularly glucoraphanin—was based on the premise that myrosinase is produced by soil microbiota and is therefore naturally present in agricultural soils[16]. Accordingly, for the purposes of this study, glucoraphanin (and other glucosinolates) can be effectively considered as precursors to the actual biofumigant agents, namely ITCs such as sulforaphane or similar compounds.

The choice of polymer was guided by extensive literature supporting their use as cost-effective, easily synthesized, and reliable hydrogel carriers for drug delivery across various application fields. Other biocompatible and biodegradable polymers, such as chitosan and pectin, were initially considered; however, the focus was ultimately placed on the most promising system, namely alginate-based hydrogel beads.

By combining hydrogel technology with plant-derived biocidal compounds, this study aims to contribute to the development of effective and environmentally responsible strategies for agricultural soil management, reducing reliance on synthetic pesticides and promoting sustainable agricultural practices.

1.2 Materials and Methods

CaCl2·2H2O (purity ≥ 99%) was purchased from Sigma Aldrich/Merck (Darmstadt, Germany) and used without further purification. Foodgrade sodium alginate polymer was purchased from Sigma Aldrich. The Brassica oleracea extract was purchased from Shanghai Qionghui Industrial Co. (Shanghai, China).

Glucoraphanin potassium salt (purity ≥ 98%; Extrasynthese, Lyon, France) and sinapine chloride (purity ≥ 98%; Extrasynthese, Lyon, France) were used as analytical standards for the extract's characterization performed via HPLC-MS. MilliQ Ultrapure (Merck Millipore, Darmstadt, Germany) water was used.

1.2.1 Hydrogel Synthesis

Crosslinked hydrogel beads were prepared similarly to what was described elsewhere[17], starting with 1% m/v aqueous ALG solution. These polymer solutions were added dropwise into saline solutions of 0.3 M $CaCl_2$ at room temperature. These concentrations were preliminarily optimized to obtain gel beads that were mechanically resistant to handling.

The promptly formed hydrogel beads (5–8 mm diameter) were then magnetically stirred for 15 min, removed from the crosslinking solutions, washed with distilled water (to remove any unreacted metal ions from the gels' surface), and stored in polyethylene containers at their equilibrium swelling degree in a slight excess of water. The 15 min stirring time in the crosslinking solution was assessed using preliminary tests to find the optimal compromise between suitable encapsulation efficiency and the hydrogel beads' mechanical properties.

The preparation of the hydrogel beads loaded with the Brassica oleracea extract was carried out similarly by alternatively mixing 1%, 2.5%, or 5% m/m of the extract powder with the two polymer solutions right before bead formation. Samples were named as ALG-0, ALG-1, ALG-2.5, ALG-5, indicating the polymeric nature of the hydrogel network and the extract concentration.

1.2.2 Brassica Oleracea Extract Characterization

The commercial Brassica oleracea extract was first characterized using an HPLC instrument (Thermo Scientific UltiMate 3000,Waltham, MA, USA), operated using the Xcalibur software (Version 4.3, Thermo-Scientific, Waltham, MA, USA) and coupled to a mass spectrometer (Thermo-Scientific

LTQ XL, Waltham, MA, USA) equipped with a linear ion trap analyzer, with ESI (electrospray ionization) as the ionization technique. For chromatographic separation, a C18 Polar Phenomenex Kinetex column (150 × 2.1 mm, 2.6 μm, 100 A) was used in combination with a Phenomenex C18 Polar (2 × 2.1 mm) pre-column, thermostated at 35 ± 1 ◦C.

The solvents used as the mobile phase were A (H2O/formic acid 0.1%, v/v) and B (acetonitrile/formic acid 0.1%, v/v), and the following gradient was set up: 0–3 min 0% B (isocratic), 3 – 20 min 25% B (linear), 20 - 25 min 50% B (linear), 25–30 min 50% B (isocratic),30–31 min 0% B (linear), 31 – 40 min 0% B (isocratic).

Each sample was analyzed in triplicate by injecting 3 μL at a flow rate of 0.4 mL/min. In more detail, an aqueous solution (1% m/v) of the extract was filtered using a Whatman PTFE syringe filter with a pore size of 0.2 μm and then analyzed. The mass spectra obtained by injecting the eluted analytes into the mass spectrometer were used to identify the main compounds present in the extract. The parameters used for ESI were spray voltage, 3000 V; sheath gas pressure, 35 AU; auxiliary gas pressure, 30 AU; capillary temperature, 350° C. The analytes in the extract were identified by comparing the MSn spectra, acquired via negative ionization $[M - H]^-$, with those reported in the literature. The quantitative determination of glucosinolate content in the extracts was performed using HPLC coupled with UV spectroscopy (HPLC-DAD) using an RS-3000 Diode Array Detector (Thermo-Scientific) at 230 nm. The gradient used for this chromatographic run was 0–3 min 0% B (isocratic), 3–5 min 70%B (linear), 5–8 min 70% B (isocratic), 8–10 min 0% B (linear), 10–15 min 0% B (isocratic).

The glucoraphanin and glucosinolates in the extract (quantified as glucoraphanin equivalents) were quantified using external calibration. The calibration curves ($R2 > 0.9986$ for both linear fittings) for glucoraphanin and sinapine were obtained by injecting standard solutions within the linear concentration range of 0.001–0.1 mM. The LOD and LOQ values were 0.0003 and 0.001 mM, respectively.

1.2.3 Equilibrium Water Content (EWC)

The EWC of the hydrogel beads was measured gravimetrically by completely drying each sample and weighing it before and after. All samples were left to equilibrate beforehand by releasing excess water. The EWC was then calculated using Equation[18] (8):

$$EWC = \frac{W_{wet} - W_{dry}}{W_{wet}} \; x \; 100 \qquad (8)$$

where W_{wet} is the weight of the swollen hydrogel and W_{dry} is the weight of the completely dry hydrogel (the sole polymeric network).

1.2.4 Differential Scanning Calorimetry (DSC) and Free Water Index (FWI)

DSC measurements were performed to calculate the free water index (FWI) of the gel systems and were carried out on a DSC Q1000 (TA Instruments, New Castle, DE, USA), using sealed aluminium pans under an inert nitrogen atmosphere (nitrogen flow 50.0 ± 0.5 cm3/min). The samples were equilibrated at −60 ◦C for 8 min, then heated from −60 ◦C up to 25 ◦C at 1 ◦C/min. The calculation of the FWI from the enthalpy of the fusion values (obtained from the integration of the DSC curve peak around 0 ◦C) was performed according to Equation[19] (9):

$$FWI = \frac{\Delta H_{fus(exp)}}{EWC \cdot \Delta H_{fus(theo)}} \qquad (9)$$

where $\Delta H_{fus(exp)}$ (J/g) is the experimental value of the enthalpy variation relative to the melting of frozen free water and $\Delta H_{fus(theo)}$ (333.1 J/g) is the theoretical value of the enthalpy of fusion for bulk water.

1.2.6 Scanning Electron Microscopy (SEM)

Scanning electron micrographs of pristine and loaded ALG gels were taken using a Quanta 400 SEM apparatus (FEI Company, Hillsboro, OR, USA) operating at a voltage of 20 kV. The hydrogel samples were freeze-dried to allow their investigation in high-vacuum conditions. Subsequently, they were placed onto stubs using double-sided conductive tape and sputter-coated with gold to make them conductive.

1.2.7 Rheometry on Polymer Solutions and Hydrogels

Rheological analyses were performed using a Discovery HR-2 rheometer (TA Instruments, New Castle, DE, USA) on ALG systems for all extract concentrations explored (0%, 1%, 2.5%, and 5%). First, the viscosity of the ALG polymeric solutions (before the crosslinking gelation process) was determined as a function of the shear rate (1/s), using a rotational rheometer with cone–plate geometry. Then, the determination of the G′ and G″ moduli was carried out on already formed hydrogels in the form of discs instead of beads. To obtain this gel shape (more suitable for rheometry), each system was crosslinked by pouring it into a Petri dish containing the crosslinker solution. Additional solution was added dropwise using a Pasteur pipette to reach an excess of cations, as in the hydrogel synthesis process described in Section 1.2.1

After 15 min, the crosslinker solutions were removed, and the hydrogels were left to rest for one day and stored, as in the previously analyzed systems. Then, they were washed and analyzed using the plate–plate geometry to avoid inconsistencies in force distribution.

1.2.8 Encapsulation Efficiency and Release Profiles

The loading kinetics and the encapsulation efficiency (EE%) were determined focusing on glucoraphanin, the most abundant glucosinolate found in the commercial Brassica oleracea extract. The EE% was calculated using the following equation (10):

$$EE\% = \frac{GRF_{sol} - GRF_{lost}}{GRF_{sol}} \text{ x } 100 \qquad (10)$$

where GRF_{sol} is the amount of glucoraphanin initially mixed in the polymer solution (its value is simply obtained by multiplying the mass of polymer solution that underwent crosslinking by the extract concentration in the same solution (1%, 2.5%, or 5%) and the glucoraphanin fraction of the Brassica oleracea extract (22.10%), as obtained by HPLC-DAD measurements; and GRF_{lost} is the total amount of glucoraphanin lost in the crosslinker and rinsing solutions, determined via HPLC-DAD analyses, as reported in Section 1.2.2

In this case, the EE% was not 100% because some of the glucoraphanin originally present in the polymeric solution used to synthesize the hydrogel beads was lost in the crosslinking saline solution during the gelation process. To determine the amount of glucoraphanin lost during this step and during the subsequent rinsing steps, both the crosslinker solution and the water used to rinse the hydrogels were collected and analyzed by means of HPLC-DAD, as described in Section 1.2.2, using an external calibration in the linear concentration range of 0.1–20 ppm.

To study the release kinetics in water and the release efficiency (RE%), a known amount of the loaded hydrogels was immersed in water (hydrogel/water 1:10, v/v) and kept under magnetic stirring to favour the release of glucosinolates. Also in this case, the analysis focused on the release profile of glucoraphanin as a representative of the glucosinolates loaded into the hydrogel.

Several 100 μL samples were taken over three hours of observation, each time replacing the sampled volume with fresh water to maintain a constant volume. The samples were then diluted 1:100 and analyzed by means of HPLCDAD, as described in Section 1.2.2, using an external calibration in the linear concentration range of 0.1–20 ppm. All measurements were performed in triplicate.

1.3 Results and Discussion

1.3.1 Brassica Oleracea Extract Characterization

First, the Brassica oleracea extract was characterized by means of HPLC-MS and HPLC–DAD analyses, as described in Section 1.2.2, to identify and quantify the main chemicals present. The chromatogram obtained from the chromatographic analysis is shown in **Figure 36A**, where peaks corresponding to the most abundant compounds present in the extract are clearly visible.

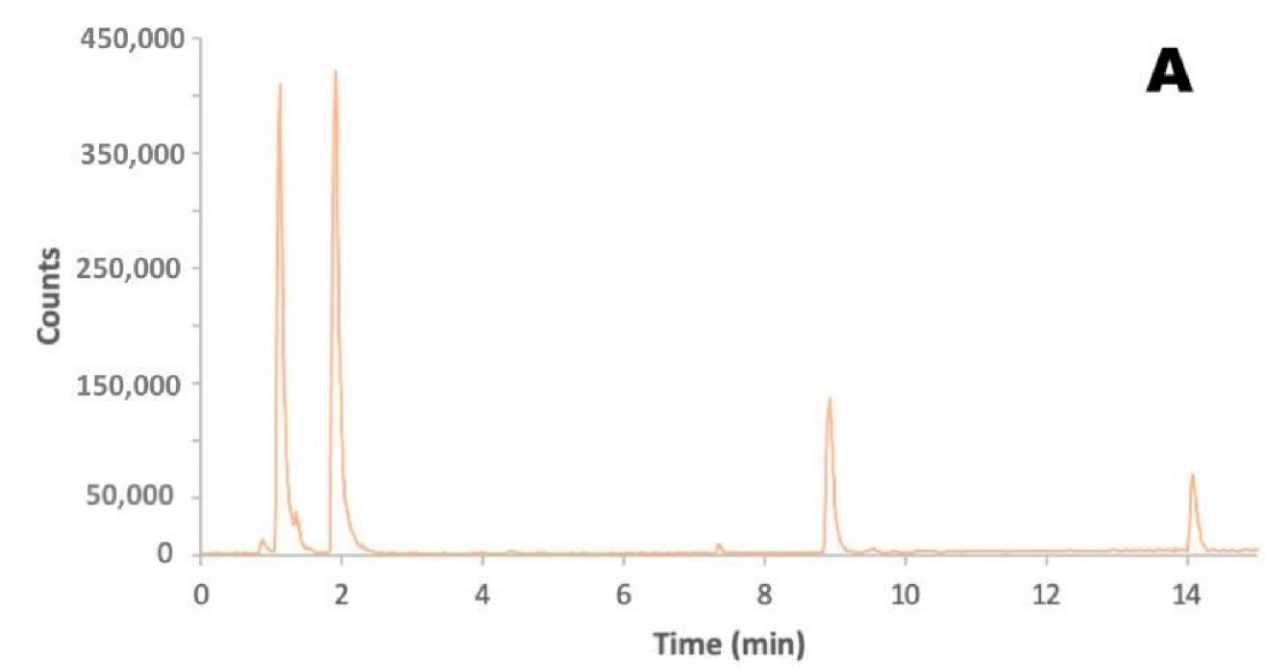

The detected analytes were fragmented using tandem mass spectrometry (MSn), with He as the collision gas inside the ion trap, in negative ion mode, according to the method described in Section 1.2.2. The use of fragmentation patterns enabled the identification of the compounds listed in **Table 20 .**

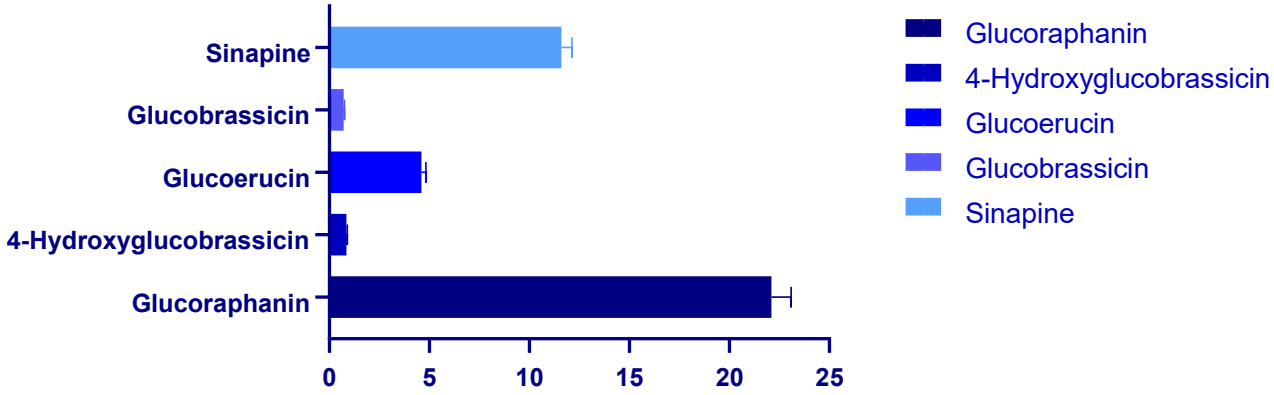

Figure 36. (**A**) Chromatogram obtained from the HPLC-DAD analysis for the characterization of the Brassica oleracea extract. (**B**) Relative amounts of the most abundant compounds identified in the Brassica oleracea extract. GRF: glucoraphanin, 22.10 ± 0.99 %; 4-Hyd-GBR: 4-hydroxyglucobrassicin, 0.85 ± 0.04 %; GER: glucoerucin, 4.61 ± 0.21 %; GBR: glucobrassicin, 0.72 ± 0.03 %; SIN: sinapine, 11.61 ± 0.52 %.

Table 20. Retention times and fragment ions for the identification of the components in the Brassica oleracea extract.

Analyte	Retention time (min)	$[M - H]^-$	Fragment Ions
Glucoraphanin	1.91	436	291, 275, 259, 194, 130
4-Hydroxyglucobrassicin	4.4	463	383,285, 275, 267, 259, 240
Glucoerucin	8.93	420	340, 291, 275, 259, 242, 227, 224, 195, 178
Glucobrassicin	9.55	447	275, 259, 251, 205
Sinapine	14.09	354	294, 279, 264, 223, 208

Several diagnostic ions for glucosinolates have been reported in the literature, those related to the loss of the HSO3− ion (m/z 96 or 97) and the neutral loss of the glucose moiety (m/z 162).

Glucoraphanin was clearly visible in the chromatogram at a retention time of 1.91 min, and the deprotonated molecule [M − H]− was identified through comparison with literature data[20].

Besides glucoraphanin, other glucosinolates were present in the extract in significant amounts, such as 4 -hydroxyglucobrassicin (an indolic glucosinolate derived from glucobrassicin), glucoerucin, and glucobrassicin, identified through their characteristic MS2 fragments[20], as reported in **Table 20**. The elution peak visible at 14.09 min in the chromatogram in **Figure 36A** was attributed to sinapine, an alkaloid derived from sinapic acid and commonly found in seeds of certain Brassicaceae plants[21]. Other minor compounds were also detected in the extract, but they were not identified. The identified glucosinolates and sinapine were then quantified by means of HPLCDAD analyses, and the results are reported in **Figure 36B**, showing a total glucosinolate content of 28.28 ± 1.27%. It is worth noting that the relatively high content (11.61 ± 0.52%) of sinapine can also contribute to the antimicrobial activity of the extract due to the demonstrated antimicrobial properties of this alkaloid[22].

1.3.2 Physico-Chemical Characterization of Hydrogel

The hydrogels based on ALG polymers were then synthesized, exploring several different extract concentrations, i.e., 0%, 1%, 2.5%, and 5% (with respect to the initial polymeric solution). The equilibrium water content (EWC), calculated as described in Section 1.2.3, was found to be 93 ± 1% for all gels, both unloaded and loaded with the extract. The FWI of the developed systems was then obtained through DSC analysis (see Section 1.2.4), and the results determined for all samples are reported in **Table 21**.

Table 21. FWI measured in ALG-based hydrogels in the 0–5% concentration range.

Sample	ΔHexp (J/g)	FWI (%)
ALG	238 ± 12	77 ± 4
ALG 1	242 ± 12	78 ± 4
ALG 2-5	279 ± 14	90 ± 5
ALG 5	288 ± 14	93 ± 5

As shown in **Table 21**, the FWI tended to increase for the alginate hydrogels loaded with higher amounts of extract. This effect was particularly pronounced in systems with higher concentrations (2.5% and 5%), where the FWI difference was more significant. In contrast, the difference between

pure alginate and alginate loaded with 1% extract was smaller. This behaviour was likely due to a complex and synergistic effect that took into account the chemical nature of the polymers; their interactions with Ca2+ cations and their interactions with the variety of compounds included in the extract.

It is indeed known that glucosinolates (particularly glucoraphanin and glucobrassicin) are prone to complexation with iron ions[23-24], while less evidence is present in the literature with respect to interactions with calcium ions.

On the other hand, the significant increase in the FWI for the ALG-based systems (especially at the 2.5% and 5% extract concentration) can be attributed to better interactions between alginate chains and the extract's compounds, which replaced water molecules inside the gel's walls.

This resulted in a weakening of the polymer network structure, which was further confirmed by rheological analyses of the hydrogels.

Figure 37 shows the frequency sweep graphs reporting the storage (G') and loss (G") moduli measured for all hydrogels. All systems exhibited a predominantly elastic behavior (characteristic of solid-like viscoelastic systems), as G' was larger than G" across the entire frequency range explored.

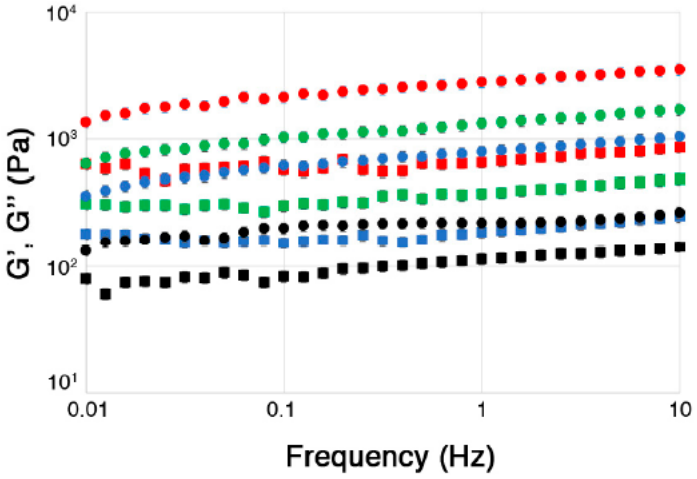

Figure 37. Frequency sweep graphs showing G' (circles) and G" (squares) moduli for all ALG hydrogel series. Black: unloaded gels, initial extract concentration = 0%; red: initial extract concentration = 1%; green: initial extract concentration = 2.5%; blue: initial extract concentration = 5%. The measurements were carried out by selecting an amplitude in the linear viscoelastic region, identified through amplitude sweep analyses.

It was observed that for the ALG hydrogels, after an initial and abrupt increase between ALG and ALG-1, both G' and G" decreased for higher extract concentrations. This suggests that the hydrogel structure, even if initially strengthened by the addition of the extract, was weakened by increasing the

amount of glucosinolates in the hydrogel. These results are consistent with the DSC findings, which suggest that the increase in the FWI for the ALG-based systems was likely due to the competition between extract and water molecules when interacting with the alginate chains, weakening the hydrogel structure[25].

SEM micrographs of ALG-based hydrogels, both loaded and unloaded, were then acquired to gather information on the micromorphology of these systems. **Figure 38A** shows the surface of an unloaded alginate bead (ALG-0). Some surface roughness is visible due to slight deformation during freeze-drying, even though the process was designed to minimize stress on the material.
Figures 38B show a cross-section of the hydrogel beads, allowing their internal structure to be observed. It is interesting to note large pores, a well-known feature of alginate/Ca^{2+} hydrogels, according to the existing literature on these systems[26].

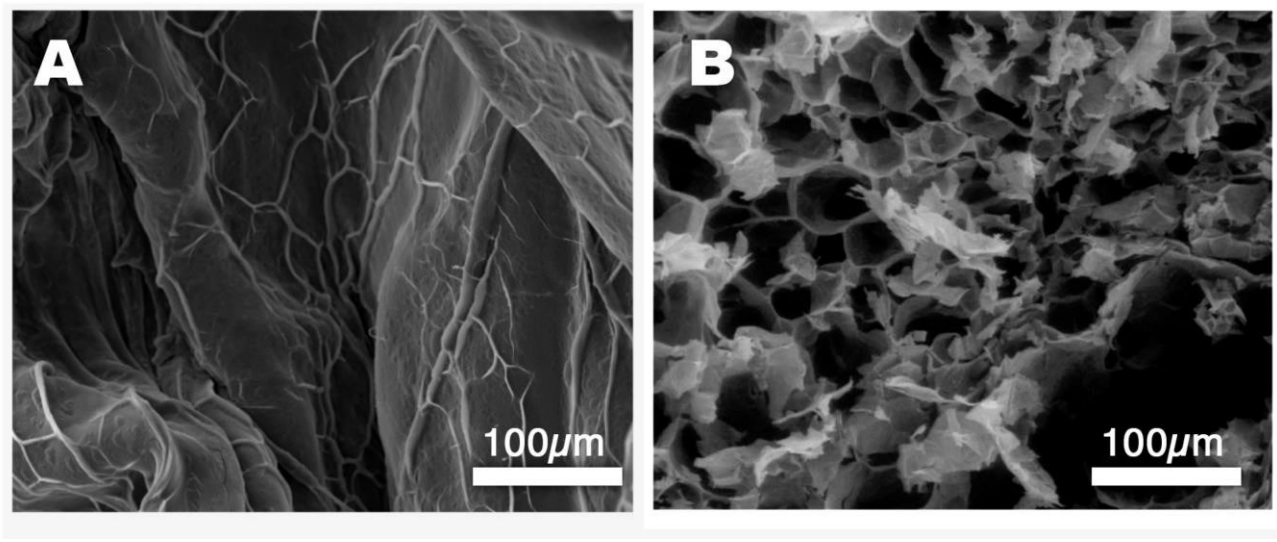

Figure 38. SEM micrographs taken on the freeze-dried hydrogels. (**A**) Surface of an ALG-0 hydrogel bead; (**B**) Cross-section of an ALG-5 hydrogel bead.

1.3.4 Encapsulation Efficiency

The encapsulation efficiency (EE%) was then measured, as described in Section 1.2.8, as it is a crucial parameter for the characterization of CR systems. In this case, it represents the amount of the active principle retained inside the hydrogels with respect to the amount initially mixed with the polymer

solution. Knowing this parameter is necessary for calculating the subsequent release efficiency (RE%) of the hydrogel beads and provides insight into the nature of the interactions between the polymer network and the extract's compounds. As mentioned above, in the present case, glucoraphanin was quantified and taken as a marker to measure the loading and release profiles, being the main glucosinolate present in the Brassica oleracea extract.

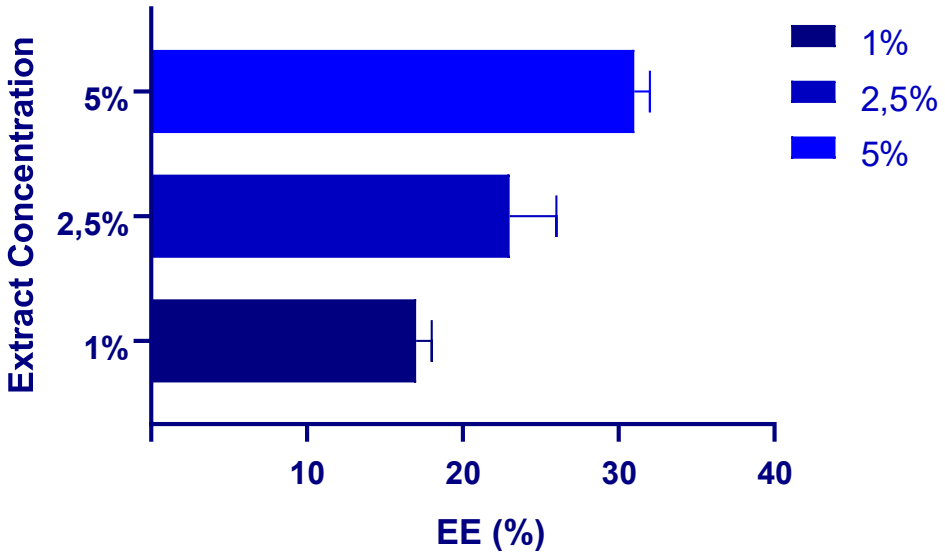

Figure 39. compares the EE% values of ALG hydrogels for different initial concentrations of the extract (1%, 2.5%, and 5%).

The EE% increased with increasing concentration of the extract in the initial polymer solution. Specifically, at a concentration of 1%, the encapsulation efficiency was the lowest among the three concentrations.

At 2.5%, a significant improvement in encapsulation efficiency was observed; at 5%, encapsulation efficiency continues to increase but at a slower rate. This could be due to a saturation effect or to physical-chemical limitations of the hydrogel in encapsulating larger amounts of extract.

In relation to EE%, another important factor must be considered, namely the average size of the hydrogel spheres. For this reason, the viscosity of the polymer solutions was also taken into account and analyzed: high viscosity of the solution could have resulted in slower dripping during the synthesis and cross-linking phase, thus forming larger hydrogel spheres with a slightly more elongated shape.

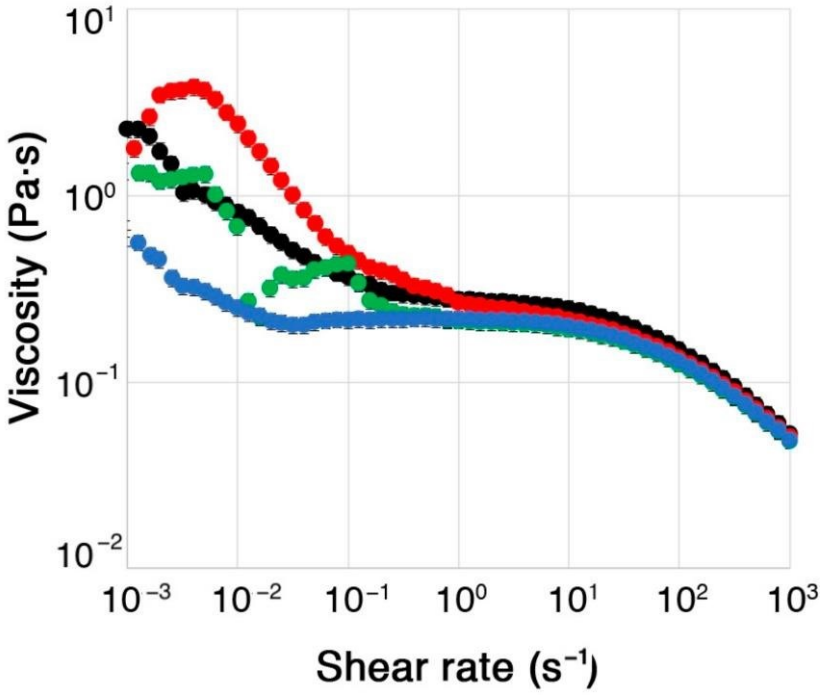

Figure 40. Viscosity of ALG polymeric solutions (with different extract concentrations) before crosslinking. Black: unloaded gels, initial extract concentration = 0%; red: initial extract concentration = 1%; green: initial extract concentration = 2.5%; blue: initial extract concentration = 5%. Error bars are not clearly visible, as they are smaller than the markers.

Apart from some not easily explainable behavior (possibly due to the complex influence of the extract's molecules on the rheological properties) at a low shear rate, all the polymer solutions exhibited a shear-thinning trend in their viscosity, which is typical of non-Newtonian fluids.

Since EE% depends on the amount of glucoraphanin lost in the crosslinking solution and rinse water as a result of glucosinolate migration from the gel to the external environment (driven by a concentration gradient), it seems reasonable that it is also related to the surface area/volume (S/V) ratio of the hydrogel beads. The sizes of the ALG hydrogel beads were therefore measured using a digital caliper. The measurements revealed that the sizes of the beads did not vary significantly with extract concentration: the ALG beads were approximately spherical in shape, characterized by an ALG S/V of $1,7 \pm 0.1$ mm^{-1}.

Regarding the encapsulation efficiency which appears to increase with extract concentration, it is important to note that the absolute amount of glucoraphanin lost in the crosslinking saline was higher for higher extract concentrations; therefore, a constant EE% could be expected over the entire range

of concentrations explored. However, this did not occur because, although increasing the initial internal concentration of glucoraphanin within the forming gel bead would have widened the concentration gradient driving the migration of the active compound, the interfacial area was the same as that for lower concentrations, meaning that the process is self-limiting (almost) asymptotic. Because of this, the amount of glucoraphanin retained within the hydrogel (namely EE%) increased with increasing concentration of the extract.

1.3.5 Release Profiles

The release efficiency (RE%) is another key parameter for characterizing hydrogels to be used as CR media, as it indicates their ability to release the active compound (crucial step in the treatment of agricultural soils).

Before studying the behavior of the loaded hydrogel beads in simulated or actual soils, their release profiles were investigated in water to compute a model system. In fact, since glucoraphanin is a water-soluble compound, it can be hypothesized that its release in soil also occurs primarily through soil moisture. By knowing the initial amount of glucoraphanin confined in the investigated systems (by exploiting the EE% values previously measured, as discussed above) and measuring the glucoraphanin (taken again as the reference glucosinolate, representative of all active compounds in the extract) released by the hydrogel beads immersed in a known amount of water (see Section 1.2.8) via HPLC-DAD, it was possible to plot the release profiles, as shown in **Figure 41**.

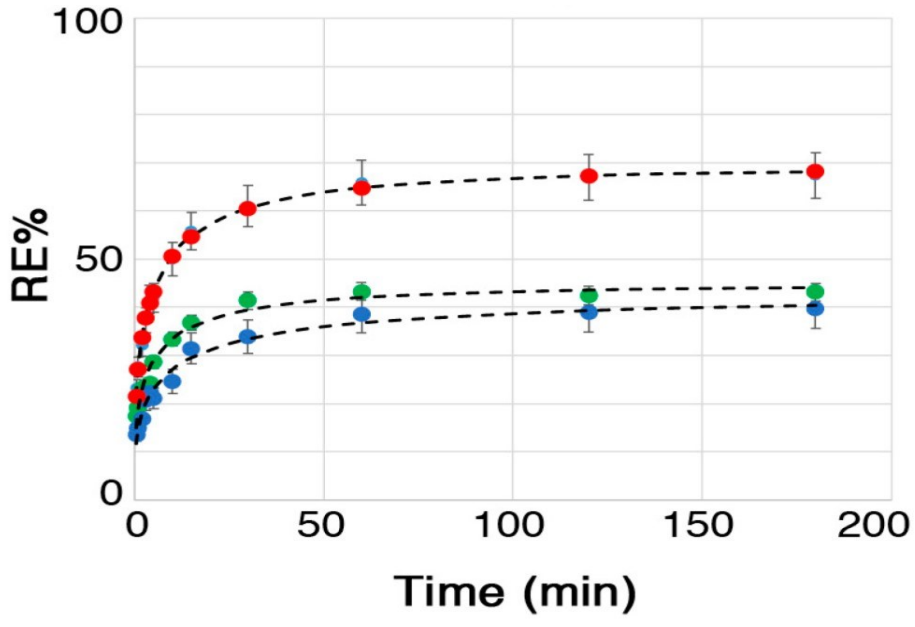

Figure 42. Release kinetics profiles of glucoraphanin for all loaded systems investigated. Red: initial extract concentration = 1%; green: initial extract concentration = 2.5%; blue: initial extract concentration = 5%. Dashed black lines represent the best-fitting curve for each system, computed using the Weibull model.

For alginate (ALG) based hydrogels, the release of glucoraphanin in water showed apparently asymptotic behavior. The release percentage (RE%) was decreased as the extract concentration increased, showing an opposite trend to the encapsulation efficiency (EE%), where higher values were obtained for hydrogels charged initially with 5% extract. These results were expected because, in this case, a high EE percentage implies that the hydrogel retained glucoraphanin better.
Furthermore, for alginate-based systems, the RE% stabilised at around 40% of the initial active substance content with increasing extract concentration. Importantly, although ALG-1 systems showed a higher maximum RE%, the absolute amount of glucoraphanin released by ALG-5 after 3 hours of release in water was 5-6 times higher.

Table 22. Weibull model fitting parameters for the release profiles in water for all investigated hydrogels.

Sample	K	α	b	Max Glucoraphanin Released[a]
ALG 1%	73%	0.50	0.42	0.7 ± 0.1
ALG 2,5%	46%	0.53	0.41	1.5 ± 1.0
ALG 5%	44%	0.42	0.38	3.3 ± 0.2

[a] The concentration (ppm) of glucoraphanin, measured in the solution in which the hydrogels were immersed, after 3 h of release.

Many suitable models can be used to fit the release kinetics of porous matrices, such as hydrogels or mesoporous particles, e.g., those proposed by Higuchi et al.[27] or Peppas and coworkers[28-29-30]. Such models represent short-time approximations of kinetic curves related to diffusion processes, which can conveniently account for approx. 60% of the whole curve[31]. In this case, similarly to what has been done before on similar systems[32-33], the Weibull model was used. This is a modified version of first-order kinetics models, and it is described by Equation (11):

$$C_t = C_\infty(1 - e^{-at^b}) \quad (11)$$

where C_t is the experimental concentration measured in the water in which the hydrogels were immersed as a function of time; C_∞ is the maximum concentration reached at infinite time (an asymptotic value); t is the time the hydrogels were immersed in water; a is a dimensionless empirical constant; and b is another dimensionless constant, which has been shown to have a linear correlation with the Peppas exponent, *n*, as reported in the following Equation (12):

$$\frac{C_t}{C_\infty} = Kt^n \qquad (12)$$

It has been demonstrated that if $b < 0.75$, the process is governed by Fickian diffusion; if $0.75 < b < 1$, a combination of Fickian diffusion and Case II diffusion takes place, while for $b > 1$, a complex diffusion mechanism occurs. In the present case, Equation (12) was normalized by the total concentration of glucoraphanin initially present in each hydrogel system (CTOT), and this gave Equation (3), which was then used to fit the experimental data and to obtain the ER% (13):

$$\frac{C_t}{C_{TOT}} = \frac{C_\infty}{C_{TOT}}\left(1 - e^{-at^b}\right) = ER\% = K\left(1 - e^{-at^b}\right) \qquad (13)$$

Table 22 shows the values obtained for the adaptation parameters (K, a, b) for all the systems studied. The most suitable curves are shown together with the experimental data in **Figure 42**.

The Weibull model fitted all six systems perfectly.

Since the values of the dimensionless constant b were all less than 0.75, the release of glucoraphanin in water followed the Fickian diffusion kinetics.

Parameter a is a measurement of the rate of release in the initial phase and in this case it can be noted that ALG-based hydrogel beads are poorly retentive compared to glucoraphanin, which is in good agreement with the previously reported results. The water release process, although only approximately approximating the actual case, provides evidence that the administration of glucosinolates is slow and gradual. This would increase control over the fumigation potential in agricultural land.

Finally, it is worth noting that, in a real soil treatment, the hydrogel beads would act well beyond 3 hours, until the gel network is completely interrupted and the active compounds are subsequently released, ensuring a long-lasting effect over time.

1.4 Conclusion

Alginate-based hydrogels (ALGs) demonstrated an equilibrium water content (EWC) of approximately 93%, indicative of their high capacity to retain water within their polymeric network. Notably, the free water index (FWI) was observed to increase concomitantly with rising concentrations of the loaded extract. This trend suggests a probable substitution mechanism whereby glucosinolate molecules displace water molecules, thereby engaging in specific interactions with the alginate polymer chains. Such molecular interactions may influence the structural and functional properties of the hydrogel matrix.

Morphological analysis using scanning electron microscopy (SEM) revealed that the alginate hydrogel spheres are relatively small in size, a characteristic attributable to the viscosity of the alginate solution before cross-linking.

The reduced bead size consequently results in an increased surface-to-volume ratio, which is advantageous in facilitating the diffusion and migration of glucosinolates from the hydrogel matrix into the surrounding aqueous environment. This physicochemical characteristic is crucial for optimizing the release profile of active compounds in soil applications.

Furthermore, the release efficiency (RE%) of glucosinolates from alginate hydrogels, as measured in aqueous media, was found to be satisfactory. The release kinetics exhibited a gradual and controlled profile, approaching an asymptotic plateau after approximately three hours of immersion. This sustained release behavior underscores the potential of alginate hydrogels as effective delivery vehicles, enabling prolonged bioavailability of active compounds for agricultural soil treatment. Such controlled release properties are essential for ensuring the efficacy and environmental sustainability of bioactive formulations used in crop protection and soil management.

Chapter 3

Food traceability is defined as the capability to provide detailed information regarding the history and origin of a product throughout the entire supply chain. This process enables comprehensive documentation of the production chain, facilitating the management and control of the product from its point of origin to the final consumer. An efficient traceability system also allows for the timely implementation of corrective measures, such as product recalls, when a product is deemed unsafe or does not comply with established quality and safety standards, thereby safeguarding consumer health. Traceability represents a fundamental element not only for food safety but also for quality assurance, contributing to the integrity of the entire food supply chain[1].

Furthermore, traceability is closely linked to food authentication, as it relies on the credibility of a product's authenticity. Numerous international and national studies have documented widespread cases of food adulteration. In Europe, between 2016 and 2018, multiple reports on adulteration, counterfeiting, and mislabeling were published, with products such as wine, spirits, olive oil, fish, meat, cheese, honey, herbs, and spices among the most frequently reported (European Commission, 2019).

To address these challenges, global standardization bodies dedicated to controlling the origin and production processes of food products have been established. A notable example is Italy's "Controlled Designation of Origin" (DOC) system, aimed at guaranteeing the authenticity and quality of regional food products. Similarly, the European Union has introduced detailed legislation to protect agricultural products, food, and beverages recognized for their quality, certified geographical origin, or traditional production methods. Council Regulation (EEC) No. 2081/92 established the criteria for key quality schemes, including Protected Designation of Origin (PDO), Protected Geographical Indication (PGI), and Traditional Specialities Guaranteed (TSG)[2].

The PDO label is reserved for products that are entirely produced, processed, and prepared within a specific geographical area, ensuring a strong link between the product and its territory of origin. The PGI designation applies to products for which at least one significant phase of production takes place within the specified geographical area, thus highlighting the relationship between the product's characteristics and its origin. The TSG designation protects traditional production methods and recipes, regardless of the geographical location of production. Collectively, these schemes aim to safeguard the reputation and uniqueness of regional products, support producers in achieving higher

market value for authentic products and combat unfair competition arising from counterfeit or non-compliant goods (EU Regulation 1151/2012).

Concurrently, food safety and quality authorities increasingly require a comprehensive and updated list of analytical techniques capable of verifying food authenticity and supporting law enforcement activities. In this context, there is a growing demand for reliable and rigorous analytical methods that can provide definitive evidence regarding the authenticity of food products. Such methodologies must be scientifically validated, precise, and reproducible, to ensure that genuine products are adequately protected and clearly distinguished from fraudulent substitutes. Numerous studies have examined various aspects of food authenticity assessment, including country of origin determination, responses to specific cases of food fraud, and public perceptions concerning food safety and traceability[3].

It is within this context that the Agritech Center (National Center for Agricultural Technologies), established under the Italian National Recovery and Resilience Plan (PNRR), plays a pivotal role, focusing particularly on the measurement, certification, and enhancement of the quality, origin, and sustainability of products, processes, and companies within the sector.

Between 2010 and 2018 infact, Italy established itself as a leader in the field of food traceability and authentication, ranking as the country with the highest number of scientific publications on the subject, accounting for 37.5% of the total studies included in this area. This prominence is likely attributable to the extensive presence in Italy of food specialties bearing quality certifications such as PDO (Protected Designation of Origin), PGI (Protected Geographical Indication), and TSG (Traditional Specialities Guaranteed), labels that guarantee high standards and are protected at the European level.

These products, owing to their recognized quality and the added value associated with their geographical origin, often command higher market prices compared to non-certified goods, thereby holding significant economic importance on a global scale. However, this economic relevance also makes them particularly vulnerable to counterfeiting and fraud, providing incentives for illicit activities aimed at imitating or adulterating authentic products.

Particular attention in the scientific literature has been given to two raw materials of great importance to the Italian and Mediterranean economy: olive oil and wine. Olive oil is frequently the subject of traceability studies due to its substantial economic impact and global distribution. Similarly, wine, a product of excellence and a symbol of Italian enogastronomic culture, has been the focus of numerous investigations related to both traceability and authentication.

It is indeed on these two primary matrices that Agritech's activities are focused.

1 Olive oil and its related products[3]

The global market for olive oil and its related products is expanding rapidly, driven by consumer preferences for healthy, high-quality foods[4]. Among the various Italian regions known for olive oil production, Tuscany stands out for its premium products, which are highly valued for their unique sensory attributes and quality[5]. However, with increasing market demand, the challenge of ensuring the authenticity of these products becomes of pivotal importance, since fraudulent practices such as mislabeling and adulteration are frequently encountered[6-7]. Thus, robust and reliable methods for assessing the geographical origin of olive oils are essential to maintain consumer trust and protect the integrity of this regional specialty. To this aim, understanding the chemical composition of olive drupes and leaves is a crucial step before investigating the final extra virgin olive oil product[8]. The phenolic profile of olive leaves, for example, is affected both by biotic and abiotic factors such as cultivar, leaf age, moisture content, and geographical origin, as well as the sampling time and/or extraction processes.[9-10-11]

Studies have shown that the phenolic profile of olive fruits and oil is influenced by environmental factors, such as water stress[12] and climatic conditions[13-14], and is likely to have a similar impact on leaves. Generally, an increased water stress implies a rise in phenolic content in fruit and oil[15-16]. Likewise, environmental stress can also modify the metabolism of polyphenols in leaves: a study conducted on Meski cultivar leaves sampled in three different climatic zones in Tunisia detected an increase in phenolic compounds, tannins, phytosterols, carotenoids and flavonoids with a concomitant decrease in chlorophyll in leaves cultivated in arid areas[17]. Several authors[18] demonstrated that the total phenolic content (TPC) of olive cultivars from six sites in Anatolia (Turkey) decreases in a directly proportional way to the geographical altitude. A recent study on leaves of the Chetoui cultivar showed that not only pedological features but also environmental conditions influence their phenolic profile[19], and, specifically, leaves from higher altitude locations are characterized by high concentrations of secoiridoids, whereas the lower ones are higher in flavonoids.

---

[3] This chapter partially reports results already published in:

Tatini, D.; Bisozzi, F.; **Costantini, S**.; Fattori, G.; Boldrini, A.; Baglioni, M.; Bonechi, C.; Donati, A.; Tozzi, C.; Riccaboni, A.; et al. Geographical Origin Authentication of Leaves and Drupes from *Olea europaea* via ^{1}H NMR and Excitation–Emission Fluorescence Spectroscopy: A Data Fusion Approach. *Molecules* **2025**, *30*, 3208.

Also, the polyphenolic content of the Chemlali cultivar showed significant variation among samples from nine Tunisian regions[20]. The phenolic profile of olive leaves can also be used to help identify the geographical origin of olive-based products[17-20-21].

The phenolic profile of olive leaves, along with the soil composition where they were grown and the agricultural practices applied, can serve as indicators of geographical origin. Characterizing their metabolic profile enables the identification of region-specific markers that may also be detected in the final product.

Several analytical procedures have been proposed for olive oil, drupes, and leaves characterization, including mass spectrometry, gas and liquid chromatography, as well as different spectroscopic techniques, often combined with statistical and chemometrics approaches.[22-25-26-27-28-29-30-31] Among these, nuclear magnetic resonance (NMR) spectroscopy, particularly ^{1}H NMR, has emerged as a powerful and reliable analytical technique for the geographical authentication of olive oils, and for the varietal and metabolomic analysis of olive drupes and leaves.[32-33-34] Three main methodologies have been explored in ^{1}H NMR and, more in general, in metabolomic investigations like mass spectrometry: target analysis, metabolic profiling, and metabolic fingerprinting.[35] Through target analysis, a specific metabolite or a class of metabolites present in olive oil is detected and quantified, usually after a selective extraction. In the metabolic profiling, different selected metabolites from various classes of compounds are identified, usually without any selective isolation. NMR metabolic fingerprinting is often performed on the full ^{1}H spectral data, excluding any a priori selection of specific metabolites. Both metabolic profiling and fingerprinting enable the classification of olive oil samples based on factors such as geographic origin, variety, harvest timing, and aging, by combining the analysis of the spectral features with multivariate statistics and chemometrics[36]. An overview of the recent progresses in the authentication of olive oils and related vegetable matrixes via ^{1}H NMR and chemometric methods can be found in the works by Fanizzi et al.[37], Camin et al.[38], Beteinakis et al.[33], Dais et al.[34], and references therein. The high reproducibility and non-destructive nature make ^{1}H NMR particularly suitable for the differentiation of products from distinct geographical regions in routine analysis[39-40].

In recent years, excitation–emission matrix (EEM) fluorescence spectroscopy has attracted increasing attention for its ability to identify and characterize fluorescent compounds in food matrices[41]. Several studies reported on the application of EEM fluorescence spectroscopy for authentication and classification purposes in wines[42], spirits[43], edible oils[44], fruits[45], cereals[46], and dairy products[47-48]. In the case of olive oils, this technique is particularly effective in detecting phenolic compounds, tocopherols, pigments, and other secondary metabolites like oxidation products that contribute to the

oil's quality and authenticity[41]. However, to the best of our knowledge, EEM fluorescence spectroscopy has not previously been applied specifically for the purpose of determining the geographical origin of olive drupes and leaves. Moreover, this technique presents several advantages, including its rapid, non-destructive nature and high sensitivity, without requiring extensive sample preparation or expensive instrumentation[49]. Within the threedimensional structures of EEM data, it is possible to detect variations in excitation and emission wavelengths and capture the complex fluorescence behavior of multiple compounds simultaneously. Nevertheless, the complexity of EEM datasets requires specific chemometric approaches to extract meaningful information. Multitensor decomposition methods, and, in particular, Parallel Factor Analysis (PARAFAC), have proven to be highly effective for resolving overlapping fluorescence signals[50-51]. PARAFAC decomposes EEM datasets into individual components representing chemically meaningful fluorophores, facilitating the isolation and identification of key compounds that contribute to geographic origin and product quality authentication. An alternative strategy for the classification of EEM data involves reshaping the 3D array into a 2D matrix, where each sample's EEM is converted into a row vector[52]. This unfolding procedure allows the application of first-order visualization and classification algorithms, such as principal component analysis (PCA), discriminant analysis (DA) or class-modeling algorithms like Soft Independent Modeling of Class Analogy (SIMCA)[53-54-55].

Despite the high molecular specificity and reproducibility of ^{1}H NMR, its implementation in routine industrial workflows is limited by practical constraints, including high acquisition and maintenance costs. In contrast, more accessible techniques such as NIR, FTIR, fluorescence, and UV-Vis spectroscopies are widely adopted in routine analysis of agrifood products[56-57-58] due to their lower operational costs, minimal sample preparation, and the availability of portable instrumentation. However, these methods often suffer from lower selectivity and resolution, particularly in nontargeted authentication. In this context, high-resolution techniques like ^{1}H NMR can play a key role in confirmatory and in-depth analyses in centralized laboratories supporting regulatory control. Moreover, integrating ^{1}H NMR with complementary and portable methods via data fusion may offer a practical compromise between analytical performance and field applicability.

The present study focuses on the geographical origin authentication of olive drupes and leaves from the 2022 harvest in Tuscany, using a comprehensive strategy combining ^{1}H NMR, EEM fluorescence spectroscopy, and multivariate analysis. The objective was to integrate an inexpensive and relatively simple technique (EEM fluorescence) together with NMR via data fusion to enhance the sample classification at a subregional level.

First, the individual datasets from the two spectroscopic techniques are analyzed independently, and PCA is applied to detect potential clustering patterns among the samples according to their geographical origin. Additionally, SIMCA was implemented to develop a classification model for samples originating from a specific subregional area.

Then, a multi-block approach is explored to improve the sample differentiation through data fusion. Data fusion strategies are emerging as a promising tool for food quality assessment and geographical origin characterization, and they can be categorized into low-level, mid-level, and high-level[59]. In this study, a mid-level data fusion approach, which implements the common dimensions (ComDim) algorithm, is applied. This method extracts shared patterns between ^{1}H NMR and EEM fluorescence blocks by identifying common dimensions (CDs) that summarize the variance-covariance structure of the combined data[60]. This approach offers the advantage of balancing the individual contributions of each dataset while maintaining interpretability of the results. The ComDim algorithm facilitates the identification of underlying trends and relationships that might not be apparent when analyzing each dataset independently. To the best of our knowledge, only one paper has reported on the application of ComDim for olive oil characterization, albeit using different analytical techniques (UV–Vis spectroscopy, Near-Infrared spectroscopy and gas chromatography)[61]; in the case of drupes and leaves this is the first study so far.

To further improve the classification performance and evaluate the benefits of data integration, a SIMCA-based one-class modeling strategy is implemented using the multiblock ComDim outputs, and its performance was systematically compared to SIMCA models developed on individual datasets.

In this perspective, this study aims to develop and validate a reliable method for the geographical origin authentication of olive vegetal matrices, starting from spectroscopic data. The findings contribute to the expanding research field on the authentication of olive-derived products, demonstrating the potential of spectroscopy and chemometrics integration to support traceability and quality assessment efforts across the production chain.

1.2 Materials and Methods

Methanol, TSP-D4 (3-(trimethylsilyl)propionic-2,2,3,3-d_4 acid sodium salt, 98% D), and deuterated solvents (D_2O, 99.9% D, methanol D4, 99.8% D, $H_2O < 0.03\%$) were purchased from Merck (Milan, Italy) and used without further purification. Bidistilled water was produced by a Direct Pure UP 10 system (Rephile Bioscience Ltd., Boston, MA, USA).

1.2.1 Sampling and Extraction Protocol

Leaves and olives (three replicates per orchard) were sampled from the four cardinal directions around the perimeter of three different trees at operator height, to ensure a good representation of the internal variability of the sampling site. The total number of samples for leaves and drupes is 31 and 51, respectively. To minimize the effect of drupes' ripening, the samples were hand-harvested within a one-week period in early October 2022, across geographically close sites in the Tuscany region. Prior to collection, fruits were visually inspected to assess ripening stage, and only healthy, undamaged specimens were selected.

Sampling was standardized to trees bearing olives at a consistent phenological stage: approximately half of the fruits were still green, while the other half had begun to transition to the pigmented stage. This ripening phase was chosen to ensure comparability across different cultivars and locations while maintaining the representativeness of typical harvest conditions. These precautions were adopted to reduce the influence of maturity-related changes in metabolite and fluorescence profiles, and to better isolate the geographical contribution in the subsequent chemometric analysis. The samples were stored in plastic bags in the dark until they arrived at the laboratory. Once there, they were washed with ultrapure water, lyophilized at −45 °C and 360 μbar until reaching a constant mass, then blade-milled (Pulverizette 11, Fritsch, Idar-Oberstein, Germany) into a fine powder (500 μm) using a liquid nitrogen bath. The powdered samples were kept frozen and in the dark until analysis. For fluorescence experiments, the leaf and drupe samples were extracted according to a modified version of the International Olive Council's protocol, as reported in *Borghini, F.; Tamasi, G.; Loiselle, S.A.; Baglioni, M.; Ferrari, S.; Bisozzi, F.;* ***Costantini, S.;*** *Tozzi, C.; Riccaboni, A.; Rossi, C. Phenolic Profiles in Olive Leaves from Different Cultivars in Tuscany and Their Use as a Marker of Varietal and Geographical Origin on a Small Scale. Molecules* ***2024****, 29, 3617*.

About 500 mg of the dried samples were extracted with 10 mL of an 80:20 methanol/water mixture for 10 min at 25 ± 2 °C in an ultrasonic bath (Sonorex, Bandelin electronic GmbH, Berlin, Germany, operating at 120 W and 35 kHz).

The resulting extracts were centrifuged at 3500 rpm for 15 min, and the supernatant was then filtered using 0.22 μm syringe filters. The procedure was repeated three times for a total of 30 mL. Prior to the acquisition of fluorescence maps, the extracts were diluted 1:100 with the 80:20 methanol/water solution.

For the ^{1}H NMR experiments, a similar protocol was followed, extracting the powdered samples with an 80:20 mixture of deuterated methanol and deuterated water. No additional dilution was required prior to NMR analysis. TSP-d4 (sodium salt of trimethylsilylpropionic acid) was added to each sample as an internal standard ($\delta = 0$) with a final concentration of 0.05% *w*/*v*. All samples and standards were carefully handled to minimize light exposure, and all the experiments were performed in triplicate.

1.2.2 Fluorescence Excitation Emission Matrix (EEM) Experiments

The fluorescence excitation emission matrix (EEM) measurements were performed on an Agilent Cary Eclipse fluorescence spectrophotometer (Agilent Technologies, Milan, Italy) equipped with a xenon flash lamp and a photomultiplier tube as detector. About 3 mL of each sample was placed in a 10 mm quartz cuvette and analyzed at room temperature.

The excitation wavelength ranges were 250–750 nm and 200–450 nm for leaves and olive samples, respectively, with 10 nm increments. The emission signals were recorded between 370–750 and 250–550 nm at 1 nm intervals. The excitation and emission ranges were selected on the basis of previous works[55-62] and optimized in order to obtain the best compromise between the inclusion of all the informative fluorescence signals and reasonable acquisition times. The slits of excitation and emission monochromators were set at 5 nm, while the scan rate was set to 600 nm/min. A blank EEM was recorded (80:20 methanol/water solution) and then subtracted from all the fluorescence excitation–emission matrices. The fluorescence excitation–emission matrices were arranged in cubic structures with dimensions of *samples* × *emission wavelength* × *excitation wavelength*. The spectra were preprocessed by removing the Rayleigh and Raman scatter (both first and second order) and interpolating the missing values according to Murphy et al.[52]. The data were normalized to unit variance in sample mode. An exploratory analysis via Parallel Factor Analysis (PARAFAC) decomposition was performed to resolve and identify the underlying fluorescent components. For the geographical origin characterization, the cubic structures were unfolded by combining the excitation and emission modes, resulting in 2-D matrices with dimensions of *samples* × (*emission wavelength*…*excitation wavelength*). These unfolded matrices were used as input for the subsequent chemometric analysis.

All the calculations were performed in a MATLAB environment (MATLAB R2023b version, The MathWorks Inc., Natick, MA, USA) using the N-way toolbox[63] and drEEM toolbox[52].

1.2.3 ^{1}H-NMR Spectroscopy

For each sample, 1 mL of the extract was placed into a 5 mm NMR test tube.
The ^{1}H-NMR spectra were recorded on a Bruker DRX-600 AVANCE spectrometer, equipped with an xyz gradient unit and operating at 600.13 MHz. Spectra were processed using Bruker TopSpin software (version 3.6.1, Bruker, Bremen, Germany). The spectra obtained by the Fourier transformation of the free induction decay (FID) were manually phased, and the chemical shifts were reported with respect to the TSP's signal set at 0 ppm.
The FIDs, relative to the ^{1}H NMR experiments, were processed by using NMRProcFlow software, 1.4 version (nmrprocflow.org, INRA UMR 1332 BFP, Bordeaux Metabolomics Facility, Bordeaux, France)[64]. The spectra were phase- and baseline-corrected manually and sectioned into regular intervals (0.04 ppm sized buckets) in the range of 0.50–10 ppm. The area within each bucket was normalized to the total intensity. The areas of the buckets in the regions 4.50–5.20 and 3.28–3.40 ppm, corresponding to the residual signals of water and methanol, respectively, were excluded. The matrices with dimensions of *samples* × *number of buckets* containing the normalized spectral intensities were used as input for the chemometric analysis.

1.2.4 Chemometric Methods

An exploratory analysis of the experimental data obtained from ^{1}H NMR and EEM fluorescence (unfolded matrices) was performed by means of Principal Component Analysis. For the geographical origin characterization, the data were analyzed by means of a Soft Independent Modeling of Class Analogy (SIMCA) chemometric model. SIMCA was originally developed by Svante Wold in 1976,[65-66] and it has been extensively used as a supervised pattern recognition method in combination with different experimental techniques for geographical origin authentication,[67-68-69] quality assessment,[70-71] and fraud detection.[72-73-74] SIMCA consists of building a PCA model to describe the variance within each class separately. Each class was described by its own PCA model, and the boundaries were defined by confidence limits based on the residual variance. The experimental data were projected onto these models to determine the class membership, allowing for the identification and characterization of distinct groups within the dataset. The classification rule is defined by the distance of the sample from the class model, which is calculated from the normalized Q residuals and normalized Hotelling T^2 values. Q residuals and Hotelling T^2 are normalized over their 95% confidence limits.

The performance of the SIMCA model was evaluated by calculating the accuracy (ratio of correctly assigned samples), sensitivity, and specificity of the classification, which are defined as follows:

$$Sensitivity = \frac{TP}{TP + FN} \quad (14)$$

$$Specificity = \frac{TN}{TN + FP} \quad (15)$$

where *TPs* are the true positives, *FNs* the false negatives, *TNs* the true negatives, and *FPs* the false positives. Sensitivity measures how well target class samples are correctly recognized, while specificity represents how many non-target class samples are rejected by the model built for the investigated class[75].

The distance threshold is not fixed, since its value is tuned and optimized in order to maximize class specificity and sensitivity, following the approach of Vitale et al.[76].

The number of principal components to be retained in order to build the PCA model for each class was selected on the basis of the minimum of root mean square error in cross-validation (RMSECV, Leave-one-out cross-validation) and the maximum of sensitivity estimated in cross-validation[77]. The model performances were evaluated using a test set validation: each dataset was split into a calibration and a validation set using the duplex algorithm with a splitting ratio of 80:20[78].

All the measurements (both ^{1}H NMR and fluorescence) were conducted in triplicate to ensure analytical reproducibility. Moreover, a careful preliminary inspection of the datasets was performed to detect and remove outliers prior to modeling, based on leverage and Q-residual diagnostics following standard PCA-based approaches. As for preprocessing, both ^{1}H NMR and EEM datasets were mean-centered prior to the chemometric analysis.

Parallel Factor Analysis (PARAFAC) decomposition was applied to decompose the threedimensional data into individual fluorescent components based on their spectral signatures. The algorithm works by fitting the data into a trilinear model, assuming that the fluorescence intensity is the product of excitation and emission spectra for each component, along with their relative concentrations[79]. The decomposition generates three sets of bidimensional matrices, or loadings: sample loadings (also referred to as scores), excitation loadings, and emission loadings. The sample loadings correspond to the relative concentration of each component across the different samples, providing insights into how the components vary across the dataset, while excitation and emission loadings represent the fluorescence excitation and emission spectra of each component, respectively. The optimal number

of components was determined on the basis of different parameters, namely the central consistency diagnostic criterion (CORe CONsistency DIAgnostic, CORCONDIA), the percentage of variance explained by the model, and visual inspection of the recovered spectral and residual profiles. Non-negative constraints were applied for all the modes.

Although the PARAFAC approach might be more suitable for identifying which fluorophores are present in the samples, contributing at the same time to geographical authentication, using unfolded data appeared more effective for the straightforward classification of olive oil, fruit, and leaf samples[80]. This difference can be attributed to the fact that the unfolded matrix retains all available data, whereas PARAFAC reduces the amount of information and is highly influenced by the number of components chosen, which may lower classification accuracy[81]. However, the major drawback of multidimensional unfolding methods is the higher complexity and the more difficult interpretation of the generated outputs, which must be refolded to restore the original modes.

All the calculations were performed in a MATLAB environment (MATLAB R2023b version, The MathWorks Inc., Natick, MA, USA) using PCA[82] and classification toolboxes for[83] MATLAB from Milano Chemometrics and QSAR Research Group.

1.2.4 Data Fusion

The multi-block analysis on the data from the two different spectroscopic techniques (^{1}H NMR spectra and unfolded fluorescence matrices) was performed according to a mid-level data fusion based on the ComDim (Common Dimension) method, a particular application of the Common Components and Specific Weights Analysis (CCSWA) procedure developed by Qannari[84]. The first step is the organization of the data into two different blocks, corresponding to the individual analytical techniques. The ^{1}H NMR data and unfolded EEMs are normalized by dividing each point by the square root of the sum of squared values[85]. After concatenation, each block is normalized by its Frobenius norm so that they all have the same total variance. The ComDim approach focuses on the variance-covariance matrices of the samples, which are all of the same dimensions. This allows for the calculation of a weighted sum of these matrices, from which the first normalized principal component, referred to as the "Common Dimension" (CD), is extracted. The algorithm then iteratively adjusts the weight, or "salience," of each data block for the identified CD. After the first CD is computed, each data block matrix is deflated, and the process is repeated to calculate subsequent CDs. As a result, each CD represents the first principal component of the weighted sum of the variance-covariance matrices of the deflated blocks.[86-86-88] The resulting scores (i.e., the

extracted common components) and loadings provide a direct visualization of sample distribution and variable contribution, enhancing the understanding of sample similarities, clustering, and correlations with the geographical origin.

To support the classification of leaf and drupe samples according to their geographical origin, a SIMCA-like model was developed based on the results of the ComDim multiblock analysis. In this approach, global scores and residuals derived from the ComDim model—applied to the integrated dataset combining ^{1}H NMR and EEM fluorescence spectroscopy—are used to calculate two metrics, the score distance (SD) and the orthogonal distance (OD), respectively, for each training sample of the target class. The ComDim scores were used as input without pre-processing. These metrics were combined into a single reduced distance, used to quantify the degree of class membership for each sample. The threshold value is optimized in order to maximize class specificity and sensitivity[75]. New samples were projected onto the ComDim model, and their reduced distance values were compared to the threshold to determine class inclusion. This methodology is analogous to the multiblock extension of the one-class classifiers that integrates ComDim with the data-driven SIMCA model originally proposed by Galván and co-workers[89]. Model performance was evaluated in terms of accuracy, sensitivity, and specificity, based on a validation strategy involving the division of the dataset into separate calibration and external test sets, as in the case of single block-based SIMCA. All the calculations were performed using the MBA-GUI toolbox for MATLAB[90] and in-house MATLAB scripts.

1.3 Results and Discussion

Fifty-one drupe and thirty-one leaf samples harvested in September and October 2022 from different geographical areas of Tuscany (Chianti–Siena, Grosseto, and Val d'Orcia) were collected and analyzed. These subregions were selected according to the Protected Designation of Origin (PDO) classification and to the chemical composition of the soil from previous studies[8-91]. The sampling sites are show in **Figure 43**.

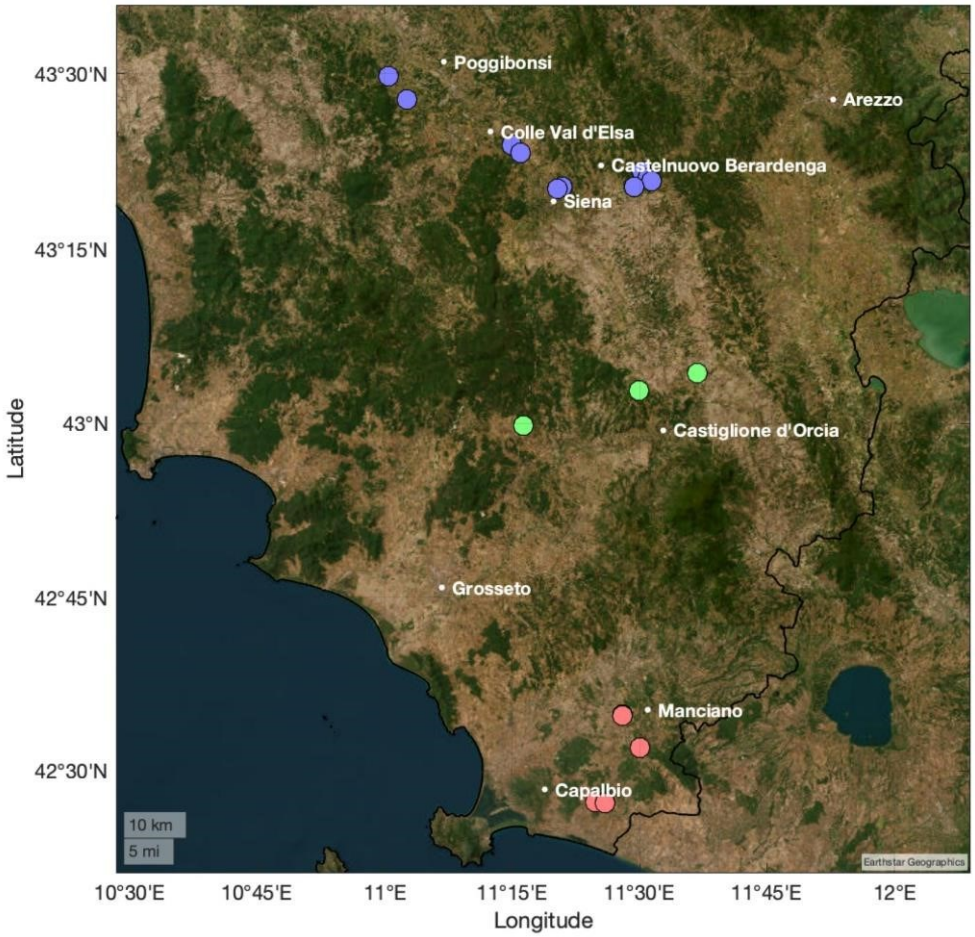

Figure 43. Sampling sites for leaves and drupes. The three different selected regions are evidenced by colored markers as follows: (blue) Chianti and Siena; (green) Val d'Orcia; (red) Grosseto.

Table 23. Description of the analyzed drupes and leaves samples, including climatic and environmental data.

DRUPES					
Sample code	**Geographical area**	**Cultivar**	**Cumulative rainfall (mm)[a]**	**Average Temperature (°C) [a]**	**Altitude (m)**
DR1	Chianti - Siena	Frantoio	439	17.3	262
DR2	Chianti - Siena	Frantoio	439	17.3	262
DR3	Chianti - Siena	Frantoio	439	17.3	262
DR4	Chianti - Siena	Frantoio	550	16.6	304
DR5	Chianti - Siena	Frantoio	550	16.6	300

DR6	Chianti - Siena	Frantoio	550	16.6	300
DR7	Chianti - Siena	Frantoio	550	16.6	279
DR8	Chianti - Siena	Frantoio	550	16.6	286
DR9	Chianti - Siena	Frantoio	519	17.5	305
DR10	Chianti - Siena	Frantoio	519	17.5	296
DR11	Chianti - Siena	Frantoio	519	17.5	296
DR12	Chianti - Siena	Frantoio	616	15.3	292
DR13	Chianti - Siena	Frantoio	616	15.3	292
DR14	Chianti - Siena	Leccino	439	17.3	299
DR15	Chianti - Siena	Leccino	439	17.3	299
DR16	Chianti - Siena	Leccino	439	17.3	262
DR17	Chianti - Siena	Leccino	439	17.3	262
DR18	Chianti - Siena	Leccino	550	16.6	313
DR19	Chianti - Siena	Leccino	550	16.6	313
DR20	Chianti - Siena	Leccino	550	16.6	300
DR21	Chianti - Siena	Leccino	550	16.6	279

DR22	Chianti - Siena	Leccino	550	16.6	286
DR23	Chianti - Siena	Leccino	519	17.5	305
DR24	Chianti - Siena	Leccino	519	17.5	296
DR25	Chianti - Siena	Leccino	519	17.5	296
DR26	Chianti - Siena	Leccino	616	15.3	292
DR27	Chianti - Siena	Leccino	616	15.3	292
DR28	Chianti - Siena	Leccino	616	15.3	268
DR29	Chianti - Siena	Moraiolo	439	17.3	262
DR30	Chianti - Siena	Moraiolo	439	17.3	262

DR31	Chianti - Siena	Moraiolo	550	16.6	300
DR32	Chianti - Siena	Moraiolo	550	16.6	300
DR33	Chianti - Siena	Moraiolo	550	16.6	279
DR34	Chianti - Siena	Moraiolo	550	16.6	286
DR35	Chianti - Siena	Moraiolo	519	17.5	305
DR36	Chianti - Siena	Moraiolo	519	17.5	305
DR37	Chianti - Siena	Moraiolo	616	15.3	292
DR38	Chianti - Siena	Moraiolo	616	15.3	292
DR39	Grosseto	Canino	429	17.0	300
DR40	Grosseto	Frantoio	467	17.3	329
DR41	Grosseto	Frantoio	429	17.0	300
DR42	Grosseto	Leccino	429	17.0	300
DR43	Grosseto	Leccino	319	17.5	217
DR44	Grosseto	Moraiolo	319	17.5	217
DR45	Val d'Orcia	Frantoio	431	15.0	339
DR46	Val d'Orcia	Frantoio	431	15.0	339
DR47	Val d'Orcia	Frantoio	431	15.0	359
DR48	Val d'Orcia	Moraiolo	431	15.0	495
DR49	Val d'Orcia	Moraiolo	431	15.0	495
DR50	Val d'Orcia	Moraiolo	431	15.0	495
DR51	Val d'Orcia	Moraiolo	431	15.0	495
TOTAL (drupes)		51			
LEAVES					
Sample code	**Geographical area**	**Cultivar**	**Cumulative rainfall (mm)** [a]	**Average Temperature (°C)** [a]	**Altitude (m)**

FO1	Chianti - Siena	Frantoio	439	17.3	299
FO2	Chianti - Siena	Frantoio	439	17.3	262
FO3	Chianti - Siena	Frantoio	550	16.6	304
FO4	Chianti - Siena	Frantoio	550	16.6	300
FO5	Chianti - Siena	Frantoio	550	16.6	286
FO6	Chianti - Siena	Frantoio	519	17.5	305
FO7	Chianti - Siena	Frantoio	519	17.5	296
FO8	Chianti - Siena	Leccino	616	15.3	292
FO9	Chianti - Siena	Leccino	439	17.3	299
FO10	Chianti - Siena	Leccino	439	17.3	262
FO11	Chianti - Siena	Leccino	550	16.6	313
FO12	Chianti - Siena	Leccino	550	16.6	300
FO13	Chianti - Siena	Leccino	550	16.6	279
FO14	Chianti - Siena	Leccino	519	17.5	305
FO15	Chianti - Siena	Leccino	519	17.5	296
FO16	Chianti - Siena	Leccino	616	15.3	292
FO17	Chianti - Siena	Leccino	616	15.3	268
FO18	Chianti - Siena	Moraiolo	439	17.3	299
FO19	Chianti - Siena	Moraiolo	550	16.6	300
FO20	Chianti - Siena	Moraiolo	550	16.6	286
FO21	Chianti - Siena	Moraiolo	519	17.5	305
FO22	Chianti - Siena	Moraiolo	616	15.3	268
FO23	Grosseto	Canino	429	17.0	300
FO24	Grosseto	Frantoio	429	17.0	300
FO25	Grosseto	Leccino	429	17.0	300
FO26	Grosseto	Leccino	319	17.5	217

FO27	Grosseto	Moraiolo	319	17.5	217
FO28	Val d'Orcia	Frantoio	431	15.0	339
FO29	Val d'Orcia	Leccino	431	15.0	339
FO30	Val d'Orcia	Leccino	431	15.0	359
FO31	Val d'Orcia	Moraiolo	431	15.0	495
TOTAL (leaves)		31			

[a] Cumulative rainfall and average temperatures were calculated between January and September 2022. The data are available here: https://www.sir.toscana.it/consistenza-rete.

The results obtained from ^{1}H NMR and EEM fluorescence experiments for the olive leaves and drupes are first examined separately to highlight the specific contributions of each technique. Then, the outcomes of the multiblock analysis on the merged datasets based on the ComDim approach are discussed.

1.3.1 Olive Leaves, ^{1}H NMR and EEM Fluorescence Spectroscopy SingleTechnique Approach

The ^{1}H NMR spectrum of a sample from the Chianti–Siena region is reported in **Figure 44**, which represents the typical NMR profile of olive leaves' extract. The visual appearance of such spectra is quite complex, due to the presence of several overlapping signals that can be ascribed to different classes of compounds like secoiridoids (oleuropein, ligstroside, oleocanthal, and oleacin), sugars, other polyphenols (tyrosol and hydroxytyrosol), and organic acids. The detailed chemical shifts assignment is listed in **table 24.**

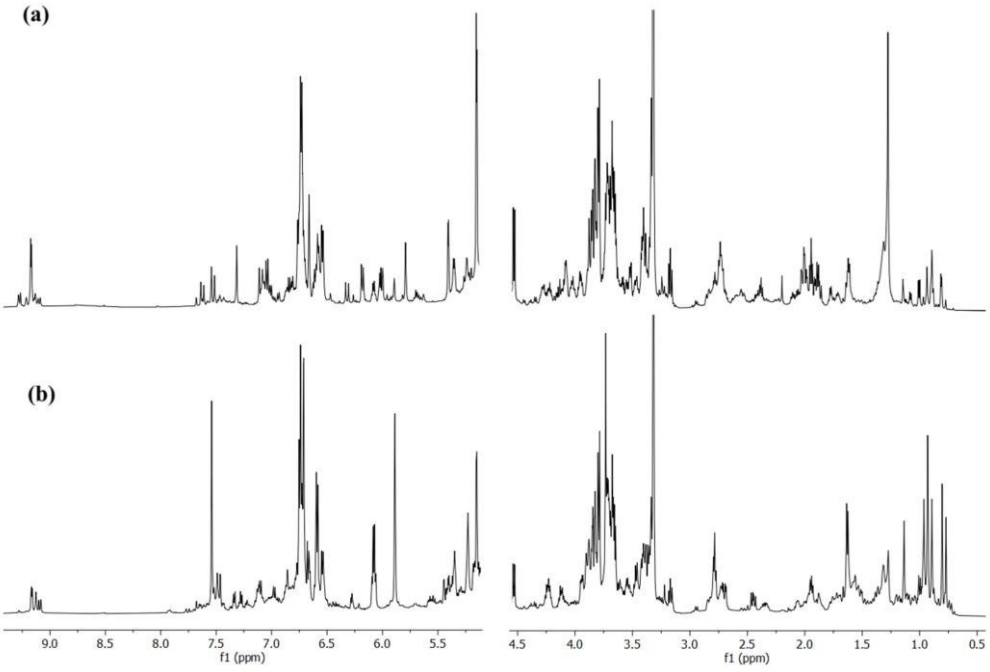

Figure 44. [1]H NMR spectra recorded for a single olive leaves' (**a**) and drupes' (**b**) sample from Siena region, which are representative of the typical NMR profile of leaf and drupe extracts.

The most intense signals are located in the 3–5.5 ppm region, and they can be primarily assigned to sugars and sugar alcohols like mannitol, glucose, and sucrose, which are the most abundant soluble sugars in olive leaves[92]. Specifically, the doublets centered at 5.13 ppm and 4.52 ppm are identified as the anomeric protons of α- and β-glucose, respectively. An additional characteristic doublet at 5.39 ppm, attributed to sucrose, is also detected[93]. Mannitol exhibits multiple signal patterns in the range 3.65–3.90 ppm[94]. Several intense NMR signals can be observed between 5.80 and 7.52 ppm and they can be attributed to oleuropein, one of the main constituent of olive leaf extracts[95]: the presence of this glycosylated secoiridoid is confirmed by additional characteristic resonances in the 1.61–4.16 ppm region[96-97].

These signals originating from oleuropein could be potentially superimposed to the signals of ligstroside, another secoiridoid that differs from oleuropein by one hydroxyl group. Nevertheless, a recent work evidenced that in the extracts of the same olive leaves' varieties the concentration of oleuropein is one order of magnitude higher than ligstroside. Signals in the 9.0–9.2 ppm range are attributed to the aldehydic proton of oleocanthal and oleacin, alongside their hemiacetal derivatives[98]. These compounds originated from the demethylation and spontaneous decarboxylation of the aglycone form of ligstroside and oleuropein, respectively[99]. A characteristic singlet at 8.48 ppm, attributed to formate, can also be detected. In the 6.22–7.52 ppm range, NMR signals corresponding to phenyl alcohol moieties of hydroxytyrosol are observed, along with different characteristic resonances of luteolin[100]. In the aliphatic region organic acids, including malic (2.29–2.70 ppm), citric

(2.50–2.70 ppm), succinic (2.40 ppm), quinic (1.80–2.09 ppm), and lactic (1.32 ppm) acids are also identified.[101] Signals between 0.70 and 1.13 ppm can be attributed to maslinic and oleanolic acids[102].

Table 24. ^{1}H NMR assignment for the olive leaves extracts.

d (ppm)	Assignment	Reference
9.16 – 9.17	Aldehydic proton of olecanthal and its hemiacetal derivative (m)	[1]
9.10 – 9.08	Aldehydic proton of oleacin and its hemiacetal derivative (m)	[1]
8.48	Formate (s)	[2]
7.52	Oleuropein (s)	[3,4]
7.35	Luteolin (m)	[5]
6.88	Luteolin (m)	[5]
6.73	Oleuropein (s)	[3,4]
6.72	Oleuropein (s)	[3,4]
6.69	Oleuropein (d, J = 2 Hz)	[3,4]
6.57	Hydroxytyrosol (dd, J_1= 8.02 Hz, J_2= 1.99 Hz)	[4]
6.52	Fumarate (m)	[2]
6.22	Luteolin (m)	[5]
6.06	Oleuropein (q, J = 6.94 Hz)	[3,4]
5.87	Oleuropein (s)	[3]
5.39	Sucrose anomeric protons (d, J = 3.80 Hz)	[2]
5.13	Anomeric proton of a-glucose (d, J = 3.71 Hz)	[2]
4.52	Anomeric proton of b-glucose (d, J = 7.91 Hz)	[2]
4.16	Oleuropein (m)	[3,4]
3.82	Mannitol (dd, J_1= 11.43 Hz, J_2= 3.32 Hz)	[5,6]
3.77	Mannitol (d, J = 8.11 Hz)	[5,6]
3.73-3.68	Mannitol (m)	[5,6]
3.71	Oleuropein (s)	[3,4]
3.65	Mannitol (dd, J_1= 11.16 Hz, J_2= 6.06 Hz)	[5,6]
3.52 – 3.13	Glucose and sucrose	[3,4]
2.76	Oleuropein (m)	[3,4]

2.70	Malic / Citric acid (d)	[2]
2.67	Oleuropein (d, J = 4.64 Hz)	[3,4]
2.50	Citric acid (d)	[2]
2.42	Oleuropein (d, J = 4.79 Hz)	[3,4]
2.40	Succinic acid (s)	[2]
2.35 – 2.29	Malic acid (m)	[2,5]
2.09 – 1.80	Quinic acid (m)	[6]
1.61	Oleuropein (dd, J_1= 7.01 Hz, J_2= 1.25 Hz)	[3,4]
1.32	Lactic acid (m)	[3,6]
1.13	Maslinic and Oleanolic acid (s)	[7]
0.97	Oleanolic acid (m)	[7]
0.96	Maslinic acid (s)	[7]
0.93	Maslinic and Oleanolic acid (s)	[7]
0.89	Maslinic and Oleanolic acid (s)	[7]
0.80	Maslinic acid (s)	[7]
0.77	Maslinic and Oleanolic acid (s)	[7]

First, an exploratory data analysis was performed via PCA on the NMR leaves dataset.

The resulting score plot for the first three principal components, accounting for 89.5% of the original variance, is reported in **Figure 45**.

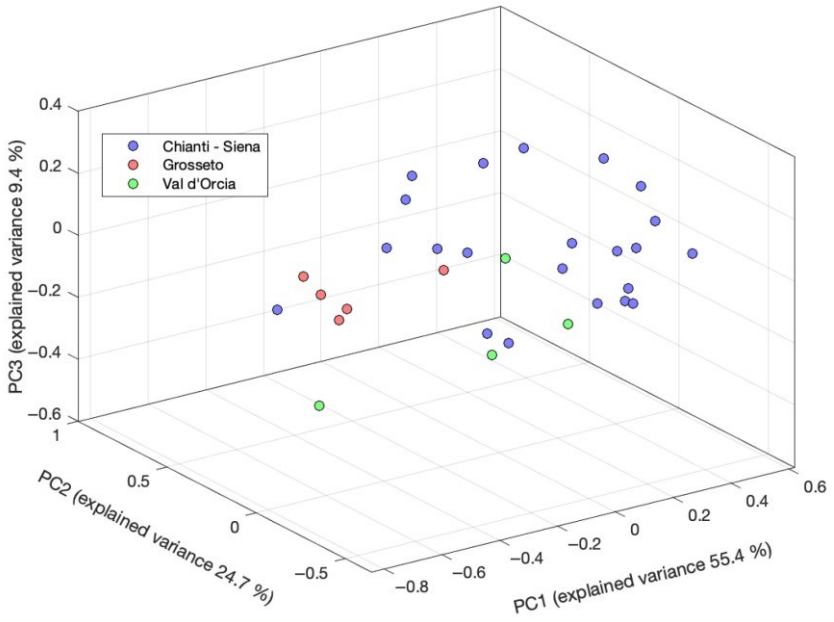

Figure 45. Three-dimensional PCA score plot for ^{1}H NMR data of the olive leaf samples.

a

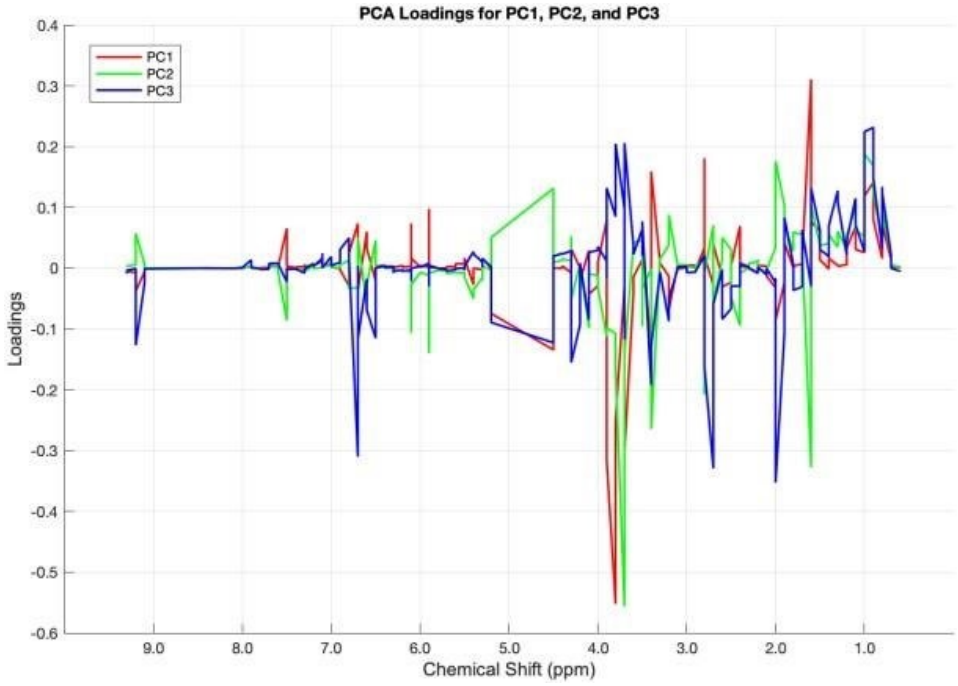

b

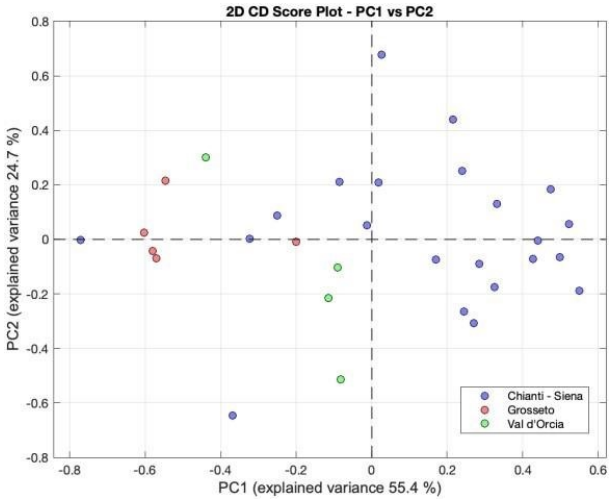

c

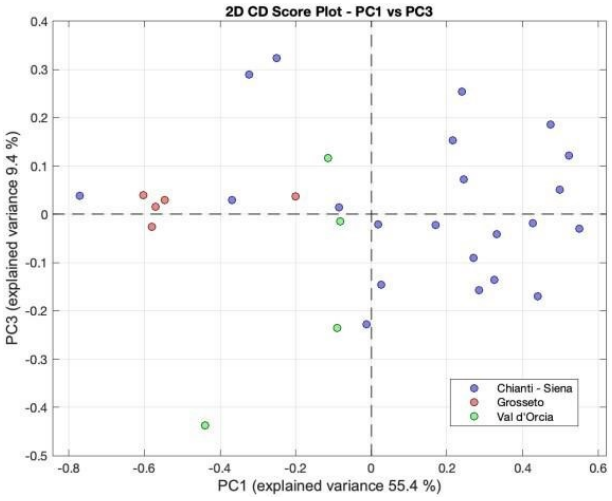

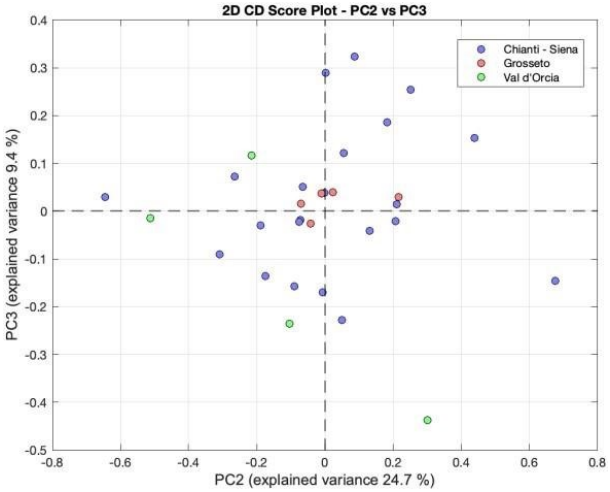

d

Figure 46. PCA loading plot for ^{1}H NMR data of the olive leaves samples (a) and 2D score plots: PC1 vs PC2 (b), PC1 vs PC3 (c) and PC2 vs PC3 (d).

The distribution of the samples along the PCs shows a partial differentiation according to the different geographical origins. The samples from Chianti–Siena region are relatively well clustered, similarly to the samples from Grosseto, which form a separate, though more scattered, group. The samples from Val d'Orcia are more widely distributed, showing a significant overlap with the other regions. The separation observed along PC1 accounts for the most significant differentiation among the groups, particularly between Chianti–Siena and the other regions. Notably, this trend seems to correlate with the latitude of the sampling sites, as evidenced in the 2D score plots in **Figure 46**. The samples from Chianti–Siena are located at positive PC1 values, which gradually shift toward more negative values when moving from Val d'Orcia to Grosseto, so from central to southern Tuscany.

The analysis of the PCA loadings reveals that the major contributions in terms of individual variables (i.e., buckets) are given by the oleuropein/ligstroside signals at 1.64, 2.80, 3.71 and 6.73 ppm, followed by mannitol (3.65, 3.81), glucose (3.37, 4.53), and quinic acid (1.96). These findings are in good agreement with the results obtained from the analysis of the phenolic composition via high-performance liquid chromatography–high-resolution mass spectrometry (HPLC-HRMS) on the same dataset, identifying ligstroside as one of the major contributors to geographic discrimination[22].

Considering the results obtained from the explorative PCA, SIMCA was implemented to build a classification model for the Chianti–Siena subregional area. Among the three geographical areas considered, the samples from this subregion exhibit a relatively more compact and coherent distribution despite the overall absence of clear global separation. This apparent in-class consistency provides a suitable foundation for a class-modeling approach, aiming to distinguish Chianti–Siena samples from those belonging to other regions.

The model performance parameters are listed in **Table 25**, while the SIMCA distance plot is reported in the **Figure 47**.

SIMCA Model for Chianti-Siena Region

	Training			Test			
	Accuracy (%)	Sensitivity (%)	Specificity (%)	Accuracy (%)	Sensitivity (%)	Specificity (%)	Explained Variance (%)
Leaves ^{1}H NMR	100	100	100	83	100	50	97
Leaves EEM	84	100	43	83	100	50	94
Drupes ^{1}H NMR	88	90	82	70	75	50	95
Drupes EEM	76	77	73	50	50	50	90

Figure 47. SIMCA normalized distances from ^{1}H NMR data of the olive leaves samples for the modelled Chianti – Siena region.

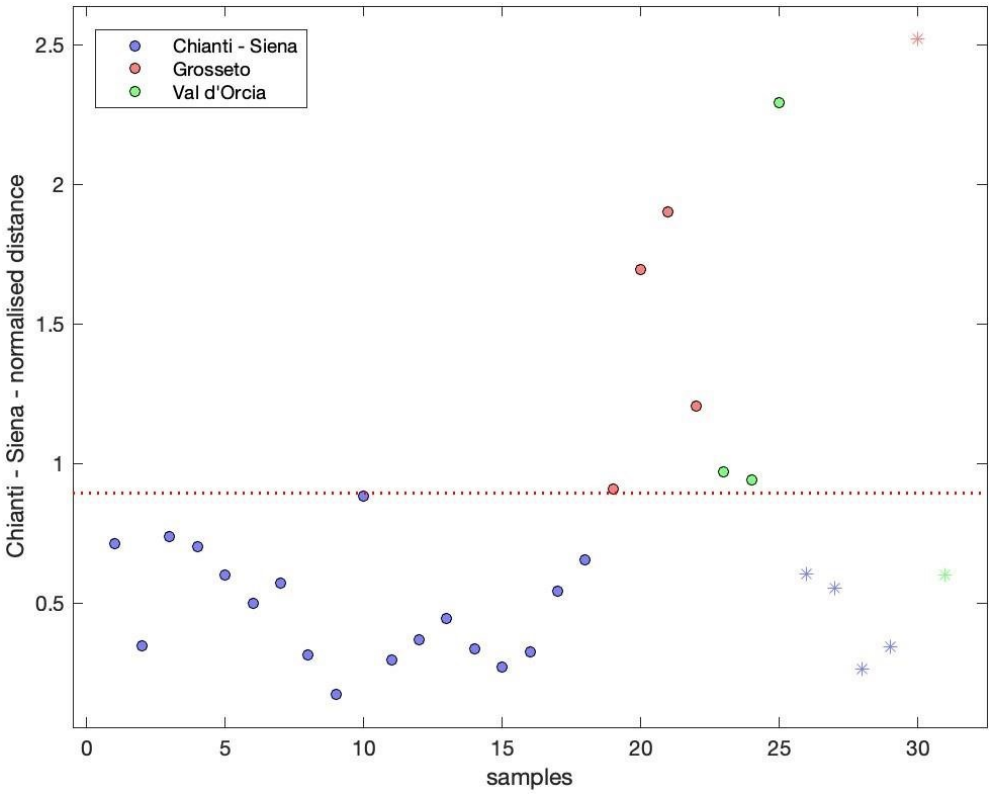

The SIMCA model shows good performance in classifying samples from the Chianti–Siena subregion in both the training and test sets, achieving a prediction accuracy of 83%, albeit with relatively low specificity. The analysis of the model loadings supports the findings from the PCA, highlighting the predominant contribution of oleuropein/ligstroside (δ 1.64, 2.80, 3.71 ppm) and sugars, specifically mannitol (δ 3.65, 3.81 ppm) and glucose (δ 3.37, 4.53 ppm).

The **Figure 48** shows the full excitation–emission landscape recorded for a single representative olive leaf sample from the Chianti–Siena region. Two main fluorescence emission regions can be detected: the first one (Region A) presents excitation and emission wavelengths in the range 300– 700 and 650–750 nm, respectively, while the second area (Region B) has excitation wavelengths from 250 to 400 nm and emission wavelengths from 370 to 530 nm.

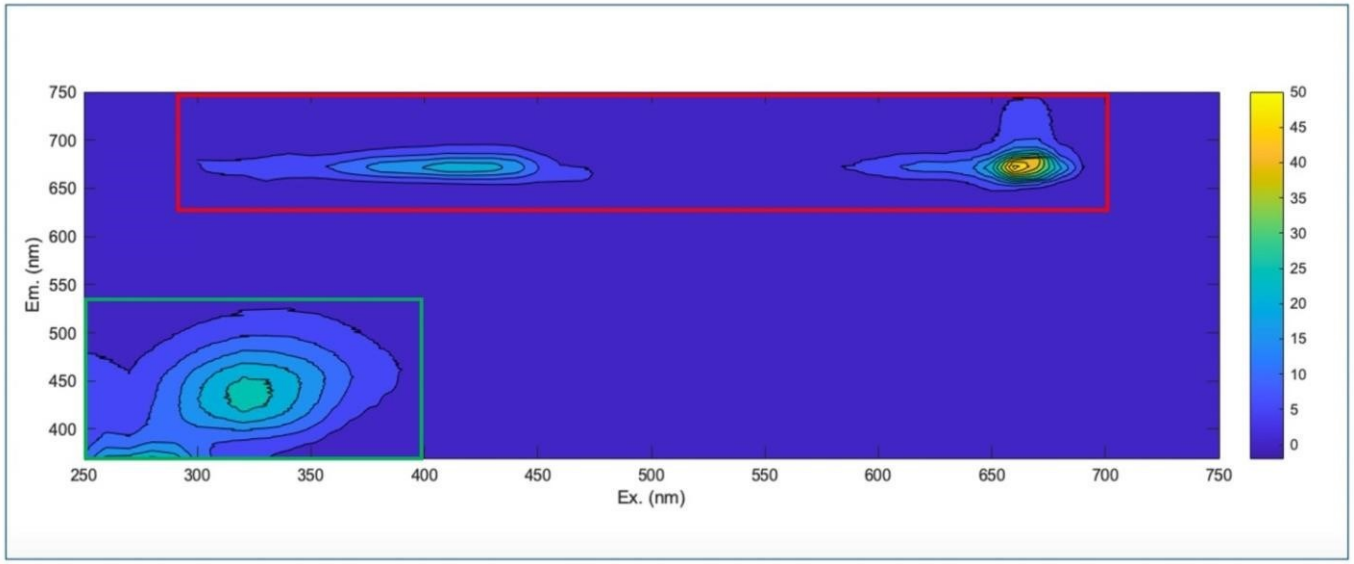

Figure 48. Processed full excitation–emission fluorescence map of olive leaves. The green area represents the chlorophylls' region (Region A), and the red area corresponds to the emission region of cellular fluorophores like amino acids, phenolic compounds, vitamins, and organic polymers (Region B).

According to the existing literature, in olive oils[103-104-105], fruit samples and grapevine leaf extracts[62], the fluorescence signals in Region A are usually ascribed to the emission of chlorophylls and pheophytins, while in Region B several fluorescent compounds may emit, like polyphenols, vitamins, amino acids, and organic polymers. To the best of our knowledge, this is the first work reporting the characterization of olive leaves' emission profiles via EEM fluorescence spectroscopy. Since chlorophylls may affect the performance and reliability of the models because of their high fluorescence intensity and high variability (mainly due to different cultivars and climatic conditions) the two emission regions were analyzed separately[106-107].

The excitation and emission loadings' profiles obtained through PARAFAC decomposition for Region A and B are shown in **Figure 49A and B** while the assignment of fluorescent compounds corresponding to the emission patterns in olive leaf samples is summarized in **Table 25**.

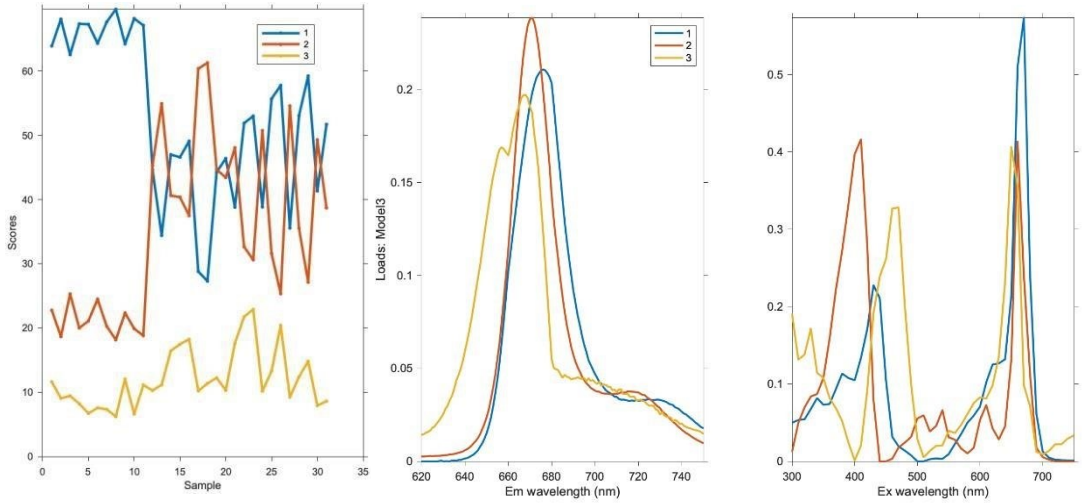

Figure 49 A. Sample, excitation and emission PARAFAC loadings for the olive leaves samples in spectral Region A.

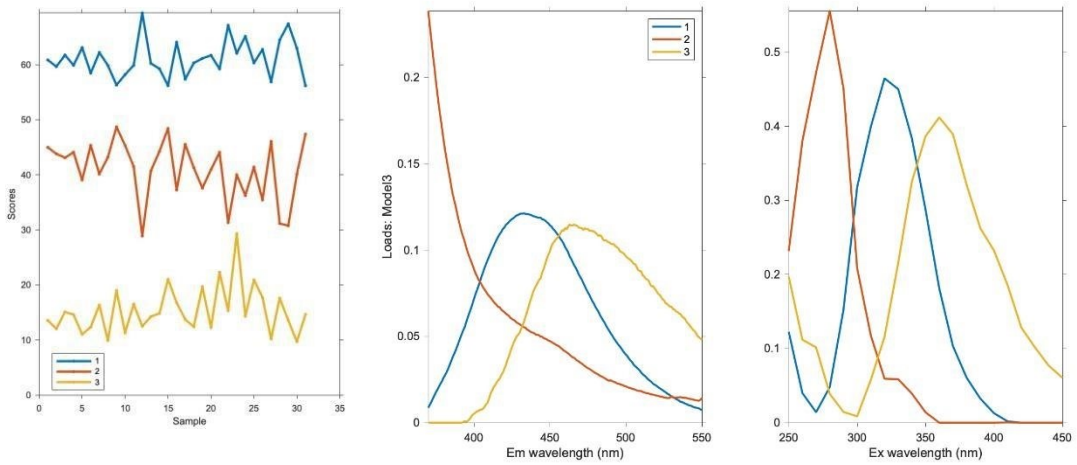

Figure 49 B. Sample, excitation and emission PARAFAC loadings for the olive leaves samples in spectral Region B.

Table 26. Fluorescent properties of compounds detected in olive leaves and drupes.

Analyzed Matrix	Fluorescence Region	Compound	Excitation Wavelength (nm)	Emission Wavelength (nm)
Leaves	Region A	Chlorophyll a	430, 670	675
		Pheophytin a	410, 660	670
		Chlorophyll b	460, 650	665
	Region B	Chlorogenic acid	320	435
		Phenolic compounds	280	<370
		Tocopherols	360	465
Drupes	Full map	Catechin/epicatechin	280	315
		Tocopherols	340	450
		Phenolic compounds	230	310

For Region A, a three-component PARAFAC model was found to produce the most accurate results: the three different contributions can be ascribed to the presence of chlorophyll *a*, chlorophyll *b*, and pheophytin *a*, respectively, in agreement with previous works[62-108]. For Region B, the optimal number of components was three: the first one exhibits a well-defined band with an excitation maximum at 320 nm and an emission maximum at 435 nm, which can be related to the presence of chlorogenic acid and related compounds[62-109]. The second component shows a single excitation maximum at 280 nm, while the emission band is only partially visible since the maximum is located below 370 nm, outside the investigated wavelength range. Nevertheless, this component can be assigned to the fluorescence profile of phenolic compounds, as extensively reported in the case of olive oil[110-111-112]. For the third component, the excitation and emission maxima occur at 360 and 465 nm, respectively, and these bands are commonly associated with the presence of tocopherols and tocotrienols[112].

The concentration mode (score plots) of the PARAFAC model is reported in **Figure 49 A** and **B** to show the relative concentrations of the different classes of fluorophores for each sample. For Region A, the concentration of the first two components, which corresponds to chlorophyll *a* and pheophytin *a*, is higher than pheophytin *b*, despite major fluctuations across the dataset. For Region B, the most abundant fluorescent component is chlorogenic acid, followed by phenolic compounds and tocopherols, respectively. For geographical authentication purposes, the chlorophyll region (Region A) was excluded from the PCA and SIMCA analysis, since the chlorophylls' content and the consequent fluorescent emission profile can be remarkably affected by different climatic conditions[53]. The PCA exploratory analysis performed on the EEM data from Region B (**Figures 50** and **51**)

indicates a limited separation among the three regions: while the samples from Chianti–Siena show a partial clustering, a considerable overlap with Grosseto and Val d'Orcia is observed.

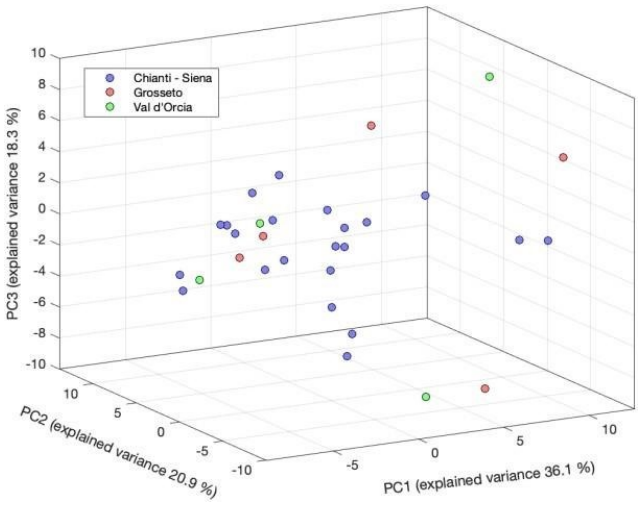

Figure 50. 3D PCA score plot for EEM (Region B) data of the olive leaves samples

a

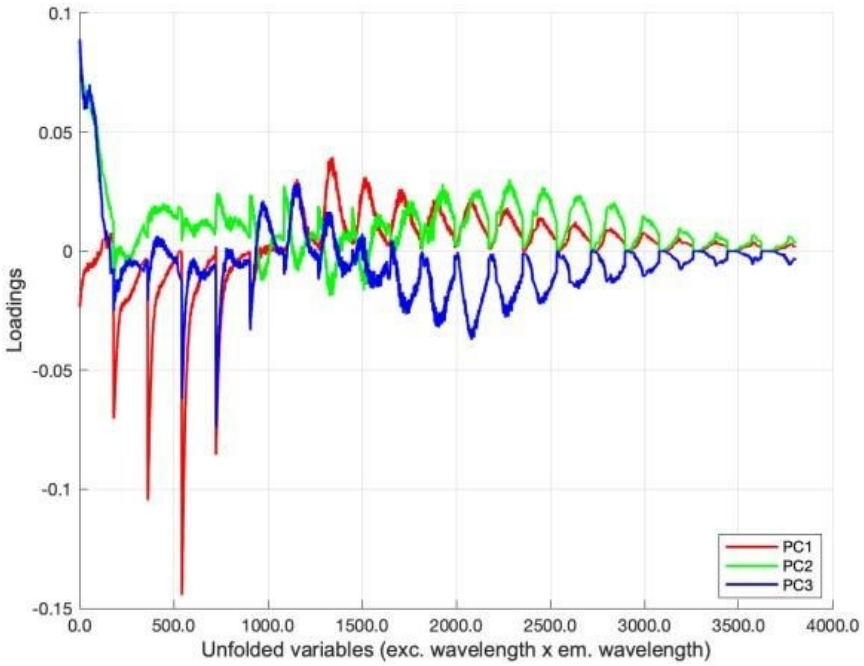

b

c

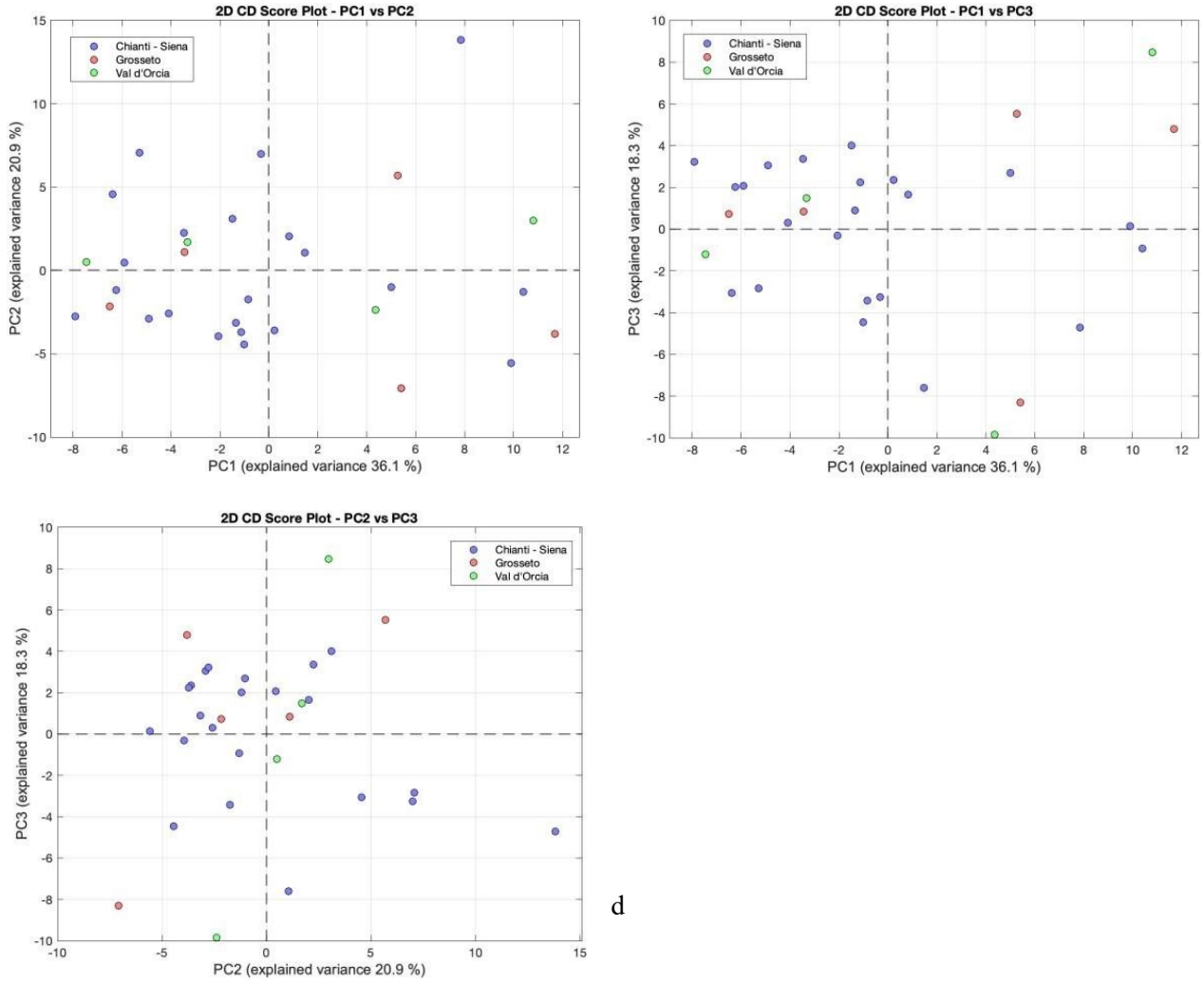

d

Figure 51. PCA loading plot for EEM (Region B) data of the olive leaves samples (a) and 2D score plots: PC1 vs PC2 (b), PC1 vs PC3 (c) and PC2 vs PC3 (d).

The loading vectors were refolded into EEM-like tridimensional data to identify the regions of the EEM that give the major contributions in the PCA model. The analysis of the refolded loadings revealed that the most relevant excitation–emission wavelength couples are centered around 280/370 nm, corresponding to the fluorescence profile of polyphenols. This result provides confirmation about the importance of these compounds as markers for geographical authentication, as reported in

previous studies[8-22]. A secondary contribution is given by excitation–emission signals at 330/435 nm (chlorogenic acid), while tocopherols and tocotrienols do not provide significant contributions.
The classification results obtained from the SIMCA model on Region B are summarized in **Table 25,** while the distance plot is reported in **Figure 52**.
SIMCA results show a predictive performance in the test set comparable to that of the ^{1}H NMR model, although slightly lower performance metrics are observed in the calibration set. In particular, the SIMCA model can effectively discriminate between the Chianti–Siena and Val d'Orcia areas, as evidenced by the sharp differences in the distance plot. The loadings analysis confirms the results obtained via PCA, indicating polyphenols and chlorogenic acid fluorescence emissions as the most relevant contributions for the geographical differentiation.

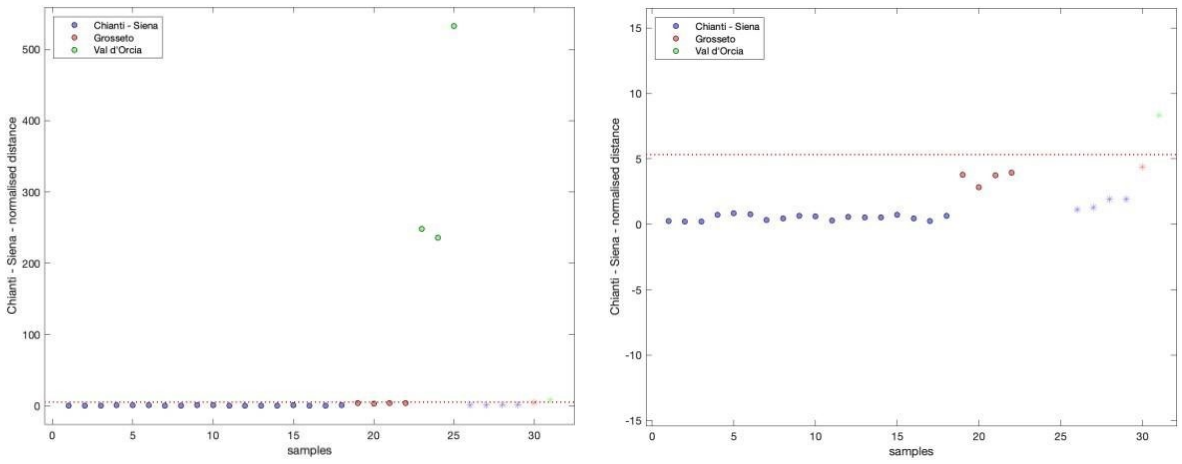

Figure 52. SIMCA normalized distances from EEM data of the olive leaves samples for the modelled Chianti – Siena region. The right panel shows a magnified view of the distance distribution.

1.3.2 Drupes, ^{1}H NMR and EEM Fluorescence Spectroscopy Single-Technique Approach

As in the case of olive leaves, the drupe extracts show a very complex NMR profile due to the presence of multiple metabolites with similar or overlapping signals. The ^{1}H NMR spectrum of a sample from the Chianti–Siena region reported in **Figure 44** is a good example of a typical olive drupes' extract. The detailed chemical shifts assignment is listed in the **Table 27**.

Table 27. Chemical shifts assignment of olive drupes' extract.

d (ppm)	Assignment	Reference
7.68	Quercetin (d, J = 2.2 Hz, H-2')	[8]
7.54	Verbascoside (m)	[9]
7.52	Oleuropein (s)	[3,4]
7.32	Luteolin (m)	[10]
7.01	Verbascoside (dd, J_1= 8.2 Hz, J_2= 2.0 Hz, H6'")	[9]
6.85	Luteolin (d, J = 9.0 Hz, H-5')	[10]
6.74 – 6.78	DHPEA-EDA (dihydroxyphenylethanolelenolic acid dialdehyde)/Oleocanthal/Oleomissional (m)	[11]
6.73	Oleuropein (s)	[3,4]
6.71	Oleuropein (d, J = 2 Hz)	[3,4]
6.63	Verbascoside (m)	[9]
6.61	Verbascoside (m)	[9]
6.59	Hydroxytyrosol (d, J = 2 Hz)	[12]
6.31	Verbascoside (d, J = 15.8 Hz)	[9]
6.07	Oleuropein (q, J = 6.94 Hz)	[3,4]
5.89	Oleuropein (s)	[3]
5.19 – 5.22	Maslinic and oleanolic acid (m)	[13]
5.15	Verbascoside (m)	[9]
4.52	Anomeric proton of b-glucose (d, J = 7.91 Hz)	[2]
4.07	Lactic acid (m)	[14]
3.83	Mannitol (dd, J_1= 11.43 Hz, J_2= 3.32 Hz)	[5,6]
3.79	Mannitol (d, J = 8.11 Hz)	[5,6]
3.73-3.68	Mannitol (m)	[5,6]
3.65	Mannitol (dd, J_1= 11.16 Hz, J_2= 6.06 Hz)	[5,6]
3.54 – 3.14	Glucose and sucrose	[3,4]
2.84	Maslinic and oleanolic acid (dd, J_1= 14.0 Hz, J_2= 4.1 Hz)	[13]
2.76	Oleuropein (m)	[3,4]
2.69	Oleuropein (d, J = 4.64 Hz)	[3,4]

2.64	Tyrosol (m)	[14]
2.61	Hydroxytyrosol (m)	[12]
2.40	Succinic acid (s)	[3]
2.36 – 2.31	Malic acid (m)	[3,5]
1.95 – 1.86	Quinic acid (m)	[6]
1.85	Acetic acid (s)	[9]
1.61	Oleuropein (m)	[3,4]
1.32	Lactic acid (m)	[3,6]
1.13	Maslinic and Oleanolic acid (s)	[7]
1.07	Verbascoside (d, J = 6.3 Hz)	[9]
0.97	Oleanolic acid (m)	[7]
0.96	Maslinic acid (s)	[7]
0.93	Maslinic and oleanolic acid (s)	[7]
0.89	Maslinic and oleanolic acid (s)	[7]
0.81	Maslinic acid (s) and oleanolic acid (s)	[7]
0.77	Maslinic and oleanolic acid (s)	[7]

The ^{1}H NMR profiles of the drupe extracts share some similarities with the spectra obtained from the leaves: several intense signals related to sugars (glucose, sucrose, and mannitol) are clearly observable between 3 and 4.5 ppm, while the characteristic peaks of oleuropein are detected at 7.52, 6.70, 5.90–6.00, 2.70, and 1.61 ppm. In the range between 5 and 8 ppm the most intense signals are attributed to the presence of verbascoside, quercetin and luteolin[113-114-115], while in the aliphatic region the characteristic resonances of maslinic and oleanolic acid[116] (0.77–1.13 ppm) along with other different organic acids as lactic (1.32 ppm), acetic (1.85 ppm), quinic (1.86–1.95 ppm), malic (2.31–2.36 ppm), and succinic (2.40 ppm) acids can be detected[117].

Exploratory PCA (**Figure 53** and **54**) does not reveal any significant clustering or separation in the sample distribution according to their geographical origin. This can be attributed to the greater chemical complexity of the drupe matrices, which may hinder the ability of unsupervised methods to capture the geographical-related variance.

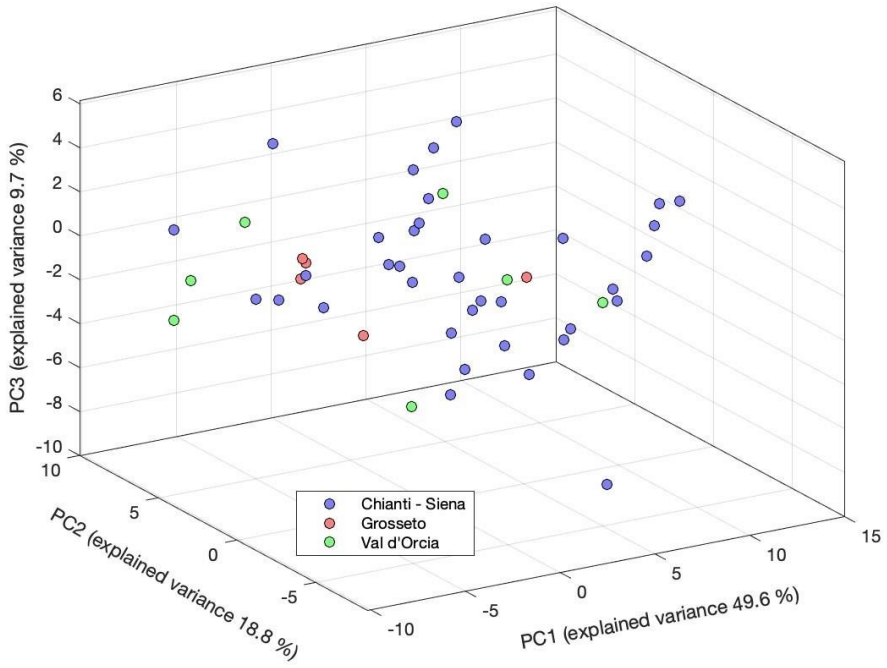

Figure 53. 3D PCA score plot for ^{1}H NMR data of the olive drupes samples.

a

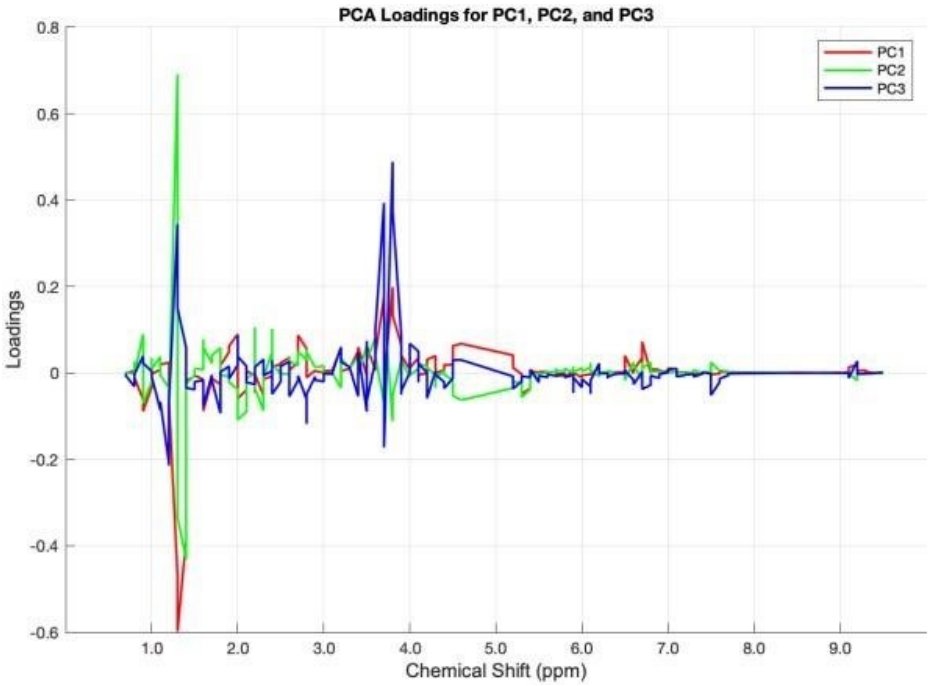

b

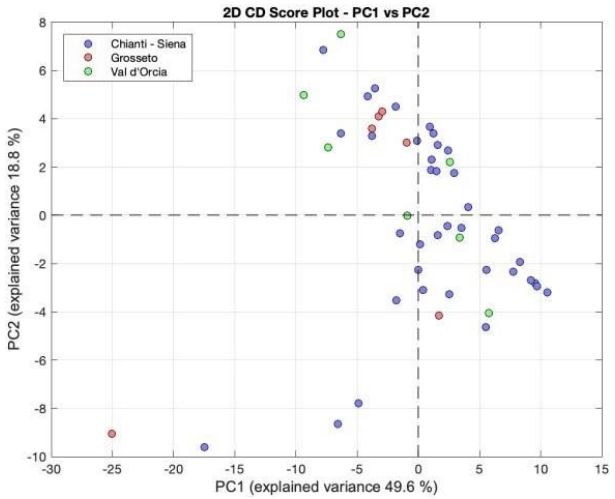

c

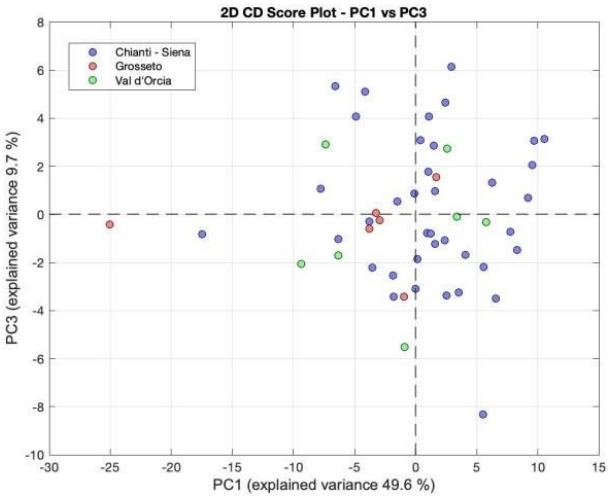

d

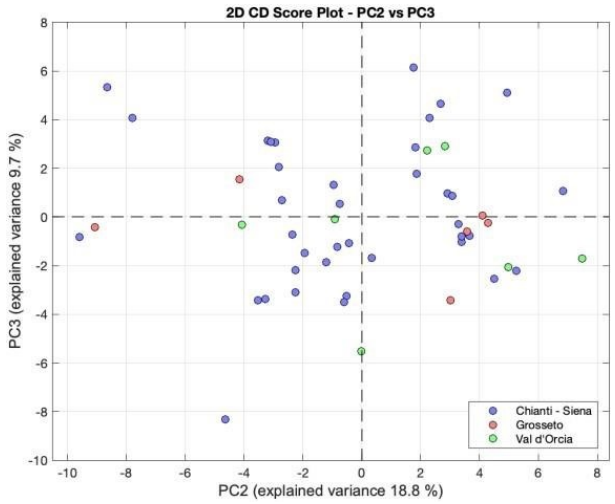

Figure 54. PCA loading plot for ^{1}H NMR data of the olive drupes samples (a) and 2D score plots: PC1 vs PC2 (b), PC1 vs PC3 (c) and PC2 vs PC3 (d).

In contrast, as evidenced in the previous section, PCA of leaf extracts (**Figure 45**) shows a more structured distribution of the samples and a partial differentiation, suggesting a clearer relationship between metabolic composition and the geographic origin.

Subsequently, the ^{1}H NMR signals were used as input for SIMCA to build a classification model for the Chianti–Siena area. The performance metrics are listed in **Table 25**, while the distance plot is reported in the **Figure 55**.

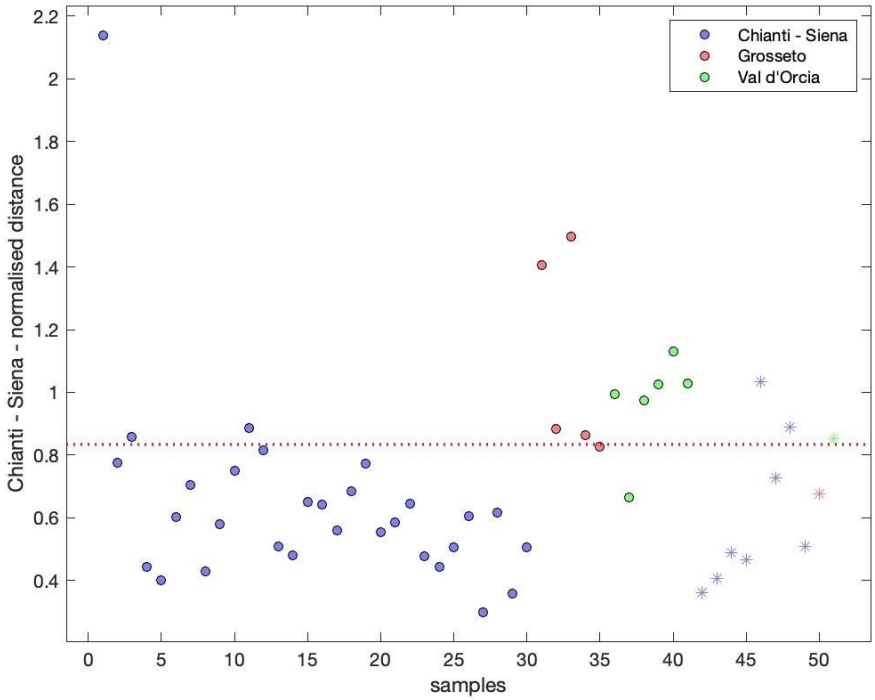

Figure 55. SIMCA normalized distances from EEM data of the olive drupes samples for the modelled Chianti – Siena region.

The model shows good overall classification performances, with slightly lower values for the test set. From the comparison with the results obtained for the different vegetable matrices, SIMCA modeling based on ^{1}H NMR data seems to provide a more accurate classification for the Chianti– Siena subregion for olive leaves.

The analysis of the loadings obtained from the SIMCA models for the drupe samples evidences that the most relevant contributions in terms of spectral buckets to the geographical classification models are provided by the signals at 1.13 (maslinic and oleanolic acid), 1.31–1.35 (malic acid), 1.80–2.00 (quinic acid), 2.65–2.75 (oleuropein, malic and citric acid), and 3.66–3.82 ppm (mannitol and oleuropein). The comparison with the loading results obtained for leaf samples reveals two noteworthy aspects: firstly, a strong correspondence exists between the metabolites primarily responsible for the classification performance of the models in both leaves and drupes. Secondly, organic acids play a predominant role among these metabolites, alongside specific signals from oleuropein and sugars.

A characteristic fluorescence excitation–emission map for a representative olive drupe extract from the Siena area is reported in **Figure 56**. Since the emission of chlorophylls and related compounds may negatively affect the chemometric models for geographical origin authentication, the EEM landscapes were acquired by excluding the pigment emission region.

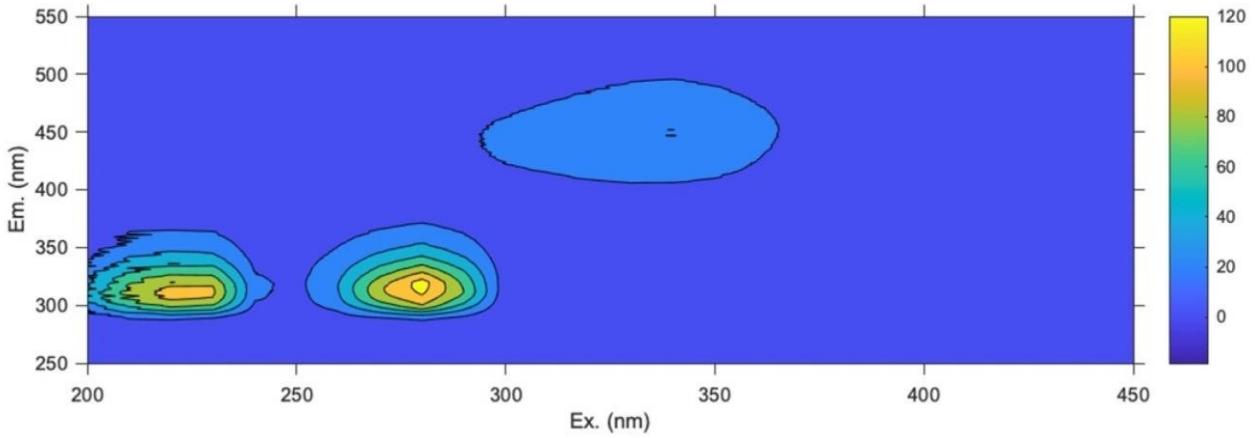

Figure 56. Processed full excitation–emission fluorescence map of olive drupes.

From a visual inspection of the fluorescence maps, three distinct emission areas can be detected, with excitation–emission maxima located at 220/310, 280/315 and 340/450 nm. The PARAFAC modeling confirmed the identification of three major classes of fluorescent components, as shown in **Figure 57**.

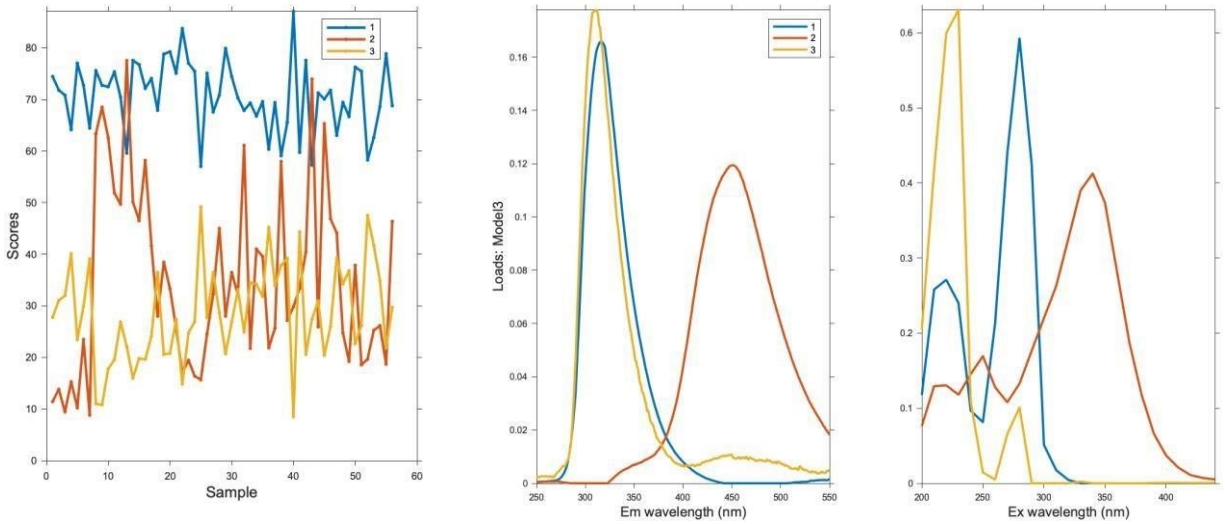

Figure 57. Sample, excitation and emission PARAFAC loadings for the drupe samples.

The first component (λ_{ex} = 280 nm; λ_{em} = 315 nm) can be ascribed to the presence of phenolic compounds like catechin and epicatechin[118], while the second component with characteristic λ_{ex} values of 340 nm and λ_{em} of 450 nm, can be associated with tocopherols and tocotrienols, similarly to the case of leaf samples. The third component shows an intense emission located at 310 nm, with an excitation maximum at 230 nm: these spectral features cannot be unambiguously assigned to specific fluorophores since several phenolic compounds may contribute to the overall emission in this wavelength range[119]. Among these compounds, oleuropein exhibits a well-defined emission band

at 310 nm, although in the case of olive oil, the excitation maximum occurs at higher wavelengths (270 nm). The PARAFAC score plot reported in the **Figure 57** shows that catechin and epicatechin are the most abundant fluorescent compounds across the entire dataset, followed by tocopherols, tocotrienols, and polyphenols/oleuropein.

Exploratory PCA performed on the unfolded EEM fluorescence data of olive drupe extracts (**Figure 58** and **59**) reveals a high degree of overlap among the samples from the three geographical regions: a partial clustering along the PC2 can be observed for Val d'Orcia and, to a lesser extent, for Grosseto areas, while the samples from Chianti–Siena region are more scattered.

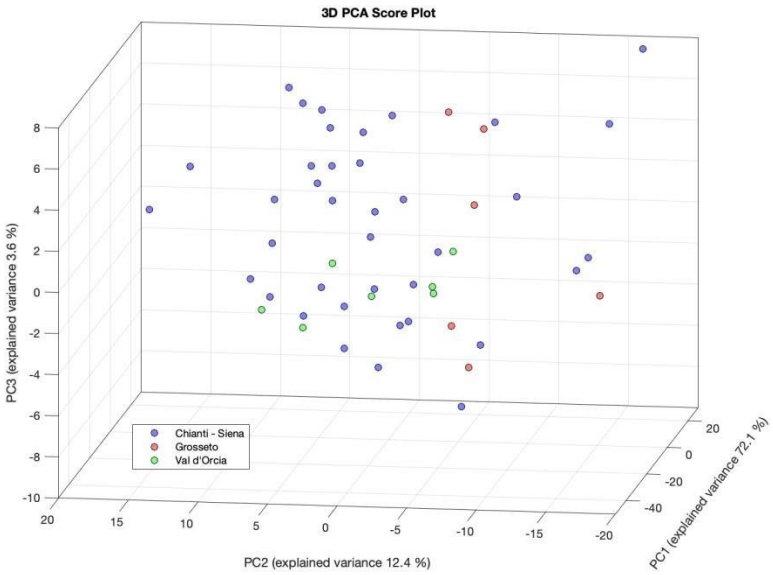

Figure 58. 3D PCA score plot for EEM data of the olive drupes samples.

a

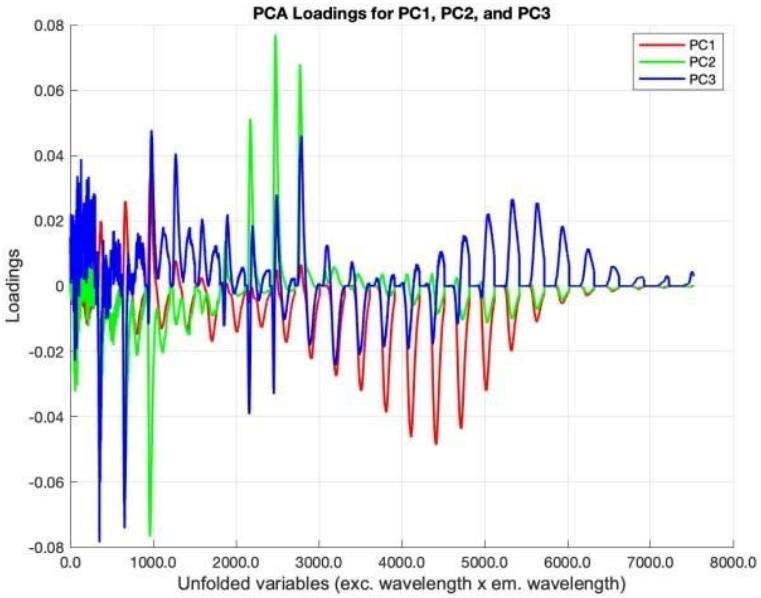
PCA Loadings for PC1, PC2, and PC3
PC1
PC2
PC3
Loadings
Unfolded variables (exc. wavelength x em. wavelength)

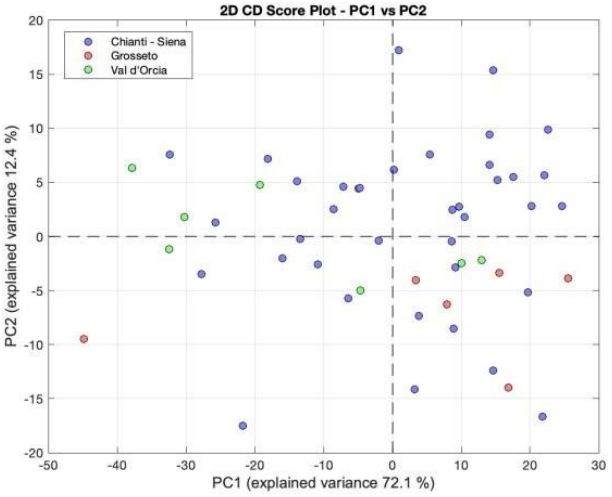
2D CD Score Plot - PC1 vs PC2
Chianti - Siena
Grosseto
Val d'Orcia
PC2 (explained variance 12.4 %)
PC1 (explained variance 72.1 %)

b

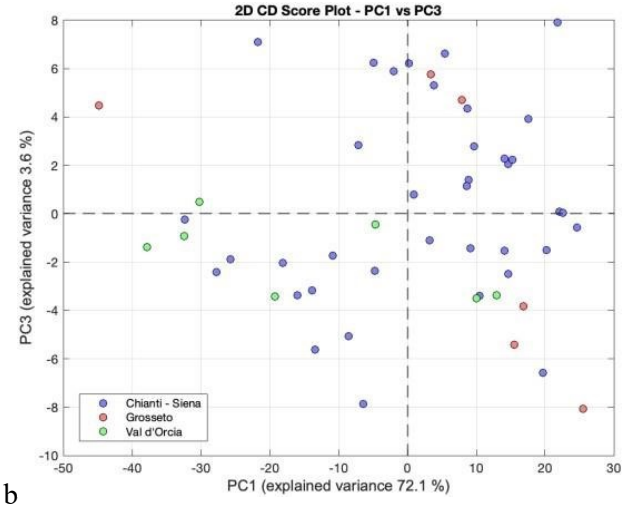
2D CD Score Plot - PC1 vs PC3
Chianti - Siena
Grosseto
Val d'Orcia
PC3 (explained variance 3.6 %)
PC1 (explained variance 72.1 %)

c

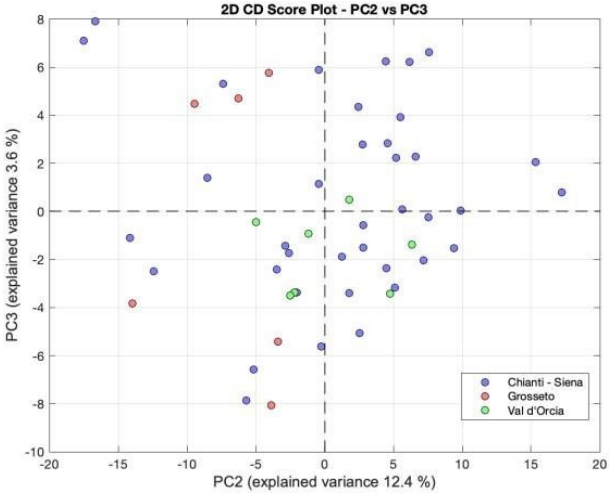
2D CD Score Plot - PC2 vs PC3
Chianti - Siena
Grosseto
Val d'Orcia
PC3 (explained variance 3.6 %)
PC2 (explained variance 12.4 %)

d

Figure 59. PCA loading plot for EEM data of the olive drupes samples (a) and 2D score plots: PC1 vs PC2 (b), PC1 vs PC3 (c) and PC2 vs PC3 (d).

The SIMCA model built for the Chianti–Siena area shows slightly reduced classification performances in both the training and test sets compared to the results obtained with ^{1}H NMR data on drupe extracts, as well as to those achieved for the leaf samples (see **Table 24** and **Figure 60**). This can be attributed to the more complex chemical composition of the drupe's matrix, which limits the ability of EEM fluorescence spectroscopy to reflect region-specific characteristics.

The examination of the refolded loadings on the principal components demonstrates that the major contributions to the model are provided by the excitation–emission wavelength couples centered at 280/315 nm and 340/450 nm, related to catechin/epicatechin and tocopherols, respectively.

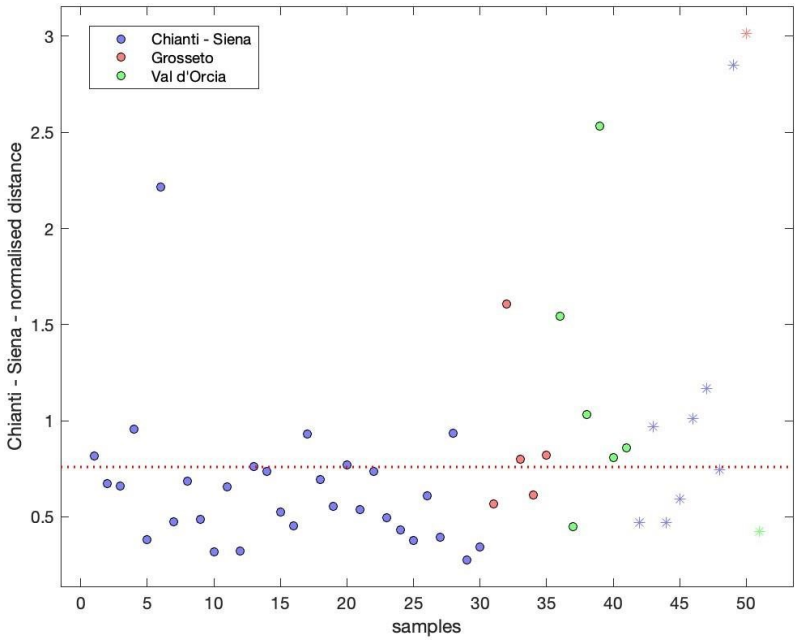

Figure 60. SIMCA normalized distances from EEM data of the olive drupes samples for the modelled Chianti – Siena region.

1.3.2 Data Fusion

To further improve the sample differentiation and gain a deeper understanding of the specific contributions provided by the two spectroscopic techniques, the application of a mid-level data fusion based on the ComDim algorithm is explored. As an unsupervised multiblock method, ComDim does not require prior knowledge of the geographical origin of the samples, allowing for an objective integration of complementary information from multiple datasets while preserving the intrinsic data structure.

As described in the Materials and Methods Section, the individual data blocks from ^{1}H NMR and EEM are normalized and concatenated, and then the common dimensions (CD) are extracted. The score plot of the first 3 CDs is reported in **Figure 61**, while for a comprehensive visualization of all the CDs, see **Figure 62**. For each CD, the saliences and loadings are calculated and shown in **Figure 63**.

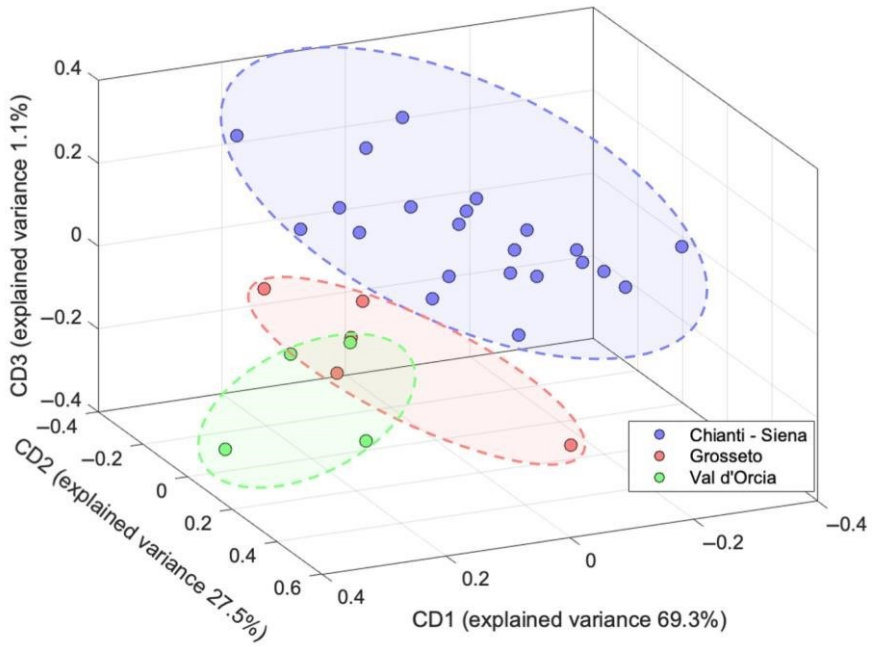

Figure 61. Three-dimensional ComDim score plot for the merged dataset of the olive leaf samples.

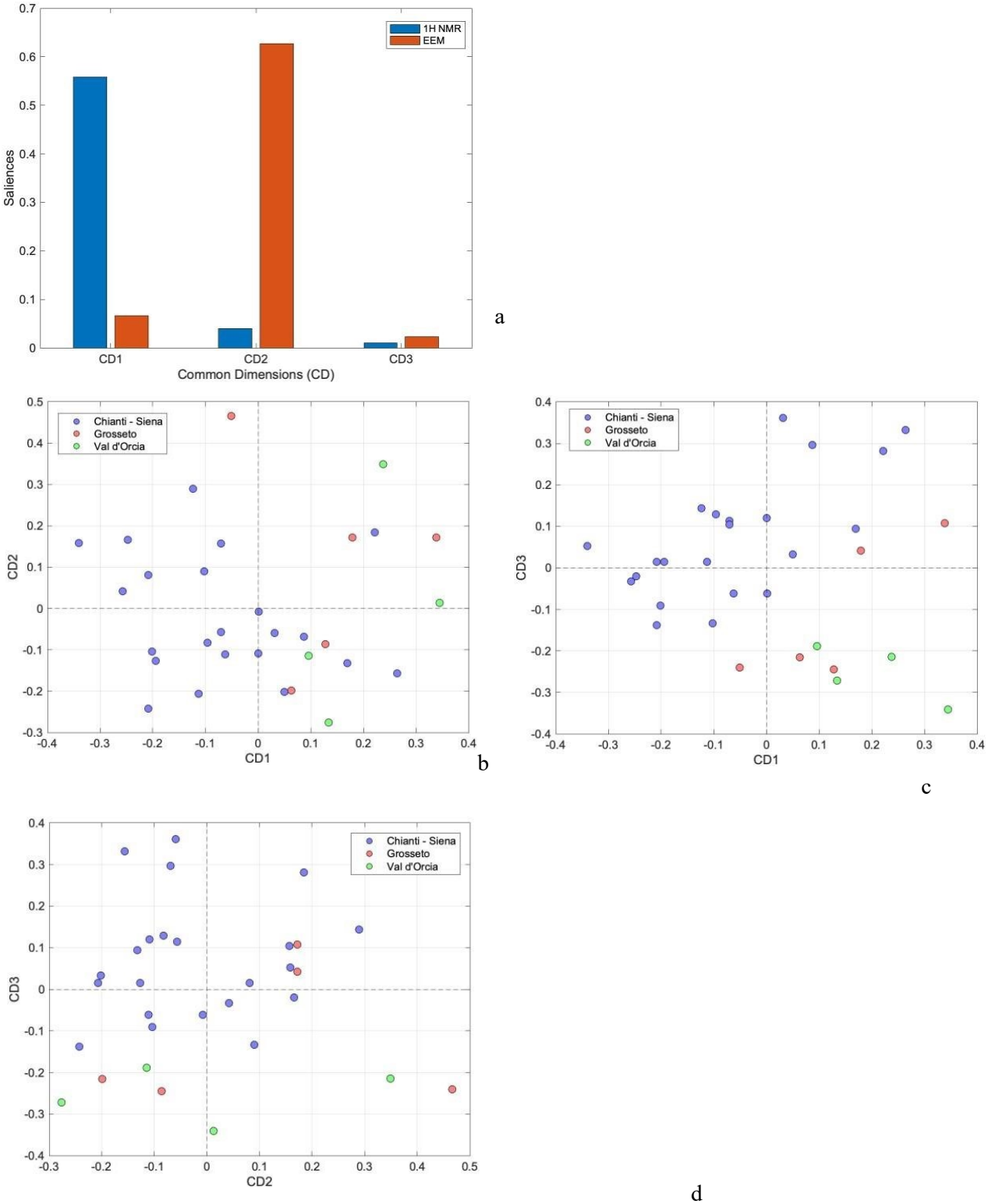

Figure 62. ComDim salience plot for the leaves samples (a) and 2D ComDim score plots: CD1 vs CD2 (b), CD1 vs CD3 (c) and CD2 vs CD3 (d).

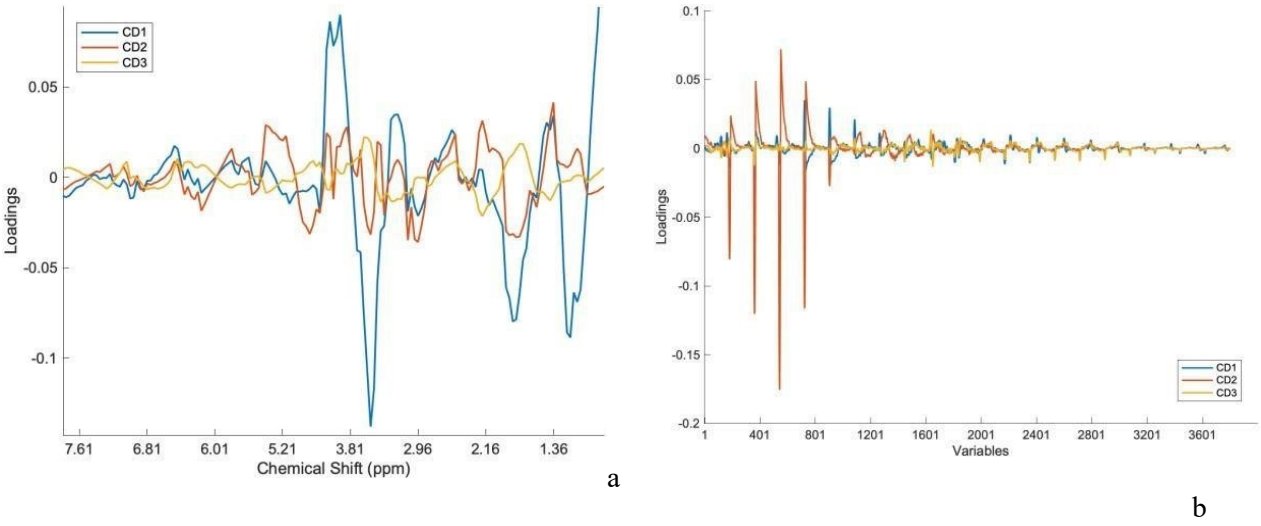

Figure 63. ComDim loadings for the ^{1}H NMR (left panel) and EEM block (right panel) for each Common Dimension calculated for the olive leaves dataset. The EEM loadings are reported as a function of the folded original variables, i.e. excitation x emission wavelengths.

A 3-CD model is computed from the ComDim analysis, accounting for 97.9% of the total variance. The analysis of the saliences evidences that the ^{1}H NMR and EEM blocks provide the major contribution to CD1 and CD2, respectively, while in CD3, the two blocks are almost equivalent. The implementation of the ComDim algorithm on the merged leaves datasets leads to a clear differentiation of the samples in three distinct clusters, as evidenced in **Figure 61**. The samples from the Chianti–Siena area are well separated from those belonging to Grosseto-Val d'Orcia: the data fusion approach brings about a significant improvement if compared to the individual techniques, in which PCA shows a partial differentiation with a consistent overlap among the different subregions. Nevertheless, despite the improved clustering, a complete separation between Grosseto and Val d'Orcia cannot be achieved.

A detailed investigation of the loadings (**Figure 63**) allows for the identification of the metabolites that are responsible for the geographical origin differentiation. Oleuropein signals at 1.64 and 3.71 ppm, followed by mannitol (3.81 ppm), and oleanolic and maslinic acids (0.90–0.97 ppm) provide the most relevant contributions to the ^{1}H NMR block. For the EEM data, the primary contributions arise from phenolic compounds (excitation at 250–280 nm and emission < 370 nm), with a secondary contribution from chlorogenic acid (exc./em. 320/435 nm).

A similar mid-level data fusion approach was followed for the investigation of the olive drupe samples. The score plot of the first 3 CDs is reported in **Figure 64**, while the 2D score plots along with the calculated saliences and loadings are shown in **Figure 65** and **66**.

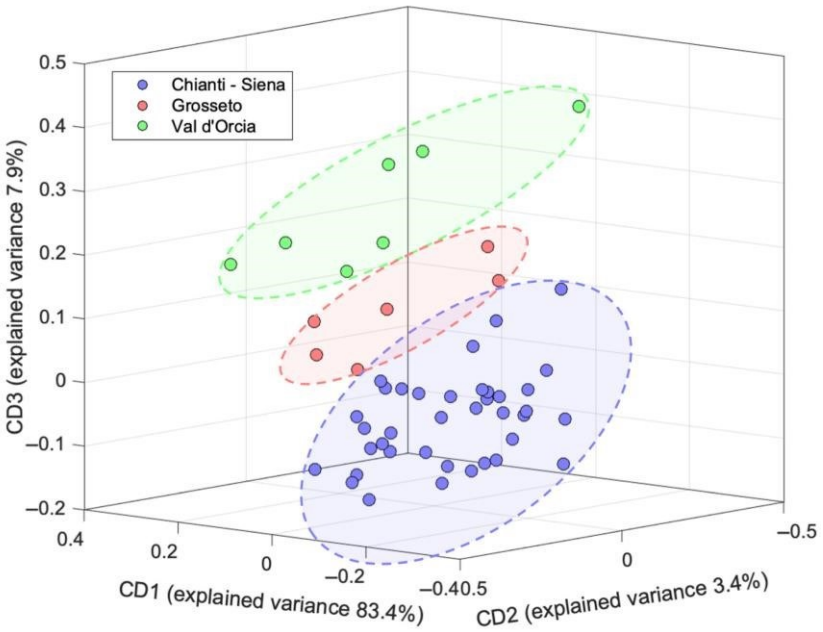

Figure 64. Three-dimensional ComDim score plot for the merged dataset of the olive drupe samples.

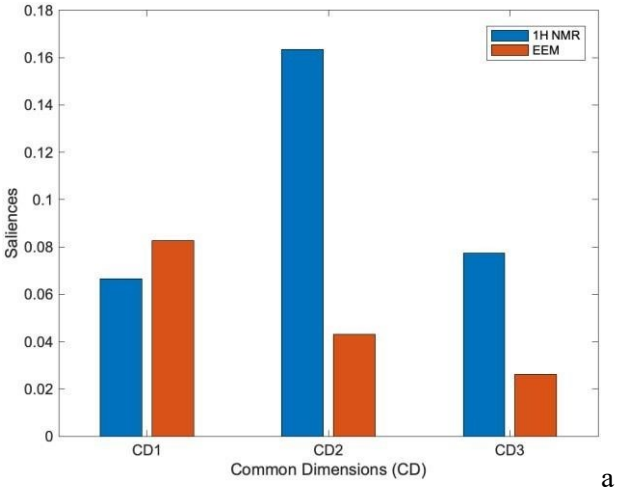
1H NMR
EEM
Saliences
0.18
0.16
0.14
0.12
0.1
0.08
0.06
0.04
0.02
0
CD1
CD2
CD3
Common Dimensions (CD)

a

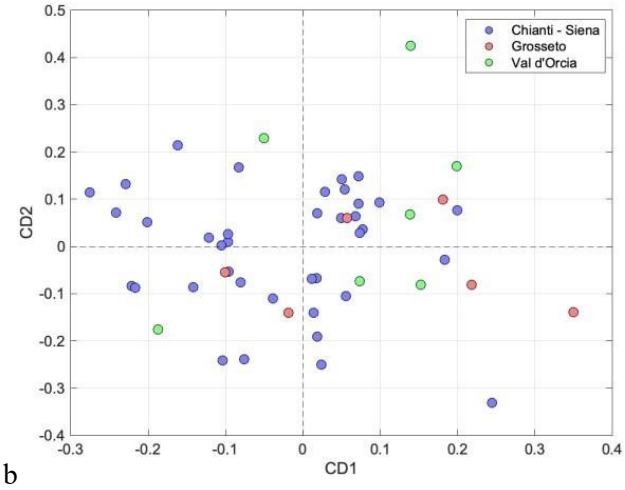
Chianti - Siena
Grosseto
Val d'Orcia
CD2
CD1
0.5
0.4
0.3
0.2
0.1
0
-0.1
-0.2
-0.3
-0.4
-0.3
-0.2
-0.1
0
0.1
0.2
0.3
0.4

b

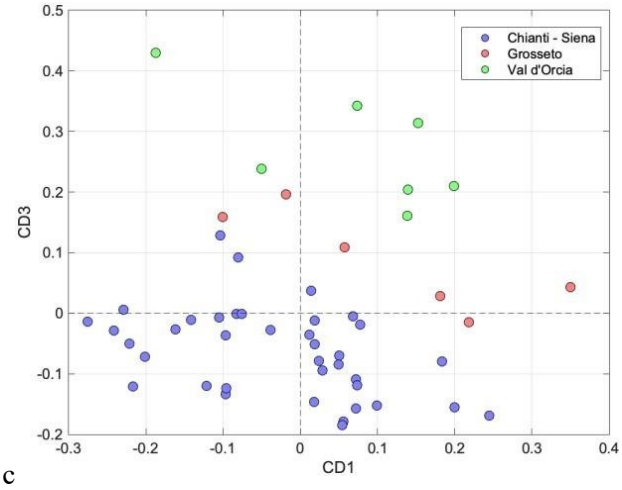
Chianti - Siena
Grosseto
Val d'Orcia
CD3
CD1
0.5
0.4
0.3
0.2
0.1
0
-0.1
-0.2
-0.3
-0.2
-0.1
0
0.1
0.2
0.3
0.4

c

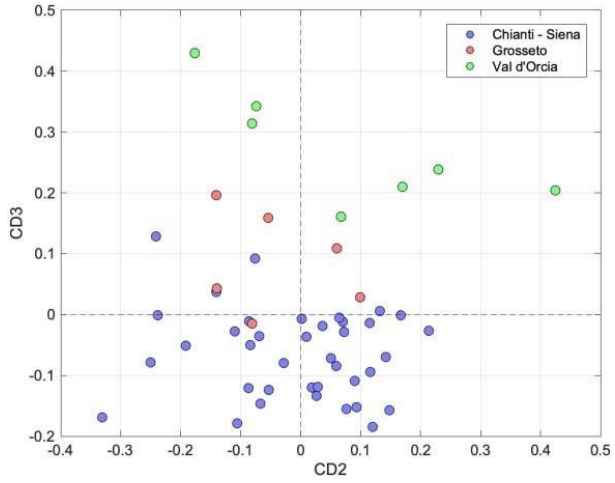

d

Figure 65. ComDim salience plot for the drupes samples (a) and 2D ComDim score plots: CD1 vs CD2 (b), CD1 vs CD3 (c) and CD2 vs CD3 (d).

a

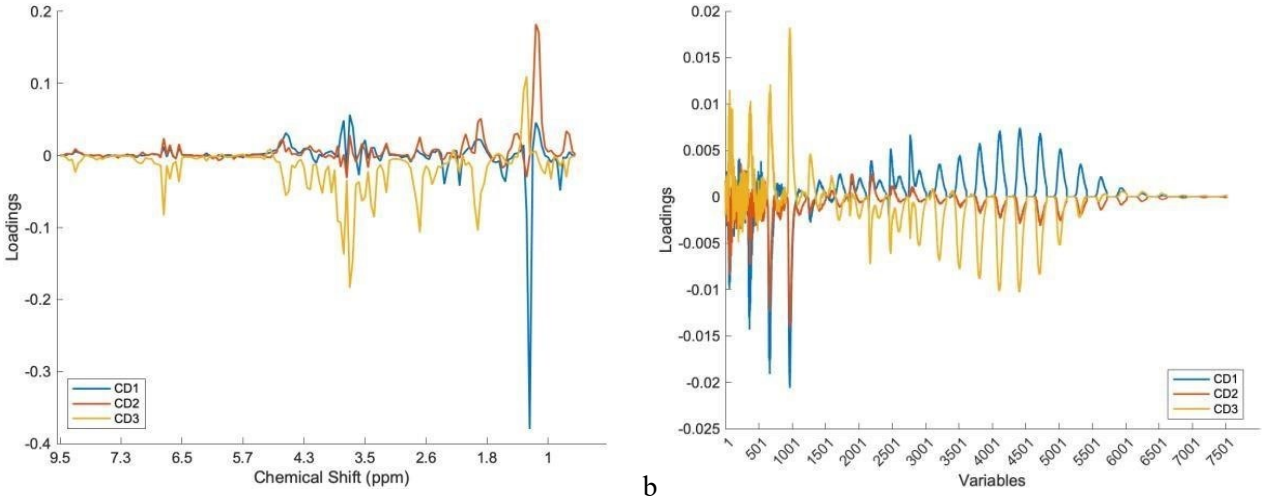

b

Figure 66. ComDim loadings for the ^{1}H NMR (left panel) and EEM block (right panel) for each Common Dimension calculated for the olive drupes dataset. The EEM loadings are reported as a function of the folded original variables, i.e. excitation x emission wavelengths.

A 3-CD model was computed, accounting for 94.7% of the total variance. The analysis of the saliences (**Figure 65**) highlights an almost equal contribution of the two analytical techniques to CD1, while the ^{1}H NMR block becomes predominant in CD2 and CD3. The 3D score plot (**Figure 64**) reveals a significantly improved geographical differentiation compared to the results obtained from the single-block PCA approach. While the unsupervised analysis of the ^{1}H NMR and EEM data

showed limited or no clear clustering according to geographical origin, the ComDim model highlights a distinct grouping of the samples from Chianti–Siena, Grosseto, and Val d'Orcia.

The investigation of the loadings plots (**Figure 66**) evidences that the most relevant contributions in terms of ^{1}H NMR signals to the different CDs are provided by the resonances located at 3.67–3.80, 2.72, 1.96, 1.32, and 1.13 ppm, corresponding to mannitol, oleuropein, quinic, lactic, maslinic and oleanolic acids, respectively. For the EEM block, the refolding of the loadings reveals that the most relevant excitation–emission wavelength couples are centered around 340/440 nm, corresponding to the fluorescence profile of tocopherols, while a secondary contribution is given by excitation–emission signals at 230/310 nm, related to phenolic compounds.

Building on the exploratory insights provided by the ComDim score plots, a class-modeling strategy was implemented to assess the ability of the combined spectroscopic information to discriminate the samples from the Chianti–Siena subregion. In particular, a one-class classification model was developed by integrating the ComDim multiblock outputs into a SIMCA-like framework. The model performance metrics are listed in **Table 28**, while the distance plots for leaves and drupes are reported in **Figure 67**.

Table 28. Classification performances obtained with the combined ComDim-based SIMCA approach for the ^{1}H NMR and the EEM fluorescence data of the olive leaf and drupe extracts for the Chianti–Siena area.

ComDim-Based SIMCA Multiblock Model for Chianti–Siena Region

	Training			**Test**			
	Accuracy (%)	**Sensitivity (%)**	**Specificity (%)**	**Accuracy (%)**	**Sensitivity (%)**	**Specificity (%)**	**Explained Variance (%)**
Leaves	84	83	86	83	100	50	95
Drupes	86	90	73	90	100	50	93

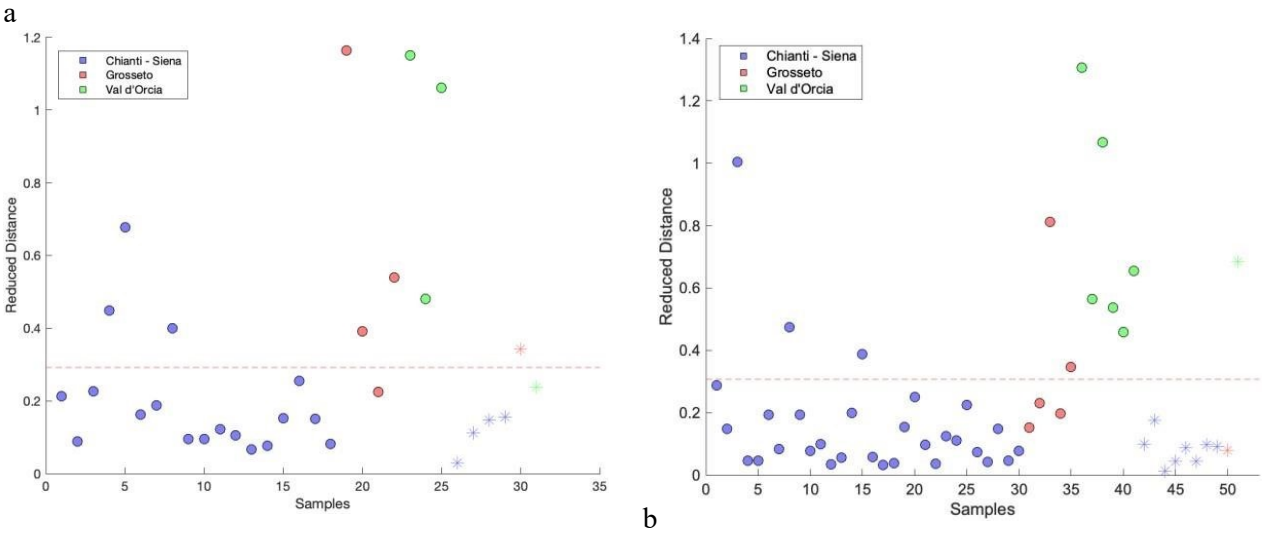

Figure 67. Reduced distances calculated from the ComDim-based SIMCA multiblock model for the leaves (a) and drupes (b) drupes samples for the Chianti – Siena region.

As the analysis of leaves is concerned, the data-fusion approach did not apport a significant improvement to separate SIMCA models, which already showed good performances, especially the one built on ^{1}H NMR data. On the other hand, in the analysis of the geographical origin of drupes, the data-fusion approach allowed for boosting the performance of the models obtainable from the single datasets.

In fact, in terms of accuracy, the multiblock classifier method leads to a significant improvement if compared to EEM-SIMCA, while the performances are similar with respect to the individual ^{1}H NMR model. In the test set, the data fusion approach outperforms both the individual models in the training set, achieving the highest overall value of 90%. Sensitivity significantly benefits from data fusion, showing a remarkable increase, particularly in the test set. However, specificity remains modest: this outcome reflects both the intrinsic complexity of the drupe matrix and the challenge of discriminating closely related geographical areas, where similar compositional profiles can limit class separation despite the advantages of multiblock integration.

These results confirm that the integration of ^{1}H NMR and fluorescence data can lead to a more robust classification model and improved classification performance compared to single-block approaches, albeit with some limitations. This enhancement is not general but rather matrix dependent, with clearer benefits observed in the case of olive drupes.

1.4 Conclusions

This study highlights the potential of ^{1}H NMR and EEM fluorescence spectroscopy in combination with single- and multi-block chemometric methods for the geographical authentication of olive leaves and drupes. Individually, each technique provided robust classification results, with ^{1}H NMR demonstrating its strength in identifying key metabolites that provide the major contribution to geographic origin differentiation, such as secoiridoids and organic acids. This is particularly evident in the case of olive leaves, where the SIMCA modeling provides excellent classification performances for the investigated geographical area. Similarly, through EEM fluorescence spectroscopy, the fluorescence profiles of the different matrices can be effectively characterized by identifying classes of emitting compounds like tocopherols, polyphenols, and chlorogenic acid, which can be used as distinct markers for sample classification.

A key novelty of this work is the application of EEM fluorescence spectroscopy for the geographical origin authentication of olive drupes and leaves, an approach that, to the best of our knowledge, has not been previously reported. The three-dimensional spectral data can be refolded and effectively used as inputs for chemometric models to discriminate between subregional areas, providing a powerful alternative for food and vegetable matrices authentication. This novel application of a relatively simple and low-cost technique, such as EEM fluorescence (especially, if compared to NMR), expands the analytical possibilities for olive product classification, offering a complementary tool alongside NMR-based metabolic profiling.

This is particularly evident, also looking at the most relevant result of the present study, i.e., the integration of these techniques through data fusion further enhanced the sample differentiation by leveraging the complementary strengths of each method. Multivariate statistical analysis based on multi-technique datasets is still relatively unexploited in the field of geographical assessment of fruit and plant matrices related to agrifood products. Here, the data fusion approach, which was based on the ComDim algorithm, allowed for an enhanced sample visualization at an exploratory level, and improved the robustness of classification models when combined with SIMCA into a multiblock one-class modeling strategy, especially for the drupe samples. In this case, in fact, the SIMCA model computed on individual datasets presented some limitations, which were significantly overcome with the inclusion of both spectroscopic data, using the aforementioned multi-block approach. This result emphasizes the importance of evaluating data fusion not as a universal improvement, but as a matrix- and context-dependent strategy with the potential to enhance model robustness when single-block approaches fall short.

Overall, this comprehensive approach underscores the value of combining advanced spectroscopic techniques with chemometric tools for food authentication.

Nonetheless, it should be acknowledged that the present study is based on an exploratory sampling design involving three subregions within Tuscany, Italy. While this provides a solid and controlled framework for assessing classification performance at the subregional level, the scope is primarily focused on feasibility rather than broad generalizability. The classification models developed herein have demonstrated their effectiveness within this localized context; however, their extension to wider geographical areas or different countries will require further validation. This is particularly relevant given that the chemical profiles of olive matrices are known to be influenced by several environmental and agronomic factors, including harvest time, climate conditions, soil characteristics, and cultivation practices.

Future studies will aim to extend the analysis to the final products, i.e., olive oils, and further refine these methodologies to address current limitations and strengthen the models' predictive ability.

Bibliography

Chapter 1

1. Izci M, Maksoudian C, Manshian BB, Soenen SJ. The Use of Alternative Strategies for Enhanced Nanoparticle Delivery to Solid Tumors. Chem Rev. 2021 Feb 10;121(3):1746-1803. doi: 10.1021/acs.chemrev.0c00779. Epub 2021 Jan 14. PMID: 33445874; PMCID: PMC7883342.
2. Adepu S, Ramakrishna S. Controlled Drug Delivery Systems: Current Status and Future Directions. Molecules. 2021 Sep 29;26(19):5905. doi: 10.3390/molecules26195905. PMID: 34641447; PMCID: PMC8512302.
3. Theresa M. Allen, Pieter R. Cullis ,Drug Delivery Systems: Entering the Mainstream.Science303,1818-1822(2004).DOI:10.1126/science.1095833
4. Mouritsen OG. Lipids, curvature, and nano-medicine. Eur J Lipid Sci Technol. 2011 Oct;113(10):1174-1187. doi: 10.1002/ejlt.201100050. PMID: 22164124; PMCID: PMC3229985.
5. Kobierski J, Wnętrzak A, Chachaj-Brekiesz A, Dynarowicz-Latka P. Predicting the packing parameter for lipids in monolayers with the use of molecular dynamics. Colloids Surf B Biointerfaces. 2022 Mar;211:112298. doi: 10.1016/j.colsurfb.2021.112298. Epub 2021 Dec 22. PMID: 34954518.
6. Insights of Lipid-Based Drug Delivery Systems with an Emphasis on Quality by Design Venkatesh Battula1 , Haranath Chinthaginjala1* , Mousami Bhavasar Telkar1 , Udit Narayan Singh1 , Nagashubha Bobbarjang2 and Bhargav Eranti2
7. Godase SS, Kulkarni NS, Dhole SN. A Comprehensive Review on Novel Lipid-Based Nano Drug Delivery. Adv Pharm Bull. 2024 Mar;14(1):34-47. doi: 10.34172/apb.2024.012. Epub 2023 Oct 14. PMID: 38585464; PMCID: PMC10997939.
8. Maja, L., Željko, K., & Mateja, P. Sustainable technologies for liposome preparation. *The Journal of Supercritical Fluids*, *165*, 104984 (2020).
9. Harashima, Hideyoshi, et al. "Enhanced hepatic uptake of liposomes through complement activation depending on the size of liposomes." *Pharmaceutical research* 11.3 (1994): 402-406.
10. Large, D. E., Abdelmessih, R. G., Fink, E. A., & Auguste, D. T. Liposome composition in drug delivery design, synthesis, characterization, and clinical application. *Advanced drug delivery reviews*, *176*, 113851 (2021).
11. Bozzuto, G., & Molinari, A. Liposomes as nanomedical devices. *International journal of nanomedicine*, 975-999 (2015).
12. Patil, Yogita P., and Sameer Jadhav. "Novel methods for liposome preparation." *Chemistry and physics of lipids* 177 (2014): 8-18.

13. Tapeinos, Christos, Matteo Battaglini, and Gianni Ciofani. "Advances in the design of solid lipid nanoparticles and nanostructured lipid carriers for targeting brain diseases." *Journal of controlled release* 264 (2017): 306-332.
14. Dolatabadi, Jafar Ezzati Nazhad, and Yadollah Omidi. "Solid lipid-based nanocarriers as efficient targeted drug and gene delivery systems." *TrAC Trends in Analytical Chemistry* 77 (2016): 100-108.
15. Naseri, Neda, Hadi Valizadeh, and Parvin Zakeri-Milani. "Solid lipid nanoparticles and nanostructured lipid carriers: structure, preparation and application." *Advanced pharmaceutical bulletin* 5.3 (2015): 305.
16. Tamjidi, Fardin, et al. "Nanostructured lipid carriers (NLC): A potential delivery system for bioactive food molecules." *Innovative Food Science & Emerging Technologies* 19 (2013): 29-43.
17. Editorial. "Let's talk about lipid nanoparticles." *Nat. Rev. Mater.* 6.99 (2021).
18. Mehraji, Sima, and Don L. DeVoe. "Microfluidic synthesis of lipid-based nanoparticles for drug delivery: recent advances and opportunities." *Lab on a Chip* 24.5 (2024): 1154-1174.
19. Joshi, Sameer, et al. "Microfluidics based manufacture of liposomes simultaneously entrapping hydrophilic and lipophilic drugs." *International journal of pharmaceutics* 514.1 (2016): 160-168.
20. Bhattacharjee, Sourav. "DLS and zeta potential–what they are and what they are not?." *Journal of controlled release* 235 (2016): 337-351.
21. Austin, J., Minelli, C., Hamilton, D. *et al.* Nanoparticle number concentration measurements by multi-angle dynamic light scattering. *J Nanopart Res* **22**, 108 (2020).
22. Bahari, L.A.; Hamishehkar, H. The impact of variables on particle size of solid lipid nanoparticles and nanostructured lipid carriers; a comparative literature review. *Adv. Pharm. Bull.* **2016**, *6*, 143.
23. Bera, Binoy. "Nanoporous silicon prepared by vapour phase strain etch and sacrificial technique." *Int. J. Comput. Appl* 975 (2015): 8887.
24. Rane, Sagar S., and Phillip Choi. "Polydispersity index: how accurately does it measure the breadth of the molecular weight distribution?." *Chemistry of materials* 17.4 (2005): 926-926.
25. Doyen, Camille, et al. "Nuclear magnetic resonance spectroscopy: a multifaceted toolbox to probe structure, dynamics, interactions, and real-time in situ release kinetics in peptide-liposome formulations." Molecular Pharmaceutics 18.7 (2021): 2521-2539.
26. Shahraeini SS, Akbari J, Saeedi M, Morteza-Semnani K, Abootorabi S, Dehghanpoor M, Rostamkalaei SS, Nokhodchi A. Atorvastatin Solid Lipid Nanoparticles as a Promising Approach for Dermal Delivery and an Anti-inflammatory Agent. AAPS PharmSciTech. 2020 Sep 25;21(7):263. doi: 10.1208/s12249-020-01807-9. PMID: 32978691; PMCID: PMC7519004.
27. Chountoulesi, M., Naziris, N., Pippa, N., Pispas, S., Demetzos, C. (2019). Differential Scanning Calorimetry (DSC): An Invaluable Tool for the Thermal Evaluation of Advanced Chimeric Liposomal Drug Delivery Nanosystems. In: Demetzos, C., Pippa, N. (eds) Thermodynamics and Biophysics of Biomedical Nanosystems. Series in BioEngineering. Springer, Singapore.
28. Ong, S.G.M.; Ming, L.C.; Lee, K.S.; Yuen, K.H. Influence of the Encapsulation Efficiency and Size of Liposome on the Oral Bioavailability of Griseofulvin-Loaded Liposomes. *Pharmaceutics* **2016**, *8*, 25.

29. Ana, R.d.; Fonseca, J.; Karczewski, J.; Silva, A.M.; Zielińska, A.; Souto, E.B. Lipid-Based Nanoparticulate Systems for the Ocular Delivery of Bioactives with Anti-Inflammatory Properties. *Int. J. Mol. Sci.* **2022**, *23*, 12102.
30. Wang, Rui, et al. "A review of nanocarrier-mediated drug delivery systems for posterior segment eye disease: Challenges analysis and recent advances." *Journal of drug targeting* 29.7 (2021): 687-702.
31. Gaballa SA, Kompella UB, Elgarhy O, Alqahtani AM, Pierscionek B, Alany RG, Abdelkader H. Corticosteroids in ophthalmology: drug delivery innovations, pharmacology, clinical applications, and future perspectives. Drug Deliv Transl Res. 2021 Jun;11(3):866-893
32. Popper, Thomas L., et al. "Structure-activity relationships of a series of novel topical corticosteroids." *Journal of steroid biochemistry* 27.4-6 (1987): 837-843.
33. Farhood, Hassan, Natalya Serbina, and Leaf Huang. "The role of dioleoyl phosphatidylethanolamine in cationic liposome mediated gene transfer." *Biochimica et Biophysica Acta (BBA)Biomembranes* 1235.2 (1995): 289-295.
34. de la Torre, Lucimara Gaziola, et al. "The synergy between structural stability and DNA-binding controls the antibody production in EPC/DOTAP/DOPE liposomes and DOTAP/DOPE lipoplexes." *Colloids and Surfaces B: Biointerfaces* 73.2 (2009): 175-184.
35. Gasperini, Antonio AM, et al. "Association between cationic liposomes and low molecular weight hyaluronic acid." *Langmuir 31.11 (2015): 3308-3317.*
36. Smith, M. C., Crist, R. M., Clogston, J. D., & McNeil, S. E. Zeta potential: a case study of cationic, anionic, and neutral liposomes. *Analytical and bioanalytical chemistry*, *409*, 5779-5787 (2017).
37. Clogston, J. D., & Patri, A. K. Zeta potential measurement. *Characterization of nanoparticles intended for drug delivery*, 63-70 (2011).
38. Michael Kaszuba, David McKnight, Malcolm T. Connah, Fraser K. McNeil-Watson, Ulf Nobbmann. Measuring sub nanometre sizes using dynamic light scattering. *Journal of Nanoparticle Research,* Volume 10, 823–829, (2008).
39. Large, D. E., Abdelmessih, R. G., Fink, E. A., & Auguste, D. T. Liposome composition in drug delivery design, synthesis, characterization, and clinical application. *Advanced drug delivery reviews*, *176*, 113851 (2021).
40. Miro, Agnese, et al. "Triamcinolone solubilization by (2-hydroxypropyl)-β-cyclodextrin: A spectroscopic and computational approach." *Carbohydrate polymers* 90.3 (2012): 1288-1298.
41. Lívia Budai, Marianna Budai, Zsófia Edit, Fülöpné Pápay, Zsófia Vilimi, István Antal. Rheological Considerations of Pharmaceutical Formulations: Focus on Viscoelasticity. *Gels*, (2023), 9, 469.
42. Naila El Kechai, Amélie Bochot, Nicolas Huang, Yann Nguyen, Evelyne Ferrary, Florence Agnely. Effect of liposomes on rheological and syringeability properties of hyaluronic acid hydrogels intended for local injection of drugs. *International Journal of Pharmaceutics*, 487 (2015) 187–196.
43. Ana Simões, Margarida Miranda, Catarina Cardoso, Francisco Veiga, Carla Vitorino. Rheology by Design: A Regulatory Tutorial for Analytical Method Validation. *Pharmaceutics,* (2020), 12, 820.

44. Tianyu Wu, Jun Xu, Haimu Ye. Review on Crystallization Strategies for Polymer Single Crystals. *Crystals*, (2024), 14, 207.
45. Peng Liu, Guiliang Chen, Jingchen Zhang. A Review of Liposomes as a Drug Delivery System: Current Status of Approved Products, Regulatory Environments, and Future Perspectives. *Molecules*, (2022), 27, 1372.
46. Luiz, Marcela Tavares, et al. "Design of experiments (DoE) to develop and to optimize nanoparticles as drug delivery systems." *European Journal of Pharmaceutics and Biopharmaceutics* 165 (2021): 127-148.
47. Gonzalez-Fernandez, Felipe M., et al. "Lipid-based nanocarriers for ophthalmic administration: towards experimental design implementation." *Pharmaceutics* 13.4 (2021): 447.
48. Cowman, Mary K. "Hyaluronan and hyaluronan fragments." *Advances in carbohydrate chemistry and biochemistry* 74 (2017): 1-59.
49. Leone, Gemma, et al. "Modified low molecular weight poly-vinyl alcohol as viscosity enhancer." *Materials Today Communications* 21 (2019): 100634.
50. Di Prima, Giulia et al. "Nanoparticelle autoassemblanti mucoadesive a base di inulina peghilata: potenziamento della permeazione transcorneale in vitro ed ex vivo dei corticosteroidi". *Journal of Drug Delivery Science and Technology* 49 (2019): 195-208.
51. Pourfarzad A, Habibi Najafi MB, Haddad Khodaparast MH, Khayyat MH. Serish inulin and wheat biopolymers interactions in model systems as a basis for understanding the impact of inulin on bread properties: a FTIR investigation. J Food Sci Technol. 2015 Dec;52(12):7964-73. doi: 10.1007/s13197-015-1939-4. Epub 2015 Jul 22. PMID: 26604368; PMCID: PMC4648905.
52. Maria Natalia Calienni, Luis Manuel Martínez, Maria Cecilia Izquierdo, Silvia del Valle Alonso and Jorge Montanari. “Rheological and Viscoelastic Analysis of Hybrid Formulations for Topical Application.” *Pharmaceutics* 15 (2023): 2392.
53. Alan Gurt and Michael Khonsari. “A Review of the Rheological Consistency of Materials.” *Lubricants* 12 (2024): 236.
54. London, Nikolas JS, Allen Chiang, and Julia A. Haller. "The dexamethasone drug delivery system: indications and evidence." *Advances in therapy* 28.5 (2011): 351-366.
55. Sultana S, Yusuf M, Sharma V. Nanovesicular Drug Delivery Systems for Rare Ocular Diseases: Advances, Challenges, and Future Directions. AAPS PharmSciTech. 2025 Jul 23;26(7):197. doi: 10.1208/s12249-025-03159-8. PMID: 40702295.
56. Gokce EH, Sandri G, Bonferoni MC, Rossi S, Ferrari F, Güneri T, Caramella C. Cyclosporine A loaded SLNs: evaluation of cellular uptake and corneal cytotoxicity. Int J Pharm. 2008 Nov 19;364(1):76-86. doi: 10.1016/j.ijpharm.2008.07.028. Epub 2008 Aug 3. PMID: 18725276.[56]

57. Faghihzadeh, F., Anaya, N. M., Schifman, L. A., & Oyanedel-Craver, V. (2016). Fourier transform infrared spectroscopy to assess molecular-level changes in microorganisms exposed to nanoparticles. *Nanotechnology for Environmental Engineering*, *1*, 1-16.

58. Sadžak, A.; Mravljak, J.; Maltar-Strmečki, N.; Arsov, Z.; Baranović, G.; Erceg, I.; Kriechbaum, M.; Strasser, V.; Přibyl, J.; Šegota, S. The Structural Integrity of the Model Lipid Membrane during Induced Lipid Peroxidation: The Role of Flavonols in the Inhibition of Lipid Peroxidation. *Antioxidants* **2020**, *9*, 430.

59. Tamburrino, L.; Traini, G.; Marcellini, A.; Vignozzi, L.; Baldi, E.; Marchiani, S. Cryopreservation of Human Spermatozoa: Functional, Molecular and Clinical Aspects. *Int. J. Mol. Sci.* **2023**, *24*, 4656.

60. Saadeldin IM, Khalil WA, Alharbi MG, Lee SH. The Current Trends in Using Nanoparticles, Liposomes, and Exosomes for Semen Cryopreservation. Animals (Basel). 10(12):2281; (2020 Dec 3).

61. Meng, S.; Cao, J.; Feng, Q.; Peng, J.; Hu, Y. Roles of chlorogenic acid on regulating glucose and lipids metabolism: A review. Evid. Based Complement. Alternat Med. 2013, 2013, 801457.

62. Naveed, M.; Hejazi, V.; Abbas, M.; Kamboh, A.A.; Khan, G.J.; Shumzaid, M.; Ahmad, F.; Babazadeh, D.; FangFang, X.; Modarresi-Ghazani, F.; et al. Chlorogenic acid (CGA): A pharmacological review and call for further research. Biomed. Pharmacother. 2018, 97,67–74.

63. Large, D. E., Abdelmessih, R. G., Fink, E. A., & Auguste, D. T. Liposome composition in drug delivery design, synthesis, characterization, and clinical application. Advanced drug delivery reviews, 176, 113851 (2021).

64. Collodel, G.; Moretti, E.; Noto, D.; Corsaro, R.; Signorini, C.; Bonechi, C.; Cangeloni, L.; Luca, G.; Arato, I.; Mancuso, F. Effects and mechanisms activated by treatment with cationic, anionic and zwitterionic liposomes on an in vitro model of porcine pre-pubertal Sertoli cells. *Int. J. Mol. Sci.* **2023**, *24*, 1201.

65. Bonechi, C.; Donati, A.; Tamasi, G.; Leone, G.; Consumi, M.; Rossi, C.; Lamponi, S.; Magnani, A. Protective effect of quercetin and rutin encapsulated liposomes on induced oxidative stress. *Biophys. Chem.* **2018**, *233*, 55–63.

Chapter 2

1. Kalyabina, Valeriya P., et al.”Pesticides: formulants, distribution pathways and effects on human health-a review.” *Toxicology reports* 8 (2021): 1179-1192.
2. Wei, Jin-Chao, et al.”Trace determination of carbamate pesticides in medicinal plants by a fluorescent technique.” *Food and Chemical Toxicology* 119 (2018): 430-437
3. Thompson, Lesa A., et al.”Organochlorine pesticide contamination of foods in Africa: incidence and public health significance.” *Journal of Veterinary Medical Science* 79.4 (2017):751-764.
4. Borah, Shikha Jyoti, et al.”Science through the Lens of Nature: Recent Advances in Biomimetic Approaches towards Pesticide Degradation.” *SynOpen* 7.01 (2023):33-42.
5. Singh, A., et al.Advances in controlled release pesticides formulations: Prospects to safer integrated pest management and sustainable agriculture. *J Hazard Mater***385**, 121525-121545 (2020).
6. Akalin, G. O. & Pulat, M. Preparation and Characterization of Nanoporous Sodium Carboxymethyl Cellulose Hydrogel Beads. *J Nanomater***2018**, 1-12(2018).
7. Peppas, Nikolaos A., and Atul R. Khare.”Preparation, structure and diffusional behavior of hydrogels in controlled release.” *Advanced drug delivery reviews* 11.1-2(1993): 1-35.
8. Buwalda, Sytze J., et al.”Hydrogel in a historical perspective: From simple networks to smart materials.” *Journal of controlled release* 190 (2014): 254-273.
9. Roorda, Wouter E., et al.”Synthetic hydrogels are drug delivery systems.” *Pharmaceutisch Weekblad* 8.3 (1986): 165-189.
10. Pacifico, D., et al. Susainable use of bioactive compounds from solanum tuberosum and Brassicaceae wastes and by-products for crop protection- a review. *Molecules**26***, 2174-2213 (2021).
11. Boulogne, I., Petit, P., Ozier-Lafontaine, H., Desfontaines, L. & Loranger-Merciris, G. Insecticidal and antifungal chemicals produced by plants: A review. *Environ Chem Lett***10**, 325-347 (2012).
12. Pardini, Alessio, et al. "Kinetics of glucosinolate hydrolysis by myrosinase in Brassicaceae tissues: A high-performance liquid chromatography approach." *Food Chemistry* 355 (2021): 129634.
13. Plaszkó, Tamás, et al. "Effects of glucosinolate-derived isothiocyanates on fungi: A comprehensive review on direct effects, mechanisms, structure-activity relationship data and possible agricultural applications." *Journal of Fungi* 7.7 (2021): 539.
14. Chan, Eng-Seng, et al. "Encapsulation of herbal aqueous extract through absorption with ca-alginate hydrogel beads." *Food and Bioproducts Processing* 88.2-3 (2010): 195-201.
15. Makarova, Anastasiya O., et al. "Ion-induced polysaccharide gelation: Peculiarities of alginate eggbox association with different divalent cations." *Polymers* 15.5 (2023): 1243.
16. Li, Duoduo, Zihao Wei, and Changhu Xue. "Alginate-based delivery systems for food bioactive ingredients: An overview of recent advances and future trends." *Comprehensive Reviews in Food Science and Food Safety* 20.6 (2021): 5345-5369.

17. Clemente, I.; Baglioni, M.; Bonechi, C.; Bisozzi, F.; Rossi, C.; Tamasi, G. Green Hydrogels Loaded with Extracts from Solanaceae for the Controlled Disinfection of Agricultural Soils. *Polymers* **2023**, *15*, 4455.
18. Łabowska, M.B.; Skrodzka, M.; Sicińska, H.; Michalak, I.; Detyna, J. Influence of Cross-Linking Conditions on Drying Kinetics of Alginate Hydrogel. *Gels* **2023**, *9*, 63.
19. Domingues, J.A.L.; Bonelli, N.; Giorgi, R.; Fratini, E.; Gorel, F.; Baglioni, P. Innovative Hydrogels Based on Semi-Interpenetrating p(HEMA)/PVP Networks for the Cleaning of Water-Sensitive Cultural Heritage Artifacts. *Langmuir* **2013**, *29*, 2746–2755.
20. Rochfort, S.J.; Trenerry, V.C.; Imsic, M.; Panozzo, J.; Jones, R. Class Targeted Metabolomics: ESI Ion Trap Screening Methods for Glucosinolates Based on MSn Fragmentation. *Phytochemistry* **2008**, *69*, 1671–1679.
21. Nandasiri, R.; Eskin, N.A.M.; Komatsu, E.; Perreault, H.; Thiyam-Holländer, U. Valorization of Canola By-Products: Concomitance of Flavor-Active Bitter Phenolics Using Pressurized Heat Treatments. *LWT* **2021**, *138*, 110397.
22. Mouterde, L.M.M.; Peru, A.A.M.; Mention, M.M.; Brunissen, F.; Allais, F. Sustainable Straightforward Synthesis and Evaluation of the Antioxidant and Antimicrobial Activity of Sinapine and Analogues. *J. Agric. Food Chem.* **2020**, *68*, 6998–7004.
23. Hanschen, F.S.; Lamy, E.; Schreiner, M.; Rohn, S. Reactivity and Stability of Glucosinolates and Their Breakdown Products in Foods. *Angew. Chem. Int. Ed.* **2014**, *53*, 11430–11450
24. Santos, C.E.B.; Yu, H.C.; Noel, M.G. Identification of Major Glucosinolates in Broccoli (*Brassica Oleracea* Var. Italica) by Liquid Chromatography—Mass Spectrometry (LC-MS) and Determination of Anticancer Properties of Broccoli Extracts. In Proceedings of the DLSU 2013 Research Congress—Commitment to Serve: Lasallian Research fo the Next 100 Years, Manila, Philippines, 7–9 March 2013.
25. Massana Roquero, D.; Othman, A.; Melman, A.; Katz, E. Iron(Iii)-Cross-Linked Alginate Hydrogels: A Critical Review. *Mater. Adv.* **2022**, *3*, 1849–1873
26. Supramaniam, J.; Adnan, R.; Mohd Kaus, N.H.; Bushra, R. Magnetic Nanocellulose Alginate Hydrogel Beads as Potential Drug Delivery System. *Int. J. Biol. Macromol.* **2018**, *118*, 640–648.
27. Higuchi, T. Rate of Release of Medicaments from Ointment Bases Containing Drugs in Suspension. *J. Pharm. Sci.* **1961**, *50*, 874–875.
28. Korsmeyer, R.W.; Gurny, R.; Doelker, E.; Buri, P.; Peppas, N.A. Mechanisms of Solute Release from Porous Hydrophilic Polymers. *Int. J. Pharm.* **1983**, *15*, 25–35.
29. Peppas, N.A.; Sahlin, J.J. A Simple Equation for the Description of Solute Release. III. Coupling of Diffusion and Relaxation. *Int. J. Pharm.* **1989**, *57*, 169–172.
30. Korsmeyer, R.W.; Peppas, N.A. Effect of the Morphology of Hydrophilic Polymeric Matrices on the Diffusion and Release of Water Soluble Drugs. *J. Memb. Sci.* **1981**, *9*, 211–227.
31. Caccavo, D. An Overview on the Mathematical Modeling of Hydrogels' Behavior for Drug Delivery Systems. *Int. J. Pharm.* **2019**, *560*, 175–190.
32. Papadopoulou, V.; Kosmidis, K.; Vlachou, M.; Macheras, P. On the Use of the Weibull Function for the Discernment of Drug Release Mechanisms. *Int. J. Pharm.* **2006**, *309*, 44–50.

33. Baglioni, M.; Clemente, I.; Tamasi, G.; Bisozzi, F.; Costantini, S.; Fattori, G.; Gentile, M.; Rossi, C. Isothiocyanate-Based Microemulsions Loaded into Biocompatible Hydrogels as Innovative Biofumigants for Agricultural Soils. *Molecules* **2024**, *29*, 3935.

Chapter 3

1. Dimitrakopoulou, Maria-Eleni, and Apostolos Vantarakis. "Does traceability lead to food authentication? A systematic review from a European perspective." *Food Reviews International* 39.1 (2023): 537-559.
2. Danezis, G. P.; Tsagkaris, A. S.; Camin, F.; Brusic, V.; Georgiou, C. A. Food Authentication: Techniques, Trends & Emerging Approaches. *TrAC - Trends Anal. Chem.* 2016, *85*, 123–132.
3. Bentivoglio, D.; Savini, S.; Finco, A.; Bucci, G.; Boselli, E. Quality and Origin of Mountain Food Products: The New European Label as a Strategy for Sustainable Development. *Journal of Mountain Science*. 2019, *16*(2), 428–440.
4. Gagour, J.; Hallouch, O.; Asbbane, A.; Bijla, L.; Laknifli, A.; Lee, L.; Zengin, G.; Bouyahya, A.; Sakar, E.H.; Gharby, S. A Review of Recent Progresses on Olive Oil Chemical Profiling, Extraction Technology, Shelf-life, and Quality Control. *Chem. Biodivers.* **2024**, *21*, e202301697]
5. Lazzerini, C.; Domenici, V. Pigments in Extra-Virgin Olive Oils Produced in Tuscany (Italy) in Different Years. *Foods* **2017**, *6*, 25.
6. Blasi, F.; Ianni, F.; Cossignani, L. Phenolic Profiling for Geographical and Varietal Authentication of Extra Virgin Olive Oil. *Trends Food Sci. Technol.* **2024**, *147*, 104444.
7. Lozano-Castellón, J.; López-Yerena, A.; Domínguez-López, I.; Siscart-Serra, A.; Fraga, N.; Sámano, S.; López-Sabater, C.; Lamuela-Raventós, R.M.; Vallverdú-Queralt, A.; Pérez, M. Extra Virgin Olive Oil: A Comprehensive Review of Efforts to Ensure Its Authenticity, Traceability, and Safety. *Compr. Rev. Food Sci. Food Saf.* **2022**, *21*, 2639–2664.
8. Nardin, R.; Tamasi, G.; Baglioni, M.; Fattori, G.; Boldrini, A.; Esposito, R.; Rossi, C. Combining Metal(Loid) and Secondary Metabolite Levels in *Olea europaea* L. Samples for Geographical Identification. *Foods* **2024**, *13*, 4017.
9. Talhaoui, N.; Taamalli, A.; Gómez-Caravaca, A.M.; Fernández-Gutiérrez, A.; Segura-Carretero, A. Phenolic compounds in olive leaves: Analytical determination, biotic and abiotic influence, and health benefits. *Food Res. Int.* **2015**, *77*, 92–108.
10. Nicolì, F.; Negro, C.; Vergine, M.; Aprile, A.; Nutricati, E.; Sabella, E.; Miceli, A.; Luvisi, A.; De Bellis, L. Evaluation of Phytochemical and Antioxidant Properties of 15 Italian *Olea europaea* L. Cultivar Leaves. *Molecules* **2019**, *24*, 1998.
11. Feng, Shiling, et al. "Comparison of phenolic compounds in olive leaves by different drying and storage methods." *Separations* 8.9 (2021): 156.
12. Gucci, R.; Caruso, G.; Gennai, C.; Esposto, S.; Urbani, S.; Servili, M. Fruit Growth, Yield and Oil Quality Changes Induced by Deficit Irrigation at Different Stages of Olive Fruit Development. *Agric. Water Manag.* **2019**, *212*, 88–98.

13. Medina, G.; Sanz, C.; Leon, L.; Perez, A.G.; De la Rosa, R. Phenolic variability in fruit from the 'Arbequina' olive cultivar under Mediterranean and Subtropical climatic conditions. *Grasas Aceites* **2021**, *72*, e438.
14. Yılmaz-Düzyaman, H.; Medina-Alonso, M.G.; Sanz, C.; Pérez, A.G.; de la Rosa, R.; León, L. Influence of Genotype and Environment on Fruit Phenolic Composition of Olive. *Horticulture* **2023**, *9*, 1087.
15. García, J.M.; Hueso, A.; Gómez-del-Campo, M. Deficit irrigation during the oil synthesis period affects olive oil quality in high-density orchards (cv. *Arbequina*). *Agric. Water Manag.* **2020**, *230*, 105858.
16. Mansour-Gueddes, S.; Saidana-Naija, D.; Bchir, A.; Braham, M. Climate change effects on phytochemical compounds and antioxidant activity of *Olea europaea* L. *Not. Bot. Horti Agrobot.* **2020**, *48*, 436–455.
17. Bilgin, M.; Selin, S. Effects of geographical origin and extraction methods on total phenolic yield of olive tree (*Olea europaea*) leaves. *J. Taiwan Inst. Chem. Eng.* **2013**, *44*, 8–12.
18. Zakraoui, M.; Hannachi, H.; Pasković, I.; Vidović, N.; Pasković, M.P.; Palčić, I.; Major, N.; Ban, S.G.; Hamrouni, L. Effect of Geographical Location on the Phenolic and Mineral Composition of Chetoui Olive Leaves. *Foods* **2023**, *12*, 2565.
19. Taamalli, A.; Arráez Román, D.; Gómez Caravaca, A.M.; Zarrouk, M.; Segura Carretero, A. Geographical Characterization of Tunisian Olive Tree Leaves (cv. *Chemlali*) Using HPLC-ESI-TOF and IT/MS Fingerprinting with Hierarchical Cluster Analysis. *J. Anal. Methods Chem.* **2018**, *2018*, 6789704.
20. Giannakopoulou, E.; Mitsopoulos, G.; Hagidimitriou, M.; Papageorgiou, V.; Komaitis, M. Influence of cultivar, harvesting season and geographical origin on phenolic content in leaves of Greek olive cultivars. *Acta Hortic.* **2011**, *924*, 437–444.
21. Brahmi, F.; Mechri, B.; Dhibi, M.; Hammami, M. Variation in antioxidant activity and phenolic content in different organs of two Tunisian cultivars of *Olea europaea* L. *Acta Physiol. Plant.* **2013**, *36*, 169–178.
22. Borghini, F.; Tamasi, G.; Loiselle, S.A.; Baglioni, M.; Ferrari, S.; Bisozzi, F.; Costantini, S.; Tozzi, C.; Riccaboni, A.; Rossi, C. Phenolic Profiles in Olive Leaves from Different Cultivars in Tuscany and Their Use as a Marker of Varietal and Geographical Origin on a Small Scale. *Molecules* **2024**, *29*, 3617.
23. Nardin, R.; Tamasi, G.; Baglioni, M.; Bisozzi, F.; Consumi, M.; Costa, J.; Fattori, G.; Tozzi, C.; Riccaboni, A.; Rossi, C. Determination of Elemental Content in Vineyard Soil, Leaves, and Grapes of Sangiovese Grapes from the Chianti Region Using ICP-MS for Geographical Identification. *ACS Food Sci. Technol.* **2024**, *4*, 2585–2599.
24. Pucci, E.; Palumbo, D.; Puiu, A.; Lai, A.; Fiorani, L.; Zoani, C. Characterization and Discrimination of Italian Olive (*Olea europaea* Sativa) Cultivars by Production Area Using Different Analytical Methods Combined with Chemometric Analysis. *Foods* **2022**, *11*, 1085.
25. Meenu, M.; Cai, Q.; Xu, B. A Critical Review on Analytical Techniques to Detect Adulteration of Extra Virgin Olive Oil. *Trends Food Sci. Technol.* **2019**, *91*, 391–408.
26. Gómez-Caravaca, A.M.; Maggio, R.M.; Cerretani, L. Chemometric Applications to Assess Quality and Critical Parameters of Virgin and Extra-Virgin Olive Oil. A Review. *Anal. Chim. Acta* **2016**, *913*, 1–21

27. Varzakas, T.; Tarapoulouzi, M.; Agriopoulou, S. *Chemometrics and Authenticity of Foods of Plant Origin*, 1st ed.; CRC Press: Boca Raton, FL, USA, 2022; ISBN 978-1-00-326616-7.
28. Cappelli, Alessio, et al. "Applying spectroscopies, imaging analyses, and other non-destructive techniques to olives and extra virgin olive oil: A systematic review of current knowledge and future applications." *Agriculture* 14.7 (2024): 1160.
29. Kalogiouri, N.P.; Aalizadeh, R.; Dasenaki, M.E.; Thomaidis, N.S. Authentication of Greek PDO Kalamata Table Olives: A Novel Non-Target High Resolution Mass Spectrometric Approach. *Molecules* **2020**, *25*, 2919.
30. Tamasi, G.; Baratto, M.C.; Bonechi, C.; Byelyakova, A.; Pardini, A.; Donati, A.; Leone, G.; Consumi, M.; Lamponi, S.; Magnani, A.; et al. Chemical Characterization and Antioxidant Properties of Products and By-Products from *Olea europaea* L. *Food Sci. Nutr.* **2019**, *7*, 2907–2920.
31. Cangeloni, L.; Bonechi, C.; Leone, G.; Consumi, M.; Andreassi, M.; Magnani, A.; Rossi, C.; Tamasi, G. Characterization of Extracts of Coffee Leaves (*Coffea arabica* L.) by Spectroscopic and Chromatographic/Spectrometric Techniques. *Foods* **2022**, *11*, 2495.
32. Girelli, C.R.; Del Coco, L.; Zelasco, S.; Salimonti, A.; Conforti, F.L.; Biagianti, A.; Barbini, D.; Fanizzi, F.P. Traceability of "Tuscan PGI" Extra Virgin Olive Oils by 1H NMR Metabolic Profiles Collection and Analysis. *Metabolites* **2018**, *8*, 60.
33. Beteinakis, Stavros, et al. "NMR-based metabolic profiling of edible olives—Determination of quality parameters." *Molecules* 25.15 (2020): 3339.
34. Dais, P.; Hatzakis, E. Analysis of Bioactive Microconstituents in Olives, Olive Oil and Olive Leaves by NMR Spectroscopy: An Overview of the Last Decade. In *Olive and Olive Oil Bioactive Constituents*; Elsevier: Amsterdam, The Netherlands, 2015; pp. 299–332. ISBN 978-1-63067-041-2.
35. Mannina, L.; Sobolev, A.P. High Resolution NMR Characterization of Olive Oils in Terms of Quality, Authenticity and Geographical Origin. *Magn. Reson. Chem.* **2011**, *49*, S3–S11
36. Beteinakis, S.; Papachristodoulou, A.; Kolb, P.; Rösch, P.; Schwarzinger, S.; Mikros, E.; Halabalaki, M. NMR-Based Metabolite Profiling and the Application of STOCSY toward the Quality and Authentication Assessment of European EVOOs. *Molecules* **2023**, *28*, 1738.
37. Calò, Francesca, et al. "Geographical origin assessment of extra virgin olive oil via NMR and MS combined with chemometrics as analytical approaches." *Foods* 11.1 (2022): 113.
38. Maestrello, V.; Solovyev, P.; Bontempo, L.; Mannina, L.; Camin, F. Nuclear Magnetic Resonance Spectroscopy in Extra Virgin Olive Oil Authentication. *Compr. Rev. Food Sci. Food Saf.* **2022**, *21*, 4056–4075.
39. Dais, P.; Hatzakis, E. Quality Assessment and Authentication of Virgin Olive Oil by NMR Spectroscopy: A Critical Review. *Anal. Chim. Acta* **2013**, *765*, 1–27.
40. Tamasi, G., Bonechi, C., Leone, G., Andreassi, M., Consumi, M., Sangiorgio, P., ... & Magnani, A. (2021). Varietal and geographical origin characterization of peaches and nectarines by combining analytical techniques and statistical approach. *Molecules*, *26*(14), 4128.

41. Sikorska, E.; Khmelinskii, I.; Sikorski, M. Fluorescence Spectroscopy and Imaging Instruments for Food Quality Evaluation. In *Evaluation Technologies for Food Quality*; Elsevier: Amsterdam, The Netherlands, 2019; pp. 491–533. ISBN 978-0-12-814217-2.
42. Ranaweera, R.K.R.; Gilmore, A.M.; Capone, D.L.; Bastian, S.E.P.; Jeffery, D.W. Authentication of the Geographical Origin of Australian Cabernet Sauvignon Wines Using Spectrofluorometric and Multi-Element Analyses with Multivariate Statistical Modelling. *Food Chem.* **2021**, *335*, 127592.
43. Sádecká, J.; Uríčková, V.; Jakubíková, M. Fluorescence Spectroscopy for the Analysis of Spirit Drinks. In *Applications of Molecular Spectroscopy to Current Research in the Chemical and Biological Sciences*; Stauffer, M.T., Ed.; InTech: Rijeka, Croatia, 2016; ISBN 978-953-51-2680-5.
44. Sikorska, E.; Gliszczyńska-Świgło, A.; Khmelinskii, I.; Sikorski, M. Synchronous Fluorescence Spectroscopy of Edible Vegetable Oils. Quantification of Tocopherols. *J. Agric. Food Chem.* **2005**, *53*, 6988–6994.
45. Latchoumane, L.; Alary, K.; Minier, J.; Davrieux, F.; Lugan, R.; Chillet, M.; Roger, J.-M. FrontFace Fluorescence Spectroscopy and Feature Selection for Fruit Classification Based on N-CovSel Method. *Front. Anal. Sci.* **2022**, *2*, 867527.
46. Lenhardt, L.; Zeković, I.; Dramićanin, T.; Milićević, B.; Burojević, J.; Dramićanin, M.D. Characterization of Cereal Flours by Fluorescence Spectroscopy Coupled with PARAFAC. *Food Chem.* **2017**, *229*, 165–171.
47. Kulmyrzaev, A.A.; Levieux, D.; Dufour, É. Front-Face Fluorescence Spectroscopy Allows the Characterization of Mild Heat Treatments Applied to Milk. Relations with the Denaturation of Milk Proteins. *J. Agric. Food Chem.* **2005**, *53*, 502–507.
48. Abbas, K.; Karoui, R.; Aït-Kaddour, A. Application of Synchronous Fluorescence Spectroscopy for the Determination of Some Chemical Parameters in PDO French Blue Cheeses. *Eur. Food Res. Technol.* **2012**, *234*, 457–465.
49. Sikorska, E.; Khmelinskii, I.; Sikorski, M. Analysis of Olive Oils by Fluorescence Spectroscopy: Methods and Applications. In *Olive Oil—Constituents, Quality, Health Properties and Bioconversions*; Boskou, D., Ed.; InTech: Rijeka, Croatia, 2012; ISBN 978-953-307-921-9
50. Murphy, K.R.; Stedmon, C.A.; Graeber, D.; Bro, R. Fluorescence Spectroscopy and Multi-Way Techniques. PARAFAC. *Anal. Methods* **2013**, *5*, 6557.
51. Amigo, J.M.; Marini, F. Multiway Methods. In *Data Handling in Science and Technology*; Elsevier: Amsterdam, The Netherlands, 2013; Volume 28, pp. 265–313. ISBN 978-0-444-59528-7.
52. Morais, C.L.M.; Lima, K.M.G. Comparing Unfolded and Two-Dimensional Discriminant Analysis and Support Vector Machines for Classification of EEM Data. *Chemom. Intell. Lab. Syst.* **2017**, *170*, 1–12.
53. Al Riza, D.F.; Kondo, N.; Rotich, V.K.; Perone, C.; Giametta, F. Cultivar and Geographical Origin Authentication of Italian Extra Virgin Olive Oil Using Front-Face Fluorescence Spectroscopy and Chemometrics. *Food Control* **2021**, *121*, 107604.

54. De Paulo, E.H.; Magalhães, G.B.; Moreira, M.P.B.; Nascimento, M.H.C.; Heringer, O.A.; Filgueiras, P.R.; Ferrão, M.F. Classification of Water by Bacterial Presence Using Chemometrics Associated with Excitation-Emission Matrix Fluorescence Spectroscopy. *Microchem. J.* **2024**, *197*, 109804.
55. Suciu, R.-C.; Zarbo, L.; Guyon, F.; Magdas, D.A. Application of Fluorescence Spectroscopy Using Classical Right Angle Technique in White Wines Classification. *Sci. Rep.* **2019**, *9*, 18250.
56. Katerinopoulou, K.; Kontogeorgos, A.; Salmas, C.E.; Patakas, A.; Ladavos, A. Geographical Origin Authentication of Agri-Food Products: A Review. *Foods* **2020**, *9*, 489.
57. Cozzolino, D. Recent Trends on the Use of Infrared Spectroscopy to Trace and Authenticate Natural and Agricultural Food Products. *Appl. Spectrosc. Rev.* **2012**, *47*, 518–530.
58. Garrido-Cuevas, M.-M.; Garrido-Varo, A.-M.; Marini, F.; Sánchez, M.-T.; Pérez-Marín, D. Enhancing Virgin Olive Oil Authentication with Bayesian Probabilistic Models and near Infrared Spectroscopy. *J. Food Eng.* **2025**, *391*, 112443.
59. Biancolillo, A.; Boqué, R.; Cocchi, M.; Marini, F. Data Fusion Strategies in Food Analysis. In *Data Handling in Science and Technology*; Elsevier: Amsterdam, The Netherlands, 2019; Volume 31, pp. 271–310. ISBN 978-0-444-63984-4.
60. El Ghaziri, A.; Cariou, V.; Rutledge, D.N.; Qannari, E.M. Analysis of Multiblock Datasets Using ComDim: Overview and Extension to the Analysis of (K + 1) Datasets. *J. Chemom.* **2016**, *30*, 420– 429.
61. Rosa, L.N.; De Figueiredo, L.C.; Bonafé, E.G.; Coqueiro, A.; Visentainer, J.V.; Março, P.H.; Rutledge, D.N.; Valderrama, P. Multi-Block Data Analysis Using ComDim for the Evaluation of Complex Samples: Characterization of Edible Oils. *Anal. Chim. Acta* **2017**, *961*, 42–48].
62. Martin-Tornero, Elisabet, et al. "Geographical discrimination of grapevine leaves using fibre optic fluorescence data and chemometrics. Determination of total polyphenols and chlorophylls along different vegetative stages." *Microchemical Journal* 181 (2022): 107647.

.

63. Andersson, C.A.; Bro, R. The N-Way Toolbox for MATLAB. *Chemom. Intell. Lab. Syst.* **2000**, *52*, 1–4.
64. Jacob, D.; Deborde, C.; Lefebvre, M.; Maucourt, M.; Moing, A. NMRProcFlow: A Graphical and Interactive Tool Dedicated to 1D Spectra Processing for NMR-Based Metabolomics. *Metabolomics* **2017**, *13*, 36.
65. Wold, S. Pattern Recognition by Means of Disjoint Principal Components Models. *Pattern Recognit.* **1976**, *8*, 127–139.
66. Wold, S.; Sjöström, M. SIMCA: A Method for Analyzing Chemical Data in Terms of Similarity and Analogy. In *Chemometrics: Theory and Application*; ACS Symposium Series; American Chemical Society: Washington, DC, USA, 1977; Volume 52, pp. 243–282. ISBN 978-0-8412-0379-2
67. Tahir, H.E.; Arslan, M.; Komla Mahunu, G.; Adam Mariod, A.; Hashim, S.B.H.; Xiaobo, Z.; Jiyong, S.; El-Seedi, H.R.; Musa, T.H. The Use of Analytical Techniques Coupled with Chemometrics for Tracing the Geographical Origin of Oils: A Systematic Review (2013–2020). *Food Chem.* **2022**, *366*, 130633.
68. Marini, F.; Bucci, R.; Magrì, A.L.; Magrì, A.D. An Overview of the Chemometric Methods for the Authentication of the Geographical and Varietal Origin of Olive Oils. In *Olives and Olive Oil in Health*

and Disease Prevention; Elsevier: Amsterdam, The Netherlands, 2010; pp. 569–579. ISBN 978-0-12-374420-3.

69. Masetti, O.; Sorbo, A.; Nisini, L. NMR Tracing of Food Geographical Origin: The Impact of Seasonality, Cultivar and Production Year on Data Analysis. *Separations* **2021**, *8*, 230.
70. Marini, F.; Biancolillo, A. Application of Spectroscopy in Food Analysis: Volume II. *Appl. Sci.* **2023**, *13*, 5633.
71. Zaldarriaga Heredia, J.; Wagner, M.; Jofré, F.C.; Savio, M.; Azcarate, S.M.; Camiña, J.M. An Overview on Multi-Elemental Profile Integrated with Chemometrics for Food Quality Assessment: Toward New Challenges. *Crit. Rev. Food Sci. Nutr.* **2023**, *63*, 8173–8193.
72. De Angelis, D.; Summo, C.; Pasqualone, A.; Faccia, M.; Squeo, G. Advancements in Food Authentication Using Soft Independent Modelling of Class Analogy (SIMCA): A Review. *Food Qual. Saf.* **2024**, *8*, fyae032.
73. Biancolillo, A.; Marini, F.; Ruckebusch, C.; Vitale, R. Chemometric Strategies for SpectroscopyBased Food Authentication. *Appl. Sci.* **2020**, *10*, 6544.
74. Rodionova, O.Y.; Pomerantsev, A.L. Chemometric Tools for Food Fraud Detection: The Role of Target Class in Non-Targeted Analysis. *Food Chem.* **2020**, *317*, 126448.
75. Vitale, R.; Cocchi, M.; Biancolillo, A.; Ruckebusch, C.; Marini, F. Class Modelling by Soft Independent Modelling of Class Analogy: Why, When, How? A Tutorial. *Anal. Chim. Acta* **2023**, *1270*, 341304.
76. Vitale, R.; Marini, F.; Ruckebusch, C. SIMCA Modeling for Overlapping Classes: Fixed or Optimized Decision Threshold? *Anal. Chem.* **2018**, *90*, 10738–10747.
77. Li Vigni, M.; Durante, C.; Michelini, S.; Nocetti, M.; Cocchi, M. Preliminary Assessment of Parmigiano Reggiano Authenticity by Handheld Raman Spectroscopy. *Foods* **2020**, *9*, 1563.
78. Snee, R.D. Validation of Regression Models: Methods and Examples. *Technometrics* **1977**, *19*, 415– 428.
79. Bro, R. PARAFAC. Tutorial and Applications. *Chemom. Intell. Lab. Syst.* **1997**, *38*, 149–171.
80. Durán Merás, I.; Domínguez Manzano, J.; Airado Rodríguez, D.; Muñoz De La Peña, A. Detection and Quantification of Extra Virgin Olive Oil Adulteration by Means of Autofluorescence Excitation Emission Profiles Combined with Multi-Way Classification. *Talanta* **2018**, *178*, 751–762.
81. Ríos-Reina, Rocío, et al. "A comparative study of fluorescence and Raman spectroscopy for discrimination of virgin olive oil categories: Chemometric approaches and evaluation against other techniques." *Food Control* 158 (2024): 110250.
82. Ballabio, D. A MATLAB Toolbox for Principal Component Analysis and Unsupervised Exploration of Data Structure. *Chemom. Intell. Lab. Syst.* **2015**, *149*, 1–9.
83. Ballabio, D.; Consonni, V. Classification Tools in Chemistry. Part 1: Linear Models. PLS-DA. *Anal. Methods* **2013**, *5*, 3790.
84. Qannari, E.M.; Wakeling, I.; MacFie, H.J.H. A Hierarchy of Models for Analysing Sensory Data. *Food Qual. Prefer.* **1995**, *6*, 309–314.

85. Zeaiter, M.; Rutledge, D. Preprocessing Methods. In *Comprehensive Chemometrics*; Elsevier: Amsterdam, The Netherlands, 2009; pp. 121–231. ISBN 978-0-444-52701-1.
86. Rocha Baqueta, M.; Coqueiro, A.; Henrique Março, P.; Mandrone, M.; Poli, F.; Valderrama, P. Integrated 1H NMR Fingerprint with NIR Spectroscopy, Sensory Properties, and Quality Parameters in a Multi-Block Data Analysis Using ComDim to Evaluate Coffee Blends. *Food Chem.* **2021**, *355*, 129618.
87. Jouan-Rimbaud Bouveresse, D.; Pinto, R.C.; Schmidtke, L.M.; Locquet, N.; Rutledge, D.N. Identification of Significant Factors by an Extension of ANOVA–PCA Based on Multi-Block Analysis. *Chemom. Intell. Lab. Syst.* **2011**, *106*, 173–182.
88. Makimori, G.Y.F.; Bona, E. Commercial Instant Coffee Classification Using an Electronic Nose in Tandem with the ComDim-LDA Approach. *Food Anal. Methods* **2019**, *12*, 1067–1076.
89. Galvan, D.; de Andrade, J.C.; Conte-Junior, C.A.; Killner, M.H.M.; Bona, E. DD-ComDim: A DataDriven Multiblock Approach for One-Class Classifiers. *Chemom. Intell. Lab. Syst.* **2023**, *233*, 104748.
90. Mishra, P.; Roger, J.M.; Rutledge, D.N.; Biancolillo, A.; Marini, F.; Nordon, A.; Jouan-RimbaudBouveresse, D. MBA-GUI: A Chemometric Graphical User Interface for Multi-Block Data Visualisation, Regression, Classification, Variable Selection and Automated Pre-Processing. Chemom. *Intell. Lab. Syst.* **2020**, *205*, 104139.
91. Costantini, E.A.C.; Barbetti, R.; Bucelli, P.; L'Abate, G.; Lelli, L.; Pellegrini, S.; Storchi, P. Land Peculiarities of the Vine Cultivation Areas in the Province of Siena (Italy), with Reference to the Viticultural and Oenological Results of Sangiovese Vine. *Boll. Della Soc. Geol. Ital. Suppl.* **2006**, *6*, 147–159.
92. Rahmanian, N.; Jafari, S.M.; Wani, T.A. Bioactive Profile, Dehydration, Extraction and Application of the Bioactive Components of Olive Leaves. *Trends Food Sci. Technol.* **2015**, *42*, 150–172.
93. Girelli, C.R.; Angilè, F.; Del Coco, L.; Migoni, D.; Zampella, L.; Marcelletti, S.; Cristella, N.; Marangi, P.; Scortichini, M.; Fanizzi, F.P. 1H-NMR Metabolite Fingerprinting Analysis Reveals a Disease Biomarker and a Field Treatment Response in Xylella Fastidiosa Subsp. Pauca-Infected Olive Trees. *Plants* **2019**, *8*, 115.
94. Girelli, C.R.; Hussain, M.; Verweire, D.; Oehl, M.C.; Massana-Codina, J.; Avendaño, M.S.; Migoni, D.; Scortichini, M.; Fanizzi, F.P. Agro-Active Endo-Therapy Treated Xylella Fastidiosa Subsp. Pauca-Infected Olive Trees Assessed by the First 1H-NMR-Based Metabolomic Study. *Sci. Rep.* **2022**, *12*, 5973.
95. Benavente-García, O.; Castillo, J.; Lorente, J.; Ortuño, A.; Del Rio, J.A. Antioxidant Activity of Phenolics Extracted from *Olea europaea* L. Leaves. *Food Chem.* **2000**, *68*, 457–462.]
96. Huertas-Alonso, A.J.; Gavahian, M.; González-Serrano, D.J.; Hadidi, M.; Salgado-Ramos, M.; Sánchez-Verdú, M.P.; Simirgiotis, M.J.; Barba, F.J.; Franco, D.; Lorenzo, J.M.; et al. Valorization of Wastewater from Table Olives: NMR Identification of Antioxidant Phenolic Fraction and Microwave Single-Phase Reaction of Sugary Fraction. *Antioxidants* **2021**, *10*, 1652.

97. Goulas, V.; Exarchou, V.; Troganis, A.N.; Psomiadou, E.; Fotsis, T.; Briasoulis, E.; Gerothanassis, I.P. Phytochemicals in Olive-leaf Extracts and Their Antiproliferative Activity against Cancer and Endothelial Cells. *Mol. Nutr. Food Res.* **2009**, *53*, 600–608

98. Karkoula, E.; Skantzari, A.; Melliou, E.; Magiatis, P. Direct Measurement of Oleocanthal and Oleacein Levels in Olive Oil by Quantitative^{1} H NMR. Establishment of a New Index for the Characterization of Extra Virgin Olive Oils. *J. Agric. Food Chem.* **2012**, *60*, 11696–11703

99. Filardo, S.; Roberto, M.; Di Risola, D.; Mosca, L.; Di Pietro, M.; Sessa, R. *Olea europaea* LDerived Secoiridoids: Beneficial Health Effects and Potential Therapeutic Approaches. *Pharmacol. Ther.* **2024**, *254*, 108595.

100. Kalampaliki, A.D.; Giannouli, V.; Skaltsounis, A.-L.; Kostakis, I.K. A Three-Step, Gram-Scale Synthesis of Hydroxytyrosol, Hydroxytyrosol Acetate, and 3,4-Dihydroxyphenylglycol. *Molecules* **2019**, *24*, 3239.

101. Wishart, D.S.; Knox, C.; Guo, A.C.; Eisner, R.; Young, N.; Gautam, B.; Hau, D.D.; Psychogios, N.; Dong, E.; Bouatra, S.; et al. HMDB: A Knowledgebase for the Human Metabolome. *Nucleic Acids Res.* **2009**, *37*, D603–D610.

102. Agatonovic-Kustrin, Snezana, et al. "The bioprofiling of antibacterials in olive leaf extracts via thin layer chromatography-effect directed analysis (TLC-EDA)." *Journal of Pharmaceutical and Biomedical Analysis* 219 (2022): 114916.

103. Guimet, F.; Ferré, J.; Boqué, R.; Vidal, M.; Garcia, J. Excitation–Emission Fluorescence Spectroscopy Combined with Three-Way Methods of Analysis as a Complementary Technique for Olive Oil Characterization. *J. Agric. Food Chem.* **2005**, *53*, 9319–9328.

104. Lia, F.; Formosa, J.P.; Zammit-Mangion, M.; Farrugia, C. The First Identification of the Uniqueness and Authentication of Maltese Extra Virgin Olive Oil Using 3D-Fluorescence Spectroscopy Coupled with Multi-Way Data Analysis. *Foods* **2020**, *9*, 498.

105. Guimet, F.; Boqué, R.; Ferré, J. Cluster Analysis Applied to the Exploratory Analysis of Commercial Spanish Olive Oils by Means of Excitation−Emission Fluorescence Spectroscopy. *J. Agric. Food Chem.* **2004**, *52*, 6673–6679.

106. Guimet, F.; Ferré, J.; Boqué, R.; Rius, F.X. Application of Unfold Principal Component Analysis and Parallel Factor Analysis to the Exploratory Analysis of Olive Oils by Means of Excitation–Emission Matrix Fluorescence Spectroscopy. *Anal. Chim. Acta* **2004**, *515*, 75–85.

107. Giuliani, A.; Cerretani, L.; Cichelli, A. Chlorophylls in Olive and in Olive Oil: Chemistry and Occurrences. *Crit. Rev. Food Sci. Nutr.* **2011**, *51*, 678–690.

108. Galeano Díaz, T.; Durán Merás, I.; Correa, C.A.; Roldán, B.; Rodríguez Cáceres, M.I. Simultaneous Fluorometric Determination of Chlorophylls a and b and Pheophytins a and b in Olive Oil by Partial Least-Squares Calibration. *J. Agric. Food Chem.* **2003**, *51*, 6934–6940

109. Navarro-Orcajada, S.; Matencio, A.; Vicente-Herrero, C.; García-Carmona, F.; LópezNicolás, J.M. Study of the Fluorescence and Interaction between Cyclodextrins and Neochlorogenic Acid, in Comparison with Chlorogenic Acid. *Sci. Rep.* **2021**, *11*, 3275.

110. Hernández-Sánchez, N.; Lleó, L.; Diezma, B.; Correa, E.C.; Sastre, B.; Roger, J.-M. Multiblock Analysis Applied to Fluorescence and Absorbance Spectra to Estimate Total Polyphenol Content in Extra Virgin Olive Oil. *Foods* **2021**, *10*, 2556.

111. Zandomeneghi, M.; Carbonaro, L.; Caffarata, C. Fluorescence of Vegetable Oils: Olive Oils. *J. Agric. Food Chem.* **2005**, *53*, 759–766.

112. Quintanilla-Casas, B.; Rinnan, Å.; Romero, A.; Guardiola, F.; Tres, A.; Vichi, S.; Bro, R. Using Fluorescence Excitation-Emission Matrices to Predict Bitterness and Pungency of Virgin Olive Oil: A Feasibility Study. *Food Chem.* **2022**, *395*, 133602

113. Tasnuva, S.T.; Qamar, U.A.; Ghafoor, K.; Sahena, F.; Jahurul, M.H.A.; Rukshana, A.H.; Juliana, M.J.; Al-Juhaimi, F.Y.; Jalifah, L.; Jalal, K.C.A.; et al. α-Glucosidase Inhibitors Isolated from *Mimosa pudica* L. *Nat. Prod. Res.* **2019**, *33*, 1495–1499.

114. Wang, L.; Li, X.; Zhang, S.; Lu, W.; Liao, S.; Liu, X.; Shan, L.; Shen, X.; Jiang, H.; Zhang, W.; et al. Natural Products as a Gold Mine for Selective Matrix Metalloproteinases Inhibitors. *Bioorg. Med. Chem.* **2012**, *20*, 4164–4171.

115. Esposito, A.; De Luca, P.F.; Graziani, V.; D'Abrosca, B.; Fiorentino, A.; Scognamiglio, M. Phytochemical Characterization of Olea Europaea L. Cultivars of Cilento National Park (South Italy) through NMR-Based Metabolomics. *Molecules* **2021**, *26*, 3845.

116. De Cássia Lemos Lima, R.; Kongstad, K.T.; Kato, L.; José das Silva, M.; Franzyk, H.; Staerk, D. High-Resolution PTP1B Inhibition Profiling Combined with HPLC-HRMS-SPE-NMR for Identification of PTP1B Inhibitors from Miconia Albicans. *Molecules* **2018**, *23*, 1755.

117. Beteinakis, S.; Papachristodoulou, A.; Stathopoulos, P.; Mikros, E.; Halabalaki, M. A Multilevel LC-HRMS and NMR Correlation Workflow towards Foodomics Advancement: Application in Table Olives. *Talanta* **2024**, *280*, 126641.

118. Du, C.; Ma, C.; Gu, J.; Li, L.; Zhu, C.; Chen, L.; Wang, T.; Chen, G. Rapid Determination of Catechin Content in Black Tea by Fluorescence Spectroscopy. *J. Spectrosc.* **2020**, *2020*, 2479612.

119. Gonçalves, T.R.; Teixeira, G.G.; Santos, P.M.; Matsushita, M.; Valderrama, P. ExcitationEmission Matrices and PARAFAC in the Investigation of the Bioactive Compound Effects from the Flavoring Process in Olive Oils. *Microchem. J.* **2023**, *187*, 10

Acknowledgments

This work was realized within the framework of the projects:

- “PROFOOD-IV—Prodotti e processi innovativi della filiera di IV gamma” (PON ARS01_00755)

- Agritech National Research Center, European Union Next-GenerationEU (PIANO NAZIONALE DI RIPRESA E RESILIENZA (PNRR)—MISSIONE 4 COMPONENTE 2, INVESTIMENTO 1.4—D.D. 1032 17/06/2022, CN00000022)

-Progetto PRIN 2022 n. 2022KPMEXC_003, Settore ERC LS7, ammesso a finanziamento con Decreto MUR n. 20425/2024 (scorrimento graduatorie), CUP B53C24007560006. 2022KPMEXC - MET agonist antibody mRNA as therapeutic tool for myocardial infarction.

I would like to express my sincere gratitude to my supervisor, Prof.ssa Claudia Bonechi, for the scientific guidance, constant availability, and expertise demonstrated throughout the entire research process. The valuable advice and methodological rigor provided have been a fundamental reference point for the development of this work. I am also deeply grateful for the trust placed in me and for the significant contribution to my academic and professional growth.
A special thanks also goes to Prof. ssa Gabriella Tamasi and Professor Claudio Rossi.

List of publications

Baglioni, M., Clemente, I., Nardin, R., Bisozzi, F., **Costantini, S.**, Fattori, G., Tamasi, G., Rossi C. "Hydrogel Beads Loaded with Glucosinolate-Rich Brassicaceae Extract as a Controlled-Release Alternative to Biofumigation." *Molecules* 30.18 (2025): 3660.

Tatini, Duccio, Bisozzi. F., **Costantini, S.**, Fattori, G., Boldrini, A., Baglioni, M., Bonechi, C., Donati, A., Tozzi, C., Riccaboni, A., Tamasi, G., Rossi, C. "Geographical Origin Authentication of Leaves and Drupes from Olea europaea via 1H NMR and Excitation–Emission Fluorescence Spectroscopy: A Data Fusion Approach." *Molecules* 30.15 (2025): 3208.

Baglioni, M., Clemente, I., Tamasi, G., Bisozzi, F., **Costantini, S**., Fattori, G., Gentile, M., Rossi C. "Isothiocyanate-Based Microemulsions Loaded into Biocompatible Hydrogels as Innovative Biofumigants for Agricultural Soils." *Molecules* 29.16 (2024): 3935.

Borghini, F., Tamasi, G., Loiselle, S. A., Baglioni, M., Ferrari, S., Bisozzi, F., **Costantini, S**., Tozzi, C., Riccaboni, A. & Rossi, C. (2024). Phenolic profiles in olive leaves from different cultivars in Tuscany and their use as a marker of varietal and geographical origin on a small scale. *Molecules*, *29*(15), 3617.

Scientific communications

Francesca Borghini, Gabriella Tamasi, Steven Loiselle, **Sara Costantini**, Stefano Ferrari and Claudio Rossi - Assessment of the varietal and geographical origin of olive leaves and drupes using multivariate analysis of phenolic profiles – Spoke 9-WP1 Agritech, Siena 19/06/2024

Duccio Tatini, **Sara Costantini**, Flavia Bisozzi, Giacomo Fattori, Claudia Bonechi, Michele Baglioni, Gabriella Tamasi, Claudio Rossi - Geographical traceability of olive products using ^{1}HNMR spectroscopy – Spoke 9–WP1 Agritech, Siena 19/06/2024

Raffaello Nardin, Gabriella Tamasi, Flavia Bisozzi, **Sara Costantini**, Marco Consumi, Michele Baglioni, Cristiana Tozzi, Angelo Riccaboni, Claudio Rossi – ICP-MS analysis of trace and ultratrace metals in agricultural goods for a multivariate geographical identification of products of the Chianti wine and EVOO supply chain – Spoke 9-WP1 Agritech, Siena 19/06/2024

Duccio Tatini, **Sara Costantini**, Flavia Bisozzi, Giacomo Fattori, Claudia Bonechi, Marco Andreassi, Michele Baglioni, Gabriella Tamasi, Claudio Rossi - Geographical origin characterization of agri-food products used in Sangiovese wine production through ^{1}H-NMR spectroscopy coupled with multivariate statistical analysis – Spoke 9–WP1 Agritech, Siena 19/06/2024

Sara Costantini, Elena Moretti, Giulia Collodel, Claudia Bonechi, Claudio Rossi - Chlorogenic acid in zwitterionic liposomes: microfluidic optimization, synthesis and physicochemical characterization – Poster presentation at ”19th European Student Colloid Conference”, European Colloid and Interface Society, Bordeaux 26/06/2024

Gemma Leone, Michele Baglioni, Raffaello Nardin, Gabriella Tamasi, Flavia Bisozzi, **Sara Costantini**, Giacomo Fattori and Claudio Rossi - Physico-chemical characterization of a chitosanbased nanocomposite film containing copper nanoparticles – PON PROFOOD-IV Workshop, Roma 19/09/2024

Gemma Leone, Michele Baglioni, Raffaello Nardin, Gabriella Tamasi, Flavia Bisozzi, **Sara**

Costantini, Giacomo Fattori and Claudio Rossi - Physico-chemical characterization of a zein-based nanocomposite film containing silver nanoparticles - PON PROFOOD-IV Workshop, Roma 19/09/2024

Michele Baglioni, Raffaello Nardin, Gabriella Tamasi, Flavia Bisozzi, **Sara Costantini**, Giacomo Fattori and Claudio Rossi - Use of dilute HClO solutions as an innovative, cost-effective, and safe method for disinfection of fresh-cut (pre-packaged) produce – PON PROFOOD-IV Workshop, Roma 19/09/2024

Michele Baglioni, Gabriella Tamasi, Flavia Bisozzi, **Sara Costantini**, Giacomo Fattori, Duccio Tatini, Claudio Rossi - Microemulsions based on synthetic pesticides loaded into controlled-release hydrogels - PON PROFOOD-IV Workshop, Roma 19/09/2024

Michele Baglioni, Duccio Tatini, Gabriella Tamasi, Flavia Bisozzi, **Sara Costantini**, Giacomo Fattori e Claudio Rossi - Physical mixtures of isothiocyanates adsorbed on biocompatible polymers for the fumigation of agricultural soils - PON PROFOOD-IV Workshop, Roma 19/09/2024

Michele Baglioni, Duccio Tatini, Ilaria Clemente, Raffaello Nardin, Gabriella Tamasi, Flavia Bisozzi, **Sara Costantini**, Giacomo Fattori and Claudio Rossi - Hydrogels for the controlled release of glucosinolates extracted from Brassicaceae – a sustainable treatment for agricultural soils - PON PROFOOD-IV Workshop, Roma 19/09/2024

Michele Baglioni, Duccio Tatini, Ilaria Clemente, Gabriella Tamasi, Flavia Bisozzi, **Sara Costantini**, Giacomo Fattori, Claudio Rossi - Isothiocyanate-based microemulsions loaded into biocompatible hydrogels as innovative biofumigants for agricultural soils - PON PROFOOD-IV Workshop, Roma 19/09/2024

Sara Costantini, Giacomo Fattori, Claudia Bonechi, Gabriella Tamasi, Alessandro Donati and Claudio Rossi - Chlorogenic acid in zwitterionic liposomes: microfluidic optimization, synthesis and physicochemical characterization – Poster presentation at Meeting of CSGI, Bari 18/09/2025

Sara Costantini, Simone Pepi, Claudia Bonechi, Gabriella Tamasi, Alessandro Donati and Claudio

Rossi - Eye gel based on hyaluronic acid and cationic liposomes: synthesis and characterization - Poster presentation at Meeting of CSGI, Bari 18/09/2025